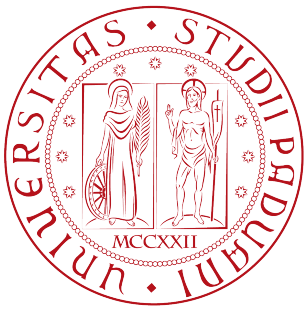

UNIVERSITÀ DEGLI STUDI DI PADOVA

Dipartimento di Fisica e Astronomia "Galileo Galilei"

PhD in Physics - XXXVI cycle

COMMISSIONING OF QUANTUM NOISE REDUCTION FOR AdV+ AND STUDY OF NON-EQUILIBRIUM THERMAL NOISE

Supervisor:
Dr. Livia Conti

Co-Supervisors:
Prof. Giacomo Ciani
Dr. Jean-Pierre Zendri

Candidate:
Luis Diego Bonavena

2023

Supervisor: Dr. Livia Conti

MANCOMANNAVA

ACKNOWLEDGEMENT

I would like to thank first of all the Virgo group of Padova for allowing me to have this experience. Special thanks go to my supervisor Livia Conti, for her guidance throughout this journey, constantly providing the right advice at the right times. Her support has been crucial and I am truly grateful for her wisdom and assistance. A big thanks to Giacomo Ciani for his support despite the distance, for teaching me the importance of not taking anything for granted, and for advising me on future choices. I want to express my sincere gratitude to Jean-Pierre Zendri for including me in Virgo activities, for his incredible patience in explaining the same concepts multiple times, and for the laughter that brought light to challenging moments. And, of course, thanks for the monitor! I would like to extend my appreciation to Marco Bazzan for imparting the valuable lesson that choosing a good wine is not solely about the price. Thanks also to Matteo Leonardi for the few but enlightening discussions.

I want to express my gratitude to the entire QNR group. Specially to Marco Vardaro for being my reliable point of reference during challenging times and for always coming to the rescue when things do not go as planned. Thanks to Martina De Laurentis for sharing infinity night shifts and for imparting the skill of alignment even when the beam disappears. Thanks to Virgo vacuum group for the loan of the ion pump that made it possible to complete the measurements in this thesis.

Thank you to Gabriella for accompanying me on this journey from the beginning to the end. To Giulio for involving me in different activities outside of work. To Andrea and Stefano for the numerous scientific (and non) constructive comparisons. To Nicole and Giulia or enhancing the experience at LNL over the past year. To the climbing group for fun times togheter. Thanks also to the Cimetti's and Cani's for the many spritz.

I want to thank Durim and Federico for the many weekends together and for trips to Venezia. Thanks to all the friends who have been there during these three years and made me feel at home.

I am extremely grateful to my family for supporting me in this choice and to Lucio and Lucia for the many relaxed moments during this period.

Finally, the most important thank you to Caterina, for the unwavering support, consistently encouraging me to give my best and standing by my side on every occasion.

ABSTRACT

The pioneering detection of gravitational waves has opened a new era of astronomy. Since the first detection in 2015, interferometric gravitational wave detectors have undergone several upgrades aimed at improving sensitivity and expanding event detection capabilities. These efforts yielded significant results during the lastest scientific observation (O3) conducted by the LIGO-Virgo collaboration, culminating in the detection of approximately one gravitational wave event per week, with a total of 74 potential candidates in less than a year [1][2]. For the following scientific observation (O4), a planned two-year break has been scheduled with the objective of significantly enhancing the sensitivity of gravitational wave interferometers across their entire frequency spectrum.

This thesis discusses two noises that limit the sensitivity of gravitational wave interferometers, specifically Quantum noise and Thermal noise. The former is due to the quantum nature of light and affects the interferometers sensitivity over the entire frequency band. Mitigate this noise is a crucial aspect of advancing the field of gravitational wave detection and in this thesis work is shown the method adopted in Virgo to overcome the Standard Quantum Limit. Thermal noise instead is dominating in the low and medium frequency range. In particular, this noise arises from the intrinsic fluctuations within the materials constituting the components of the interferometer, such as suspension fibers and mirrors. In this work, it is described an on-bench experiment dedicated to the study and characterization of the thermal noise in and out of the thermodynamic equilibrium.

Addressing quantum noise remains a crucial aspect of the effort during the O4 commissioning. During O3, quantum noise was partially mitigated in both the two Advanced LIGO and in Advanced Virgo by employing Frequency Independent Squeezing (FIS), targeted at reducing noise in the high-frequency range. However, addressing broadband quantum noise necessitates the adoption of Frequency-Dependent Squeezing (FDS). FDS involves the utilization of a detuned cavity, enabling the rotation of the squeezing ellipse to simultaneously suppress quantum noise at both low and high frequencies.

The first part of this thesis delves into the technical aspects of the FDS technique and its integration into the Virgo interferometer. Following a theoretical introduction to elucidate the potential enhancements that squeezed states can offer in terms of interferometer sensitivity, an overview of the Quantum Noise Reduction system (QNR) in Virgo is provided. The primary focus of our work is directed towards the methods that we used for establishing an efficient and stable stand-alone FDS. We give special attention to characterizing the system, particularly addressing potential losses that may impact the squeezing injection. A key part of our work is the implementation of a method to measure the FSR of the filter cavity after each unlock. This enable the first long-term measurements of the stand-alone FDS. Concluding this first part is a detailed account of the efforts invested in the initial application of FIS injection. At this stage we are able to reestablish alignment between the QNR system and the interferometer, close all control loops, and measure the first effects of injecting squeezed vacuum states on interferometer sensitivity. This serves as a preliminary step during the commissioning of the interferometer in preparation for the scientific run O4.

The second part of this thesis focuses on the implications of deviating from the conventional assumption of thermodynamic equilibrium for components contributing to thermal noise. The experiment presented focuses on quantifying the thermal noise of a mechanical oscillator through its longitudinal resonance mode, both in and out of equilibrium due to thermal differences between the extremes. The oscillator motion is recorded using an interferometric readout. After we restored and improved the readout optical line, our efforts are focused to to enhance the experiment performance and its calibration. In particular we worked to reduce different noise sources, optical and mechanical, and to characterize the calibration problems that can arise from the optics imperfections. Finally, we acquired thermal noise measurements under thermodynamic equilibrium conditions to verify the correspondence between the effective temperature obtained by longitudinal resonance mode and the room thermodynamic temperature. All the data acquired has been analyzed with a Python code developed during this thesis work.

CONTENTS

I GRAVITATIONAL WAVE DETECTION

The purpose of this chapter is to introduce the field of gravitational waves (GW) and GW interferometric detectors. This provides context for the studies presented in this thesis. In the subsequent chapters, we delve into essential noise contributions that impact gravitational wave sensitivity, specifically quantum noise (§ III.1) and thermal noise (§ V.2).

I.1. Introduction to gravitational waves

Gravitational waves (GW) are a fundamental prediction of Albert Einstein's general theory of relativity, which is the most accepted theory of gravity. These waves are, essentially, ripples in the structure of space-time, generated by bodies and events that animate the Universe. From an observational point of view, the most energetic of these astrophysical occurrences produce the most intense signals and are potentially easily detectable. Traveling at the speed of light, these GWs carry unique and valuable information about their origin and the nature of gravity, which cannot be obtained solely through the observation of the Cosmos using electromagnetic radiation. This section aims to briefly describe this phenomenon and its origin.

I.1.1. Overview of General Relativity

The theory of General Relativity revolutionized the way gravity is conceived and studied. That is, gravity is not considered an attractive force of massive bodies anymore, as in the Newtonian depiction, but became a description of how mass and energy can curve the space-time in which the masses themselves exist and move. In other words, the gravitational field can alter the geometry of space-time, changing the way the distance between two events is measured. Therefore, by describing space-time as a four-dimensional manifold, the separation between events is defined as an invariant quantity in the four-vector formalism of the following form [3]:

$$ds^2 = g_{\mu\nu} dx^\mu dx^\nu \tag{I.1}$$

where $g_{\mu\nu}$ represents a mathematical quantity referred to as the metric tensor that outlines each coordinate's reciprocal behavior when the others undergo a transformation.

The Einstein field equations, which represent the core of the whole theory, describe how the curvature of space-time is determined by mass and energy density. Curvature is described by the Einstein tensor $G_{\mu\nu}$, which includes combinations of the metric $g_{\mu\nu}$ and its derivatives. Mass and energy are represented by the energy-momentum tensor $T_{\mu\nu}$ that describes the energetic properties of the source of the gravitational field. The equations are written as follows:

$$G_{\mu\nu} = \frac{8\pi G}{c^4} T_{\mu\nu} \tag{I.2}$$

where c is the speed of light and G is the Newtonian gravitational constant. I.2 consists of ten coupled partial differential equations. A key characteristic of these equations is their non-linear nature with respect to the metric, indicating that the gravitational field interacts with itself [4]. The complexity arising from this non-linearity makes finding solutions challenging. Nonetheless, certain approximations, like considering scenarios of weak gravitational fields, can be used to simplify and solve these equations [5].

I.1.2. Gravitational waves in linearized theory

GWs arise as wave solutions to Einstein field equations. This kind of solution manifests clearly in the case of the weak field approximation as discussed below.
In Einstein's theory of special relativity, where the effect of gravity is not taken into account, space-time is described as flat. In this special case of null gravity, there is at least one choice of coordinates x_μ for which, the invariant interval can be written as:

$$ds^2 = \eta_{\mu\nu} dx^\mu dx^\nu \tag{I.3}$$

where $\eta_{\mu\nu}$ is called Minkowski metric that, in Cartesian coordinates is given by:

$$\eta_{\mu\nu} = \begin{pmatrix} -1 & 0 & 0 & 0 \\ 0 & 1 & 0 & 0 \\ 0 & 0 & 1 & 0 \\ 0 & 0 & 0 & 1 \end{pmatrix} \tag{I.4}$$

In the small gravity regime, the metric can be described as the sum of the flat Minkowski metric tensor $\eta_{\mu\nu}$ and a small perturbation $h_{\mu\nu} \ll 1$ due to the weak gravitational field [5]:

$$g_{\mu\nu} = \eta_{\mu\nu} + h_{\mu\nu} \tag{I.5}$$

In this approximation, the Einstein equations take on a linear form and are more easily solvable. By selecting a suitable set of coordinates (Lorentz gauge) and taking into account symmetry properties [5], they can be represented in this simplified form:

$$\Box \bar{h}_{\mu\nu} = -\frac{16\pi G}{c^4} T_{\mu\nu} \tag{I.6}$$

where $\Box$ is the flat space d'Alambertian $\Box = \eta_{\mu\nu}\partial^\mu\partial^\nu$ and $\bar{h}_{\mu\nu} = h_{\mu\nu} - \frac{1}{2}\eta_{\mu\nu}h$, with $h = Tr(h_{\mu\nu})$. At this point, the solutions for the propagation of the waves in vacuum are obtained by moving to a space with no sources, i.e. by placing $T_{\mu\nu} = 0$, where:

$$\Box \bar{h}_{\mu\nu} = 0 \tag{I.7}$$

The equation (I.7) is a wave equation for the space-time perturbation $\bar{h}_{\mu\nu}$ and its solution is a complete set of plane waves, where the real ones represent physical gravitational waves [5]:

$$\bar{h}_{\mu\nu} = \mathcal{R}e(\epsilon_{\mu\nu} e^{ik^\alpha x_\alpha}) \tag{I.8}$$

In this context, $\epsilon_{\mu\nu}$ denotes the polarization matrix, which is a symmetric and complex matrix that characterizes the various potential polarization states of the gravitational wave. k^α is the wave vector $k^\alpha = (\frac{\omega}{c}, \vec{k})$, which implies that these metric perturbations travel at the speed of light through space-time, with ω the gravitational wave's angular frequency. Using the residual gauge freedom, the coordinates can be chosen (TT-gauge) such that, for a wave propagating in the z-direction, the metric is as follows:

$$h_{\mu\nu} = (h_+ \epsilon^+_{\mu\nu} + h_\times \epsilon^\times_{\mu\nu}) e^{i(\omega t + kz)} \tag{I.9}$$

The tensors $\epsilon^+_{\mu\nu}$ and $\epsilon^\times_{\mu\nu}$ form a basis for the polarization tensor $\epsilon_{\mu\nu}$:

$$\epsilon^+ = \begin{pmatrix} 0 & 0 & 0 & 0 \\ 0 & 1 & 0 & 0 \\ 0 & 0 & -1 & 0 \\ 0 & 0 & 0 & 0 \end{pmatrix} \qquad \epsilon^\times = \begin{pmatrix} 0 & 0 & 0 & 0 \\ 0 & 0 & 1 & 0 \\ 0 & 1 & 0 & 0 \\ 0 & 0 & 0 & 0 \end{pmatrix} \tag{I.10}$$

The two independent modes of polarization are called "plus" + and "cross" $\times$. A way of visualizing the effect of GWs on matter is to consider a set of test masses arranged along a circumference on a plane. The passage of a GW in a direction perpendicular to that plane causes a tidal deformation in the distance between the masses at the wave's frequency, as shown in figure I.1. In both the polarization cases, the deformation occurs along two perpendicular axes and is inherently differential. This means that if one axis is stretched, the other is shrunk. This relative deformation, identified as strain amplitude, is a representation of the amplitude of the gravitational wave, typically denoted by h.

I.1.3. Gravitational waves: sources and detection

To solve the linearized Einstein's equation in the presence of a source, Eq. I.6, it is used the retarded potential solution which can be expanded in terms of multipole [5]. Unlike electromagnetic radiation, where the dipole term dominates under specific conditions, in GW production, particularly when the source dimensions are negligible compared to its distance, the leading order is the quadrupole. In practice, this means that to produce GWs, it is needed a system that, moving in a gravitational field, shows an asymmetry with non-zero time derivative on a different axis with respect to one of its central motion. The most intense and non-negligible

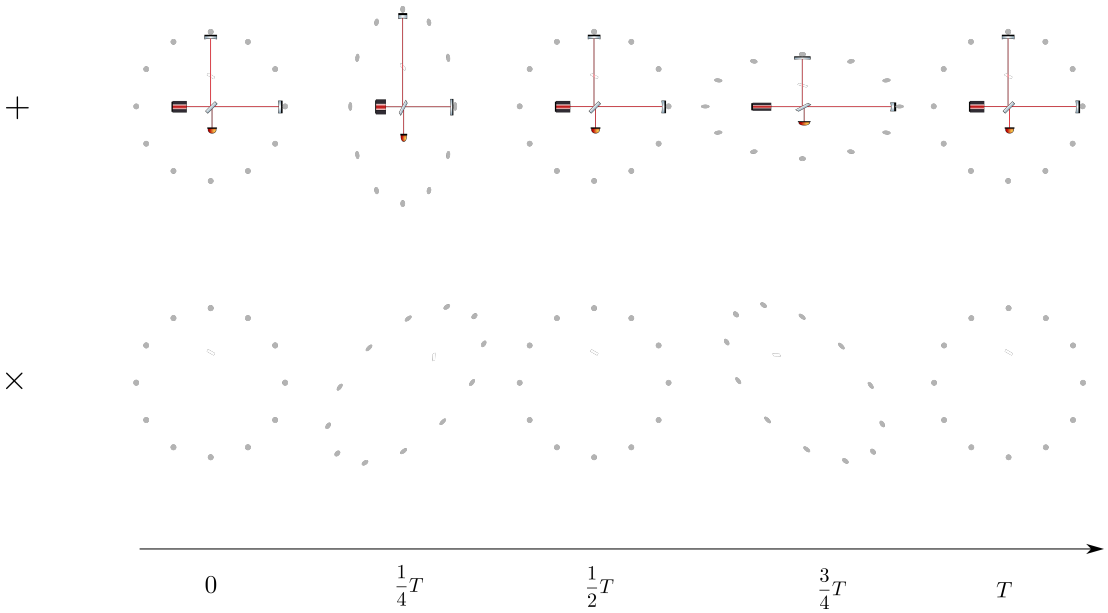

FIGURE I.1: Impact of a gravitational wave on a ring of free falling test masses throughout an entire period T. The propagation direction is orthogonal to the page, displaying the two independent modes of polarization, referred to as "plus" (top row) and "cross" (bottom row). Additionally, the image includes a Michelson interferometer, exhibiting the effect of the passing wave on its two interferometer arms.

space-time perturbations are produced by massive astrophysical objects undergoing extreme events.

The detection of the first GW was possible with the LIGO detector. Currently, there is a network of ground-based GWs detectors made of different five main interferometers: the two European, Virgo (V1) in Italy and GEO600 (G1) in Germany; the two American, LIGO Hanford (H1) and LIGO Livingston (L1); one in Japan, KAGRA (K1). These facilities work in synergy to increase the chances of detecting the signals and to give better constraints on their measurements and their parameter estimations. From an experimental point of view, important characteristics of a GW source are the frequency content of its signal, the expected amplitude at Earth, and their rate. Typically, GW sources are classified by their duration in continuous and transients. A list of the primary sources of interest for current-generation ground-based detectors is briefly reported and discussed in the following paragraphs.

COMPACT BINARY COALESCENCES

The only sources of GWs that have been detected so far are those produced by compact binary coalescences made of neutron stars and black holes, which belong to the "transient" category. Compact binaries are astrophysical systems made of two massive and dense objects bound together by their gravitational field. The two bodies rotate around the system's center of mass: in doing so, the system loses energy by emission of gravitational waves, and consequently their orbits shrink and the bodies inspiral, getting closer and closer, until they merge into one single more massive object. The final body has a mass that is smaller than the sum of the two initial masses mainly due to the energy loss by gravitational wave emission [3].
The coalescence's signal is known to have three distinct phases: the inspiral, the merger, and the ringdown. The inspiral is the phase when the two objects orbit one around each other. The merger is the signal's peak when the two objects merge. The ringdown is a damped final phase due to the settling of the newborn final object reaching equilibrium. The last two are the most difficult phases to study analytically since gravity is in a strong regime of interaction, and some approximations can not be taken anymore into account [5]. Figure I.2 presents an example

of the signal. As the two starting objects draw nearer and nearer in the inspiral phase, their angular velocity increases, and consequently, the frequency and amplitude of the signal emitted. In fact, their typical signature is the frequency evolution in time as they approach one other in the inspiral phase, which under an assumption of circular orbit can be written as follows [3]:

$$\nu(\tau_c) = \frac{1}{\pi}\Big(\frac{G\mathcal{M}}{c^3}\Big)^{-5/8}\Big(\frac{5}{256\,\tau_c}\Big)^{3/8} \tag{I.11}$$

where τ_c represents the time left for the two objects to merge, ν is the gravitational wave frequency, $\mathcal{M}$ is the chirp mass defined as:

$$\mathcal{M} = \mu^{2/3}M^{2/5} \tag{I.12}$$

Considering m_1 and m_2 the masses of the two bodies, $\mu = \frac{m_1 m_2}{m_1+m_2}$ is the reduced mass and $M = m_1 + m_2$ is the total mass of the system. At the same time, the signal's amplitude increases along with the frequency. In fact, the strain amplitude of gravitational waves observed at a distance r from the source and considering aligned spins is:

$$h \simeq 10^{-21}\left(\frac{\mathcal{M}}{M_\odot}\right)^{5/6}\left(\frac{\nu}{100\text{ Hz}}\right)^{5/6}\left(\frac{15\text{ Mpc}}{r}\right) \tag{I.13}$$

For the current detector infrastructure, binaries that produce detectable gravitational waves are those made of the most dense compact objects: neutron stars and astrophysical black holes. Both of them are the leftover core of the death of massive stars. The mass range of Neutron star roughly runs between 1 and 3 $M_\odot$, while black holes of stellar origin can go up to around 100 $M_\odot$. The measure of the precise value of the threshold mass that separates neutron stars and black holes is an open scientific question, mainly because the exact internal equation of the state of neutron stars still needs to be established. The signals observed can be classified according to the nature of the bodies in the merging binary:

- Binary Neutron Star (BNS): a binary system of two neutron stars;
- Binary Black Hole (BBH): a binary system of two black holes;
- Neutron Star-Black Hole Binary (NSBH): a binary system of a neutron star and a black hole.

Each distinct binary pair generates a unique GW signal determined by all the various factors describing the system, including the masses of the objects, the position of the source, their orbital orientations with respect to Earth, the spins, the tidal deformability for neutron stars, and the distance of the source. For example, consider a system of two neutron stars with a chirp mass of $\mathcal{M} = 1.21 M_\odot$ at a distance of 100 Mpc. At a time of 2 s before the merger, the signal reaches a frequency of $\sim$ 100 Hz and a strain amplitude of $h \sim 4 \cdot 10^{-23}$.

Continuous Gravitational Waves

Continuous GWs are expected to be produced by a single spinning massive object like a neutron star when it exhibits some degree of asymmetry on an axis different from the rotational one, meaning that they have a distortion from the perfect spherical shape on another axis. In other words, when they have a non-zero quadrupole moment variation in the gravitational potential. In addition, these sources experience a weak spindown in their rotation. Given this, these sources are expected to produce a continuous and quasi-monochromatic gravitational signal with a frequency directly connected to their rotational period. It can be written as [6]:

$$h \simeq 3 \cdot 10^{-25}\left(\frac{\epsilon}{10^6}\right)\left(\frac{I}{10^{-38}\text{ kg}\cdot\text{m}^2}\right)\left(\frac{\nu}{1\text{ kHz}}\right)^2\left(\frac{10\text{ kpc}}{r}\right) \tag{I.14}$$

where I is the moment of inertia, and ϵ the equatorial non-axisymmetry ellipticity accounts for the asymmetry of the system, and r is the source distance. From an observational point of

view, the so-called targeted search is one of the most common ways to try to measure this signal. In fact, sometimes, can be observed neutron stars that emit regular beams of electromagnetic radiation from their magnetic poles, which gives them the name of Pulsars. This emission occurs when the magnetic axis of the staris misaligned with respect to its rotational axis [7]. Suppose one can resolve the neutron star as a pulsar and consequently know its rotational period and other source parameters (such as position and spindown). At this point, one can look for the corresponding gravitational signal. Other types of searches, like directed and all-sky, can be conducted, but are computationally more expensive [8]. Even if the expected strain is relatively weak, the continuous nature of the signal allows it to be integrated over a long period, consequently increasing the signal-to-noise ratio (SNR) and the probability of detection [9].

Core Collapse Supernovae

Current generation detectors are expected to be sensitive to events of core-collapse supernova distant up to a few kpc, that belong to the "transient" signals category. Unfortunately, within a volume of this radius, the rate of supernova events is low, so next-generation detectors will be potentially needed to increase the chance of measuring a supernova event [10]. An upper-bound for their occurrence frequency in our Galaxy is $f_{collapse} < 0.13\text{yr}^{-1}$ with 90% confidence level [11].
Core collapse supernovae are energetic events that occur when a massive star reaches the end of its nuclear-burning potential. When such stars (approximately $\geq 8\text{M}_{\odot}$) reach a state in which they have an iron core, there are no more reactions that are energetically favorable to be accomplished. Without any energetic fuel, the core then starts to shrink, subsequently causing the collapse of the star. When the core overpasses nuclear densities, the shrinking is interrupted abruptly, the envelope matter rebounds over it, and a powerful shock wave propagates outward. The dynamical details of such events are still not completely understood, so it is difficult to reconstruct their gravitational waveform. Two primary explosion mechanisms seem to be favored: the neutrino and magnetorotational. The first one is based on a strong neutrino emission driving the explosion. The particles are strongly supposed to contain almost 99% of the released energy, and the associated gravitational wave arising contains components generated by matter's turbulence. The signal is expected to last for $\sim 0.3 - 2$ s with an amplitude of $\sim 10^{-22}$ at a distance of 10 kpc [12]. The second mechanism considers an explosion driven by the rotation and magnetic field of the star. The collapse will imprint a deformation on the rapidly rotating core, leading to a significant change in the derivative of the quadrupole moment. This main feature of the signal is the spike at the core rebound, and typically are expected to last less than those neutrino driven and have an amplitude of $\sim 10^{-21}$ at 10 kpc [12].

The proposed list is not exhaustive of the wide variety of gravitational wave sources that have been hypothesized and will be of interest to future-generation gravitational wave detectors. A key example is that of the various species of stochastic backgrounds. Stochastic Backgrounds are stochastic signals due to the incoherent superposition of signals produced by unresolved astrophysical sources and cosmological events [5].

I.1.4. Gravitational wave events catalogue

The large number of detected events during the observing runs, made it necessary to establish a catalog. The LIGO-Virgo collaboration has facilitated access to data related to these detection events through the Gravitational Waves Open Science Center (GWOSC) [13]. These events are documented in the Gravitational Wave Transient Catalog (GWTC), which is periodically updated following subsequent observing runs:

- GWTC-1 documents the events from the first (O1) and second (O2) Observing Runs. Specifically, O1 contains 3 binary black hole mergers, while O2 recorded 7 BBH events and the first-ever observed binary neutron star event, GW170817 [14].

- GWTC-2 corresponds to the initial segment of the third Observing Run (O3a), during which 39 gravitational wave events were identified. This catalog includes BBH mergers and events with components that could not be definitively classified as either neutron stars or black holes. Notably, this is the first appearance of systems with significantly unequal mass ratios in the catalog [2].
- GWTC-2.1 expands GWTC-2, where a reanalysis of the O3a data revealed eight new high-significance BBH events [15].
- GWTC-3 is associated with the latter part of the third Observing Run (O3b) and contains records of 35 compact binary coalescences. Each event has been confirmed as either a BBH or a neutron star-black hole (NSBH) merger, with none classified as a BNS [16].

A summary of the detections that occurred up to the end of O3 is given in Figure I.3, where the masses of each measured coalescence's initial and final objects are shown. In the following part, a list of some of the most noticeable events from both a historical and scientific point of view will be presented.

GW150914

On the 14th of September 2015, the Advanced LIGO interferometers detected a signal from the merger of two black holes, then named GW150914. This event marked the first-ever direct observation of a GW. Analysis of the signal indicated that the masses of the two coalescing bodies were $M_1 = 36^{+5}_{-4}\,\mathrm{M}_\odot$ and $M_2 = 29^{+4}_{-4}\,\mathrm{M}_\odot$, that made it clear to be in front of a pair of black holes. The system is at a distance of $410^{+160}_{-180}\,\mathrm{Mpc}$ [17]. Figure I.2 shows the plots relative to the signal detection.

GW170814

In 2017 Advanced Virgo joined the two American interferometers in the observations. The 14th of August of the same year was the time for the first event observed by three interferometers at a time. The GW event, then called GW170814, was produced by a binary black hole system with $M_1 = 30.5^{+5.7}_{-3.0}\,\mathrm{M}_\odot$ and $M_2 = 25.3^{+2.8}_{-4.2}\,\mathrm{M}_\odot$, at a distance of $540^{+130}_{-210}\,\mathrm{Mpc}$ [18]. This event showed the importance of observing GW signals with at least three detectors. In fact, the localization of GW sources in the sky is done by triangulation, that is, by measuring the mutual delay with which the signal arrives at the different detectors. This means that at least three interferometers are needed to detect a unique area in the sky, and the accuracy with which this area is detected increases as the number of observatories involved increases [19].

GW170817

After three days, on the 17th of August, the network of Advanced LIGO-Virgo triggered another signal. Subsequent analysis revealed that this signal originated from two bodies with masses of $M_1 = 1.46^{+0.12}_{-0.10}\,\mathrm{M}_\odot$ and $M_2 = 1.27^{+0.09}_{-0.09}\,\mathrm{M}_\odot$ at a distance of $40^{+7}_{-15}\,\mathrm{Mpc}$ [20], indicative of a binary neutron star system, the first one to be ever detected. This event marked a crucial transitional moment in the history of astronomy. This was not only the first binary neutron star to be seen but also the first multi-messenger observation with both electromagnetic and gravitational waves. For the first time in history, information from these two different "messengers" of the same event was combined, involving an extensive worldwide network of astronomical facilities. Combining multiple messengers is of high scientific significance, as it provides access to more information about the sources and their environment, cosmology, and fundamental physics [21].

I.2. Interferometric detectors

The initial gravitational radiation detectors, pioneered by Weber at the University of Maryland in the 1960s, were made up of massive (order of a ton) cylinders, hence the name of bar detectors.

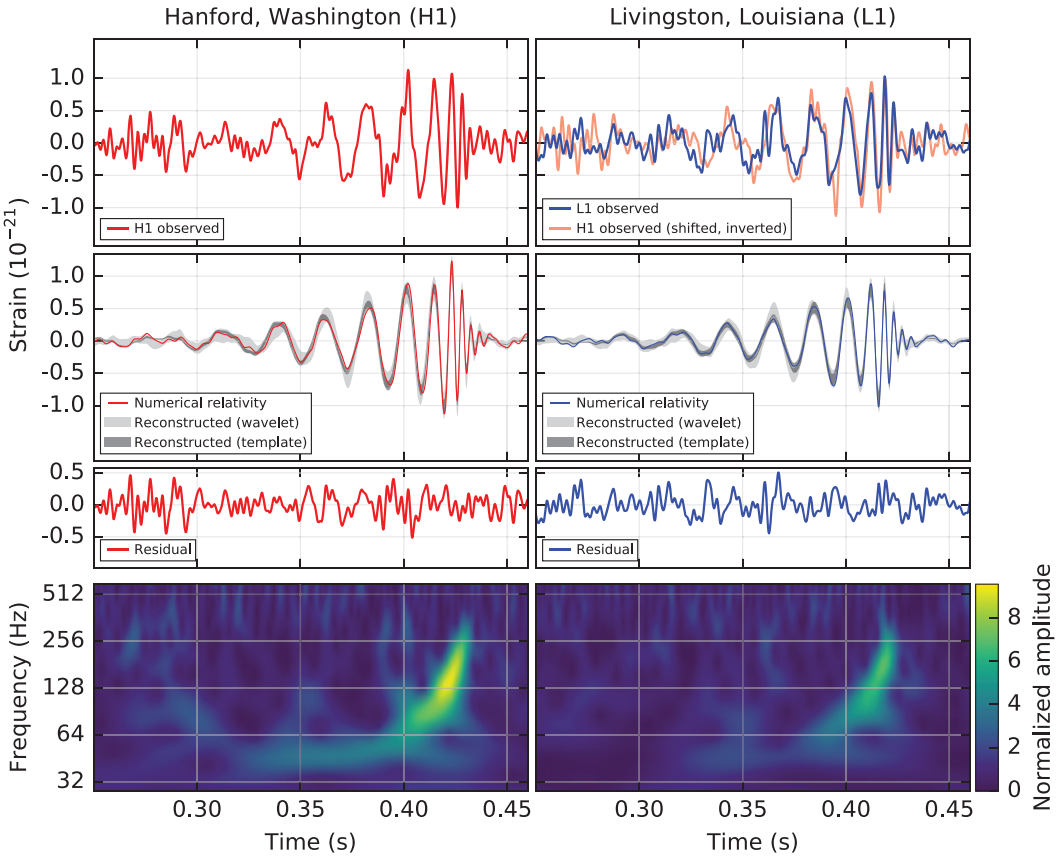

FIGURE I.2: The image shows some plots relative to the event GW150914. (top) A display of the strain signal at the time of the event. On the left the signal detected by Hanford (H1) and on the right the signal at Livingston (L1). (center) The solid red line represents a reconstructed numerical relativity signal with the same parameters as those of the events, and the two shaded grey areas represent two different reconstructions of the 90% credible intervals, one with an astrophysical template of the signal (dark grey), the other with an unmodeled superposition of sine-Gaussian wavelets (light grey). (bottom) The two images present the leftover signal after subtracting the numerical relativity template from the data. Fourth row: time-frequency map of the signal, highlighting the rise in frequency over time. [17]

These cylinders were designed to resonate in their first quadrupolar mode at about 900 Hz where signals from supernova explosions were expected: the bar would absorb energy from the incoming signal and this is read as an excitation of the resonant mode via a (typically capacitive) transducer. However, these early instruments exhibited low sensitivity and bandwidth, prompting the need for more advanced methods to detect the faint signals carried by GWs. In parallel, the construction of interferometric detectors began. These highly sensitive devices use laser beams to measure the difference in the length of two perpendicular, long arms, each terminated with mirrors. The transit of a GW triggers the displacement of two mirrors, resulting in a change in the interference of the beams that have propagated along the arms and which are then recombined. By analyzing the data from this signal, it is feasible to trace the presence of the GW.

I.2.1. Working principle of simple Michelson interferometer

The differential deformations due to the passage of a GW are ideally captured by a Michelson interferometer (see Figure I.1), an optical device made to translate the length difference between

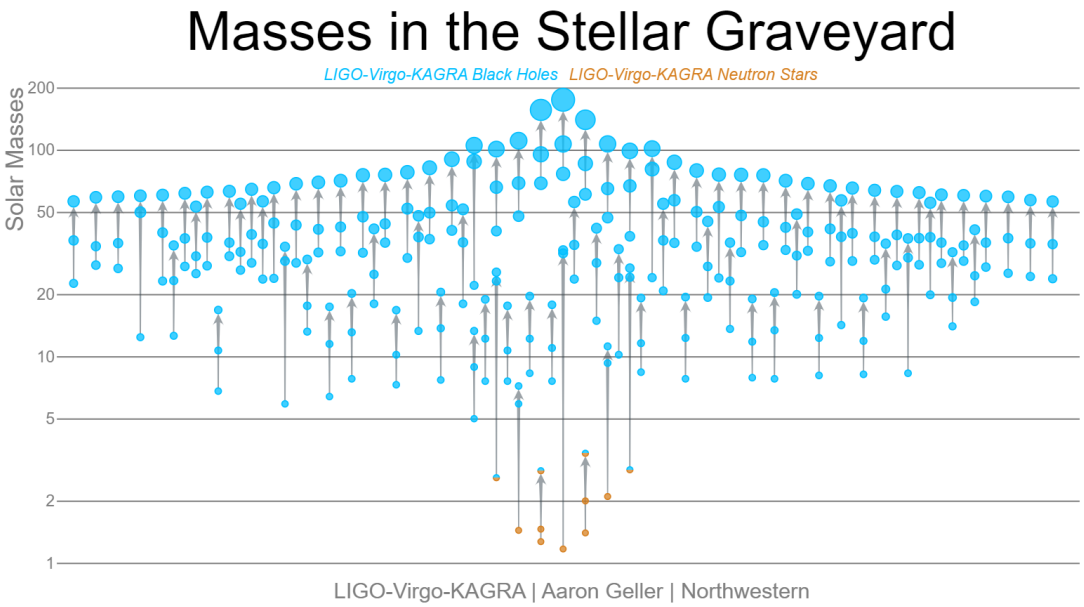

FIGURE I.3: Summary of all the compact binary coalescences detected up to the end of O3. The plot shows the masses of the initial and final objects in solar mass units. Credit: LIGO-Virgo / Aaron Geller / Northwestern University

two perpendicular paths into an optical signal. Here, the detailed derivation of all the expressions of the laser into the interferometer is not delved into. (see [5] for details). The discussion starts directly with the the total electric field amplitude at the detection photodiode:

$$E_{PD} = \frac{i}{2} E_{in} \left(e^{i2kL_x(t)} - e^{ik2L_y(t)} \right) \tag{I.15}$$

where E_{in} is the field amplitude of the laser input, $L_x(t)$ and $L_y(t)$ are the lengths of the two interferometer arms defined as a function of the strain $h(t)$:

$$L_x(t) = L \left(1 + \frac{1}{2} h(t) \right) \tag{I.16}$$

$$L_y(t) = L \left(1 - \frac{1}{2} h(t) \right) \tag{I.17}$$

Here L is the length of the two arms in the absence of the GW. The magnitude of the GW is embedded within the phase difference accumulated between the two arms. This is most explicitly represented by defining two quantities:

$$L \equiv \frac{L_x + L_y}{2} \tag{I.18}$$

$$\delta L \equiv \frac{L_x - L_y}{2} \tag{I.19}$$

The first one represents the interferometer size while the second unperturbed arm length difference. Rewriting these equations while taking into account the effect of a GW yields:

$$L(t) = L \tag{I.20}$$

$$\delta L(t) = \delta L + \frac{1}{2} h(t) L \tag{I.21}$$

The Eq. (I.15) becomes:

$$E_{PD} = E_{in} e^{i2kL} \sin\left(2k \cdot \delta L + kL \cdot h(t) \right) \tag{I.22}$$

The detected power by the PD is given by $P_{PD} = |E_{PD}|^2$:

$$P_{PD} \sim \frac{P_{in}}{2} \left[1 - \cos\left(2k \cdot \delta L + kL \cdot h(t)\right)\right] \tag{I.23}$$

The approximation is done in the limit $h(t)L/\lambda \ll 1$. In the last equation, there are two contributions, the first term depends on the interferometer configuration while the second one depends also on the GW signal. The general approach aims to reduce the impact of the constant signal generated by the detector configuration. This is achieved by minimizing the offset on the differential arm length δL, and focusing exclusively on the signal itself. The figure of merit used in GW interferometers is the amplitude spectral density of the signal with the GW information:

$$\tilde{S}_h(t) \propto P_{in} \frac{2\pi}{\lambda} L h(t) \tag{I.24}$$

This basic model highlights that the GW signal is directly linked to the input power of the laser P_{in}, and the length of the interferometer arms L. These parameters play a critical role in enhancing the GW signal and are optimized to reach high performance. The Advanced Virgo Plus is significantly more complex than a standard Michelson interferometer. In fact, as detailed in §III.1, several techniques are employed to elevate the detector's performance, including the integration of resonant cavities along its arms. These techniques make it possible to overcome the structural limitations of having two 3-km arms by also increasing the power of the laser circulating inside the interferometer.

I.2.2. Dual-recycled cavity Michelson interferometer

The optical configuration, illustrated in Figure I.4, shows how a real GW interferometer is designed. The shown layout, in contrast to a classical Michelson setup, integrates several optical cavities (§III.2) such as the Input Mode Cleaner (IMC), the Output Mode Cleaner (OMC), and the arm cavities (NI-NE and WI-WE). The IMC is located at the input of the ITF and cleans and enhances the laser beam before it enters the ITF arms; the OMC is positioned at the output of the ITF and helps in extracting the fundamental mode from the returning light, improving the spatial and frequency characteristics of the signal. The arm cavities instead are specifically designed to extend the effective length of the arms, maximizing the collection of signals from the passing GW.

The GW detectors for the O4 run operate in the Dual Recycled Michelson configuration, a setup that enhances sensitivity and overall performance when compared to the Michelson configuration with only the FP cavities in the arms. One significant addition that characterizes this configuration is the power-recycling mirror (PR), as illustrated in Figure I.4. The PR mirror reflects the input power from the symmetric port back into the interferometer, amplifying the circulating power in the arms. This increase in optical power reduces shot noise, particularly at high frequencies, approaching the optimal power for reaching the standard quantum limit (§III.1.3).

In addition to the PR mirror, the second generation of GW detectors includes a signal recycling mirror (SR). The SR mirror reflects the signal emerging from the dark port back into the arm cavities, effectively recycling the signal. The SR mirror allows the detector to operate in broadband or narrow-band configurations. This flexibility enhances detection capabilities for specific astrophysical sources of GWs [22].

Managing such an intricate system necessitates employing a range of diagnostics and feedback loops, ultimately adding to the overall complexity of the detector.

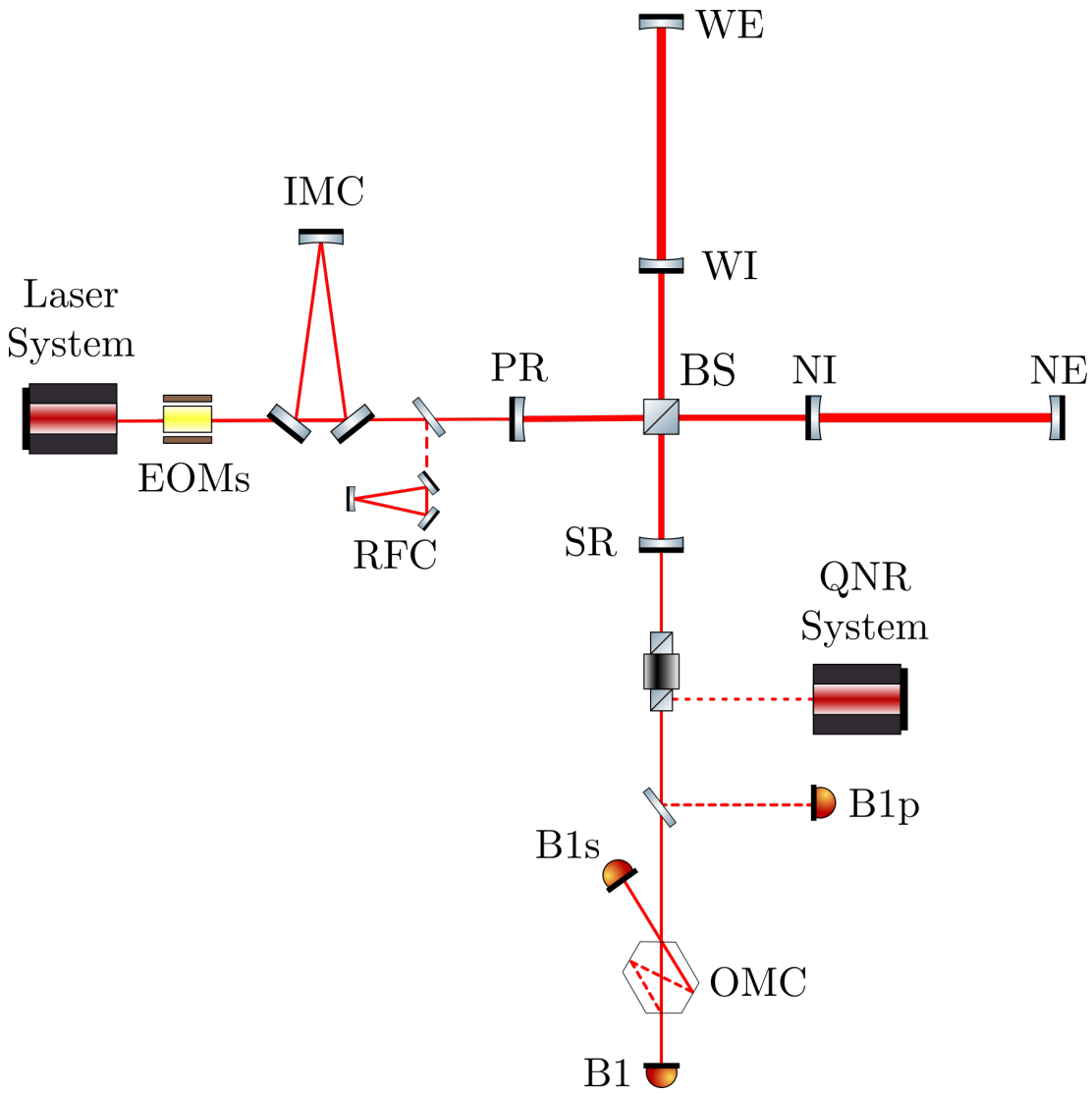

FIGURE I.4: Optical layout of Advanced Virgo Plus as an example of a dual recycled Michelson interferometer. A detailed explanation of the role of the readout photodiodes (B1, B1p, and B1s) in the context of the Quantum Noise Reduction (QNR) system is provided in Section IV.4. The relevant acronyms are as follows: EOMs: Electro-Optical Modulators; IMC: Input Mode Cleaner RFC: Reference Cavity; PR: Power Recycling Mirror; BS: Beam Splitter; NI, NE: North Input, North End Mirrors WI, WE: West Input, West End Mirrors SR: Signal Recycling Mirror; SQZ source: Vacuum Squeezed Source; OMC: Output Mode Cleaner.

I.2.3. Sensitivity limit

To detect GWs, it is crucial to minimize the impact of noise sources and maximize the signal-to-noise ratio. These fluctuations are due to the different sources of noise that affect the interferometers. Some of these sources, namely the most relevant for Virgo, and the different approaches to reduce the noise are briefly described. Some of these, which are relevant to this thesis, are discussed in depth in the following chapters.

Shot Noise: this noise refers to random fluctuations in the detected signal caused by the quantized nature of light. Shot noise is particularly relevant in optical systems, leading to variations in the signal intensity, and its impact becomes more pronounced in low-light conditions. It is discussed in detail in §III.1.

Radiation Pressure Noise: the uneven arrival of photons over time, coupled with their non-zero momentum, leads to a varying radiation pressure force on the reflecting test masses. This effect contributes to a fluctuation in the positions of the test masses, thereby constraining the interferometer's sensitivity. It is discussed in detail in §III.1.

Seismic Noise: the surface of the Earth experiences continuous vibrations, known as seismic noise, arising from various sources. Lower frequencies, typically below 1 Hz, primarily result from natural phenomena. These ground vibrations are several orders of magnitude higher than the displacement induced by a GW. Above 1 Hz, seismic noise is mainly produced by human activities. A typical vibration spectrum above 1 Hz is given by [23]:

$$\tilde{S}_x^{sism}(\nu) = 10^{-7} \left(\frac{1 \text{ Hz}}{\nu} \right)^2 \frac{\text{m}}{\sqrt{\text{Hz}}} \tag{I.25}$$

To achieve a sensitivity of 10^{-23} at 100 Hz, such noise must be reduced by more than 10 orders of magnitude. Interferometers use the pendulum's filtering properties to isolate test masses from seismic noise (see Figure V.3).

Newtonian Noise: the fluctuations in the local gravitational field near the interferometer generate displacement noise for the test masses, which can not be shielded. This change is a result of variations in mass distribution caused by seismic waves in the ground and fluctuations in atmospheric density [6]. As it is impossible to shield test masses from this type of disturbance, one of the strategies is to measure this noise source independently and then subtract it from the measurements made by the interferometer. Because it has been observed that this type of noise can be reduced by placing the interferometer underground, detectors such as Kagra and the future Einstein Telescope are designed this way.

Thermal noise: this noise in GW detectors is a crucial factor that imposes a fundamental limit on their sensitivity. The nature of this noise is discussed in detail in the second part of this thesis (see §V.1.2). Thermal noise can manifest in various components of GW detectors, affecting different parts of the instruments and influencing their overall performance. In particular, it is present in the mirrors' coating and in the pendulums that suspend the mirrors (see §V.2).

Two different sources of noise are treated separately in the two parts of this thesis. The first one is the quantum noise (see §III), caused by shot and radiation pressure noises, which, unlike the other noise sources, dominates over the entire sensitivity spectrum of the interferometer. The second one concerns the study of thermal noise (see §V). In particular, the study focuses on the behavior of this noise outside thermodynamic equilibrium. The sensitivity curves for the configuration illustrated in Figure I.4, incorporating all noise contributions to the Virgo sensitivity, are depicted in Figure I.5. Specifically, the presented sensitivity is the one projected for O4, utilizing the parameters listed in Table I.1.

Parameter	Symbol	Value
	Injection	
Laser power	P	40 W
IMC	L_{IMC}	143 m
IMC Finesse	$\mathcal{F}_{IMC}$	1000
	Interferometer optical configuration	
Arm cavities length	L	3 km
Arm cavities Finesse	$\mathcal{F}_{arm}$	450
Input mirrors mass	M_E	42 kg
End mirrors mass	M_E	42 kg
	Detection	
OMC Finesse	$\mathcal{F}_{OMC}$	1000
PDs Quantum efficiency	η	99%
	Quantum noise reduction	
Squeezed vacuum source	FDS	12 dB
Filter Cavity length	L_{FC}	285 m
FC Finesse	$\mathcal{F}_{FC}$	117
Phase noise	ϕ	40 mrad

Parameter	Type
Suspension	
Mirror suspension	Monolithic fused silica fibers
Vibration isolation	Super-attenuators

TABLE I.1: Main parameters of AdV+ taken from [24]

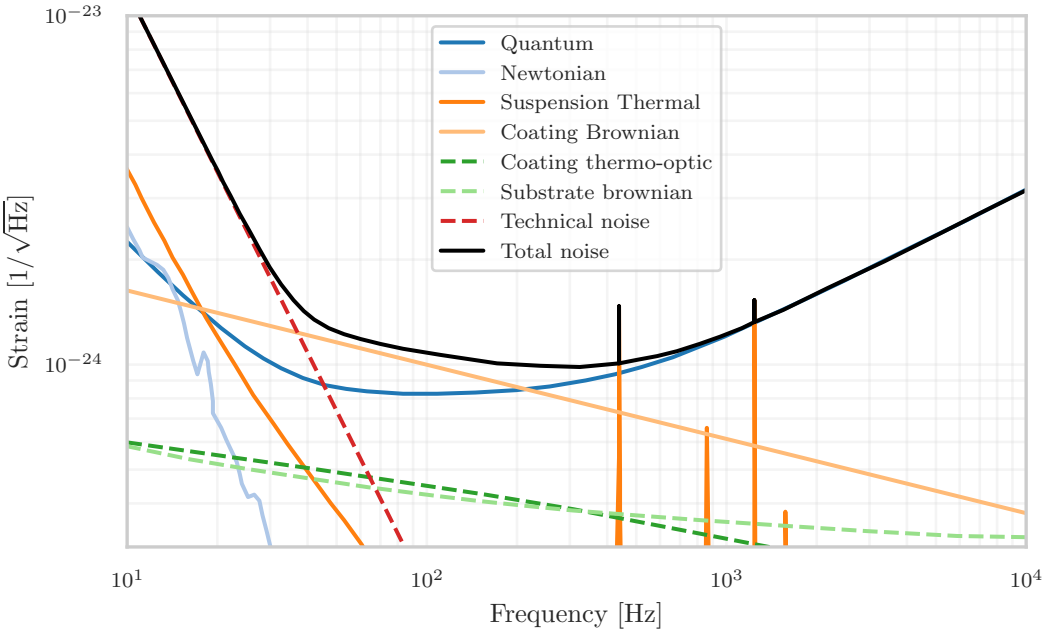

FIGURE I.5: Predicted sensitivity of AdV+ during the Observation run 4 (O4) (black curve) [24]. The other curves represent the different noise contributions.

Part I: O4 commissioning for AdV+

II | QUANTUM OPTICS AND LIGHT

This chapter aims to elucidate the fundamental concepts of quantum optics, setting the stage for understanding the production of squeezed states and their role in reducing quantum noise in GW interferometers. Starting with the quantization of the electromagnetic field, the chapter describes different quantum states and their graphical representation.

II.1. Second quantization

This section explores the principles of the second quantization of the electric field, its mathematical formulation, and its applications in quantum optics. The second quantization serves as a foundational concept in both quantum optics and quantum field theory. It provides a framework for understanding the quantum characteristics of electromagnetic radiation and its interaction with matter. Through the second quantization formalism, the electromagnetic field is described using creation and annihilation operators, responsible for generating and eliminating photons, respectively. These operators allow for the quantization of the electromagnetic field, enabling the characterization of its behavior in discrete, quantized units of energy. Such an understanding is important for unraveling various phenomena in quantum optics, including coherent and squeezed states, and quantum entanglement.

II.1.1. Quantization of the electromagnetic field

The classical electromagnetic field is described by the Maxwell's equations:

$$\vec{\nabla} \cdot \vec{E} = \rho \tag{II.1}$$

$$\vec{\nabla} \cdot \vec{B} = 0 \tag{II.2}$$

$$\vec{\nabla} \times \vec{B} - \frac{1}{c}\frac{\partial \vec{E}}{\partial t} = \frac{\vec{J}}{c} \tag{II.3}$$

$$\vec{\nabla} \times \vec{E} + \frac{1}{c}\frac{\partial \vec{B}}{\partial t} = 0 \tag{II.4}$$

where $\vec{E}$ and $\vec{B}$ are the electric and the magnetic fields, c is the speed of light in vacuum, $\rho = \rho(\vec{r}, t)$ is the charge density and $\vec{J} = \vec{J}(\vec{r}, t)$ is the current density. Introducing the antisymmetric tensor $F^{\mu\nu}$ defined as:

$$F^{i0} = E^i, \qquad F^{jk} = \varepsilon^{ijk} B^i \tag{II.5}$$

The two homogeneous Maxwell's equations become:

$$\partial^\mu F^{\nu\gamma} + \partial^\nu F^{\gamma\mu} + \partial^\gamma F^{\mu\nu} = 0 \tag{II.6}$$

with $\gamma \neq \nu \neq \mu$. The two nonhomogeneous equations can be written as:

$$\partial_\mu F^{\mu\nu} = J^\nu \tag{II.7}$$

where $J^\nu = (\rho, \frac{1}{c}\vec{j})$ is the four-current, and the (II.7) are satisfy by the relation:

$$F^{\mu\nu} = \partial^\nu A^\mu - \partial^\mu A^\nu \tag{II.8}$$

in which a vector potential A^μ is defined. Using this new field the equations (II.7) can be written as:

$$\partial_\mu F^{\mu\nu} = \Box A^\nu - \partial^\nu(\partial_\mu A^\mu) = J^\nu \tag{II.9}$$

that become:

$$\Box \vec{A} = 0 \tag{II.10}$$

where $\Box = \nabla^2 - \frac{1}{c^2}\frac{\partial^2}{\partial t^2}$ is the d'Alambertian operator and its role in expressing wave equations. If A^μ satisfies the Lorentz gauge condition $\partial_\mu A^\mu = 0$ and there is no charge nor current. A solution of the equation (II.10) is:

$$\vec{A}(\vec{r}, t) = \sum_{\vec{k}} \sum_{\lambda=0,1} [\alpha_{\vec{k}\lambda} \vec{u}_{\vec{k}\lambda}(\vec{r}, t) + \alpha^*_{\vec{k}\lambda} \vec{u}^*_{\vec{k}\lambda}(\vec{r}, t)] \tag{II.11}$$

where:

$$\vec{u}_{\vec{k}\lambda}(\vec{r},t) = \frac{1}{\sqrt{V}}\vec{\epsilon}_{\vec{k}\lambda}e^{i\vec{k}\vec{r}-i\omega_{\vec{k}}t} \tag{II.12}$$

are wave plane solutions in which $\vec{\epsilon}_{\vec{k}\lambda}$ is the polarization vector, λ is the polarization label, $\vec{k}$ and $\omega_{\vec{k}}$ are respectively the wave vector and the frequency. The entire formulation is within the volume V where the vector potential is defined. The transition to the quantum regime is realized by associating the annihilation operator of the quantum harmonic oscillator $\hat{a}_{\vec{k}\lambda}$ to the amplitude $\alpha_{\vec{k}\lambda}$ and the creation operators $\hat{a}^{\dagger}_{\vec{k}\lambda}$ to the amplitude $\alpha^{*}_{\vec{k}\lambda}$ [25]. Now it is possible to write the equation (II.11) as a quantum operator:

$$\hat{A}(\vec{r},t) = \sum_{\vec{k}}\sum_{\lambda=0,1}\gamma_k[\hat{a}_{\vec{k}\lambda}\vec{u}_{\vec{k}\lambda}(\vec{r},t) + \hat{a}^{\dagger}_{\vec{k}\lambda}\vec{u}^{*}_{\vec{k}\lambda}(\vec{r},t)] \tag{II.13}$$

where γ_k is the normalization factor to the operators $\hat{a}_{\vec{k}\lambda}$ and $\hat{a}^{\dagger}_{\vec{k}\lambda}$. Given that each mode of the vector potential is identified by a quantum harmonic oscillator with wave vector $\vec{k}$, frequency $\omega_{\vec{k}}$, and polarization λ, then the Hamiltonian of the single mode is the same one of the harmonic quantum oscillator:

$$\hat{H}_{\vec{k}\lambda} = \hbar\omega_{\vec{k}}\left(\hat{a}^{\dagger}_{\vec{k}\lambda}\hat{a}_{\vec{k}\lambda} + \frac{1}{2}\right) \tag{II.14}$$

The terms "creation" and "annihilation" operators are aptly named for their roles in generating and eliminating a quantum of energy on the mode $\vec{k}$ with polarization λ equivalent to an energy of $\hbar\omega_{\vec{k}}$. The operators $\hat{a}^{\dagger}_{\vec{k}\lambda}$ and $\hat{a}_{\vec{k}\lambda}$ satisfy the following equation:

$$\hat{a}^{\dagger}_{\vec{k}\lambda}\left|n_{\vec{k}\lambda}\right\rangle = \sqrt{(n_{\vec{k}\lambda}+1)}\left|n_{\vec{k}\lambda}+1\right\rangle \tag{II.15}$$

$$\hat{a}_{\vec{k}\lambda}\left|n_{\vec{k}\lambda}\right\rangle = \sqrt{n_{\vec{k}\lambda}}\left|n_{\vec{k}\lambda}-1\right\rangle \tag{II.16}$$

where $|n_{\vec{k}\lambda}\rangle$ represents the eigenstate of the *Number Operator* $\hat{n}_{\vec{k}\lambda} \equiv \hat{a}^{\dagger}_{\vec{k}\lambda}\hat{a}_{\vec{k}\lambda}$ providing the number of quanta of energy in the electromagnetic field, referred as photons. The annihilation operator's effect on the vacuum state is expressed as:

$$\hat{a}_{\vec{k}\lambda}\left|0\right\rangle = 0 \tag{II.17}$$

Distinct modes of the electromagnetic field operate independently, and this mathematical independence is expressed through the commutation of creation and annihilation operators:

$$\left[\hat{a}_{\vec{k}\lambda}, \hat{a}^{\dagger}_{\vec{k}'\lambda'}\right] = \delta_{\vec{k}\vec{k}'}\delta_{\vec{\lambda}\vec{\lambda}'} \tag{II.18}$$

This implies that when the labels $\vec{k}$ and λ differ from $\vec{k}'$ and λ', the commutator is zero. This relationship is analogous to the one valid for the quantum harmonic oscillator:

$$\left[\hat{a}_{\vec{k}\lambda}, \hat{a}_{\vec{k}\lambda}\right] = \left[\hat{a}^{\dagger}_{\vec{k}\lambda}, \hat{a}^{\dagger}_{\vec{k}\lambda}\right] = 0 \tag{II.19}$$

The results for the transverse electric operator are derived from operator versions of the expression:

$$\vec{E}_T = -\partial\vec{A}/\partial t \tag{II.20}$$

Consequently, the complete electric-field operator is given by:

$$\hat{E}_T(\chi) = \sum_{\vec{k}}\sum_{\lambda=0,1}\gamma_k\omega_k\left(\hat{a}_{\vec{k}\lambda}e^{-i\chi} + \hat{a}^{\dagger}_{\vec{k}\lambda}e^{i\chi}\right) \tag{II.21}$$

Here, $\chi = \omega_k t - \vec{k}\cdot\vec{r} - \frac{\pi}{2}$. Going forward, the notation is simplified by considering a monochromatic plane wave with a defined polarization and, consequently, the subscripts of the operators $\hat{a}$ and $\hat{a}^{\dagger}$ are omitted.

II.1.2. Quadrature operators

From (II.19), it follows that the creation and annihilation operators are not Hermitian, meaning that they do not represent physical observables for measurement. To address this issue, quadrature operators are introduced, which are utilized later in the discussion of squeezed light (§II.2.3). The operators $\hat{a}$ and $\hat{a}^\dagger$ can be reformulated as:

$$\hat{a} = \hat{X} + i\hat{Y} \tag{II.22}$$

$$\hat{a}^\dagger = \hat{X} - i\hat{Y} \tag{II.23}$$

where $\hat{X}$ is the *amplitude quadrature*, and $\hat{Y}$ is the *phase quadrature*. With the inverse relations, it is obtained:

$$\hat{X} = \frac{1}{2}\left(\hat{a} - \hat{a}^\dagger\right) \tag{II.24}$$

$$\hat{Y} = \frac{i}{2}\left(\hat{a} + \hat{a}^\dagger\right) \tag{II.25}$$

The electric field expressed in the relation (II.21) can be redefined as:

$$\hat{E}(\chi) = \hat{X}\cos\chi + \hat{Y}\sin\chi \tag{II.26}$$

II.1.3. Heisenberg Uncertainty Principle

The Heisenberg Uncertainty Principle, rooted in the statistical interpretation of quantum mechanics, holds a crucial role in the understanding of the microscopic world. It reveals the intrinsic uncertainty that emerges when attempting to simultaneously determine precise information about two non-commuting observables [26]. This principle fundamentally limits our ability to precisely measure certain pairs of observables, underscoring the inherent nature of uncertainty in quantum systems. By examining the commutation relation between these observables, the profound implications of the Heisenberg Uncertainty Principle and its significance for our understanding of quantum phenomena are explored. The uncertainty relation between two observables can be described by:

$$\Delta O_i \Delta O_j \geqslant \frac{1}{2}\left|\left\langle\left[\hat{O}_i, \hat{O}_j\right]\right\rangle\right| \tag{II.27}$$

where ΔO is the standard deviation of the respective operator. The variance $V(\hat{O})$ of the operator $\hat{O}$ is defined as.

$$V(\hat{O}) = \langle\hat{O}^2\rangle - \langle\hat{O}\rangle^2 \tag{II.28}$$

Considering the amplitude and phase quadrature operators (II.24) and (II.25), the commutation relation is:

$$\left[\hat{X}, \hat{Y}\right] = \frac{i}{2} \tag{II.29}$$

This relation leads to the uncertainty equation:

$$\Delta X \Delta Y \geqslant \frac{1}{4} \tag{II.30}$$

As a result, it is not possible to precisely measure the amplitude and phase quadratures simultaneously. This intrinsic uncertainty is commonly known as the quantum noise of the electromagnetic field. If the fluctuations of a state satisfy the lower bound of the Uncertainty Principle, $\Delta X \Delta Y = 1$, the state is referred to as a minimum uncertainty state.

II.2. Quantum states of light

Exploring various states of light is a crucial focus in quantum optics research. Among the well-established and extensively studied quantum states of light, number states, coherent states, and squeezed states hold significant prominence. Number states represent the foundational states in the quantum theory of light, characterized by a definite number of photons. Coherent states, resembling classical states of light, exhibit minimal uncertainty in both amplitude and phase quadratures. On the contrary, squeezed states are characterized by a reduction in uncertainty in one quadrature at the cost of increased uncertainty in the other quadrature. Given their crucial role in reducing quantum noise in gravitational wave interferometers, the focus is on vacuum squeezed states (§III).

II.2.1. Number states

The foundational states in the quantum theory of light are the photon number states. Several properties of these states are derived in § II.1.1. As mentioned, the single-mode states are represented by the notation $|n\rangle$ and are eigenstates of the number operator $\hat{n}$:

$$\hat{a}\,|n\rangle = n\,|n\rangle \tag{II.31}$$

and constitute a complete set of the states of a single mode. This last equation implies that the expectation value of the photon number is $\langle n\rangle = n$ indicating no uncertainty in the number of photons, with a vanishing variance$\left(\Delta n^2\right) = 0$ [25]. The eigenvalue relation (II.14) can be reformulated in terms of the quadrature operators:

$$\hat{H}\,|n\rangle = \hbar\omega\left(\hat{X}^2 + \hat{Y}^2\right)|n\rangle \tag{II.32}$$

resulting in the expectation values:

$$\langle n|\,\hat{X}\,|n\rangle = \langle n|\,\hat{Y}\,|n\rangle = 0 \tag{II.33}$$

and

$$(\Delta X)^2 = (\Delta Y)^2 = \frac{1}{2}\left(n + \frac{1}{2}\right) \tag{II.34}$$

The properties of the number states are identical for both the quadrature operators. Their variances achieve the lowest values only when the state has $n = 0$, representing the vacuum state. Thus, the state $|0\rangle$ serves as a quadrature minimum-uncertainty state.

II.2.2. Coherent states

Coherent states are an essential concept in quantum optics due to their classical-like properties. In fact, laser light, for example, can be approximately described by a coherent state. These states exhibit minimal uncertainty in both amplitude and phase quadratures, making them useful for describing the behavior of optical systems. Represented by the notation $|\alpha\rangle$, they are theoretical superpositions of number states:

$$|\alpha\rangle = e^{-\frac{|\alpha|^2}{2}}\sum_{n=0}^{\infty}\frac{\alpha^n}{\sqrt{n!}}|n\rangle \tag{II.35}$$

Here, α is the complex *coherent amplitude* and $|n\rangle$ is the nth number state. Coherent states possess two key properties, normalization:

$$\langle\alpha|\alpha\rangle = e^{-|\alpha|^2}\sum_{n=0}^{\infty}\frac{\alpha^{*n}\alpha^n}{\sqrt{n!}} = 1 \tag{II.36}$$

and non-orthogonality:

$$\langle\alpha|\beta\rangle = e^{-\frac{1}{2}|\alpha|^2 - \frac{1}{2}|\beta|^2 + \alpha^*\beta} \tag{II.37}$$

They are eigenstates of the annihilation operator $\hat{a}$ and $\hat{a}^\dagger$:

$$\hat{a}\,|\alpha\rangle = \alpha\,|\alpha\rangle \tag{II.38}$$

$$\langle\alpha|\,\hat{a}^\dagger = \langle\alpha|\,\alpha^* \tag{II.39}$$

These relations facilitate obtaining the coherent-state expectation values of quadrature operators (II.24) and (II.25):

$$\langle\alpha|\,\hat{X}\,|\alpha\rangle = \mathrm{Re}\alpha = |\alpha|\cos\phi \tag{II.40}$$

$$\langle\alpha|\,\hat{Y}\,|\alpha\rangle = \mathrm{Im}\alpha = |\alpha|\sin\phi \tag{II.41}$$

where the complex number α is written as $\alpha = |\alpha|e^{i\phi}$. The expectation values of the squares of the quadrature operators are determined as:

$$\hat{X}^2 = \frac{1}{4}\left(\hat{a}^\dagger\hat{a}^\dagger + 2\hat{a}^\dagger\hat{a} + \hat{a}\hat{a} + 1\right) \tag{II.42}$$

$$\hat{Y}^2 = \frac{1}{4}\left(-\hat{a}^\dagger\hat{a}^\dagger + 2\hat{a}^\dagger\hat{a} - \hat{a}\hat{a} + 1\right) \tag{II.43}$$

and it follows that the quadrature variances are:

$$(\Delta X)^2 = (\Delta Y)^2 = \frac{1}{4} \tag{II.44}$$

Thus, in contrast to the variances for the number-state given by (II.34), the coherent state is a quadrature minimum-uncertainty state for all mean photon numbers $|\alpha|^2$.

II.2.3. Squeezed states

Squeezed states, a distinct category of minimum uncertainty states, maintain the lower bound of Eq. (II.30). However, unlike an even distribution of uncertainty between the two quadratures, one quadrature experiences reduced uncertainty at the expense of the other. The *squeezed vacuum state* is defined as:

$$|\zeta\rangle = \hat{S}(\zeta)\,|0\rangle \tag{II.45}$$

where $\hat{S}$ is the *squeeze operator* defined as:

$$\hat{S}(\zeta) = \exp\left(\frac{1}{2}\zeta^*\hat{a}^2 - \frac{1}{2}\zeta(\hat{a}^\dagger)^2\right) \tag{II.46}$$

and ζ is the *complex squeeze parameter* with squeezing amplitude s and squeezing phase θ defined by:

$$\zeta = se^{i\theta} \tag{II.47}$$

The exponential form in Eq. (II.46), specifically its dependence on $\hat{a}$ and $\hat{a}^\dagger$, indicates that the squeezed vacuum state consists entirely of a superposition of number states with values of n. Similar to the coherent-state superposition of number states presented in Eq. (II.35), the squeezed vacuum state can be expressed through its expansion in terms of number states as:

$$|\zeta\rangle = (\mathrm{sech}s)^{1/2}\sum_{n=0}^{\infty}\frac{[(2n)!]^{1/2}}{n!}\left[-\frac{1}{2}\exp(i\theta)\tanh s\right]^n|2n\rangle \tag{II.48}$$

The expectation value of the number operator $\hat{n}$ is:

$$\langle n\rangle = \sinh^2 s \tag{II.49}$$

This implies that for a squeezed vacuum state, the number of photons is non-zero, indicating some optical power in the squeezed beam.

The significance of the squeezed vacuum state lies not in its photon number distribution, but rather in its quadrature operator properties. Using the Baker Hausdorf lemma [27] it is possible to obtain the variances of the quadrature operators:

$$V(\hat{X}) = \frac{1}{4}\left\{e^{2s}\sin^2\left(\frac{1}{2}\theta\right) + e^{-2s}\cos^2\left(\frac{1}{2}\theta\right)\right\} \tag{II.50}$$

$$V(\hat{Y}) = \frac{1}{4}\left\{e^{2s}\cos^2\left(\frac{1}{2}\theta\right) + e^{-2s}\sin^2\left(\frac{1}{2}\theta\right)\right\} \tag{II.51}$$

substituting $\theta = 0$ it is derived:

$$V(\hat{X}) = V_- = \frac{1}{4}e^{-2s} \tag{II.52}$$

$$V(\hat{Y}) = V_+ + \frac{1}{4}e^{+2s} \tag{II.53}$$

A squeezed state with $\theta = 0$ represents a minimum uncertainty state, in which the fluctuations of the amplitude quadrature operator are suppressed (squeezed (SQZ)) by a factor of e^{-2s} compared to the fluctuations of a coherent state. Conversely, the fluctuations of the phase quadrature operator are increased (anti-squeezed (ASQZ)) by a factor of e^{+2s}. In contrast, a *bright squeezed beam* takes the form:

$$|\alpha, \zeta\rangle = \hat{D}(\alpha)\hat{S}(\zeta)\,|0\rangle \tag{II.54}$$

where $\hat{D}(\alpha) = e^{\alpha\hat{a}^\dagger - \alpha^*\hat{a}}$ is the *displacement operator*. The mean photon number in this case is given by:

$$\langle n\rangle = |\alpha|^2 + \sinh^2 s \tag{II.55}$$

The photon number of a squeezed state is slightly higher than that of a coherent state. If $\alpha = 0$, the state returns to a squeezed vacuum state. This optical power represents the energy required to modify the statistical properties of the vacuum state's noise. In the absence of squeezing, when $s = 0$, the mean photon number becomes zero, reducing the squeezed vacuum state to the standard vacuum state. The squeezing or anti-squeezing level is commonly denoted in decibels (dB), typically represented in terms of the variances $V_\pm$ (+ for ASQZ and - for SQZ) with respect to the variance of a vacuum state V_{vac}. The level is expressed by the following equations:

$$R_\pm[dB] = 10\log_{10}\left(\frac{V_\pm}{V_{vac}}\right) = 20\log_{10}\left(R_\pm\right) \tag{II.56}$$

where the *squeezing ratios* are introduced:

$$R_\pm = \sqrt{\left(\frac{V_\pm}{V_{vac}}\right)} = e^{\pm s} \tag{II.57}$$

II.2.4. Quantum phasor diagram

In the study of waves and oscillations, the phasor diagram is a powerful graphical tool for visualizing and analyzing complex amplitudes and phase relationships of harmonic signals. It provides a concise representation of the magnitude and phase of a sinusoidal waveform, simplifying the analysis of wave properties such as superposition, interference, and resonance. Considering the classical electric field:

$$E(t) = E_0 e^{i\omega_0 t + i\phi} \tag{II.58}$$

In the complex plane rotating at angular frequency ω_0, the field $E(t)$ is represented by a vector with amplitude E_0 and phase ϕ (the phasor). According to the Heisenberg Uncertainty Principle (II.29), the field amplitude and phase do not have well-defined values. Therefore, for the definition of a quantum state, the phasor diagram needs to be adapted. Using a coherent state

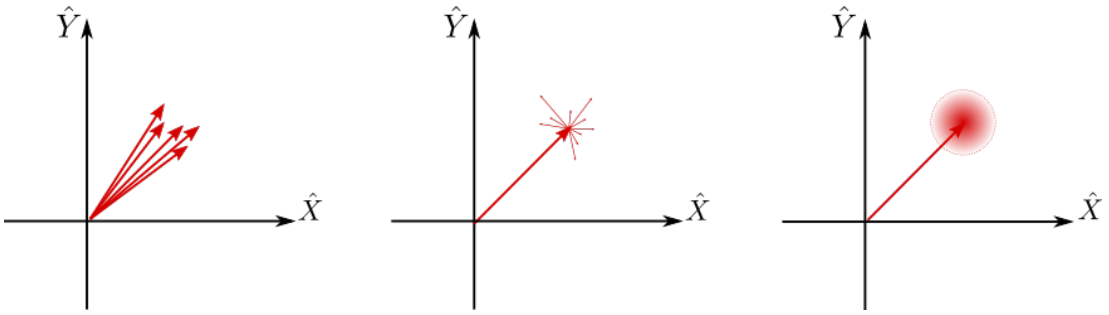

FIGURE II.1: (left) Multiple phasors are depicted representing different possible amplitudes and phases. (center) To simplify the representation, an equivalent single phasor is used, with a time-varying non-deterministic uncertainty vector. (right) The phasor is represented as a narrow with a distribution of the quadrature uncertainty.

as an example, a multitude of phasors with different amplitudes and phases becomes possible, as depicted in the left-side of Figure II.1. These multiple phasors can be equivalently represented by a single phasor accompanied by a non-deterministic, time-varying uncertainty vector in amplitude and phase, as illustrated in the central part of Figure II.1. In a coherent state, where the uncertainty on both quadratures is equal ($\Delta X = \Delta Y = 1/4$), the time-varying vectors are expected to be isotropically distributed, with a probability in magnitude that diminishes as the distance from the mean value increases. This representation enables the visualization of the quantum phasor diagram, illustrated on right-side of Figure II.1. This diagram provides a hybrid representation in the quadrature space (X, Y), offering insights into both classical and quantum properties of the considered state. In Figure II.2, various quantum phasor diagrams are shown for different states. Notably, states with squeezed quadratures exhibit a distinctive elliptical distribution, highlighting their unique quantum characteristics.

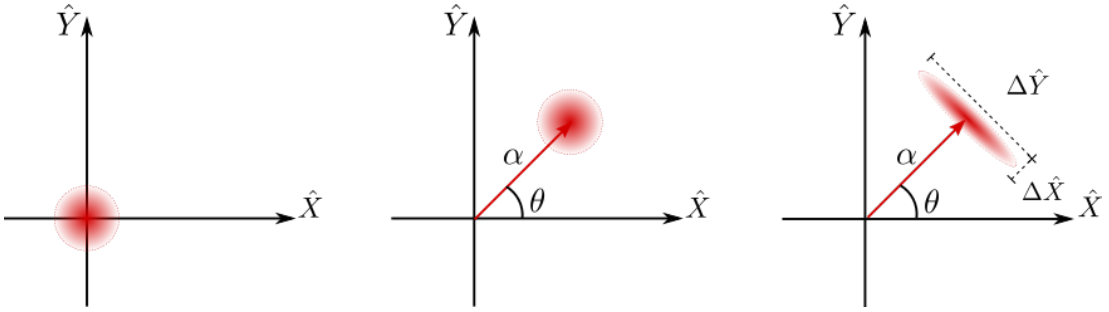

FIGURE II.2: Quantum phasor representation of different quantum states. (left) Vacuum state. (center) Coherent state. (right) Bright squeezed state. When the amplitude $\alpha = 0$ the state collapses to a squeezed vacuum state with the ellipse centered at the origin of the axes.

II.3. QUANTUM DETECTION

This section elucidates the detection and quantification of quantum states. Specifically, it explores how the electronic signal registered by a photodetector (PD) depends with the presence of photons and outlines the utilization of multiple PDs for the measurement of squeezed beams.

II.3.1. Operator linearization

Quantum operator linearization is a technique used in quantum optics to simplify mathematical expressions and facilitate intuitive interpretations. A generic operator $\hat{O}$ is expressed as:

$$\hat{O}(t) = \langle \hat{O} \rangle + \delta\hat{O}(t) \tag{II.59}$$

$$\hat{O}^\dagger(t) = \langle \hat{O}^\dagger \rangle + \delta\hat{O}^\dagger(t) \tag{II.60}$$

Here, it is assumed that the fluctuating component $\delta\hat{O}$ ($\delta\hat{O}^\dagger$) has a zero average and, in general, is significantly smaller than the average counterparts $\langle \hat{O} \rangle$ ($\langle \hat{O}^\dagger \rangle$):

$$\langle \delta\hat{O}(t) \rangle = \langle \delta\hat{O}^\dagger(t) \rangle = 0 \tag{II.61}$$

$$|\delta\hat{O}(t)| \ll 1 \quad |\delta\hat{O}^\dagger(t)| \ll 1 \tag{II.62}$$

This ensures that the steady state solution $\langle \hat{O} \rangle$ ($\langle \hat{O}^\dagger \rangle$) is time-independent, allowing the previous expansions (II.59) and (II.60) to be limited to the first order. Applying this decomposition to both the annihilation and creation operators yields:

$$\hat{a} = \alpha + \delta\hat{a} \tag{II.63}$$

$$\hat{a}^\dagger = \alpha^* + \delta\hat{a}^\dagger \tag{II.64}$$

Considering Eq.(II.24) and (II.25), the fluctuations of the quadrature operators are then expressed as:

$$\delta\hat{X} = \delta\hat{a}^\dagger + \delta\hat{a} \tag{II.65}$$

$$\delta\hat{Y} = i(\delta\hat{a}^\dagger - \delta\hat{a}) \tag{II.66}$$

Applying this operation to the number operator $\hat{n}$ gives:

$$\begin{aligned} \hat{n} &= \hat{a}\hat{a}^\dagger \\ &= (\alpha + \delta\hat{a})(\alpha^* + \delta\hat{a}^\dagger) \\ &\approx \alpha^2 + \alpha\delta\hat{X} \end{aligned} \tag{II.67}$$

In the last step, non-linear terms ($\delta\hat{a}^\dagger\delta\hat{a}$) are neglected, indicating that the number of photons is proportional to the square of the amplitude α. Additionally, the quantum fluctuations are proportional to the fluctuations in the amplitude quadrature of the field $\hat{a}$.

II.3.2. Beam-Splitter

A Beam-Splitter (BS) is an optical device designed to divide a single input light beam into two output beams. This is achieved by directing the incident light onto a partially reflective surface, which separates the light into distinct paths based on the properties of the device's material or coating. A typical BS comprises a surface that reflects a portion of the incoming light, allowing the remaining portion to be transmitted. When used to combine two light beams represented by the operators $\hat{a}$ and $\hat{b}$ (see Figure II.3), the resulting output fields are represented by the operators $\hat{c}$ and $\hat{d}$. The relationship between the inputs and the output is expressed as follows:

$$\begin{bmatrix} \hat{c} \\ \hat{d} \end{bmatrix} = \begin{bmatrix} r & t \\ t & -r \end{bmatrix} \begin{bmatrix} \hat{a} \\ \hat{b} \end{bmatrix} \tag{II.68}$$

Here, r and t represent the reflectance and the transmittance of the BS, respectively. The proportion of light transmitted versus reflected, known as the splitting ratio, can be adjusted by manipulating characteristics like the angle of incidence or the properties of the optical coating that directly affect r and t.

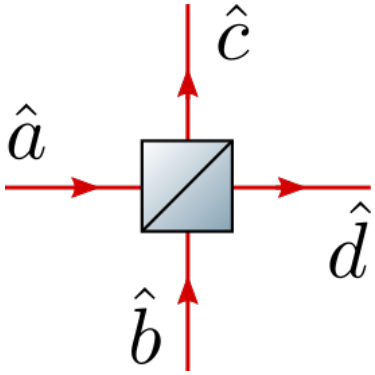

FIGURE II.3: Optical scheme of a BS. The two fields $\hat{a}$ and $\hat{b}$ are combined generating the two output fields $\hat{c}$ e $\hat{d}$.

II.3.3. PHOTODETECTION

Photodetection is a fundamental technique used to detect and measure light intensity, finding applications in various fields, including telecommunications, imaging, spectroscopy, and optical sensing.

This technique relies on the conversion of photons into an electrical signal through interaction with a photosensitive material, typically realized with a photodiode (PD).

The PD, composed of a semiconductor material or a combination of materials exhibiting the photoelectric effect, generates charge carriers (electrons or holes) upon absorbing incident photons. The most straightforward photodetection method involves a photodiode (illustrated on the left-side of Figure II.4). In this scheme, photons are converted into electrons within the PD with a *quantum efficiency* represented by η_{PD}. The conversion process results in the generation of a current operator $\hat{i}$, which corresponds to the amount of detected light:

$$\hat{i} = \rho P_{opt} = \frac{e\eta_{PD}}{\hbar\omega} P_{opt} = \frac{e\eta_{PD}}{\cancel{\hbar\omega}} \cancel{\hbar\omega}\hat{n} \tag{II.69}$$

In this equation, ρ is the photodetector responsivity (in units of A/W), $\hbar\omega$ is the energy of a single photon and e is the electron charge. The photocurrent is directly proportional to the number of photons present in the optical field. To analyze this relationship, the linearized number operator (II.67) can be employed:

$$\hat{i} = e\eta_{PD}\hat{n} = e\eta_{PD}(\alpha^2 + \alpha\delta\hat{X}) \tag{II.70}$$

The photocurrent comprises two components: the DC term, $\langle i \rangle \propto \alpha^2$, directly proportional to light intensity, and the AC term, $\delta i \propto \alpha\delta X$, scaling the amplitude of the DC field. A measurement device that solely captures the DC term is commonly known as a power meter. Such a device measures the average value of the photocurrent, providing information about the overall intensity of the light.

II.3.4. HOMODYNE DETECTION

Homodyne detection (HD) is a powerful technique used in quantum optics to detect and characterize quantum states of light [28], particularly those involving squeezing. In HD, a BS is employed to combine a signal beam, which contains the field to be measured, with a *local oscillator* beam (LO) that serves as a reference beam with a known phase and amplitude. The two fields, as shown in Figure II.4, are represented by the two operators $\hat{a}$ and $\hat{b}$ respectively. The two fields are linearized according to the theory illustrated in §II.3.1:

$$\hat{a} = \alpha + \delta\hat{a} \tag{II.71}$$

$$\hat{b} = (\beta + \delta\hat{b})e^{i\phi} \tag{II.72}$$

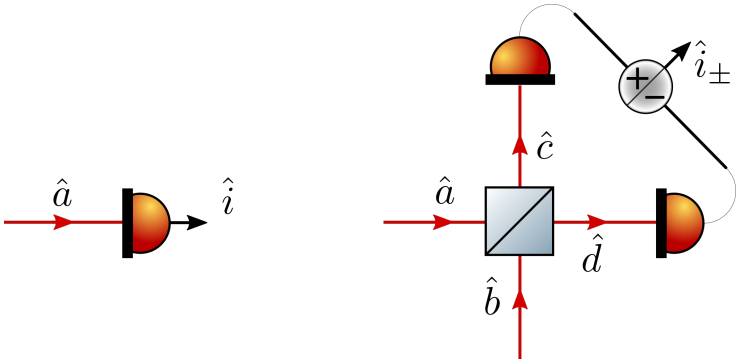

FIGURE II.4: The image shows two different schemes of detection. (left) The direct measurement of the field $\hat{a}$. (right) Homodyne detection is performed on the incident fields $\hat{a}$ and $\hat{b}$, which are combined on the beam splitter. Subsequently, the resultant fields $\hat{c}$ and $\hat{d}$ are captured by two photodiodes, and the sum and difference of the photocurrents are analyzed.

where ϕ is an arbitrary phase between the LO and the other field. The two outputs of the BS are detected by two distinct PDs. Recalling that the photocurrent is expressed as in Eq. (II.69), the photocurrent generated by the transmitted field $\hat{c}$ can be expressed as:

$$\begin{aligned}\hat{i}_c &= \eta_q e(r\hat{a}^\dagger + t\hat{b}^\dagger)(r\hat{a} + t\hat{b}) \\ &\approx \eta_q e\left[r^2\alpha^2 + 2rt\alpha\beta\cos\phi + t^2\beta^2 + 2r\alpha\left(r\delta\hat{X}_a + t\delta\hat{X}_{b,-\phi}\right) + 2t\beta\left(t\delta\hat{X}_b + r\delta\hat{X}_{a,\phi}\right)\right]\end{aligned} \tag{II.73}$$

Similarly, the photocurrent generated by the the reflected field $\hat{d}$ is equal to:

$$\begin{aligned}\hat{i}_d &= \eta_q e(t\hat{a}^\dagger - r\hat{b}^\dagger)(t\hat{a} - r\hat{b}) \\ &\approx \eta_q e\left[r^2\alpha^2 - 2rt\alpha\beta\cos\phi + t^2\beta^2 + 2r\alpha\left(r\delta\hat{X}_a - t\delta\hat{X}_{b,-\phi}\right) + 2t\beta\left(t\delta\hat{X}_b - r\delta\hat{X}_{a,\phi}\right)\right]\end{aligned} \tag{II.74}$$

Higher-order terms are neglected in both expressions, allowing for a simplified representation. Additionally, the following notation is introduced:

$$\hat{X}_{a,\phi} = \frac{1}{2}\left(\hat{a}e^{-i\phi} + \hat{a}^\dagger e^{i\phi}\right) = \hat{X}_a\cos\phi + \hat{Y}_a\sin\phi \tag{II.75}$$

If the sum and the difference between the two photocurrents is calculated, it is obtained:

$$\hat{i}_+ = \hat{i}_c + \hat{i}_d \approx 2\eta_q e\left[r^2\alpha^2 + t^2\beta^2 + 2r\alpha\delta\hat{X}_a + 2t\beta\delta\hat{X}_b\right] \tag{II.76}$$

$$\hat{i}_- = \hat{i}_c - \hat{i}_d \approx 4rt\eta_q e\left[\alpha\beta\cos\phi + \alpha\delta\hat{X}_{b,-\phi} + \beta\delta\hat{X}_{a,\phi}\right] \tag{II.77}$$

Suppose the intensity of the signal field, represented by α, is significantly smaller than the intensity of the LO field, denoted by β. In this case, the last two expressions can be further simplified as follows:

$$\hat{i}_+ \approx 2\eta_q e\left[t^2\beta^2 + 2t^2\beta\delta\hat{X}_b\right] \tag{II.78}$$

$$\hat{i}_- \approx 4rt\eta_q e\left[\alpha\beta\cos\phi + \beta\delta\hat{X}_{a,\phi}\right] \tag{II.79}$$

In these simplified expressions, the sum signal $\hat{i}_+$ predominantly carries information about the LO and the fluctuations of its quadrature $\hat{X}_b$. On the other hand, the difference signals $\hat{i}_-$ consists of two terms: the first term describes the interference between the two fields, while the second term contains the fluctuations of a quadrature of the signal beam rotated by an angle ϕ with respect to the $\hat{X}$, $\hat{Y}$ plane. By utilizing the expression provided in Equation (II.75), the difference signal can be further refined:

$$\hat{i}_- \approx 4rt\eta_q e\left[\alpha\beta\cos\phi + \beta\left(\delta\hat{X}_a\cos\phi + \delta\hat{Y}_a\sin\phi\right)\right] \tag{II.80}$$

Thus, the difference signal consists of a DC component and its fluctuations. To obtain information about the rotated quadrature, the power spectral density of the difference signal is measured. The Wiener-Khinchin theorem states that the power spectrum of a stationary process is equal to the Fourier transform of its autocorrelation function. Therefore, by computing the PSD of the difference signal, information about the fluctuations of the quadrature can be extracted. In HD, if the signal field is a squeezed vacuum state, the level of squeezing can be measured using this technique. Specifically, the fluctuations of the amplitude quadrature $\hat{X}$ are measured by setting the relative phase between the LO and the signal field to 0. On the other hand, the fluctuations of the phase quadrature are measured by setting the relative phase to $\pi/2$. The relative phase between the two beams can be adjusted by manipulating the optical beam paths. In this thesis, the HD is designed with a self-subtracting scheme, directly subtracting the two photocurrents before applying electronic conditioning to the signals from the two photodiodes. This design aims to minimize gain differences between the two signals, which could otherwise introduce discrepancies between the generated and measured squeezing level [29].

II.4. Squeezing degradation

Squeezed states are primarily affected by two mechanisms of degradation of degradation: one related to the optical losses sensed by the squeezing beam and the second from the angular jitter of the squeezing ellipse. These two contributions are discussed below, and the models presented are utilized in the §IV for measuring losses within the Virgo squeezing system.

II.4.1. Losses

In the context of quantum state propagation, optical losses are commonly represented as a BS with a power reflectivity equal to the power loss l. From the unused port of the beam splitter, a coherent vacuum field $\hat{a}$ enters the system and is combined with the transmitted fraction of the squeezed field $\hat{b}$ producing at the BS output the filed $\hat{a}_l$:

$$\hat{a}_l = \sqrt{1-l}\hat{a} + \sqrt{l}\hat{b} \tag{II.81}$$

The variance of the quadrature of the resulting output state is given by:

$$V(\hat{X}^l_{a,\phi}) = (1-l)V(\hat{X}_{a,\phi}) + lV(\hat{X}_{b,\phi}) \tag{II.82}$$

where it is assumed that the fluctuations of $\hat{b}$ and those of $\hat{a}$ are uncorrelated. For a squeezed state with initial variances $V_\pm$:

$$V^l_\pm = (1-l)V_\pm + lV_{vac} \tag{II.83}$$

where V_{vac} is the variance of the coherent vacuum field. The last equation can be reformulated in terms of the squeezing ratios:

$$R^l_\pm = (1-l)R_\pm + l \tag{II.84}$$

This relation is shown in Figure II.5. Optical losses arise from several mechanisms, including optical absorption, scattering, clipping, non-unitary quantum efficiency of photodiodes, and issues such as mode mismatch or misalignment when squeezing is coupled with optical resonators.

II.4.2. Phase noise

Variations in the relative angle between the squeezed and measured quadratures adversely impact squeezing performance, as they facilitate the transfer of noise from the anti-squeezed quadrature into the measurement quadrature. This phenomenon can be represented by introducing a time-varying phase offset $\phi(t)$:

$$V^\phi_\pm(t) = V_\pm \cos^2\phi(t) + V_\mp \sin^2\phi(t) \tag{II.85}$$

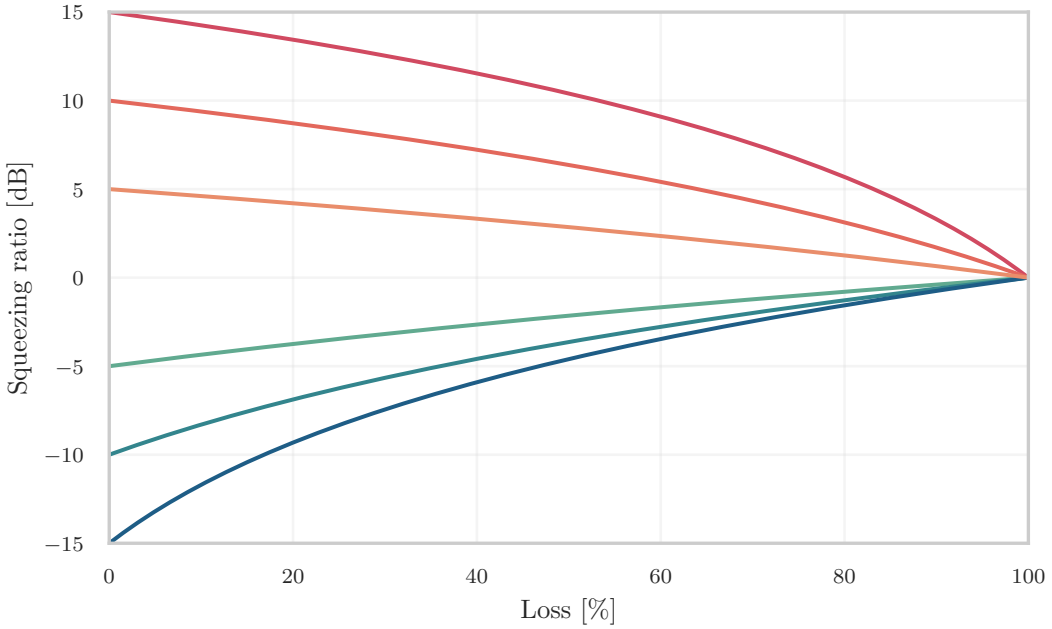

FIGURE II.5: Squeezing ratio with different input levels degraded by the optical losses. The initial level of squeezing is assumed 15 dB. Note how the SQZ quadrature (cold palette) degrades faster than the ASQZ (warm palette) quadrature. For 100% loss, the state collapses into a vacuum state.

resulting in a combination of the two variances. While the squeezing phase is actively controlled (§ IV.2.3), it is easy to control the mean value of the phase However, even in the most precise controls, a minimum of random fluctuation remains present. Assuming these fluctuations follow a normal distribution centered around $\langle\phi\rangle$=0 with a small root-mean-square (RMS) deviation ϕ_{RMS}, the average variance of the resulting measurement can be expressed as follows [30]:

$$\begin{aligned} V_{\pm}^{\phi_{RMS}} &= \int_{-\infty}^{+\infty} dx \frac{e^{x^2/2\phi_{RMS}}}{\sqrt{2\pi}\phi_{RMS}} \left(V_{\pm}\cos^2 x + V_{\mp}\sin^2 x\right) \\ &\approx V_{\pm}\cos^2\phi_{RMS} + V_{\mp}\sin^2\phi_{RMS} \end{aligned} \tag{II.86}$$

For minor fluctuations ($\phi_{RMS} \leq 100$ mrad), an RMS phase error effectively behaves like a constant offset of similar magnitude. The various mechanisms contributing to fluctuations in the squeezing angle are thoroughly examined in detail in [31]. The adverse impact of RMS phase noise becomes more noticeable for heavily squeezed states, where the variance of the anti-squeezed quadrature is greatly amplified (see Figure II.6). With a fixed degree of phase error, there exists a threshold beyond which increasing the input squeezing parameter s results in diminishing measurement performance. This establishes a maximum level of squeezing that can be effectively employed in the presence of phase noise.

II.5. GRAPHIC REPRESENTATION

II.5.1. CLASSICAL SIDEBAND PICTURE

Modulation in optics refers to the deliberate manipulation of the properties of light, such as intensity, phase, polarization, or frequency for various applications. It plays a crucial role in modern optics and photonics technologies, enabling the control, manipulation, and transmission of light signals with precision and versatility. Various modulation schemes exist, each tailored to the specific needs of the application.

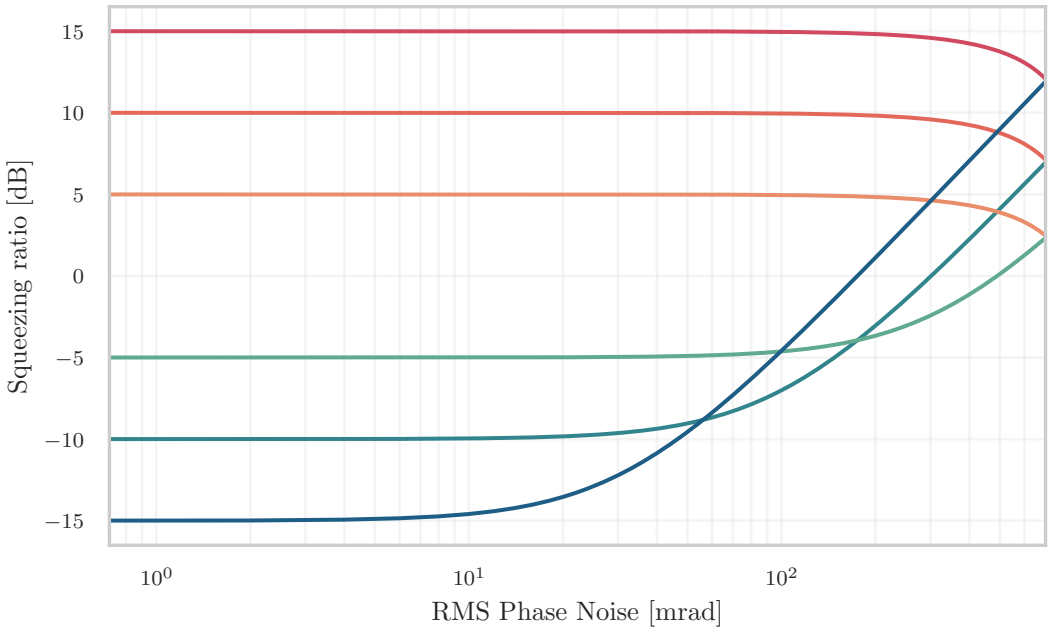

FIGURE II.6: Squeezing ratio with different input levels degraded by the phase noise obtained by plotting the small angle approximation (II.86). The fluctuation of the phase generates a mixing of the quadrature variances that leads to squeezing level degradation. The effect is more relevant when a large amount of SQZ is generated. The upper limit is in correspondace of the value $\phi_{RMS} = \pi/4$ where V_+ and V_- assume the same value.

Amplitude modulation (AM) involves varying the intensity of the light wave to encode information. Phase modulation (PM) alters the phase of the wave, while frequency modulation (FM) modifies the frequency. Each modulation scheme offers distinct advantages and is chosen based on factors such as data rate, signal-to-noise ratio, bandwidth, and compatibility with the system [32].

AMPLITUDE MODULATION

Consider a field undergoing amplitude modulation with a modulation frequency Ω and a modulation depth M, as expressed by the following equations [33]:

$$E_{AM}(t) = E_0 e^{i\omega_0 t}(1 + M\cos(\Omega t)) \tag{II.87a}$$

$$= E_0 e^{i\omega_0 t}(1 + \frac{M}{2}e^{i\Omega t} + \frac{M}{2}e^{-i\Omega t}) \tag{II.87b}$$

In this context, $E_{AM}(t)$ represents the amplitude-modulated field, that can be decomposed into a carrier field with amplitude E_0 and frequency ω_0 along with two sidebands at frequencies $\omega_0 \pm \Omega$ and amplitude $E_0\frac{M}{2}$.

This decomposition is visually represented in Figure II.7, with the chosen reference frame being the rotating frame of the carrier. The sidebands at $\omega_0 + \Omega$ and $\omega_0 - \Omega$ rotate clockwise and anti-clockwise with frequency Ω. In Figure II.7, the amplitude-modulated field evolves over time.

On the left-hand side, a sideband representation corresponds to the right-hand side of Eq. (II.87b). The two light blue sidebands rotate in opposite directions around the frequency axis at a frequency Ω while the carrier field, represented in green, remains temporally invariant.

On the right-hand side, the summation of the individual fields (light blue and green) at the sideband frequency Ω, is depicted as a red phasor. This representation aligns more closely with

the right-hand side of Eq. (II.87a). Notably, the combined phasor exhibits periodic variations in its length due to the different orientations of the sidebands, while the phase remains constant.

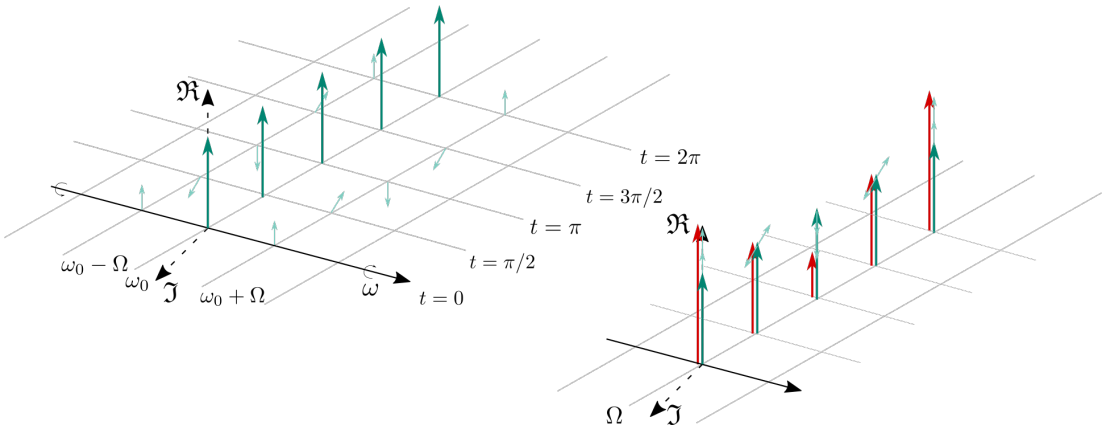

FIGURE II.7: The amplitude-modulated field can be visualized in the sideband picture for different discrete times within one modulation period. (left) The two light blue sidebands rotate at frequency Ω in opposite directions around the frequency axis, while the carrier field in green remains constant over time. This visualization corresponds to the Equation (II.87b). (right) The sum of the three individual fields (green and light blue) for the sideband frequency Ω is represented as a red phasor. The sum phasor undergoes periodic variations in length due to the different orientations of the sidebands, while its phase remains constant.

PHASE MODULATION

A similar analysis can be applied to phase modulation [33]:

$$E_{PM}(t) = E_0 e^{i(\omega_0 t + M\cos(\Omega t))} \tag{II.88a}$$
$$\approx E_0 e^{i\omega_0 t}(1 + iM\cos(\Omega t)) \tag{II.88b}$$
$$= E_0 e^{i\omega_0 t}(1 + i\frac{M}{2}e^{i\Omega t} + i\frac{M}{2}e^{-i\Omega t}) \tag{II.88c}$$

In (II.87b), the approximation is made that the modulation index M is significantly smaller than unity ($M \ll 1$). This approximation is crucial to avoid encountering a comb of sidebands at frequencies $n\Omega$, $n \in \mathbb{N}$ introducing excessive spectral complexity.

The outcome of Equation (II.88c) reveals that the phase-modulated field can be decomposed into three distinct components. Firstly, there is a stationary carrier field at frequency ω_0, characterized by an amplitude E_0. Secondly, there are two sidebands at frequencies $\omega_0 \pm \Omega$, each with an amplitude of $iE_0\frac{M}{2}$, directed along the complex axis.

In Figure II.8, the time evolution of this phase-modulated field is observed through the sideband picture representation, as well as the combined fields depicted in a phasor diagram. This figure serves as the phase modulation counterpart to Figure II.7, which is explained in the preceding paragraph.

II.5.2. QUANTUM SIDEBAND PICTURE

The quantum sideband picture is obtained from the classical sideband picture by calculating the time average of each sideband. As each sideband displays entirely random behavior, the result is a two-dimensional Gaussian distribution, particularly in the case of coherent states. This quantum noise distribution replaces the previous quantum noise phasors at frequencies $\pm\Omega$.Extending this process to all frequencies $\pm n\Omega$ yields a quantum sideband picture that characterizes quantum noise or vacuum noise (Figure II.9).

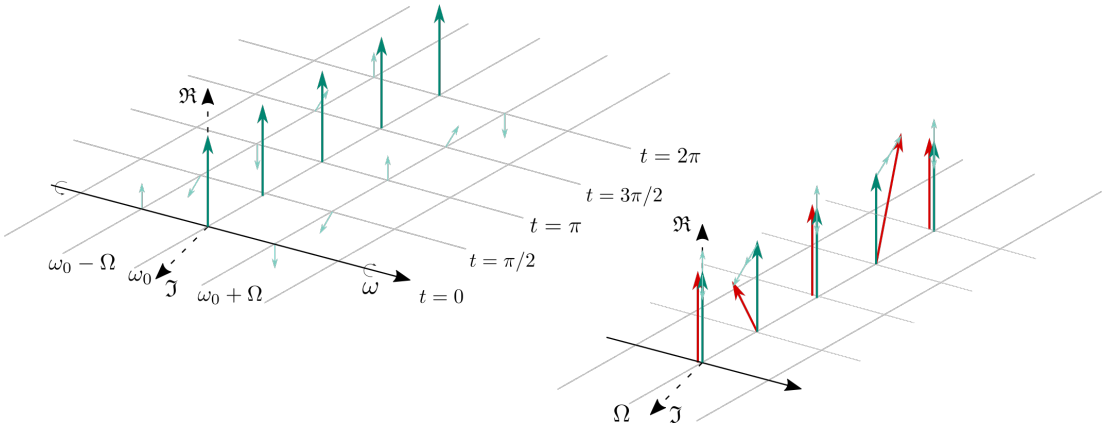

FIGURE II.8: (left) The phase-modulated field can be visualized in the sideband picture for different discrete times within one modulation period. The two light blue sidebands rotate at frequency Ω in opposite directions around the frequency axis, while the carrier field in green remains unchanged over time. This sideband picture representation corresponds to the Equation (II.88c). (right) The summation of the individual fields (green and blue) at the sideband frequency Ω is depicted as a red phasor. This phasor undergoes periodic variations in phase due to the different orientations of the sidebands, but the amplitude stays constant for small modulation indices.

VACUUM NOISE

Figure II.10 illustrates the representation of vacuum noise in the quantum sideband picture. On the left side, a quantum noise distribution is showcased at each sideband frequency $\pm n\Omega$, where there is no coherent amplitude at frequency ω_0. The time evolution within one modulation period remains constant, indicating that the quantum noise distribution inherently represents an average of quantum noise phasors over time.

In the central part of the figure, the time evolution of combined vacuum noise distributions at frequency Ω is evident, and it remains constant. This essentially captures a high-resolution measurement of a vacuum state, achieved by isolating the sideband frequency Ω through spectral filtering. Consequently, the axes' labels shift from quadratures to measured photocurrents, with $i_{\phi=0^\circ}$ and $i_{\phi=90^\circ}$denoting the measured photocurrents corresponding to the respective quadrature.

On the right side, the quantum phasor picture for the vacuum state at frequency Ω unfolds, derived by averaging the measurement shown in the middle section of Figure II.10.

COHERENT STATE

Figure II.11 displays the time evolution of a coherent state. It features a coherent amplitude at frequency ω_0 and vacuum noise distributions at all sideband frequencies. In the center of the figure, the time evolution of the measured photocurrent at frequency Ω for the quadratures of the coherent state can be observed. On the right, the corresponding quantum phasor picture is depicted, derived by averaging the measurement shown in the middle.

QUANTUM AMPLITUDE MODULATION

Figure II.12 showcases the combination of amplitude modulation, as depicted in Figure II.7, with vacuum noise. The phasors in both figures are identical, but in this case a quantum noise distribution is added. For clarity, the vacuum noise distributions are only displayed at the modulation frequencies $\pm\Omega$ and not shown at other frequencies. In the middle of II.12, the time evolution of the measured quadratures of the photocurrent at frequency Ω for the amplitude-modulated state is observed. Throughout one modulation period, the length of the

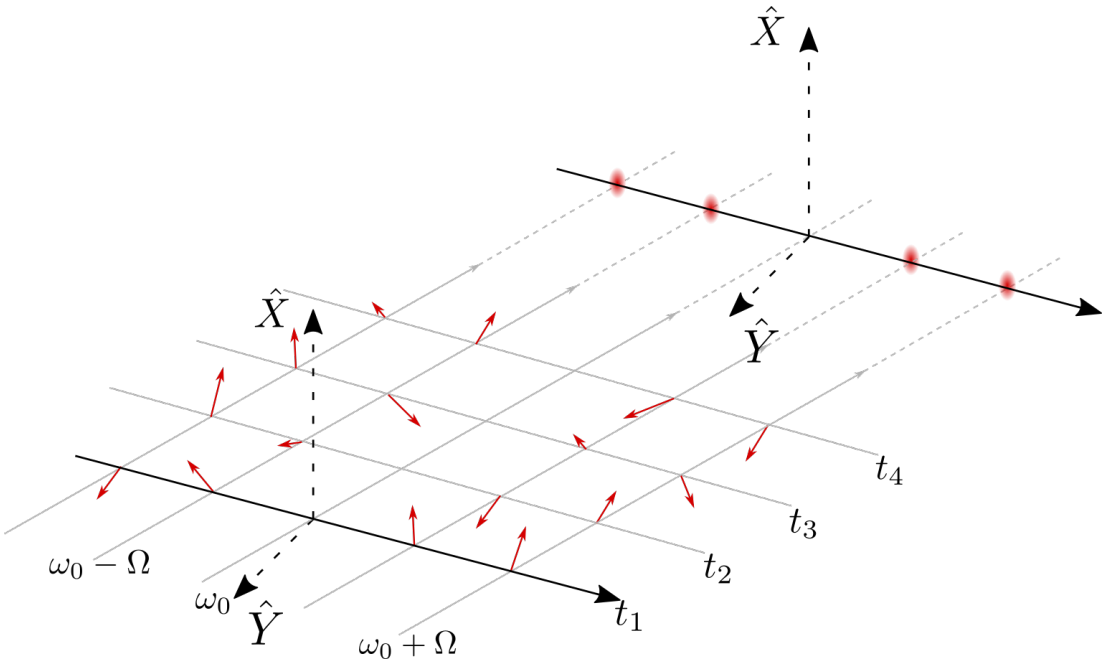

FIGURE II.9: Quantum noise representation in the sideband picture and its transformation into the quantum sideband picture. In the sideband picture, small phasors (red arrows) in quadrature space are used to visualize quantum noise at different frequencies. These quantum noise phasors exhibit a time-varying behavior, with their length following a Gaussian distribution and their phase changing indeterministically over time. To switch into the quantum sideband picture, the two quantum noise phasors at frequencies $\omega_0 \pm \Omega$, where Ω is a positive real number, are combined by beating them together and then averaging over time. This process results in a two-dimensional Gaussian distribution with unity variance, represented by a red dashed circle.

resulting red phasor undergoes periodic variations. Additionally, the quantum phasor picture is included on the right-hand side of Figure II.12, derived from averaging the measurement depicted in the middle. Comparing it to the vacuum noise distribution, the resulting amplitude noise distribution in the amplitude quadrature is significantly larger due to the presence of coherent sidebands. However, in the phase quadrature, the variance of the amplitude noise distribution remains identical to that of the quantum noise distribution. Consequently, the amplitude-modulated field exhibits pronounced amplitude noise but minimal phase noise at frequency Ω. This representation corresponds to amplitude squeezing

QUANTUM PHASE MODULATION

Similarly, combining the phase-modulated field illustrated in Figure II.8 with vacuum noise yields Figure II.13. In this case, the resulting quantum phasor picture on the right-hand side of the figure also displays an elliptical noise distribution. Notably, the variance in the phase quadrature is significantly larger compared to the vacuum noise distribution, while the variance along the amplitude quadrature remains the same. Consequently, this phase-modulated field exhibits substantial phase noise but minimal amplitude noise at frequency Ω. This representation corresponds to phase squeezing.

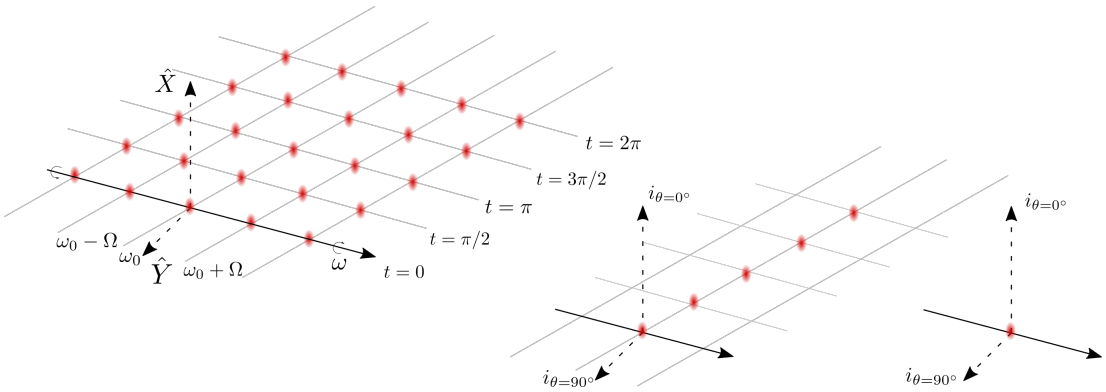

FIGURE II.10: Representation of the vacuum state in different pictures. (left) Time evolution of vacuum noise in the quantum sideband picture. At each sideband frequency $\pm\Omega$, a red quantum noise distribution represents the vacuum noise. The average of the time evolution remains constant over time. (center) Time evolution of the sum of two vacuum noise distributions at frequency Ω. This representation corresponds to a measurement of the vacuum state with high time resolution, spectrally filtered to retain only the sideband frequency Ω. The labels of the axes change from the quadratures to the measured photocurrents $i_{\theta=0°}$ and $i_{\theta=90°}$ of the corresponding quadratures. (right) Quantum phasor picture for the vacuum state at frequency Ω. It is derived by averaging the measurement shown in the central figure, resulting in a two-dimensional Gaussian distribution with unity variance. This quantum phasor picture provides a convenient way to represent the vacuum state in the quantum sideband picture at a specific frequency Ω as shown previously in Figure II.2.

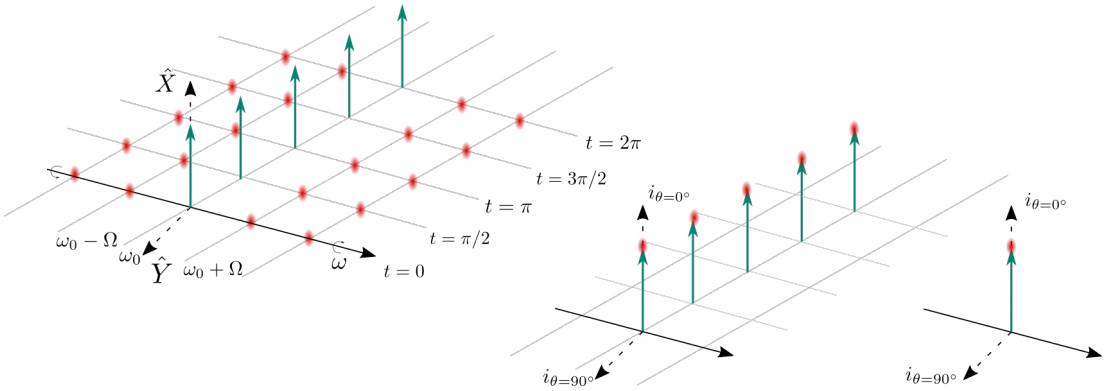

FIGURE II.11: Coherent states representation in different pictures. (left) Time evolution of vacuum noise in the quantum sideband picture. At frequency ω_0, a green arrow represents the coherent amplitude of the carrier field, while at each sideband frequency $\pm\Omega$, a red quantum noise distribution represents the vacuum noise. (center) Time evolution of the measured quadratures of the photocurrent at frequency Ω. (right) Quantum phasor picture of the coherent state at frequency Ω. It is derived by averaging the measurement shown in the central figure, resulting in a two-dimensional Gaussian distribution with unity variance. This quantum phasor picture provides a convenient way to represent the coherent state at a specific frequency Ω in the quantum sideband picture as shown previously in Figure II.2.

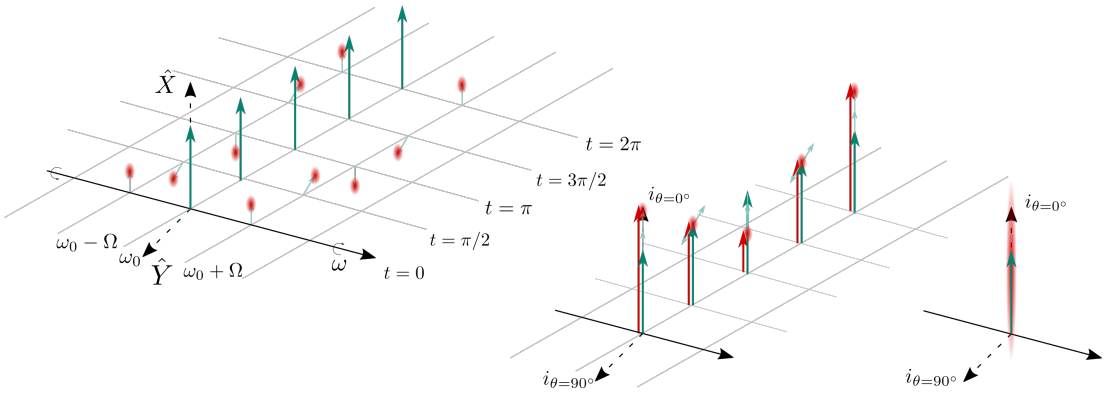

FIGURE II.12: The amplitude-modulated field at different times within one modulation period, using three physical pictures. (left) Quantum sideband picture representation. The two light blue sidebands rotate with frequency Ω in opposite directions around the frequency axis, while the carrier field in green remains constant over time. Vacuum noise distributions are located on top of the sideband phasors. (center) Results of measurements taken with an arbitrary high time resolution of the photocurrent at frequency Ω for the different quadratures. This can be represented by the sum of the three (light blue and green) individual fields as a red phasor, which includes the vacuum noise distribution. The sum phasor alters its length periodically in time due to the different orientations of the sidebands, but its phase remains constant. (right) Quantum phasor picture of the amplitude modulation. The green phasor represents the constant coherent amplitude of the amplitude-modulated field, and in red, the amplitude noise distribution is displayed. Compared to the vacuum noise distribution, the amplitude noise distribution is enlarged along the amplitude quadrature due to the beat and averaging process of the two amplitude modulation sidebands and their corresponding vacuum noise distribution.

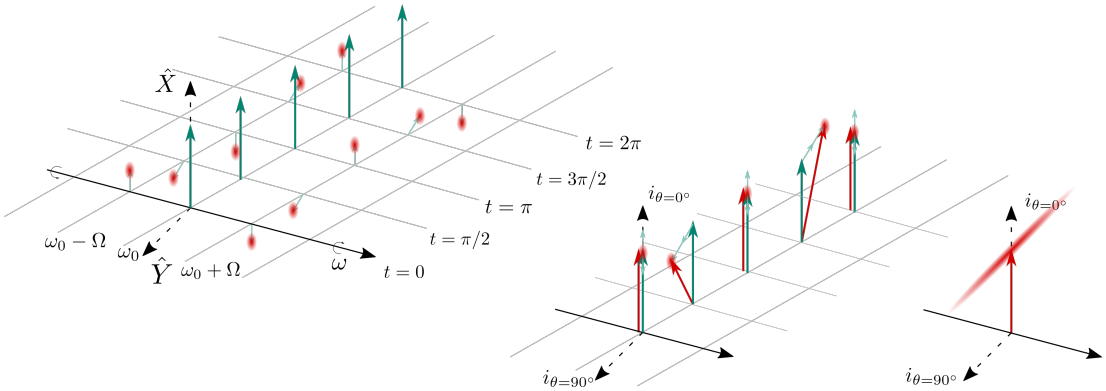

FIGURE II.13: Phase-modulated field at different times within one modulation period, using three physical pictures. (left) Quantum sideband picture representation. The two light blue sidebands rotate with frequency Ω in opposite directions around the frequency axis, while the carrier field in green remains constant over time. The sum phasor alters its length periodically in time due to the different orientations of the sidebands, but its phase remains constant. (center) Results of measurements taken with an arbitrary high time resolution of the photocurrent at frequency Ω for the different quadratures. This can be represented by the sum of the three (light blue and green) individual fields as a red phasor, which includes the vacuum noise distribution. The sum phasor alters its phase periodically in time due to the different orientations of the sidebands, but its amplitude remains constant for small modulation indices. (right) Quantum phasor picture of the amplitude modulation. The green phasor represents the constant coherent amplitude of the amplitude-modulated field, and in red, the amplitude noise distribution is displayed. Compared to the vacuum noise distribution, the phase noise distribution is enlarged along the phase quadrature due to the beat and averaging process of the two phase modulation sidebands and their corresponding quantum noise distribution.

III | SQUEEZED STATES GENERATION IN GW DETECTORS

This chapter explores the application of squeezed vacuum states to mitigate the impact of quantum noise on the GW detector. Initially, the standard quantum limit in gravitational wave detectors is derived. Subsequently, the chapter demonstrates how this limit can be surpassed by injecting squeezed vacuum states into the antisymmetric port of the detector. Additionally, the chapter briefly discusses the fundamentals of optical cavities, both as widely used elements within the interferometer and as a key component in generating frequency-dependent squeezing. Finally, the generation of the latter is explored from the sideband picture perspective.

III.1. Quantum noise in Michelson interferometer

In the quantum domain, particles and light exhibit inherent uncertainty, defying classical notions of determinism. As discussed in Chapter §II, this uncertainty manifests as fluctuations in diverse physical observables, even in the absence of external disturbances. In the context of GWs, these fluctuations assume significance, shaping and constraining the sensitivity of detectors. Within GW detectors, quantum noise introduces two primary contributions: radiation pressure and noise shot noise. Both originate from vacuum fluctuations entering the interferometer through the interferometer's dark port.

III.1.1. Radiation pressure noise

Radiation pressure refers to the force exerted by electromagnetic waves on objects or surfaces, arising from the transfer of momentum from the radiation to the body [32]. The uncertainty in the amplitude quadrature (ΔX) introduces fluctuations in the photon number at a specific position over time, giving rise to *radiation pressure noise*. The strain amplitude spectral density (ASD) of a simple Michelson interferometer, influenced by radiation pressure noise, is expressed as [34]:

$$h_{rad}(\nu) = \frac{1}{\pi M L \nu^2}\sqrt{\frac{\hbar P}{2\pi c\lambda}} \tag{III.1}$$

Here, P is the laser optical power, λ is the wavelength of the laser, m is the mass of the test mass, c is the speed of light, and ν the frequency. Although radiation pressure noise is a common feature in optical experiments, it is frequently overshadowed by other sources of noise, particularly thermal noise (see §V). However, in second-generation and future gravitational-wave detectors, radiation pressure noise is expected to become a significant limiting factor in sensitivity. Addressing and mitigating the effects of radiation pressure noise is therefore crucial for achieving higher precision measurements in these advanced detectors.

III.1.2. Shot noise

Shot noise is an intrinsic noise source that affects the measurement precision of various systems, including gravitational wave detectors. It arises from the fundamental discrete nature of light, where the detection of photons introduces statistical fluctuations in the measured signal. In particular, it arises from the inherent uncertainty associated with the phase quadrature (ΔY). Mathematically, shot noise contribution in a simple Michelson interferometer is proportional to the inverse of the optical power [34]:

$$h_{shot}(\nu) = \frac{1}{L}\sqrt{\frac{\hbar c\lambda}{2\pi P}} \tag{III.2}$$

Here, L is the length of the interferometer arm. Shot noise becomes particularly significant in situations where the available optical power is limited or in experiments with low photon counts. Understanding and managing shot noise is crucial for optimizing the sensitivity of GW detectors.

III.1.3. Standard Quantum Limit

Radiation pressure noise and shot noise arise from the inherent uncertainty imposed by the Heisenberg uncertainty principle. Interestingly, these noise sources exhibit opposite power dependencies. When combined, they give rise to a total quantum noise:

$$h_{QN}(\nu) = \frac{1}{L}\sqrt{\frac{\hbar c\lambda}{2\pi P} + \left(\frac{1}{M\pi\nu^2}\right)^2 \frac{\hbar P}{2\pi c\lambda}} \tag{III.3}$$

Due to the $1/\nu^2$ dependence of the radiation-pressure noise, this component becomes predominant at lower frequencies, while shot noise prevails at higher frequencies.

These two contributions depend on the optical power. This parameter serves as a means to regulate the coupling of quantum noise to the interferometer signal. Nevertheless, the power's impact on the coupling mechanism is complementary, preventing arbitrary reduction of quantum noise. Attenuating one noise source automatically amplifies the other. The quantum noise can be minimized at each frequency by balancing the two contributions ($h_{rad} = h_{shot}$) in relation to laser power:

$$P_{SQL} = \pi c \lambda M \nu^2 \tag{III.4}$$

The envelope comprising all power values that minimize the equation (III.3) is defined as Standard Quantum Limit (SQL):

$$h_{SQL}(\nu) = \frac{1}{\pi\nu\, L}\sqrt{\frac{\hbar}{M}} \simeq 1.68 \cdot 10^{-22} \left(\frac{1\ \text{Hz}}{\nu}\right) \frac{1}{\sqrt{\text{Hz}}} \tag{III.5}$$

This term represents the fundamental limit imposed by quantum mechanics on the precision of repeated measurements. The determined value is applicable to Virgo, given a $M = 42$ kg and $L = 3$ km.

In Figure III.2, the strain sensitivity of a simple Michelson interferometer is depicted (blue curve). The graph includes traces representing the contributions of radiation pressure noise and shot noise, as well as the SQL and the total quantum noise. By adjusting the input laser power, the overall quantum noise curve can be mapped to the SQL at different sideband frequencies. The SQL means the ultimate boundary for measurement sensitivity in the presence of radiation pressure noise and shot noise. Surpassing the SQL requires the implementation of advanced techniques and strategies, such as squeezed states, to reduce or manipulate these noise sources and achieve higher precision measurements.

The Michelson interferometer serves as the fundamental configuration for GW detectors, as discussed in §I.2. In the simple Michelson setup, two end mirrors are isolated and suspended on a pendulum, functioning as quasi-free test masses to detect the influence of passing gravitational waves [34]. GW interferometers operate in the dark fringe condition. This implies that all the laser power is back reflected to the symmetric interferometer port (the port where the laser enters) along with the classical and quantum source noises. Simultaneously, the near-dark anti-symmetric port of the Michelson interferometer (where the PD reads the signal), known as the AS port, is subject to quantum noise. In this port, quantum noise arises from the fluctuations in the incident vacuum state, which enters the AS port, undergoes reflection by the interferometer, and is subsequently detected by the readout PD. The optical layout of a simple Michelson interferometer affected by quantum noise is shown in Figure III.1.

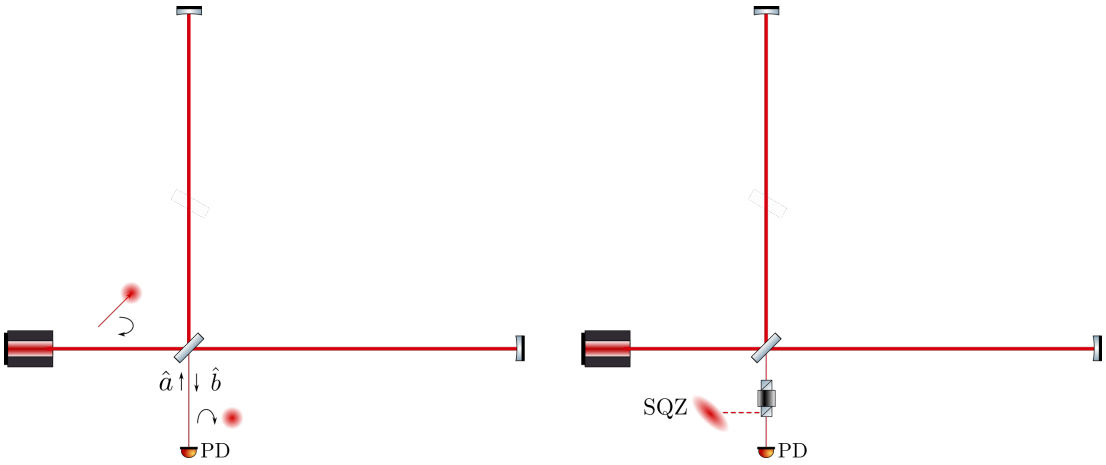

FIGURE III.1: Optical layout of a simple Michelson interferometer. (left) Quantum phasor diagrams (§II.5) illustrate that the bright beam is reflected to the symmetric port, while quantum noise enters and returns to the anti-symmetric ports. (right) The diagram depicts the injection of the vacuum squeezed state into the ITF to reduce quantum noise.

III.1.4. Squeezing contribution

Quantum noise can be mitigated by replacing the vacuum state entering the AS port with a squeezed vacuum state (Figure III.1). By carefully selecting the squeezing angle θ (see Eq. (II.47)), a squeezed state has the potential to reduce the quantum noise below the SQL, resulting in improved sensitivity [35]. In this case, the single-sided spectral density is:

$$h_{SQZ} = \frac{h_{SQL}}{\sqrt{2}} \left(\frac{1}{\mathcal{K}} + \mathcal{K} \right)^{1/2} \cdot \left[\cosh 2s - \cos\left(2(\theta + \Phi)\right) \sinh 2s \right]^{1/2} \tag{III.6}$$

Here, the (III.3) is redefined therms of the quantity $\mathcal{K} = \frac{P}{Mc\lambda\pi\nu^2}$, and s is the squeezing factor, as mentioned in (II.47), and $\Phi = \operatorname{arccot} \mathcal{K}$ [36]. The strain sensitivity of a simple Michelson

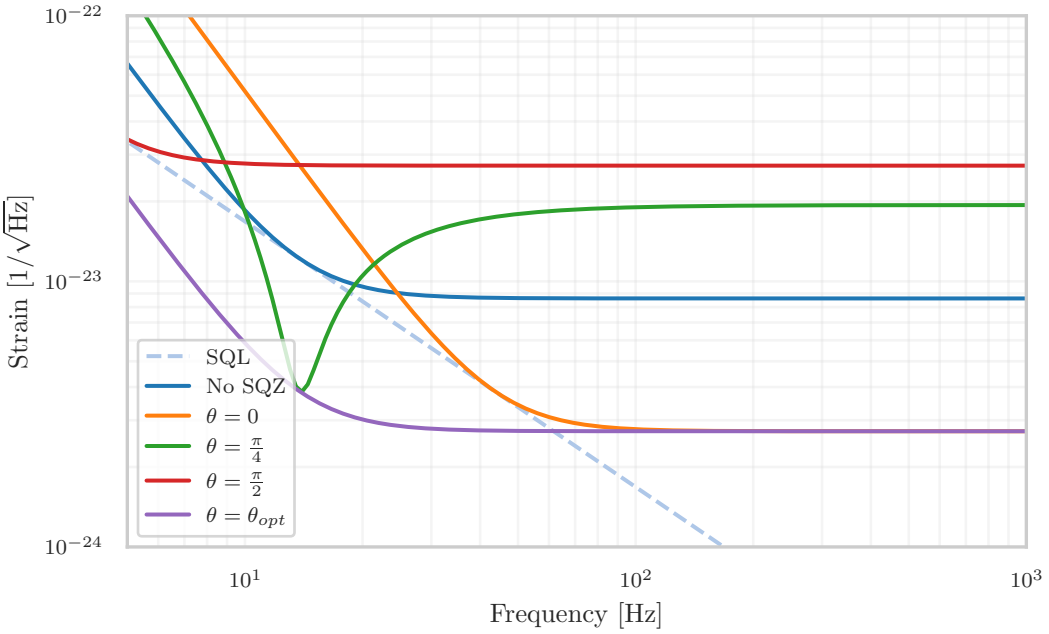

Figure III.2: Strain sensitivity of a simple Michelson interferometer with 10 dB injected squeezing at various squeezing angles. The purple curve refers to the optimal frequency dependent squeezing injection. The calculation is done by using Virgo's parameters [24].

interferometer with injected squeezing is illustrated in Figure III.2 for different squeezing angles. When an injected phase squeezed state ($\theta = -\frac{\pi}{2}$) is used, the reduction in shot noise contribution to the total quantum noise comes at the expense of an increase in radiation pressure noise. This is analogous to having a quantum noise-limited interferometer with a higher input power. Conversely, an amplitude-squeezed state ($\theta = 0$) leads to the opposite effect. Choosing a squeezing angle of $\theta = -\frac{\pi}{4}$ enhances sensitivity below the SQL within a restricted frequency range. However, this improvement comes at the cost of increased noise at all other frequencies, accompanied by reduced sensitivity in both the shot-noise and radiation-pressure-limited regimes. To maximize the benefits of injected squeezing across all sideband frequencies, it is necessary to employ a frequency-dependent squeezed (FDS) state. This involves utilizing an amplitude squeezed state ($\theta = 0$) in the low-frequency regime dominated by radiation pressure noise, rotating it to $\theta = -\frac{\pi}{4}$ around the SQL frequency, and further rotating it to a phase squeezed state ($\theta = -\frac{\pi}{2}$) in the high-frequency regime dominated by shot noise. The optimal squeezing angle can be determined by considering the specific characteristics of the system [36]:

$$\theta_{optm}(\Omega) = -\operatorname{arccot} \mathcal{K} \tag{III.7}$$

Substituting this relationship into the previous one yields:

$$h_{SQZ} = \frac{h_{SQL}}{\sqrt{2}} \left(\frac{1}{\mathcal{K}} + \mathcal{K} \right)^{1/2} e^{-2s} \tag{III.8}$$

The curve related to this relation is shown as purple line in Figure III.2.

III.2. Optical Resonator

In gravitational wave detectors, optical resonators, named also optical cavities, are employed principally in the arms of the interferometer to extend the effective path length. In fact, when the FP cavities are in resonance, light reflects back and forth inside, effectively extending the optical path traveled by the laser beam. In addition to the FP, PR, and SR cavities (§I.2.2), various other cavities exist (e.g. OMC, RFC, etc), including the one designed for quantum noise reduction. The implementation of the FDS technique involves the use of a detuned filter cavity, allowing for the rotation of the squeezing ellipse.

Optical resonators, in their simplest form, consist of two mirrors with reflectances r_1 and r_2, facing each other and separated by a distance of L. When laser light is injected into the cavity through the input mirror, a portion is immediately reflected back, while the remaining light is transmitted into the cavity. Inside the cavity, the light undergoes multiple reflections between the mirrors, eventually reaching a steady-state regime. Under specific conditions, the optical field undergoes constructive interference, resulting in resonance within the cavity. This resonance amplifies the intracavity optical power. The properties of an optical cavity, including resonance, are influenced by mirror properties, cavity geometry, and optical beam characteristics. Two distinct types of modes can be identified in an optical cavity: longitudinal modes and transverse modes. These modes describe the resonance conditions within the cavity.

III.2.1. Longitudinal modes

Longitudinal modes are associated with the phase accumulation along the longitudinal propagation direction, determining the relationship between the wavelength of light and the length of the cavity. Describing these modes involves considering the optical field as a complex amplitude in the plane wave approximation, neglecting evolution in the transverse plane (xy). The amplitude only evolves along the z direction and can be described as shown in Equation (II.58):

$$E(z) = E_0 e^{ikz} \tag{III.9}$$

The field before entering the cavity is considered as $E(0) = E_0$. The Input Mirror (IM) has a reflectance r_1 and a transmittance t_1 and it is separated from the End Mirror (EM) by a distance L (Figure III.3). The EM has reflectance r_2 and transmittance t_2. After the interaction with the IM, the incident beam splits into two components (the losses due to scattering and absorption are not considered). The first component is the reflected beam, denoted as $E_{0,r} = r_1 E_0$, and the second one is the transmitted beam, denoted as $E_{0,t} = i t_1 E_0$. The transmitted beam propagates within the cavity until it reaches the second mirror, taking the value $E_L = E_{0,t} e^{ikL}$. The EM back-reflects the beam into the cavity until it reaches again the IM, accumulating another phase term $E_{L,r} = E_{0,t} r_2 e^{ik2L}$. By repeating this process n times, the field E_n is obtained, reaching the IM after n round trips:

$$E_n = i t_1 E_0 \left(e^{ik2L} r_1 r_2 \right)^n \tag{III.10}$$

Each time incoming the light is transmitted from the IM, it interferes with the field from the previous round trip., giving rise to an *intracavity field*:

$$E_{cav} = \sum_{n=0}^{+\infty} E_n = E_{0,t} \sum_{n=0}^{+\infty} \left(e^{ik2L} r_1 r_2 \right)^n = \frac{i t_1 E_0}{1 - r_1 r_2 e^{ik2L}} \tag{III.11}$$

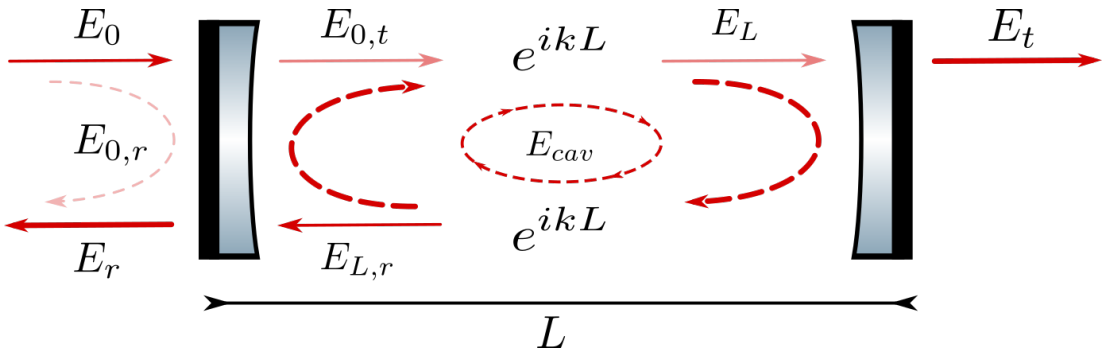

FIGURE III.3: Conceptual layout of a linear optical cavity. This configuration comprises a pair of mirrors positioned at distance L. The incident optical beam within the cavity undergoes a continuous cycle, maintaining a steady-state trajectory. The portion of light that exits through the End Mirror constitutes the transmitted beam E_t, while the portion transmitted through the Input Mirror merges with the promptly reflected component producing the reflected beam E_r.

This last equation represents the steady-state solution of the light inside the cavity. The fields which are transmitted and reflected by the cavity are respectively: :

$$E_t = E_0 \frac{t_2 t_1 e^{ikL}}{1 - r_1 r_2 e^{ik2L}} \tag{III.12}$$

$$E_r = E_0 \frac{r_1 - (r_1^2 + t_1^2) r_2 e^{ik2L}}{1 - r_1 r_2 e^{i2kL}} \tag{III.13}$$

These expressions represent the fields at the IM and the EM, respectively. The intracavity field E_{cav} plays a crucial role in describing the behavior of light within the optical cavity.

RESONANCE CONDITION

With the elements discussed, the spectral properties of the cavity, such as the *resonance condition*, can be studied. This condition is defined as the one that maximizes the beam power into the cavity relative to L:

$$P_{cav} = |E_{cav}|^2 = \frac{T_1}{(1 - r_1 r_2)^2 + 4 r_1 r_2 \sin^2 kL} P_0 \tag{III.14}$$

where P_0 is the power of the input beam and the transmissivity of the IM is defined as $T_1 = t_1^2$. The condition that maximizes (III.14) is $kL = n\pi k$ with $n \in \mathbb{N}$, from which it is obtained:

$$kL = \arcsin(0) \;\Rightarrow\; L = n\frac{\lambda}{2} \tag{III.15}$$

where n is an integer. The same condition in terms of the laser frequency can be expressed as:

$$\nu_{cav} = n\frac{c}{2L} \tag{III.16}$$

From this relation, the Free Spectral Range (FSR) can be defined, which is the frequency spacing between two consecutive transmitted optical intensity maxima:

$$\Delta\nu_{FSR} = \frac{c}{2L} \tag{III.17}$$

Another crucial parameter providing information about the frequency response is the resonance linewidth, defined as the Full-Width Half Maximum (FWHM) of the internal cavity power [32]. The linewidth is related to the free spectral range as follows:

$$\Delta\nu_{FWHM} = \Delta\nu_{FSR} \left[\frac{1}{\pi} \arcsin\left(\frac{1 - r_1 r_2}{2\sqrt{r_1 r_2}} \right) \right] \tag{III.18}$$

The proportionality with FSR is significant because it allows the derivation of an important quantity known as Finesse, expressed as:

$$\mathcal{F} = \frac{\Delta\nu_{FSR}}{\Delta\nu_{FWHM}} = \left[\frac{1}{\pi}\arcsin\left(\frac{1-r_1r_2}{2\sqrt{r_1r_2}}\right)\right]^{-1} \approx \frac{\pi\sqrt{r_1r_2}}{1-r_1r_2} \tag{III.19}$$

This approximation considers high-reflectivity mirrors with $|r_i|^2 \simeq 1$. The optical response of the cavity can be characterized by three distinct fields: the reflected field, the transmitted field, and the internal field. From this perspective, the cavity can be effectively represented as an equivalent mirror, with its properties fully described by the reflectance, transmittance, and internal gain:

$$r_{cav} = \frac{E_r}{E_0} = \frac{r_1 - (r_1^2 + t_1^2)r_2 e^{i2\pi\nu/\Delta\nu_{FSR}}}{1 - r_1r_2e^{i2\pi\nu/\Delta\nu_{FSR}}} \tag{III.20}$$

$$t_{cav} = \frac{E_t}{E_0} = \frac{t_2t_1e^{i2\pi\nu/\Delta\nu_{FSR}}}{1 - r_1r_2e^{i2\pi\nu/\Delta\nu_{FSR}}} \tag{III.21}$$

$$G_{cav} = \frac{|E_{cav}|^2}{|E_0|^2} = \frac{|t_1|^2}{(1-r_1r_2)^2 + 4r_1r_2\sin^2\left(\pi\frac{\nu}{\Delta\nu_{FSR}}\right)} \tag{III.22}$$

Notably, these parameters are frequency-dependent. The cavity can be distinguished into two regimes:

Resonance: in this condition, where $\nu = n\Delta\nu_{FSR}$, the cavity parameters become:

$$G_{cav} = \frac{|t_1|^2}{(1-r_1r_2)^2} \tag{III.23}$$

$$r_{cav} = \frac{r_1 - (r_1^2 + t_1^2)r_2}{1 - r_1r_2} \tag{III.24}$$

$$t_{cav} = \frac{t_2t_1}{1-r_1r_2} = \sqrt{G_{cav}}t_2 \tag{III.25}$$

From Equation (III.25) it can be observed that the transmittance of the cavity increases due to the cavity gain. The reflectance instead has three different behaviors depending on the sign:

$$\begin{cases} r_{cav} > 0 & \text{if} \quad r_1 > (1-\rho_1)r_2 \\ r_{cav} = 0 & \text{if} \quad r_1 = (1-\rho_1)r_2 \\ r_{cav} < 0 & \text{if} \quad r_1 < (1-\rho_1)r_2 \end{cases} \tag{III.26}$$

where $\rho_1 = 1 - (r_1^2 + t_1^2)$ is the IM optical loss.

Anti-resonance: in this case, where $\nu = (n + \frac{1}{2})\Delta\nu_{FSR}$ and the power inside the cavity reaches the minimum. the cavity behaves as a single mirror:

$$r_{cav} = r_1 + r_2\frac{t_1^2}{1+r_1r_2} \tag{III.27}$$

$$t_{cav} = i\frac{t_2t_1}{1+r_1r_2} \tag{III.28}$$

The reflectance of the cavity is primarily determined by the input mirror, with a small contribution from the second mirror. On the other hand, the transmittance of the cavity is lower than that of the individual mirrors, and there is a 90° phase shift.

III.2.2. Transversal modes

The transverse modes of a cavity describe the spatial distribution of the optical field in the transverse plane perpendicular to the direction of propagation. In this context, the amplitude of an optical beam can be represented as:

$$E(x,y,z) = U(x,y,z)e^{-ikz} \tag{III.29}$$

where $U(x, y, z)$ is the beam shape, and x and y are the transverse coordinates, while z denotes the propagation distance along the beam axis. Applying the paraxial approximation simplifies the analysis of the beam propagation inside the cavity. This approximation is valid when the beam divergence is small, allowing to neglect of higher-order spatial derivatives and the treatment of the beam evolution as a linear process. The Paraxial Helmholtz Equation [37] governs the beam shape under this approximation::

$$\nabla_{\perp}^2 U(x, y, z) + 2ik\frac{\partial U(x, y, z)}{\partial z} = 0 \tag{III.30}$$

where $\nabla_{\perp}^2 = \frac{\partial^2}{\partial x^2} + \frac{\partial^2}{\partial y^2}$.

To solve this equation, the amplitude along the xz and xy planes needs to be decoupled, resulting in two differential equations. Solving the equation for the xz plane yields:

$$\left(\frac{\partial^2}{\partial x^2} + i2k\frac{\partial}{\partial z}\right) u(x, z) = 0 \tag{III.31}$$

The solutions of this equation, denoted as $u_n(x, z)$, represent the transverse modes of the electric field. These modes represent a complete set of functions describing the two-dimensional amplitude of the beam. In general, the selection of these solutions is guided by the symmetry inherent in the system. When the beam profile exhibits circular symmetry, it is aptly described using Laguerre-Gaussian modes. Conversely, when the amplitude can be described using Cartesian coordinates x and y, Hermite-Gaussian modes are employed:

$$u_n(x, z) = \mathbb{H}_n\left(\frac{x}{w(z)}\right)\exp\left(-\frac{(x - x_0)^2}{w(z)^2}\right)\exp(-ikz)\sqrt{\frac{2^{-n}}{n!w(z)\pi}} \tag{III.32}$$

Here, $\mathbb{H}_n$ is the Hermite-Polynomial of order n, $w(z)$ is the beam radius and x_0 is the waist beam position.

The different transverse modes are distinguished by the Hermite polynomials, $H_n(x)$, which shape the beam profile. These polynomials play a crucial role as they enforce orthogonality among the modes. The orthogonality among these modes is expressed by the integral:

$$\langle u_n(x, z)|u_m(x, z)\rangle = \int_{-\infty}^{\infty} u_m(x, z)u_n^*(x, z)dx = \delta_{mn} \tag{III.33}$$

Solving the same equation in the XY plane allows combining the solutions in three-dimensional space:

$$U_{nm}(x, y, z) = u_n(x, z) \times u_m(y, z) \tag{III.34}$$

These modes, known as Transversal Electrical $\mathbf{TEM}_{nm}$ or Hermite-Gauss $\mathbf{HG}_{nm}$, are shown in Figure III.4. These modes provide insight into misalignment (first-order modes) and mismatch (second-order modes) between the main beam in the mode $\mathbf{TEM}_{00}$ and a cavity.

III.3. Squeezing in the sideband picture

Building on the concepts discussed in the preceding paragraphs, the role of squeezing in reducing quantum noise can be explored, using the graphical representation introduced in Section II.5.

Equation (II.55) reveals an important distinction between a vacuum state and a squeezed vacuum state: the latter has a non-zero expectation value of the number operator. Squeezed vacuum states are associated with fields represented by sideband phasors, typically spread along the frequency spectrum. However, the distribution can be limited to a specific bandwidth determined by the experimental setup, such as the linewidth of the optical parametric oscillator (OPO) cavity where the squeezed state is generated. The length of these sideband phasors is directly related to the degree of squeezing, and the sidebands at $\pm\Omega$ exhibit correlations that depend on the type of squeezing generated.

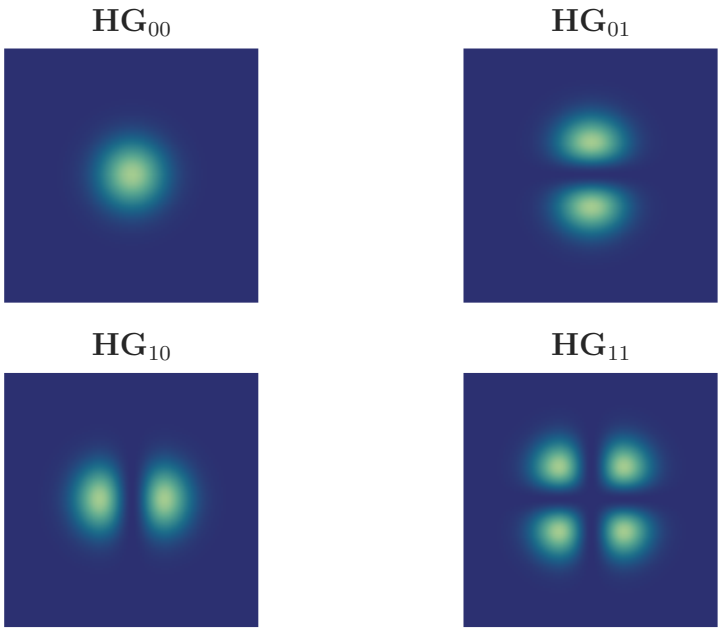

FIGURE III.4: Amplitude profile of the Hermite Gauss Modes classified by their mode order $N = n + m$. The figure illustrates some of the modes up to $N = 2$

III.3.1. AMPLITUDE SQUEEZED STATE

Figure III.5 provides a sideband picture representation of an amplitude-squeezed state. In this case, the sidebands are aligned in the phase quadrature and counter-aligned in the amplitude quadrature. Unlike amplitude and phase modulations (as shown in Figures II.7 and II.8), squeezing sidebands evolve over time and do not rotate continuously. The orientation between them maintains a fixed correlation while the orientation of the correlated pairs of sidebands remains random over time. Consequently, the correlated sideband phasors at frequencies $\pm\Omega$ represent the squeezed state at frequency Ω. In Figure III.5, these phasors are depicted in light blue.

Conversely, the uncorrelated portion of a squeezed state is characterized by a quantum noise distribution with a smaller standard deviation compared to vacuum noise. This uncorrelated noise is represented by the yellow distributions associated with the correlated sidebands. Figure III.5 showcases both the correlated and uncorrelated components of an amplitude-squeezed state. The left-hand side of the figure illustrates the time evolution, with no carrier field. Only the correlated and uncorrelated portions of the squeezed state are shown at the sideband frequencies $\pm\Omega$, while other frequencies are omitted for simplicity. A notable distinction between amplitude and phase modulation is the evident random orientation of the sidebands over time.

In the central part of Figure III.5, a photocurrent measurement is shown with high time resolution and a frequency filter isolating the sideband frequency Ω. The resulting phasor is the sum of the correlated components of the amplitude squeezing (light blue phasors) and the superimposed uncorrelated distribution.

The right side shows the quantum phasor representation of the amplitude squeezed state, obtained from the averaged measurement. The average coherent amplitude is zero, and the fluctuations are illustrated by the large yellow distribution, resulting from the combined correlated and uncorrelated fractions of the squeezed state.

The elliptical shape of the amplitude-squeezed state is evident, with the variance of the amplitude of the photocurrent quadrature $i_{\theta=0^\circ}$ matching the variance of the squeezed vacuum noise distribution. However, the distribution along the phase quadrature is enlarged compared

to the vacuum noise distribution, representing the anti-squeezed quadrature of the squeezed state.

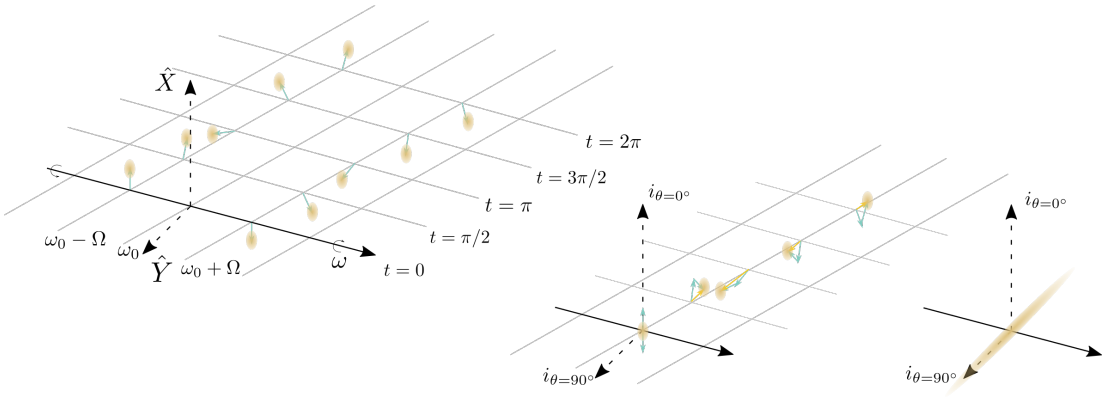

FIGURE III.5: Amplitude squeezing field at different times within one modulation period, using three physical pictures. (left) Quantum sideband picture representation. The correlated portion of the amplitude-squeezed state is depicted by the light blue phasors at frequencies $\pm\Omega$, while the uncorrelated portion is depicted by the yellow vacuum noise distribution. The sidebands are co-aligned in the phase quadrature and counter-aligned in the amplitude one. However, the overall orientation of the sideband pair varies randomly over time. (center) Results of measurements of the photocurrent at frequency Ω. The outcome is showcased through a yellow phasor, achieved by combining the correlated sideband phasors with their respective uncorrelated components. (right) Mean of the detected photocurrent: the correlated and uncorrelated segments constitute the squeezing ellipse, illustrating reduced variance along the amplitude quadrature and enhanced variance along the phase quadrature of the photocurrent. This is distinct from the vacuum states hown in Figure II.10.

III.3.2. PHASE SQUEEZED STATE

Figure III.6 shows the analogous diagram for a phase-squeezed state. The properties observed in the amplitude-squeezed states remain applicable, with the only distinction being the orientation of the correlated fractions in the quadratures: they are co-aligned in the amplitude quadrature and counter-aligned in the phase quadrature. This is evident in the right-hand side of the figure where the phasor representation is shown. Here, the variance of the phase of the photocurrent quadrature $i_{\theta=90°}$ matches the variance of the squeezed vacuum noise distribution, indicating the reduction of noise in this quadrature due to squeezing. However, for the amplitude quadrature of the photocurrent, the distribution is enlarged compared to the vacuum state, indicating an increase in noise or anti-squeezing in this quadrature.

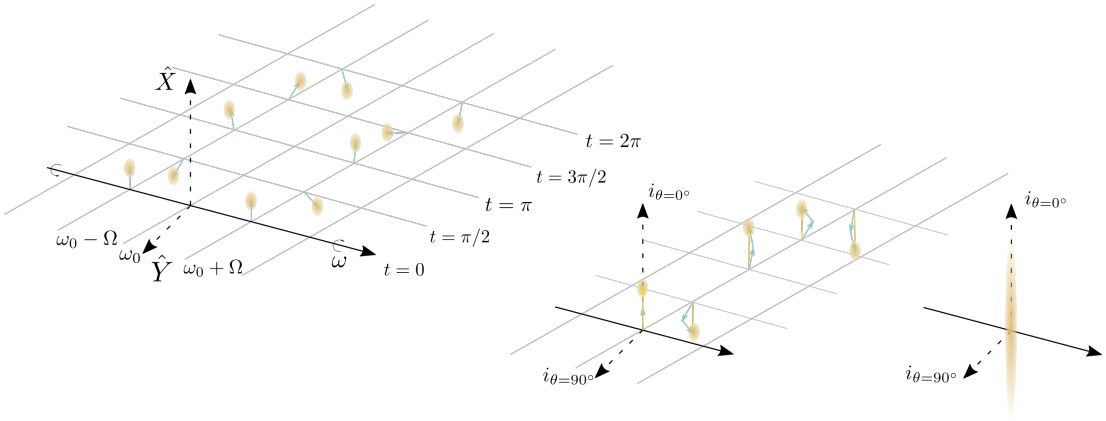

FIGURE III.6: Phase squeezing field at different times within one modulation period, using three physical pictures. (left) Quantum sideband picture representation. The correlated portion of the phase-squeezed state is depicted by the light blue phasors at frequencies $\pm\Omega$, while the uncorrelated portion is depicted by the yellow vacuum noise distribution. In this case, the sidebands are co-aligned in the amplitude quadrature and counter-aligned in phase one. However, the overall orientation of the sideband pair varies entirely in a random manner over time. (center) Results of measurements of the photocurrent at frequency Ω. The outcome is showcased through a yellow phasor, achieved by combining the correlated sideband phasors with their respective uncorrelated components. (right) The mean of the detected photocurrent is showcased. In this scenario, the correlated and uncorrelated segments constitute the squeezing ellipse. This ellipse illustrates a reduced variance along the phase quadrature and an enhanced variance along the amplitude quadrature of the photocurrent, distinct from the vacuum state illustrated in Figure II.10.

III.3.3. Frequency-dependent squeezing

As mentioned in §III.1.4, to overcome the SQL and gain with the squeezing injection both at high and low frequencies, it is necessary to inject a squeezing state with an optimally rotated ellipse, as a function of the frequency. In the Virgo interferometer, this Frequency-Dependent Squeezing (FDS) is obtained by the dispersion in reflection of a frequency-independent vacuum field through a detuned optical cavity. The latter refers to an optical cavity where the resonant frequency of the cavity ω_{cav} (see Eq. (III.16)) is intentionally shifted or "detuned" from the frequency laser. This detuning can be achieved by adjusting the lengths of the cavity mirrors or using other techniques like changing the laser frequency. Squeezed states, as explained earlier, exhibit correlations between $\pm\Omega$ sidebands, and the angle of the squeezing ellipse is determined by the relative phase between these correlated sidebands. By adjusting the relative phase between the two sidebands, the angle of the squeezing ellipse can be modified.

For a detuned cavity, the reflectivity can be written as:

$$r_{cav}(\Omega) = \frac{r_1 - (r_1^2 + t_1^2) r_2 e^{i(\Omega - \Omega_d)L/c}}{1 - r_1 r_2 e^{i(\Omega - \Omega_d)L/c}} \tag{III.35}$$

where $\Omega_d = \omega_{cav} - \omega_0$ is the detuning frequency. When a squeezed vacuum state is directed into the cavity at frequency ω_0, the reflected vacuum state exhibits a frequency-dependent squeezing angle $\theta(\Omega)$ (see Eq. (II.47)) as:

$$\theta(\Omega) = \arctan\left(\frac{(1 - \frac{\Lambda_{rt}^2}{\mathcal{F}}) \Delta\nu_{FWHM}^2 \Omega_d)}{(1 - 2\frac{\Lambda_{rt}^2}{\mathcal{F}}) \frac{\Delta\nu_{FWHM}^2}{4} + \Omega_d^2 + \Omega^2} \right) \tag{III.36}$$

where $\Delta\nu_{FWHM}$ is the FWHM of the cavity (III.18), $\mathcal{F}$ is the finesse (III.19), and Λ_{rt} represents the round trip losses of the cavity. The round-trip losses in a cavity are defined via energy conservation as [38]:

$$\Lambda_{rt} = \frac{P_0 - P_r - P_t}{P_{cav}} \tag{III.37}$$

where P_0 is the power entering into the cavity, P_r is the reflected, P_t is transmitted and P_{cav} is the power of the beam inside the cavity. This angle proves to be optimal for interferometers operating in the tuned configuration [39], including Virgo and LIGO. As with the previous cases, a faster and more intuitive graphical representation of the FDS can be produced using the sideband picture. The initial reference point to understand the FDS is Figure III.7, where the depiction of coherent quantum noise and a phase vacuum squeezed state is compared. Both examples are detailed in Figures II.10 and III.6, respectively. The essential distinction lies in

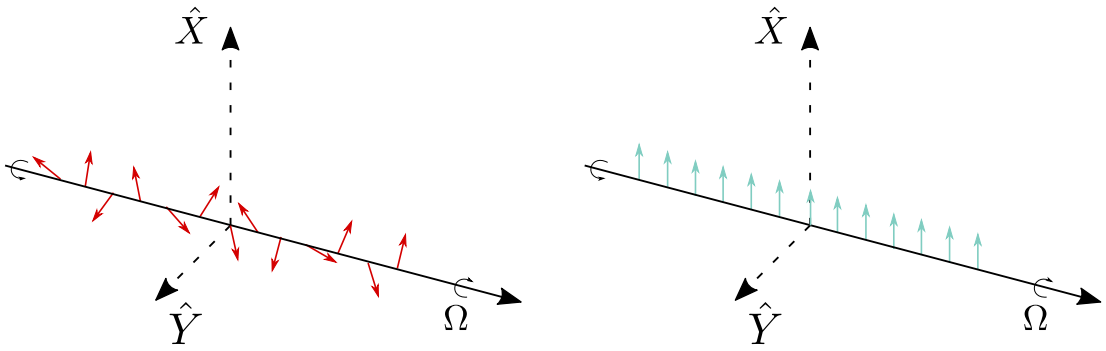

Figure III.7: Comparison between coherent quantum vacuum noise and vacuum phase squeezed state. (left) Quantum noise phasors exhibit a time-varying behavior, with their phase changing indeterministically over time: there is no correlation between the sifdebands at $\pm\Omega$. (right) The vacuum phase squeezed shows the correlations between the $+\Omega$ and $-\Omega$ sidebands.

the fact that, unlike in coherent quantum noise where each sideband at $\pm\Omega$ is associated with a

phasor featuring a completely random phase, the phase-squeezed state exhibits a well-defined phase relationship. When a squeezed state is reflected by a detuned cavity, each sideband's phase is altered based on the frequency. Figure III.8 shows the effect of reflection from a cavity detuned by Ω_d with respect to the reference frequency in the sideband picture. The figure displays both the frequency-dependent amplitude reflectivity of the detuned cavity (red line) and the dispersion of the reflected sidebands (blue lines). The frequency-dependence of the phase dispersion causes a phase shift of $\pm 180°$ for the phasors at high frequencies $\pm\Omega$. At these frequencies, the beating of the phasors still results in perfect phase squeezing. Near the resonance frequency ω_{cav}, the phase shift of the phasors at frequency Ω is rotated 180° with respect to the one at -Ω, resulting in a phase squeezing. Far from ω_{cav}, both the phasors at frequency $\pm\Omega$ are equally rotated, maintaining the squeezing state for those frequencies. Around the resonance frequency, the phase shift slowly varies with increasing frequency, ranging from 0° to $\pm 180°$. Consequently, the squeezed quadrature transitions gradually from the phase quadrature to the amplitude quadrature and then back to the phase quadrature.

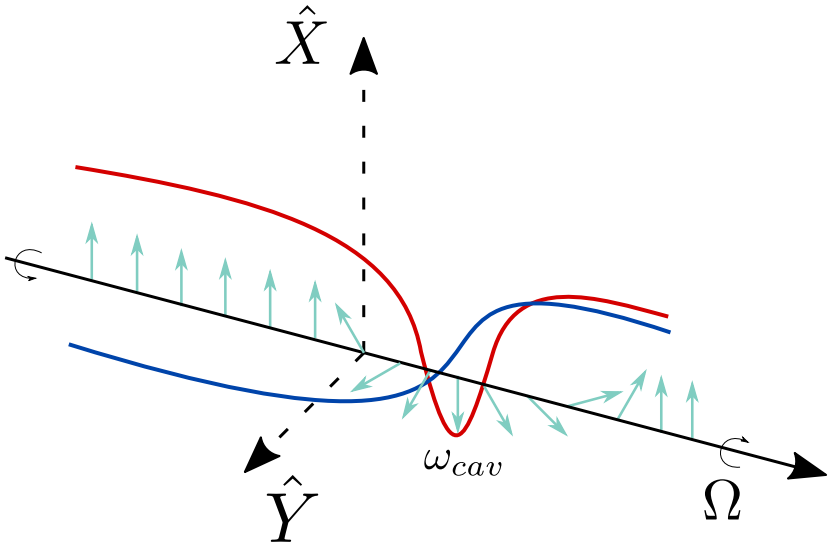

FIGURE III.8: Frequency-dependent squeezing in the sideband picture. The red curve illustrates the reflectivity of the filter cavity, while the blue curve depicts the phase dispersion. The sidebands represented by the phasors at different frequencies, due to reflection within a slightly detuned cavity, undergo frequency-dependent phase shifting. For Ω much greater than ω_{cav} they undergo a phase shift of $\pm 180°$. Around ω_{cav} the phase shift decreases until it becomes 0 at the resonant frequency. At this point, the state transitions from being phase squeezed to amplitude squeezed, as only the negative sideband undergoes a phase shift of 180°

.

IV | QUANTUM NOISE REDUCTION SYSTEM IN VIRGO

This chapter explores the Quantum Noise Reduction (QNR) system implemented in Virgo. It presents an overview of the system's general scheme and the control methods used to inject SQZ states into the interferometer. This thesis focuses on the Filter Cavity, as part of the work detailed in § IV.2. The challenges related to controlling this optical resonator are specifically addressed. The Filter Cavity plays a crucial role in rotating the squeezing ellipse, thereby enabling the generation of Frequency-Dependent Squeezing (FDS).

IV.1. General design of the squeezing system

In modern GW interferometric detectors, squeezed vacuum states are injected through the asymmetric port of the BS [35]. Hence, to make injection easier, the optical benches for the squeezing generation are positioned near the interferometer's Detection (DET) benches. Figure IV.1 presents a simplified scheme of the QNR system in relation to the Virgo interferometer (ITF).

IV.1.1. Optical layout

The Squeezing system is based on the same core system used for FIS injection during the O3 science run. The new setup for O4 includes the addition of other optical benches, both in air and suspended, each of which has a different purpose. Some of these are entirely modified, or added, to generate FDS for the O4 science run. The system is divided into four main parts: EQB1, SQB1, EQB2 and the FC. Each of these are discussed in the next paragraphs explaining both the role of the individual parts and describing the elements housed in them.

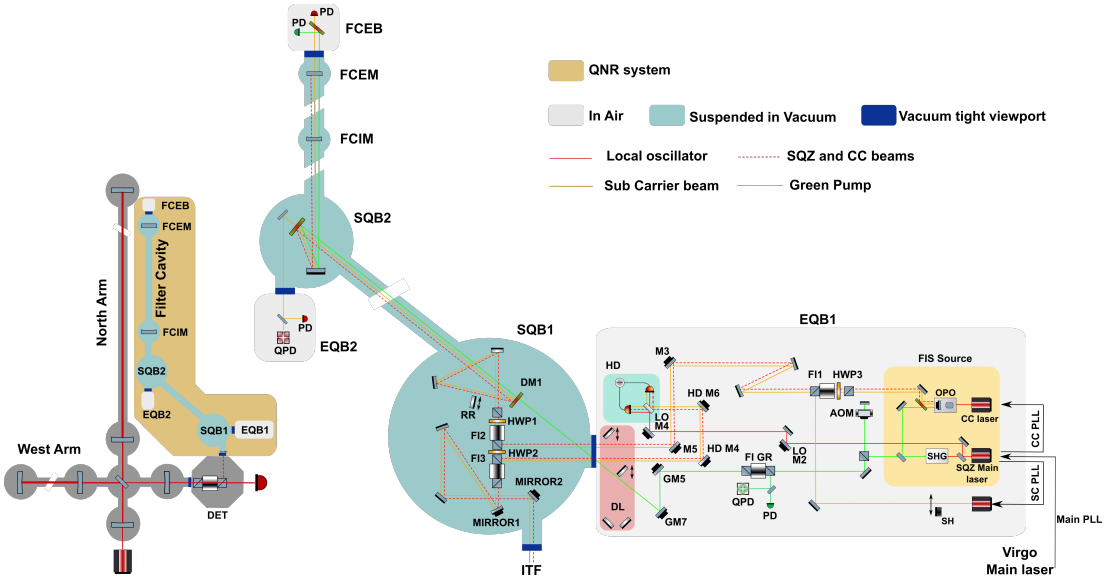

Figure IV.1: Experimental setup (not in scale) of the Quantum Noise Reduction system installed in the Virgo experiment at the European Gravitational Observatory (EGO). Figure reproduced from [40]. The system is located in the north-est area with respect to the interferometer (dark yellow area). The core of the experiment (EQB1 and SQB1) is connected to the detection DET bench and it extends along the north arm of the interferometer with the SQB2, EQB2 and the FC generating the FDS. On the right, is a zoomed scheme of the optical layout. The main elements are: AOM, acoustic-optic modulator; HWP, half-wave plate; M, mirror; DM, dichroic mirror; SHG, second harmonic generator; OPO, optical parametric oscillator; HD, homodyne detector; QPD, rf quadrant photodiode; PD, photodiode; PLL, phase locked loop; SH, beam shutter; PS, polarizing beam splitter; FCIM and FCEM, filter cavity input and end mirror, respectively: DL, Delay line

EQB1

The External Quantum Bench 1 (EQB1) is completely in the air and can be considered the system's core since the squeezing source is housed on this bench. The squeezing source was employed during the last Observing Run O3 to inject FIS [41]. By using an Optical Parametric Oscillator (OPO), this system is capable of generating a squeezed vacuum up to 13 dB of squeezing [42]. This bench hosts all the main beams that are used within the system:

SQZ main beam: it is the squeezed vacuum state generated by the OPO [43]. Its wavelength is at 1064 nm. During O3 this beam was directly injected inside the interferometer. As the main focus of this thesis is on other aspects, the detailed discussion related to the squeezer is not reported. For more comprehensive and detailed information on this topic, refer to [42].

Grean beam (GR): it is the pump beam used to generate the squeezed vacuum field. It is generated via the SHG technique [44] and its wavelength is 532 nm, corresponding to half of the SQZ main laser wavelength. It has a crucial role in the first phase of the Filter Cavity control and is responsible for generating error signals for the cavity alignment.

Local Oscillator (LO): it is a pick-off of the SQZ main beam before the vacuum SQZ generation. It is used as the local oscillator of the diagnostic homodyne detector, to measure the quadrature components of the SQZ with the QNR system stand-alone both in FIS and in FDS configuration.

Sub Carrier (SC): it is an additional laser source that has a wavelength of 1064 nm with a small offset concerning the IR beam. It is a bright reference of the vacuum SQZ beam and it is used to couple finely the SQZ beam with the FC and the ITF. Due to its specific function, the beam has a frequency offset of $\Omega_{SC} = 1.26$ GHz with respect to the main beam. After being prepared, the beam enters inside a Faraday Isolator (FI1 in figure IV.1) and is directed to the OPO. Here because of the frequency offset, it is entirely reflected. Mirrors in the optical path of the SC allow the beam is overlapped with the squeezed beam. To ensure proper overlap with the SQZ beam, careful alignment, and mode matching are performed between the SC and OPO.

Coherent Control beam (CC): this additional beam is generated by an additional laser source frequency locked with offset 4 MHz to the squeezer main laser. Its role is to generate error signals to stabilize the angle of the squeezing ellipse with respect to the selected LO. This method is proposed in [45].

Bright Alignment Beam (BAB): this is a bright auxiliary beam that is injected in the OPO for alignment and mode matching purposes. It is generated from the SQZ main laser and used as an alternative to the squeezed light generation.

The bench also hosts several beam control elements (not all shown in Figure IV.1) such as:

- The matching telescope between SC and OPO, the mirrors with PZT Tip Tilt actuators for self-alignment of SC in OPO.
- The pre-matching telescope between GR and filter cavity. The purpose is to have the size of GR and IR identical (apart from a $\sqrt{2}$ factor which compensates for the different wavelength) when they overlap at the dichroic mirror (DM1) on SQB1.
- EOM on the GR and on the SC to generate the PDH signals to lock the filter cavity longitudinally, and to generate the signals of the filter cavity self-alignment via the differential wavefront sensing technique. PZT tip-tilt actuators are also present for the AA of IR on FLT and for pointing the green on FLT. The QPDs are present and used for AA of the filter cavity on the green and the PD for extracting the PDH signal in reflection from the filter cavity.
- An acousto-optic modulator (AOM) on the GR is employed to introduce a frequency offset to the GR beam. This offset is crucial for managing the detuning between the IR and the FC components, especially when the FC is controlled using green light.
- The HD detector allows making some diagnostic measurements on the squeezed vacuum fields without injecting it into the ITF; the telescope for the matching between LO and SQZ on the homodyne, actuators for self-alignment between SQZ and LO, and phase shifters for implementing the squeezing ellipse angular control.

- A Delay Line (DL) is composed of two motorized mirrors that reflect the IR beams (SQZ and SC) and prevent them from leaving the bench: this is useful to characterize the FIS performance accounting only for the losses occurring on the EQB1.
- Shutters to block all the GR, SC, IR, LO beams, preventing them from exiting this bench.
- Beam monitor cameras and PDs.

SQB1

The Suspended Quantum Bench 1 (SQB1) is hosted in a vacuum chamber and it is suspended using a multistage seismic attenuation system [46] identical to that already in use in Advance Virgo for other auxiliary optical benches. In the current setup, SQB1 supports the optics used to send the beams coming from EQB1 to the FC and those coming from the filter cavity either to the interferometer for enhancing the sensitivity or to EQB1 for diagnostic purposes. Two Faraday Isolators (FIs) are used to isolate the squeezing source from backscattering coming from the interferometer. The double FI is designed in such a way that it allows sending the SQZ toward ITF or HD. The selection of the two configurations is possible using a motorized HWP that rotates by 90° the linear polarization between the two stages so that the beam can get reflected (hence directed towards the HD), or transmitted (hence directed towards the ITF) by the input polarizer of the second stage. Relevant elements within SQB1 are (see Figure IV.1):

- Mirrors equipped with pico motors for both IR and GR alignment.
- Adichroic mirror (DM1) is used to superimpose the green and IR beams and send them together toward the filter cavity.
- The first mirror of the matching telescope for SQZ and GR toward the filter cavity.
- Mirrors with pico motors to remotely align all beams towards the ITF. This is very important since the bench is in vacuum and the alignments need to be tuned remotely;
- Two PZT tip-tilt actuated mirrors (MIRROR 1 and MIRROR2) are used for the alignment of the SQZ toward the output mode cleaner of the ITF (see §IV.4.1). Unlike the mirrors with the pico motors, these two are used for the auto-alignment loop.
- A system of cameras (near-field and far-field) placed in reflection to a polarizer of the second FI that serves to monitor the spurious beam coming from ITF and pre-align SQZ and ITF.
- A telescope that is used to match the FDS system and the interferometer.
- A moving mirror (called Retro Reflector (RR)) is used to bypass the filter cavity. When this mirror is used, the FIS is directly injected into the ITF instead to be used for FDS production. This mirror is also a backup solution if the FDS fails.
- Amoving shutter is placed as the last optic that serves to protect the interferometer both from unintended squeezing injections and especially from effects due to scattered light from both beams coming from SDB1, EQB1, and SQB2.

SQB2

The Suspended Quantum Bench 2 (SQB2) is a vacuum-suspended bench essential for directing beams from SQB1 towards the FC. This bench is linked to the SQB1 bench (10 meters away) through a 25 cm diameter vacuum pipe and to the filter cavity (40 meters away). In addition to the steering optics, the bench hosts the second curved mirrors of the filter cavity mode-matching telescope. It also houses the IR optical line, directing 1 ‰of the power IR pickoff towards an external bench named EQB2. The EQB2 bench operates in the air and houses both the longitudinal and RF quadrant photodiodes necessary for the longitudinal and angular control of the filter cavity with IR.

Filter cavity

The filter cavity (FC) is used to provide the FIS rotation for the optimal FDS generation [24]. The FC has been designed to achieve a linewidth of about 25 Hz, that matches the optimal detuning frequency of the Virgo interferometer (§III.1), taking into account the interferometer parameters for the next observing run (O4) [40]. Once the detuning is known, the cavity length is based on a trade-off between two factors. Some squeezing degradation mechanisms, such as cavity round-trip losses, are inversely proportional to the cavity length [47]. In fact, with a shorter cavity, and consequently higher finesse, the squeezed vacuum would bounce more times inside the cavity increasing the total losses. Hence, increasing the cavity length can reduce the impact of these degradation effects on the squeezing performance. From the infrastructure viewpoint, a shorter cavity is preferable. Hence, the choice of cavity extension involves a meticulous balance between these contrasting requirements. Selecting a FC length of 285 m, while aiming for a linewidth of 25 Hz, results in a finesse of approximately $\mathcal{F}_{IR} \sim O(10^4)$. The FC is situated within the Virgo detector's north tunnel, parallel to the interferometer north-arm (refer to Figure IV.1). The cavity consists of two concave mirrors with a diameter of about 150 mm. The radius of curvature (558 m) has been selected to minimize the round-trip losses of the cavity, avoiding degeneracy with higher order modes [48]. The mirrors are seismically isolated using a scaled-down version of the Virgo super-attenuator inverted pendulum [46], and are controlled using the Virgo marionette concept [49]. Table IV.1 details some construction parameters of the FC. In addition, as reported in [50], ring heaters are installed in vacuum close to the mirrors in case there is a need to change the radius of curvature. The parameters useful for quantifying the performance of the FC in the context of the FDS for Advanced Virgo are defined in [24]. Here, §IV.3, the measurements of some of them are reported.

At the FC end, an additional in-air bench named Dilter Cavity End Bench (FCEB) is installed, hosting a dichroic mirror to separate IR and GR light in the transmission of the FC. For both beams, a camera and a photodiode are incorporated for monitoring purposes. The photodiodes serve the dual purpose of monitoring the power of the beams transmitted by the cavity and acting as a trigger to engage the lock of the filter cavity. The IR photodiode is also used to study the co-resonance between the bright alignment beam of the SQZ (BAB) and the SC. The cameras are used instead to monitor the shape and the position of the transmitted beam by the filter cavity over time.

IV.2. Control strategy

This section shows the different strategies used within the QNR system to maintain the stability of the various laser beams in terms of alignment, frequency, and relative phase and thus have a robust generation of FDS states.

IV.2.1. Optical phase locked loops

As presented in the previous section, the FDS source for AdV+ relies on three laser sources: the SQZ main laser, the CC laser, and the SC laser source. Each laser has a function that must meet specific requirements and operate with its specific frequency offset. To maintain these offsets, three Phase Locked Loops (PLLs) are implemented. The PLL boards, designed and developed at INFN Padova for the Virgo Squeezing system, incorporate two distinct servo loops that can be engaged independently and act directly on the actuators that are present on the laser sources. The initial one is termed the *FAST servo loop* which operates on the piezoelectric element of the laser head. The second one, referred to as the *SLOW loop*, operates on the laser's Peltier. The fast loop has a high bandwidth (40 kHz) and is used to achieve a low residual phase error, while the slow loop is used to maintain high dynamics and thus long-term stability of the system.

Parameter	Symbol	Value
Length	L	284.9 m
Mirror diameter	D	149.9 mm
Input mirror radius of curvature	R_1	556.0 m
End mirror radius of curvature	R_2	557.1 m
Input mirror flatness $\Phi 50mm$	R_1	0.58 nm
End mirror flatness $\Phi 50mm$	R_2	0.67 nm
PARAMETERS FOR INFRARED		
Input mirror transmissivity	T_1	562 ppm
End mirror transmissivity	T_2	3.16 ppm
Finesse	$\mathcal{F}$	9582 - 10204
Linewidth	$\Delta\nu_{FWHM}$	51.6 - 54.9 Hz
PARAMETERS FOR GREEN		
Input mirror transmissivity	T_1	2.6 %
End mirror transmissivity	T_2	2.7 %
Finesse	$\mathcal{F}$	117
Linewidth	$\Delta\nu_{FWHM}$	4502 Hz

TABLE IV.1: Summary of the filter cavity parameters. The table is divided into three parts, one for the parameters regarding the IR, one for the GR beam, and another one for the parameters in common. For the finesse $\mathcal{F}$ and linewidth with the IR beam, the extremes of variations of the measured values are reported, obtained in several estimations made at different times.

SQZ MAIN PLL

The first PLL is employed to achieve frequency locking between the Virgo main laser and the SQZ main laser. The Virgo main laser is brought to the DET laboratory, hosting the vacuum chamber where the SQZ beam is injected into the ITF, by a 50 m long optical fiber. The beam emerging from the fiber is at an offset of 80 MHz from the main laser, therefore the PLL offset frequency must also be set at 80 MHz to ensure proper synchronization and coherent operation between the two lasers. An important aspect of this PLL lies in the fact that the Virgo main laser is pre-stabilized in frequency and amplitude in order to lock the interferometer. This means that with good PLL precision, the frequency noise of the SQZ laser is significantly reduced because it is locked to an already pre-stabilized laser (i.e. the Virgo main laser). Otherwise, the frequency noise of the SQZ laser would be too high to lock the filter cavity.

CC PLL

The second PLL is used to lock the CC laser to the SQZ main laser with a frequency offset of 4 MHz. The choice of this value is determined by the following considerations:

- The offset is chosen to be sufficiently large to prevent any technical noise from the CC that could degrade the degree of squeezing produced in the OPO.
- The frequency offset has to ensure that the CC is reflected by the ITF to enhance the efficiency of the injection process.
- The frequency offset is designed so that the CC beam back-reflected by the ITF is partially transmitted by the Output Mode Cleaner (OMC). This has a free spectral range $\Delta\nu_{FSR}^{OMC}$ = 834 MHz and a $\mathcal{F}$= 1000 which corresponds to $\Delta\nu_{FWHM}$ = 800 kHz.

SC PLL

The third PLL is used to shift the SC frequency with respect to the SQZ main laser. Again, the choice of frequency offset ν_{SC} is dictated by several requirements:

- The frequency offset is chosen to prevent any interference between the Sub Carrier and the main laser of the interferometer.
- The SC must not resonate within the OPO but it must be totally reflected (free spectral range $\Delta\nu_{FSR}^{OPO} = 3$ GHz).
- The SC must be totally reflected by the OMC ($\Delta\nu_{FSR}^{OMC} = 834$ MHz).
- The SC has to be resonant into the FC. In fact, it plays a significant role in the precise stabilization of the FC length and the frequency detuning between the generated SQZ and the frequency at which it is measured. This detuning ensures that the rotation of the squeezing angle takes place at the crossover frequency, where the interferometer's Radiation Pressure Noise is equal to the Shot Noise. This condition is given by:

$$\nu_{SC} = \nu_{SQZ} + \Delta\nu_d + N \cdot \Delta_{FSR}^{FC} \tag{IV.1}$$

  where ν_{SQZ} is the SQZ beam frequency, $\Delta\nu_d$= 25 Hz is the required frequency detuning for the squeezing angle rotation, $\Delta\nu_{FSR}$= 526 kHz is the FC FSR, and N an integer equal to $N = 2395$. $N \cdot \Delta\nu_{FSR}^{FC}$ has been chosen so that not overlap with the $\Delta\nu_{FSR}^{OPO}$ and $\Delta\nu_{FSR}^{OMC}$. This leads to a value, mentioned earlier, equal to ν_{SC} =1.26 GHz.

The first two PLLs were developed and installed during the O3 science run for FIS injection (at that time the CC had an offset of 7 MHz). For technical details of these elements, please refer to [24]. In order to work during FDS generation and injection, the locking routine must be performed hierarchically i.e., by first locking the SQZ laser to Virgo's main laser and then locking the other two lasers. In case of Virgo laser instability, the system can work stand-alone with the SQZ laser unlocked and free-running. The only limitation is not being able to lock the FC due to the high-frequency noise of the SQZ main laser not locked to the Virgo main laser (as explained in §IV.2.1).

IV.2.2. Filter cavity controls

The successful injection of FDS into the interferometer requires precise control over FC length, optical path length, and alignment of the squeezed vacuum field. This meticulous control is essential to minimize squeezing ellipse angle errors and noise, as well as to reduce optical losses on both the FC and the Interferometer. The control logic relies on a combination of two references. The green beam serves as a reference for FC length and angular control, whereas the SC field is utilized for second-stage longitudinal control of the FC. The reasons for using two optical references are:

GR beam: it provides a simpler signal for longitudinal lock acquisition, particularly due to the low finesse of the FC at the green wavelength (see Table IV.1). It is suitable for providing longitudinal and angular control signals for the FC in scenarios where a bright IR beam might not be available. For instance when the system is in SQZ measurement mode into the HD.

SC beam: it offers a more precise reference for longitudinal control, as it is less dependent on cavity dispersion compared to the green field. Additionally, the SC field provides an accurate alignment reference for the squeezed vacuum field, as it is carefully matched at the OPO.

Longitudinal control

The mirrors of the FC are precisely maintained around their working position through a Local Control system. This system consists of three optical levers installed on each marionette that suspend the mirrors, which sense their angular and longitudinal motions and generate error signals. These error signals are then utilized by the actuators installed on the payload to

maintain the mirrors in the desired positions. To simplify the locking procedure, the FC is initially locked with the GR beam. In this configuration, the finesse is lower, contributing to simplifying the overall lock. Then, the control is switched to the SC beam to optimize the cavity length and fine-tune the cavity detuning. Both control methods employ the Pound-Drever-Hall technique based on phase modulation with an Electro-Optical Modulator (EOM). The phase modulation frequency for the GR beam was determined using the software *Finesse* [24]. This value is set at 5.5 MHz. The RF photodiode used to produce the GR error signal for the loop is hosted in the EQB1 bench (see Figure IV.1) and a PD is located in the transmission of the FC to trigger the loop. When the transmitted power overcomes a threshold the length control is engaged. The correction signals below 100 Hz are sent to the actuator on the FC end mirror, while the higher-frequency corrections are sent to the laser frequency control. Figure IV.2 shows the typical output of the cameras used to check the beams' position and shape during the locking procedure. The cameras are positioned in proximity to the photodiodes employed for locking purposes, both in transmission and reflection from the FC. For what concerns the SC,

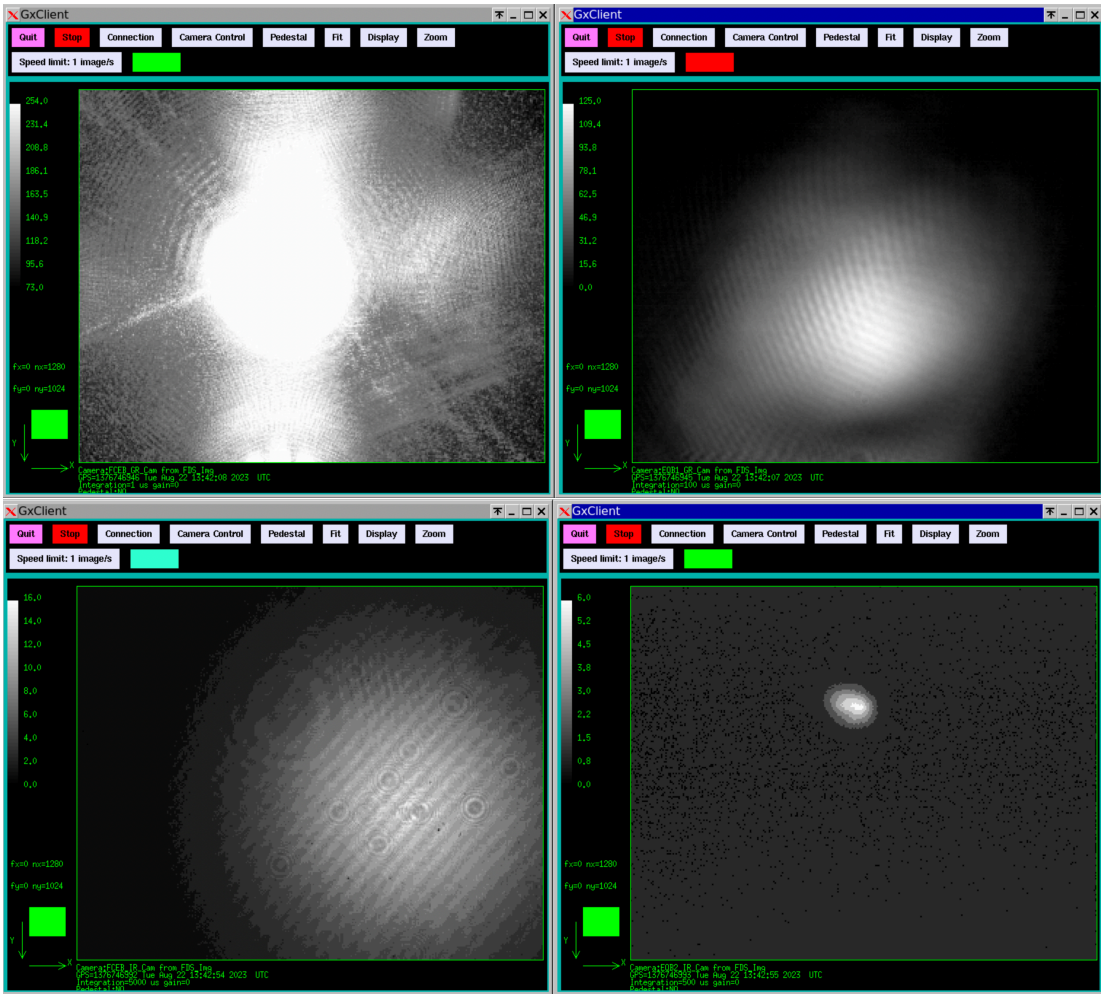

FIGURE IV.2: (top left) Field of View (FoV) of the GR camera in transmission from the FC into the FCEB. (top right) Fov of the EQB1_GR camera in reflection from the FC. (bottom left) FoV of the FCEB_IR camera in transmission from the FC. (bottom right) FoV of the EQB2_IR camera in reflection from the FC. All the cameras show the fundamental mode TM_{00} of the GR and the SC beams when the FC is locked.

given the offset in frequency with respect to the SQZ beam, the choice of modulation frequency was chosen using *Finesse*. In this case, constraints regarding the interaction of this beam with the interferometer cavities were also considered (i.e. OMC and SR), leading to a modulation

frequency of 11 MHz. The sensing process involves a combination of signals for the stabilization of the system. A DC signal from PD in the transmission of the FC is used as a trigger (GR PD in Figure IV.1). The PDH signal is obtained by demodulating the reflected signal from the FC using the PD located in EQB2. At this step, the signal used for FC mirror coil is now used for GR AOM frequency. The frequency of the AOM is scanned until IR PD on FCEB reaches a specific threshold. Once this threshold is met, the PDH signal is enabled to drive the AOM frequency to have the GR and the IR co-resonant, ensuring proper stabilization of the system.

GR alignment

When the cavity is locked to the GR beam, the angular position of the two cavity mirrors must be stabilized with respect to the GR beam orientation. Due to the limited linear range of the quadrant photodiodes on EQB1, a preliminary alignment of the mirrors on the laser beam might be necessary before engaging the loop based on the Ward sensing method[51]. After engaging the galvo loop to maintain the beam centered on the quadrant photodiodes QD1 and QD2 on EQB1 (the loop acts on galvo mirrors), the automatic alignment (AA) loop is turned on. The AA uses the same modulation sidebands used for the longitudinal control and acts on the angular degrees of freedom (DOFs) of the mirrors. The error signals are generated by digitally demodulating the RF outputs of EQB1_GR_QD1 and EQB1_GR_QD2 with the 5 MHz signal that drives the GR EOM. Once the optical axis of the cavity is kept fixed through the AA, a loop based on dither lines is engaged to get the GR beam centered as much as possible on the mirrors. This loop uses actuators mounted on two steering mirrors placed on EQB1 (EQB1_GM5 and EQB1_GM7).

IR alignment

To make the IR beam enter co-aligned with the GR on the FCIM, AA loops are engaged: the error signals derive from the demodulation of the signals of the quadrant photodetectors in reflection from the FC (specifically on EQB2). The actuators for these AA loops are on two mirrors M3 and M5 located on EQB1

IV.2.3. CC Loop

The efficacy of the quantum noise suppression explained in §III has as a prerequisite to maintain a constant phase for the squeezed field in relation to the phase of the main field circulating within the ITF. Variations in the squeezed ellipse, along with optical losses, lead to a reduction in the effective squeezing level. These variations arise due to mechanical and acoustic disturbances inducing random alterations in the optical path of the radiation field. Deriving a signal that encodes the phase difference between the two fields is imperative for acting on the squeezing ellipse angle. Because the squeezed beam does not have enough power to extract an error signal, an auxiliary bright beam, called *Coherent Control* (CC) (§IV.2.1), which has the same information as the squeezed beam and is used for phase stabilization [45]. The CC beam is injected into the OPO, where it overlaps with the main SQZ beam. In this way, the CC experiences the same nonlinear interaction with GR, the parametric amplification, as it does with the infrared vacuum field at frequency ω_0. Consequently, the phase of the GR (SQZ phase) is encoded in the phase of the generated sidebands. Additionally, the beating of these sidebands with the local oscillator (LO) enables the estimation of the phase relative to the LO. From this information, it is possible to generate two error signals to control the relative phase between the CC and the OPO pump and between the CC and the local oscillator used for the squeezing measurements. The latter (IV.1) in the case of HD detector and the ITF main beam in the case of SQZ injection into the ITF. The following paragraph shows a brief mathematical discussion of the CC to derive how it carries information related to the squeezing phase and how the loop to keep the phase fixed is implemented. First, the loop is shown in the general case, and then the case is implemented in the QNR system in Virgo.

CC field

As described in §IV.1, the CC has a frequency offset of 4MHz with respect to the SQZ main beam. The expectation values of the annihilation operators of the upper and lower sideband fields at frequencies $\omega \pm \Omega$ are:

$$\langle \hat{a}_+ \rangle_{CC} = \langle \hat{a}(\omega + \Omega) \rangle_{CC} = \alpha_\Omega \tag{IV.2}$$
$$\langle \hat{a}_- \rangle_{CC} = \langle \hat{a}(\omega - \Omega) \rangle_{CC} = 0 \tag{IV.3}$$

so the single sideband field can be described by the real-valued amplitude α_Ω. As in §II.1.2 two quadrature operators are introduced:

$$\hat{a}_1(\Omega)_{CC} = \frac{\hat{a}_+ + \hat{a}_-^\dagger}{\sqrt{2}} \tag{IV.4}$$
$$\hat{a}_2(\Omega)_{CC} = \frac{\hat{a}_+ - \hat{a}_-^\dagger}{i\sqrt{2}} \tag{IV.5}$$

When the CC enters the OPO, it interacts with the nonlinear medium: because of the parametric amplification process induced by the pump at 2ω, a portion of the pump photons undergoes conversion into photon pairs at frequencies $\omega + \Omega$ and $\omega - \Omega$ through the process of parametric amplification [44]. This can be described by applying the squeezing operator (II.46) to the two quadratures (IV.4) and (IV.5). After some calculation, the new quadrature operator $\hat{b}_{1,2}$ expectation is obtained:

$$\langle \hat{b}_1(\Omega) \rangle_{\mathrm{CC}} = \frac{\alpha_\Omega}{\sqrt{2}} \left[(\cosh s + \sinh s \cos\theta) - i \sinh s \sin\theta \right] \tag{IV.6}$$
$$\langle \hat{b}_2(\Omega) \rangle_{\mathrm{CC}} = \frac{\alpha_\Omega}{\sqrt{2}} \left[\sinh s \sin\theta - i(\cosh s - \sinh s \cos\theta) \right] \tag{IV.7}$$

Performing the Fourier transforms of $\hat{b}_1(\Omega)$ and $\hat{b}_2(\Omega)$:

$$\hat{b}_{1,2}(t) = \hat{b}_{1,2}(\Omega) e^{-i\Omega t} + \hat{b}_{1,2}^\dagger(\Omega) e^{i\Omega t} \tag{IV.8}$$

From this point, the electrical field of the CC that exits the OPO can be determined as follows:

$$E_{\mathrm{CC}}(t) \propto \langle \hat{b}^{(+)}(t) + \hat{b}^{(-)}(t) \rangle \tag{IV.9}$$

with:

$$\hat{b}^{(\pm)}(t) \equiv \frac{1}{\sqrt{2}} \left(\hat{b}_1(t) \pm i \hat{b}_2(t) \right) e^{\mp i\Omega t} \tag{IV.10}$$

Finally, it is obtained:

$$\langle E(t) \rangle_{\mathrm{CC}} \propto \frac{1-g}{\sqrt{2}} \alpha_\Omega \cos((\omega + \Omega)t) - \frac{1-g}{\sqrt{2}} \alpha_\Omega \cos((\omega - \Omega)t - \theta) \tag{IV.11}$$

where $\sqrt{g} = \exp(2s)$ is used. The last equation shows how the parametric amplification or de-amplification process within the OPO affects the coherent control field. The resulting electric field emerges from the squeezed light source, characterized by two sidebands symmetrically spaced apart by Ω relative to the central carrier frequency ω. In particular, the sideband at $-\Omega$ contain the phase difference between the CC and the GR pump used in the parametric amplification process.

Phase control of the GR pump field

To generate the error signal utilized in the feedback loop for adjusting the phase of the pump field relative to that of the CC, a signal in reflection concerning the injection of the CC field is

employed. The photocurrent generated by the PD is directly proportional to the square of the incoming field:

$$I_{CC} \propto \langle \hat{E}(t) \rangle^2_{CC} \tag{IV.12}$$

By performing demodulation of this signal at a 2Ω the error signal is derived:

$$S_{GR_{err}} \propto \frac{(-1+g^2)\alpha_\Omega^2 \sin 2\theta}{4g} \tag{IV.13}$$

This dependency is contingent on the squeezing angle (θ), more precisely, the phase difference between the squeezed vacuum and the GR pump. With this error signal, a feedback loop is implemented to stabilize the angle θ to a fixed value. The actuator of this loop is a longitudinal piezoelectric actuator (PZT) glued on a mirror in the GR path. Its objective is to modify the optical path of the pump field to lock its phase, thereby locking the quadrature of the SQZ field with the phase of the CC. The optical and electrical scheme of the loop to control the phase of GR pump is shown in Figure IV.3.

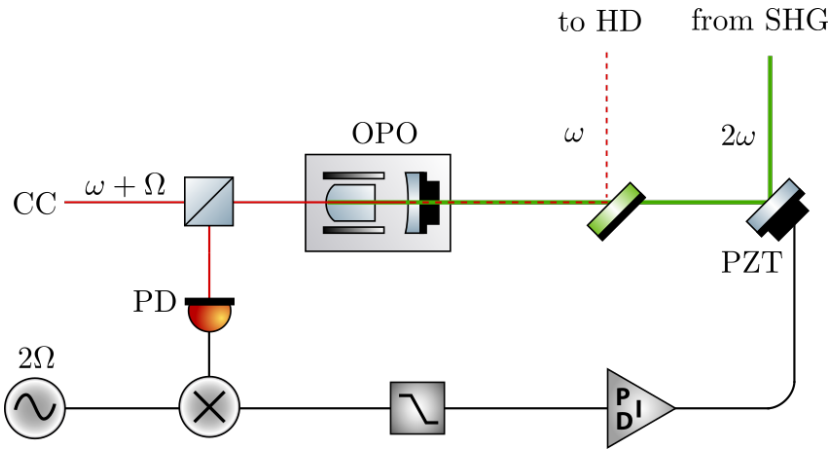

FIGURE IV.3: Optical and electrical layout of the CC loop to lock the GR pump phase

PHASE CONTROL OF THE HOMODYNE LO

The CC is transmitted by the OPO and, along with the SQZ beam, reaches the HD, which interferes with the LO. The latter can be described within the HD as follows:

$$E_{LO}(t) \propto \alpha_{LO} e^{-i(\omega t+\varphi)} \tag{IV.14}$$

with α_{LO} is the classical field's amplitude. The signals detected at the two photodetectors of the HD (§II.3.4) are determined by using the BS matrix described in (II.68). By subtracting and subsequently applying lowpass filtering to both homodyne photocurrents, the following is determined:

$$\begin{aligned} i_-(t) &\propto |E_{PD_1}(t)|^2 - |E_{PD_2}(t)|^2 \\ &\propto \frac{2\sqrt{2}\alpha_{LO}\alpha_\Omega(-1+g)}{\sqrt{g}} \cos(\Omega t + 2\theta + \varphi) \end{aligned} \tag{IV.15}$$

Then, within the HD electronics, this signal is demodulated by multiplying it with $\cos(\Omega t)$. The result of this operation is low-pass filtered. In this way, the error signal is:

$$S_{LO_{err}} \propto \frac{2\sqrt{2}\alpha_{LO}\alpha_\Omega(-1+g)}{\sqrt{g}} \sin(2\theta + \varphi) \tag{IV.16}$$

This error signal depends on both the relative phase φ between the GR pump and the LO, and the SQZ angle θ. However, as shown in the previous section, the SQZ angle can be stabilized independently by acting directly on the pump. Consequently, θ can be considered as a constant. The phase φ that remains to be controlled is the phase of the LO field with respect to the CC field, which represents the squeezing quadrature read with the HD. Figure IV.4 shows the basic scheme of the loop. In the QNR system, the fluctuations of the phase φ need to be corrected in a wide frequency range, i.e. up to 5-10kHz, which is generally greater than the bandwidth of a PTZ actuator. The following section describes how this problem is addressed.

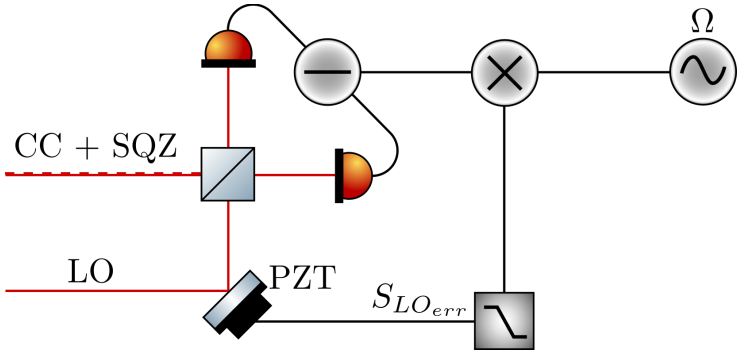

FIGURE IV.4: Optical and electrical layout of the CC loop to lock the LO phase

PHASE CONTROL IN VIRGO QNR

In the QNR system, the GR pump control remains the same as the one just shown. However, the current approach divides the phase correction into three parts. The first two are on the LO path and use two different actuators: one acting on the mirror LO_M2 which is a PZT with small displacement (3 μm) and high bandwidth, and the other one on LO_M4, a slow PZT with a larger range 30 um (see FigureIV.1). The loop on M2 corrects fast fluctuations. However, due to its limited range, it would saturate immediately. Therefore, its correction is kept around zero by acting on the long-range piezo that corrects slower fluctuations. This solution is not sufficient to maintain a squeezing measurement for more than 20 minutes. Given the size of the system, the distance between EQB1 and the input mirror of the filter cavity moves about 1 mm day-night. To overcome this problem when measuring FDS, a third actuator is added at the longitudinal position of the inverted pendulum (along z) of the filter cavity input mirror. This loop tends to vanish the correction signal to M4 so it stays within the M4 actuator range.

CC DURING SQZ INJECTION

What has been said in this section is valid in the case where the QNR system is in stand-alone mode. In the case of injecting squeezing into the dark port of the interferometer, the LO is represented by the interferometer carrier. In this scenario, changing the LO phase, i.e. the ITF phase, is not possible. Therefore, it is needed to act on the squeezed vacuum field. In this case, the error signal utilized for phase control is extracted from the detected light passing transmitted by the OMC (§IV.4.2). In this process, the CC beats with Virgo main laser on the PD B1 (see Figure I.4) and the beat note is demodulated at the same frequency of the CC (4 MHz). The resulting error signal is used to implement a control loop that acts directly on the SQZ main laser PLL. By acting on the 80MHz frequency offset of the main PLL, there is an indirect impact on the CC PLL, which introduces a frequency offset of 4MHz. Since the phase is the derivative of time with respect to frequency, maintaining a constant phase relationship between two signals implies that both signals (ITF and SQZ) are maintained at the same frequency. This method, implemented for the scientific run O3, is slightly different from what was shown in the previous section in which the squeezing phase is changed by moving a mirror across the optical path of

the pump beam. One of the advantages of this method is that the squeezed vacuum remains unaffected by scattering on the moving mirror, leading to a reduction in concerns related to stray light.

IV.2.4. Active FSR measurement

During the first long-term measurements of the FDS, as discussed in §IV.3.3, a limitation for measurement and optimal FDS preparation arose. The issue stems from the fact that between two FC unlocks, the two mirrors are free to move. The locking length of the cavity is determined by the initial positions of the mirrors, resulting in a typical variation of δL between successive lock points. This variation has a consequential impact on the relative detuning between the GR and IR beams, as detailed in [52]:

$$\Delta_d = \frac{c \cdot \delta_{AOM}}{2L\lambda_{GR}(\lambda_{GR} + \delta_{AOM})}\delta L \approx 1.3 \cdot 10^5 \frac{\text{Hz}}{\text{m}} \cdot \delta L \tag{IV.17}$$

Here, δ_{AOM} represents the change in the GR wavelength λ_{GR} induced by AOM. The detuning Δ_d arises because the GR beam utilized for controlling the FC length differs from the one employed for squeezing generation. This discrepancy results from an additional frequency offset introduced using an AOM of 80 MHz. More precisely, the frequency offset is twice as much, i.e. 160 MHz, because of the double passing in the AOM.

The second effect of the change in the cavity length is the detuning between the IR beam and the SC.

This effect can be justified by considering the relationship between the two beams, particularly the shift in frequency of ∼1260 MHz (2395 FSR, as discussed in §IV.2.1) with respect to the IR. This relationship is expressed in (IV.1).

When the FC unlocks and relocks, the change in length results in a FSR alteration. The frequency of the SC may not be an integer multiple of the new FSR, leading to a modification in the SQZ detuning.

To keep a constant squeezing detuning frequency and decouple the two effects, a method named FMODERR is implemented. This method measures the cavity length after each unlock. This approach is based on the determination of the FSR of the cavity from the frequency difference between the SC and phase-modulation sidebands added of the SC, when both of which resonate in the cavity [53]. It is worth noticing that these sidebands are additional, distinct from the 11 MHz sidebands used for PDH signals to lock the cavity (§IV.2.2). The frequencies of the new sidebands are selected to be an integer multiple, specifically $n = 150$, of the FSR) ($\sim$ 78 MHz). To achieve resonance conditions for the sidebands after an unlock, a frequency dither line is introduced to the FMODERR sidebands. This is achieved by applying a 13 Hz AC voltage to the FM input of the radiofrequency (RF) generator responsible for producing the sidebands. As a result, the power transmitted by the FC acquires a component at the same frequency, which diminishes when the sidebands become resonant in the FC. This condition is accomplished through a loop that introduces a DC signal to the FM channel until the 13 Hz component in the FC transmitted light is canceled out. Ultimately, the FSR of the cavity is estimated as the sum of the central frequency of the generator and the DC frequency applied to the FM input, divided by 150. After a lock/unlock cycle. the steps to measure FSR and set the correct detuning are as follows:

- Set the SC beam in resonance with the FC using the IR PDH error signal.
- Set the SC sidebands in resonance with the FC using the described procedure, estimating the FC FSR.
- Once the FSR is determined, the frequency offset of the SC beam is set to the 2395th FSR, and overlapped with the SQZ beam. At this stage, both the SC and the SQZ fields are out of resonance.
- Utilize the PDH signal of the SC to act on the GR AOM to bring GR, SC, and SQZ in resonance.

- Achieve the desired SQZ detuning $\Delta\nu_d$ by adding $\Delta\nu_d$ to the SC PLL offset.

Implementation

Before implementing the described method, the detuning produced by the equation (IV.17) was verified experimentally. For this test, the SQZ system is changed to the BAB mode. The test is performed manually with the following steps:

1. With the FC locked on the GR and the SC, the latter is shuttered, and acting on the GR AOM, the IR in BAB mode is put in resonance.

2. The SC is unshuttered and acting on SC PLL reference it is also put in resonance.

3. With the two beams in resonance, the FC is unlocked by opening the control loop. The FCIM is moved manually changing the FC length by -220 μm.

4. The cavity is then relocked. For the BAB to be in resonance, a shift of 60 Hz in its offset is required, while the SC offset has to change by 900 Hz for resonance.

The last point confirms the two effects that need to be compensated: both the detuning between the BAB (and so the SQZ) and the GR and the SC offset. The SC frequency offset relative to the BAB frequency is $FSR \cdot 2935$. Consequently, when the length of the FC changes, the SC experiences an amplified change by a factor of 2395. Two sidebands are added to the SC EOM, in addition to the PDH sidebands. This addition is achieved using a commercial generator (Agilent 33250A) that allows frequency modulation, with central frequency set to: $f_{gen} = 78.920364$ MHz. This value corresponds to $N_{FSR}^{f_{gen}} = 150$ FSR of the filter cavity [1]. The generator settings are shown in Table IV.2 As described in the previous section, the FSR estimation is measured

Sidebands settings	
Amplitude	0.9 V
Frequency	78.920759 Hz
FM range	200 Hz
FM settings	
Amplitude	0.25 V
Frequency	13 Hz

Table IV.2: Settings of the Agilent 33250A. The value set on the generator is slightly different from that used in the loop because the generator output was measured with a frequency meter. The FM settings are used to generate a dither line on the sidebands.

as :

$$FSR = \frac{(f_{gen} + f_{corr} \cdot cal)}{N_{FSR}^{f_{gen}}} \tag{IV.18}$$

where f_{corr} represents the DC voltage applied to the FM generator to counteract the effects of the dither signal at 13 Hz in the FC transmission. The constant "cal" signifies the voltage-to-frequency conversion of the FM channel. This conversion is determined through measurements conducted by applying various DC voltages to the FM channel, which operates akin to a Voltage-Controlled Oscillator (VCO). The corresponding frequency of the generated signal is then measured using a frequency meter. From the fit shown in Figure IV.5 $cal = 39.4$ Hz/V is obtained.

The entire procedure for testing the ability to restore the detuning condition after FC unlock is summarized in the following points:

1. The cavity is locked on the GR.

[1] The procedure used to measure manually the FSR of FC is described in [54]

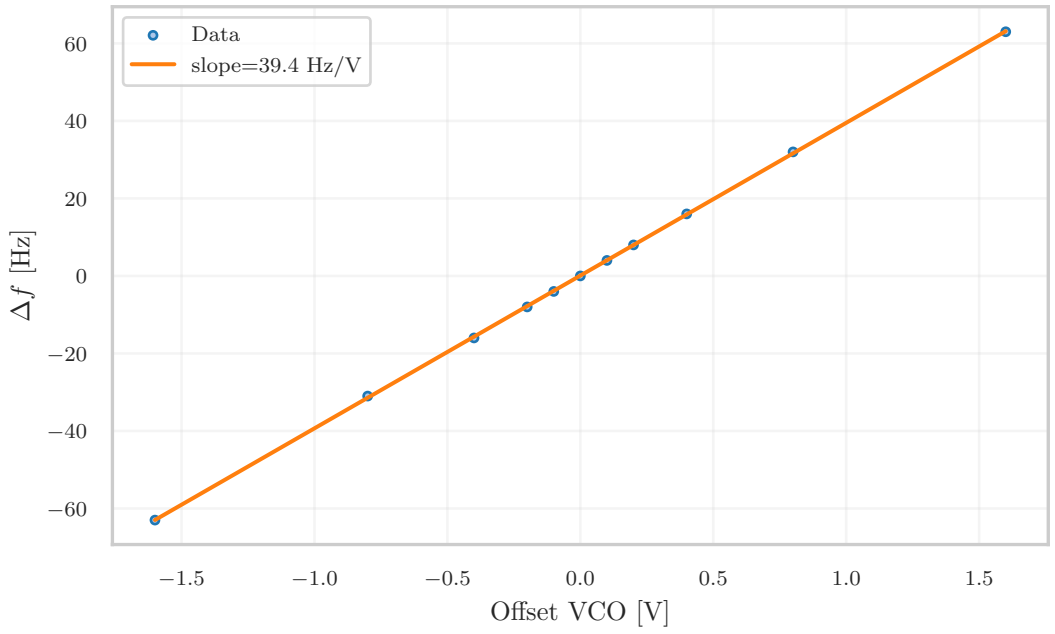

FIGURE IV.5: Calibration of the FM input of the signal generator. The zero of the vertical axis is when the signal frequency equals that set on the signal generator F_{gen}

2. With the SC shuttered, the BAB is put in resonance acting on the GR AOM modulation frequency.
3. The SC beam is unshuttered and put in resonance acting on the frequency offset of SC PLL.
4. With an IR detuning at 0 Hz the FC is unlocked.
5. Acting on the z DoF of FCEM suspension (along the beam propagation), the length of the FC is reduced by 300 μm.
6. The FC is relocked on the GR. Once the cavity is locked, the BAB transmission is reduced, while the SC transmission vanishes. This observation confirms that both beams have gone out of resonance.
7. The BAB is left with its initial detuning and the SC is put in resonance acting only on the SC PLL frequency. The IR_AA loop is switched on.
8. The FMODERR loop is closed to measure the cavity FSR, as described above.
9. The IR_AA loop is opened and SC is set at the frequency deduced by the measurement of the cavity FSR expressed by (IV.18).
10. Neither the IR beam nor the SC is perfectly in resonance with the cavity. To address this, adjustments are made to the GR AOM modulation frequency, and the SC is brought in resonance using the SC PDH error signal.
11. By shuttering the SC, it is observed that the IR is in resonance. Therefore, the initial detuning (zero-detuning) is restored as required.

Figure IV.6 shows a ∼15 hours measurement of FSR without actuation (up to point 8 of the above procedure). The SC is maintained in resonance acting on the SC PLL reference frequency. As can be seen from the bottom right figure, this method uncovers a frequency drift once the

system is stabilized and FSR jump is corrected. This effect is the additional detuning of GR with respect to IR due to the different behavior of the coatings depending on the temperature of the mirrors. Prior to implementing this method, automated FDS measurements (as discussed in §IV.3.3) faced challenges in maintaining the stability of the FC detuning frequency for an extended duration, mainly due to the occurrence of FC unlock/lock cycles. However, upon integrating this procedure into the Virgo automation, the setting of the detuning frequency no longer caused problems with the measurements.

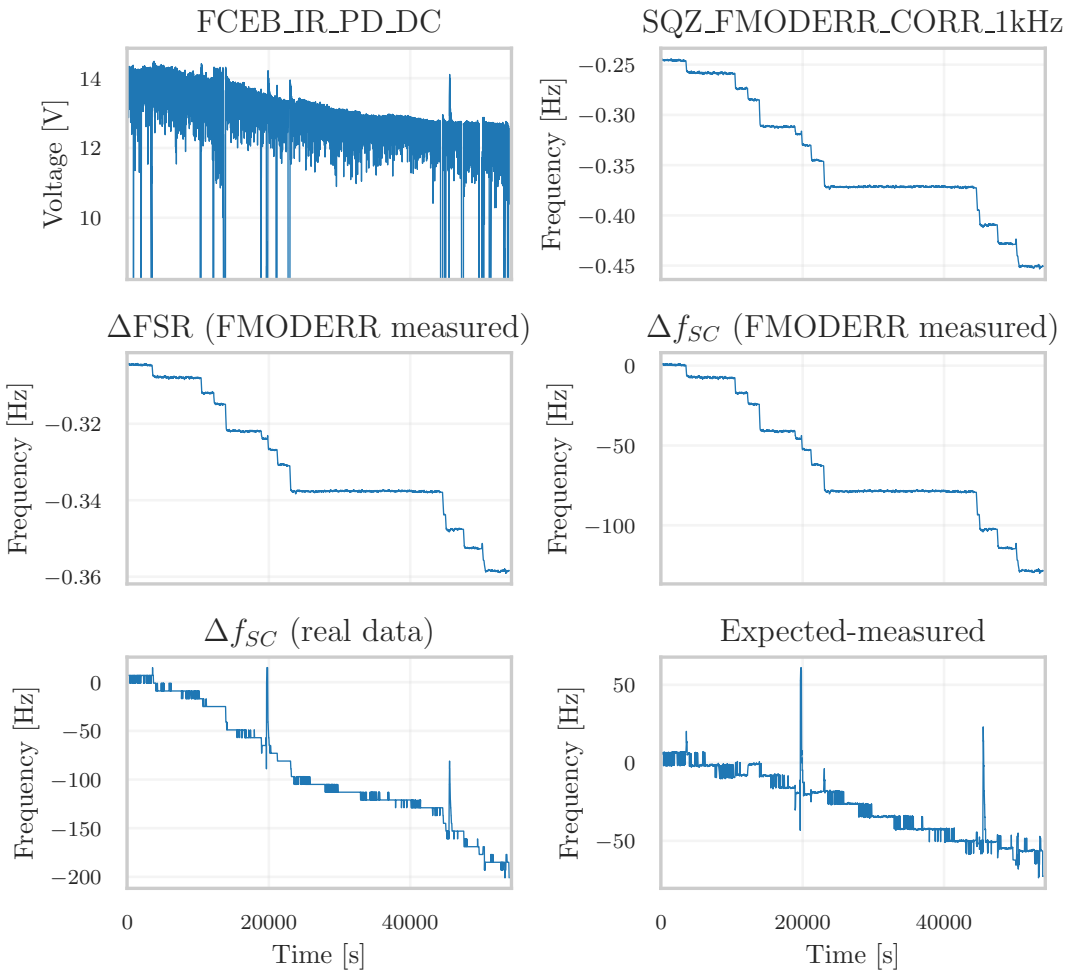

FIGURE IV.6: Data collected in a 15h long period of the signals for the FMODERR method, to measure the FSR without actuation. Both SC and BAB are injected in the FC. (top left) The transmission of the SC drops from 14 to 12.3 V, this means that the BAB went out of resonance (detuning more than 50 Hz). (top right) The FMODERR sensing SQZ_FMODERR_CORR_1kHz channel jumps at every unlock (change of FSR length) but it is stable during a lock. (center left) FSR variation is measured using FMODERR. (center right) Upon recomputing the SC PLL frequency from the SC, a drift of approximately 120 Hz is observed. This value represents the cumulative effect of all the unlocks. (bottom left) To keep the SC beam in resonance, the SC PLL is moved by 180 Hz. (bottom right) The difference between the measured frequency of the PLL SC and the one computed with FMODERR drifts continuously up to 60 Hz after 15 hours.

IV.3. Squeezing characterization

The efficacy of frequency-dependent squeezed vacuum is significantly impacted by any optical losses that might occur along the pathway between the generation of the quantum state within the OPO and its ultimate measurement at the HD or the ITF. As mentioned above, the QNR system can generate and measure both FIS and FDS in stand-alone mode, that is, without the interferometer. This mode is useful to characterize and optimize. In fact, the system is modular, allowing losses to be isolated and measured only on EQB1, EQB1+SQB1, and FDS produced in reflection of the FC. The measurements shown below led to the article [40]. Finally, in addition to the loss estimation, the long-term operation has been characterized.

IV.3.1. System alignment

To be able to measure the degree of squeezing or anti-squeezing, it is necessary to align the optical path up to the HD, where the SQZ beam and the LO overlap. To minimize the detection losses, it is required that the LO and the SQZ beams have the same beam waist, perfect spatial overlap, and polarization overlap. Moreover, to reduce the effect of technical noise from the LO, it is necessary to maintain the splitting ratio of the HD BS as close as possible to 50%. After selecting the LO position, the next step is to align and match the SQZ beam. However, since it is a vacuum beam, this process requires to switch to BAB mode. The first coarse alignment is achieved using two cameras on EQB1. Using a mirror mounted on a slider before one of the two HD PDs, the beams are directed towards two CCD cameras separated by an appropriate Guoy phase (Near Field camera (NF) and Far Field camera (FF)). Here, the beams are overlapped manually by visually checking the cameras and performing beam steering. The fine alignment is achieved by removing the flip mirror and maximizing the visibility of the interference fringes between BAB and LO using the HD PDs. To maximize matching, action is taken on the different telescopes in the system, on the length of the delay line, and on the length of the optical return path between SQB1 and EQB1. After achieving well-aligned LO and BAB with minimized losses, the transition to SQZ mode occurs. The magnitude of the 4 MHz beat note between LO and CC, which propagates with the SQZ beam at the HD, serves as the figure of merit. The best alignment between SQZ and LO is obtained when the CC beat note amplitude is maximized. The final alignment is kept by maintaining the signal detected through the 4 MHz magnitude at its maximum. This is achieved through an Auto Alignment system acting on the x and y DoF of two mirrors on the SQZ optical path (HD_M4 and HD_M6). It can be demonstrated that the ratio of the maximum to minimum magnitude of the 4 MHz signal, expressed in dB, as a function of the CC phase, indicates the achieved level of squeezing. By experimentally estimating this value and comparing it with the measured squeezing level along the SQZ path, it becomes possible to infer information about optical losses and phase noise. The following measurements are made by assessing the amount of SQZ and ASQZ at different pumping powers of the source, resulting in different values of generated SQZ.

IV.3.2. Loss budget

In practical scenarios involving squeezing, the amount of observable squeezing (or anti-squeezing) is affected by several factors including optical losses, classical noise contributions, phase noise, and backscatter noise. The contributions of these factors can be evaluated by measuring the squeezing performance. A common approach involves modifying the parametric gain and measuring the resulting levels of observed squeezing and anti-squeezing. At lower parametric gains, the impact of losses is dominant. As the gains increase, the relevance of phase noise becomes more pronounced[2]. The analysis that follows is carried out using a joint model of contributions. Combining the equations (II.84) and (II.86), the expression for the observed squeezing ratio $R_{\pm}^{\tilde{\phi}_{RMS},l}$ in the presence of phase noise $\tilde{\phi}_{RMS}$ and total losses l can be reformulated

[2]Effects due to dark noise and backscatter noise were not considered in this discussion. To explore these aspects further, refer to [55]

as follows:

$$R_{\pm}^{\tilde{\phi}_{RMS},l} = (1-l)\left(R_{\pm}\cos^2\tilde{\phi}_{RMS} + R_{\mp}\sin^2\tilde{\phi}_{RMS}\right) + l \tag{IV.19}$$

where the SQZ ratio $R_{\pm}$ is the quantity defined in (II.57). The initial characterization involves the same mode used during O3, which is the generation of FIS. Two scenarios are analyzed in this configuration:

1. The laser circulates only within EQB1 by folding the beam using a DL which intercepts the light before the injection to SQB1.

2. The squeezed beam enters SQB1 and before proceeding to the FC is reflected by the Retro Reflector (RR) (see Figure IV.1). This mirror reflects the laser either toward EQB1 or by turning the HWP2 in the middle of the double stage FI, toward the interferometer to inject FIS.

SQZ beam on EQB1 using the Delay Line

These measurements aim to characterize the FIS only on EQB1 by using the DL. The DL consists of a series of mirrors, two of which are mounted on a motorized slider to intercept IR beams before they leave EQB1 to arrive at SQB1 (see the red area in Figure IV.1). Subsequently, the beams are reflected inside EQB1 to reach the HD. This setup allows for an estimation of losses and phase noise specifically on EQB1, facilitating a comparison with other parts of the system. As mentioned above, the measurements conducted in this and other configurations are conducted for different pump power values, thereby resulting in different parametric gains. For each gain value, data spanning a time stretch of approximately 3 minutes are acquired for SQZ (and ASQZ). The power spectral densities, expressed in dB relative to the shot noise, of the acquired signal at different pump levels (and hence different gains) are shown in Figure IV.7. The corresponding values are reported in Table IV.3 Analyzing the data with the theoretical

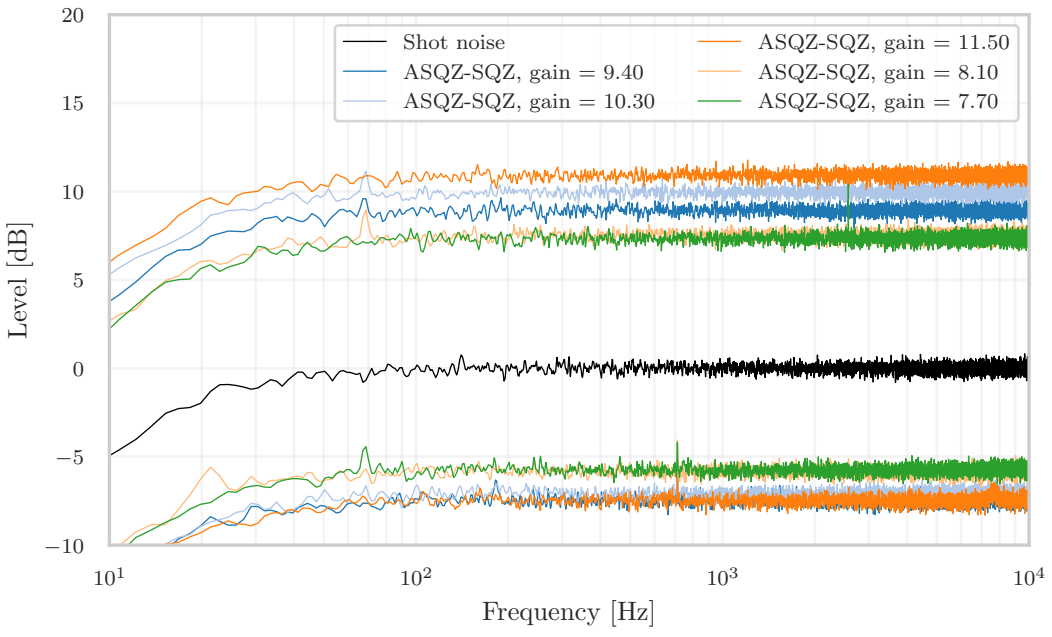

Figure IV.7: Characterization of FIS from DL at different GR pump power (i.e. at different parametric gain). The figure shows different spectra of EQB1_HD_DIFF_AUDIO channel in SQZ and ASQZ mode. The level of noise on the HD (in dB) is normalized to the shot noise (black curve).

FIS MEASUREMENTS (DL)		
Generated SQZ [dB]	SQZ level [dB]	ASQZ level [dB]
7.7 ± 0.1	5.8 ± 0.1	7.3 ± 0.1
8.1 ± 0.1	5.8 ± 0.1	7.5 ± 0.1
9.4 ± 0.1	6.7 ± 0.1	8.9 ± 0.1
10.3 ± 0.1	7.1 ± 0.1	9.9 ± 0.1
11.5 ± 0.1	7.5 ± 0.1	10.9 ± 0.1

TABLE IV.3: The table shows the values of SQZ and ASQZ levels for each pump power value.

model of equation (IV.19) (see Figure IV.8), (11 ± 1) % of losses and (53 ± 6) mrad of phase noise are obtained.

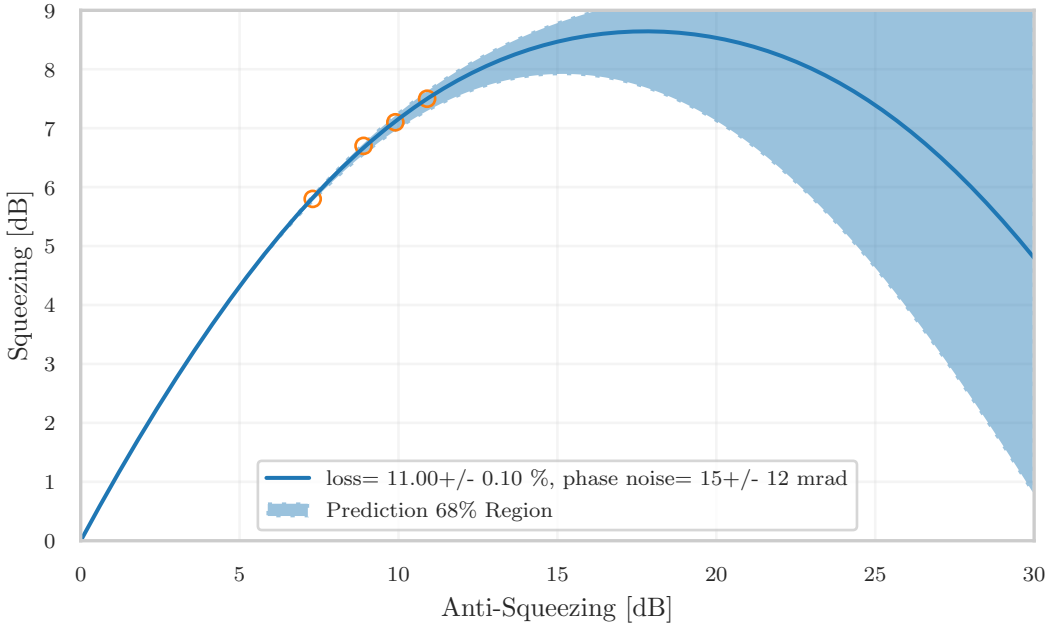

FIGURE IV.8: Outcomes fitting the theoretical model IV.19 to the data collected during variations in OPO pump power with the DL. The plot displays the estimated parameters with the indicated uncertainty representing the statistical error.

SQZ BEAM ON EQB1 AND SQB1, USING THE RETRO REFLECTOR

In this case, the DL is removed and the beams go to SQB1 in the direction of FC. The RR is a mirror inside SQB1, mounted on a vertical slide that is raised when FIS is to be injected into the interferometer. By turning HWP2 on SQB1, it is possible to direct the beam toward EQB1 and thus toward the HD. Through the x and y DoFs of the RR, the magnitude of the 4 MHz demodulated signal is maximized. These adjustments are used to keep the RR parallel to FCIM so that the alignment of the SQZ beam is the same for both FIS and FDS injections into the interferometer. The measurements are shown in Figure IV.9 and the values of SQZ-ASQZ levels obtained are reported in Table IV.4. Unlike the previous case, at low frequencies (below 20-25 Hz) there is a large bump that degrades the measurements. This effect is due to a non-stationary noise generated by the scattered light produced in the LO path, which then recombined with the squeezed field [56]. From the analysis of the data (see Figure IV.8), results indicate (14.9 ± 0.4) % of losses and (20 ± 11) mrad of phase noise. The phase noise level is compatible with

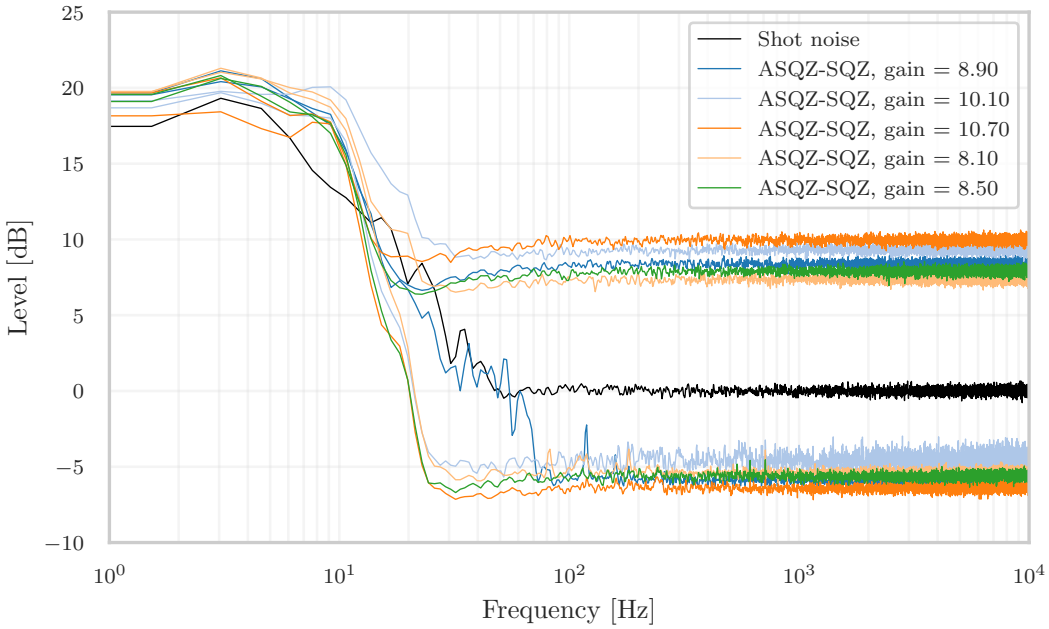

FIGURE IV.9: Characterization of FIS from RR at different GR pump power (i.e. at different parametric gain). The figure shows different spectra of EQB1_HD_DIFF_AUDIO channel in SQZ and ASQZ mode. The level of noise on the HD (in dB) is normalized to the shot noise (black curve).

FIS MEASUREMENTS (RR)		
Generated SQZ [dB]	SQZ level [dB]	ASQZ level [dB]
8.1 ± 0.1	5.4 ± 0.1	7.4 ± 0.1
8.5 ± 0.1	5.6 ± 0.1	7.9 ± 0.1
8.9 ± 0.1	5.9 ± 0.1	8.4 ± 0.1
10.1 ± 0.1	6.2 ± 0.1	9.3 ± 0.1
10.7 ± 0.1	6.5 ± 0.1	10.0 ± 0.1

TABLE IV.4: The table shows the values of SQZ and ASQZ levels for each pump power value.

the one measured with the DL line, whereas 4% more additional losses due to the double pass in SQB2 FI is measured.

SQZ IN REFLECTION FROM THE FILTER CAVITY

The remaining focus is on the segment of SQZ path that extends to the FC, specifically involving measurements in FDS mode. As mentioned earlier in this chapter, the design of AdV+ utilizes the SC to be reflected by the OMC and for FC alignment without disturbing the detection sensitivity. However, this configuration is unsuitable for system diagnostics and performing FDS measurements with the HD. The challenge arises from the significantly higher power of the SC compared to the SQZ beam, resulting in photodiode saturation in the HD. For this reason, the system is controlled through the procedures described in §IV.2.2 but with the SC shuttered. For the measurement, spectra are again acquired at different pump powers. The results are illustrated in Figure IV.11, and the corresponding data is presented in Table IV.5. Observing the figure reveals an anomaly where the ASQZ never descends below the shot noise. This discrepancy is likely attributed to inaccuracies in the alignment of the FC, suggesting that the lock precision of the FC was insufficient. Analyzing the data (see Figure IV.12), (17 ± 3)

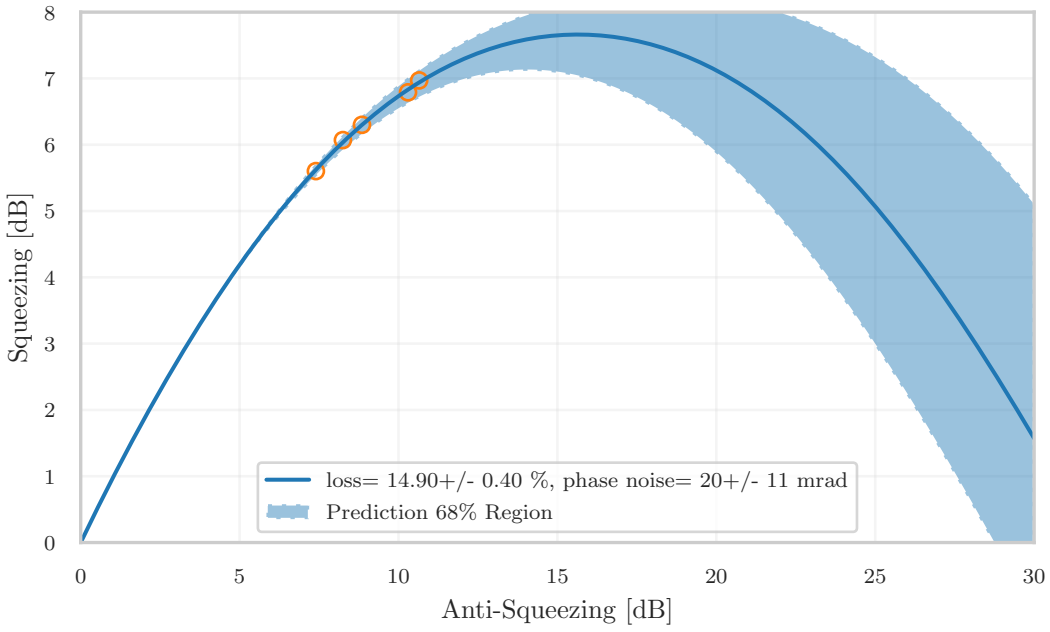

FIGURE IV.10: Outcomes fitting the theoretical model IV.19 to the data collected during variations in OPO pump power with the RR. The plot displays the estimated parameters with the indicated uncertainty representing the statistical error.

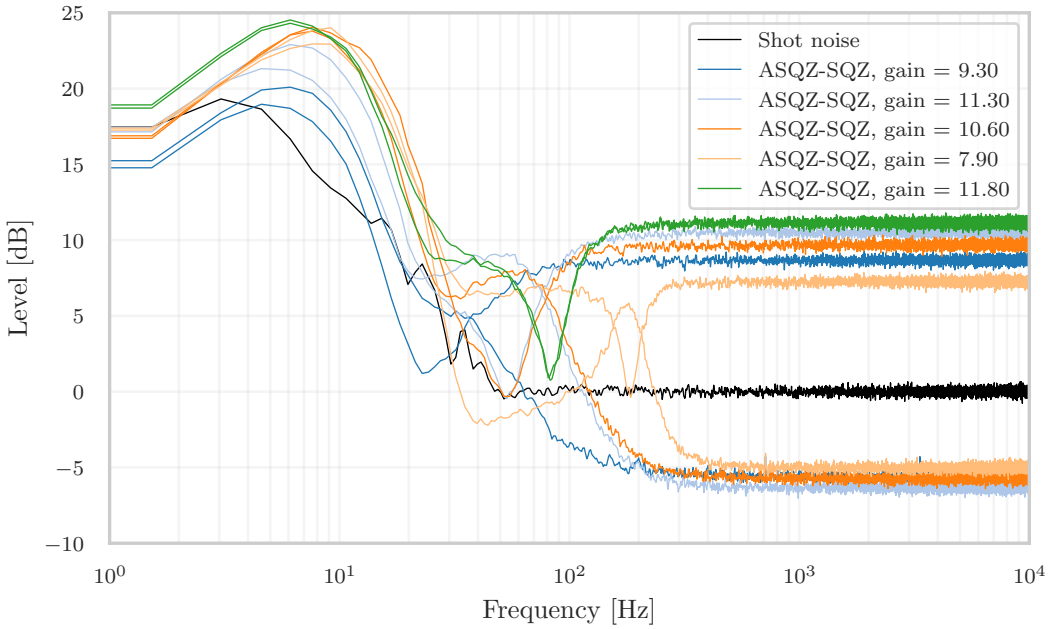

FIGURE IV.11: Characterization of FDS at different GR pump power (i.e. at different parametric gain). The figure shows different spectra of EQB1_HD_DIFF_AUDIO channel in SQZ and ASQZ mode. The level of noise on the HD (in dB) is normalized to the shot noise (black curve).

% of losses and (31 ± 21) mrad of phase noise are obtained. Some additional terms contributing

FDS MEASUREMENTS		
Generated SQZ [dB]	SQZ level [dB]	ASQZ level [dB]
7.9 ± 0.1	5.0 ± 0.1	7.3 ± 0.1
9.3 ± 0.1	5.6 ± 0.1	8.7 ± 0.1
10.5 ± 0.1	5.8 ± 0.1	9.6 ± 0.1
10.6 ± 0.1	5.8 ± 0.1	9.7 ± 0.1
11.3 ± 0.1	6.3 ± 0.1	10.5 ± 0.1
11.8 ± 0.1	6.5 ± 0.1	11.2 ± 0.1

TABLE IV.5: The table shows the values of SQZ and ASQZ levels for each pump power value.

to FC losses are measured individually by different methodologies, and the results are included in Table IV.6.

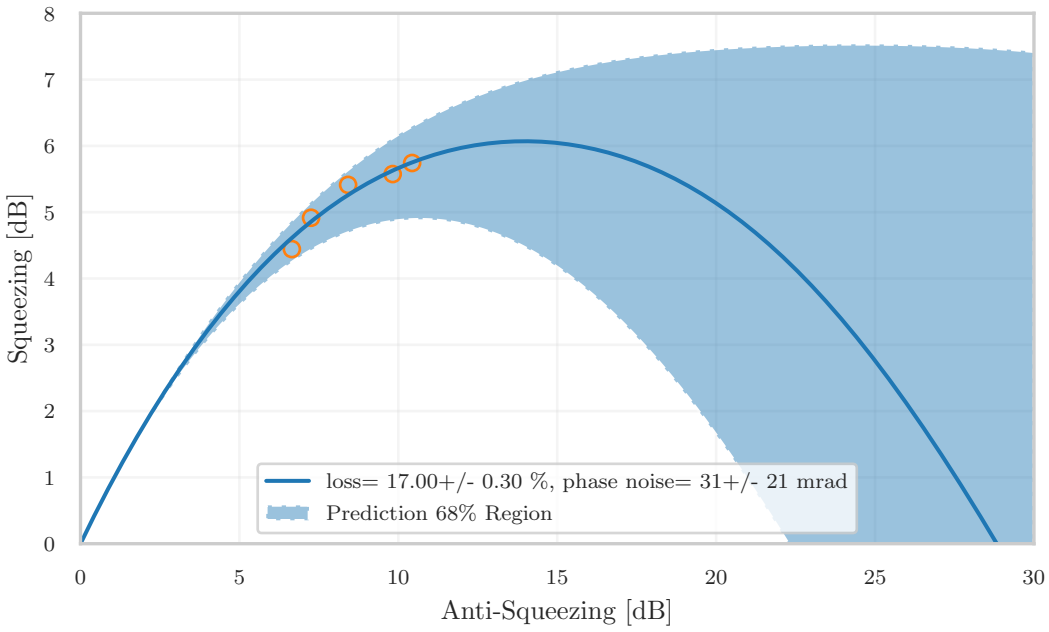

FIGURE IV.12: Outcomes fitting the theoretical model IV.19 to the data collected during variations in OPO pump power with the FC. The plot displays the estimated parameters with the indicated uncertainty representing the statistical error.

Given that the SC beam achieves a mode matching of 99.8% with the OPO cavity, it is used as a valuable indicator for assessing the mode matching between the SQZ and the FC. This assessment reveals a mode matching of approximately 98.5% for the FC, characterized by long-term fluctuations below 1%. The FC round-trip losses are determined with three different methods [48][57]. The resulting values vary within the range of (50-90) ppm, exceeding the predicted value based solely on mirror roughness (∼ 30 ppm). Although the reason for this discrepancy remains unresolved, its impact translates into a minimal deterioration of the calculated BNS merger horizon for O4, amounting to less than 1%. For the estimation of readout losses, it was considered HD contrast (98 ± 1)%, dark noise clearance (1%), and photodiodes quantum efficiency (99%) [42]. Table IV.6 compiles a comparative overview of the measured parameters compared to the maximum target values set for O4. With the exception of the previously discussed FC RTL, the intended target values have been successfully attained. However, it is important to acknowledge that as FDS injection has not been incorporated into the interferometer, some additional sources of losses are expected.

Degradation Parameter	Measured Value	O4 Design
Injection losses [%]	10 ± 1	13
FC Round-trip losses [ppm]	50 - 90	60
Mode mismatch SQZ-FC [%]	1.5 ± 1	2
Phase noise - rms [mrad]	31 ± 21	40
FC length fluctuation - rms [Hz]	∼ 1	1

TABLE IV.6: Measurements and O4 target parameters. The measured injection losses and phase noise parameters do not include the interferometer contribution, which is instead included in the target parameter column.

IV.3.3. FREQUENCY-DEPENDENT SQUEEZING MEASUREMENT

Throughout the commissioning period, various types of FDS measurements are conducted. In the subsequent pages, the characterization of squeezing measurements involving changes in the squeezing ellipse angle and long-term measurements to assess the stability of the system are detailed.

HOMODYNE ANGLE SCAN

Figure IV.13 shows the results of a systematic campaign of FDS measurements with different ellipse angles θ_{HD}. The measurements are conducted with the detuning frequency kept above the designed 25 Hz to avoid the stray light bump [40], as shown in Figure IV.11. It is noteworthy that this issue is expected to be less relevant for SQZ injections into the interferometer. In such cases, the LO of the HD are shuttered, and the interference of the interferometer LO is anticipated to be constrained by the Faraday isolators incorporated into the squeezed path (refer to Figure IV.1 on the left) [24].

Before starting the measurements, the FC detuning is set at 45 Hz. The adjustment of the squeezing ellipse θ_{HD} seen by the HD is achieved by modifying the path length of the LO beam. Employing the theoretical model outlined in [47], the detuning frequency and HD angle are fitted. During this process, the parameters for the loss budget are set according to those reported in Table IV.6, considering the ranges of experimental uncertainties. Over time, the detunings perceived by the SQZ state exhibit a drift of approximately 10 Hz (refers to Figure IV.13 label). The underlying cause of this phenomenon is examined in the following paragraph. At frequencies close to $\Delta\omega_{cav}$, the squeezing level is degraded by the FC round-trip losses. However, even within this frequency range, an observed shot-noise suppression of at least 2 dB has been recorded. At higher frequencies, squeezing levels as high as 5.6 dB are obtained with about 8.5 dB of produced squeezing.

These outcomes substantially surpass the reference values documented in earlier publications [58][59], establishing the current leading edge for frequency-dependent squeezing sources designed for integration into GW interferometric detectors.

LONG RUN STABILITY

The long-term operation of the FDS system requires meticulous system controls to counteract the daily motion occurring among all the suspended benches. All these processes, along with the management of the squeezing source controls, are seamlessly automated within a hierarchical locking procedure overseen by a finite state machine [60]. In this way, the complete engagement of the FDS measurement after any system failure (i.e. a filter cavity unlock) is automatically achieved in less than 4 minutes [40]. Figure IV.14 shows the time-frequency plot of the FDS level for an HD angle of 90° over approximately 24 h. During this period, squeezing is continuously produced. The stability of detuning can be influenced by various factors when the cavity is operated using bichromatic control (the locking process first with the GR beam and then with IR) [52]. One such influence is the temperature drift of the cavity mirrors. The phase accumulated

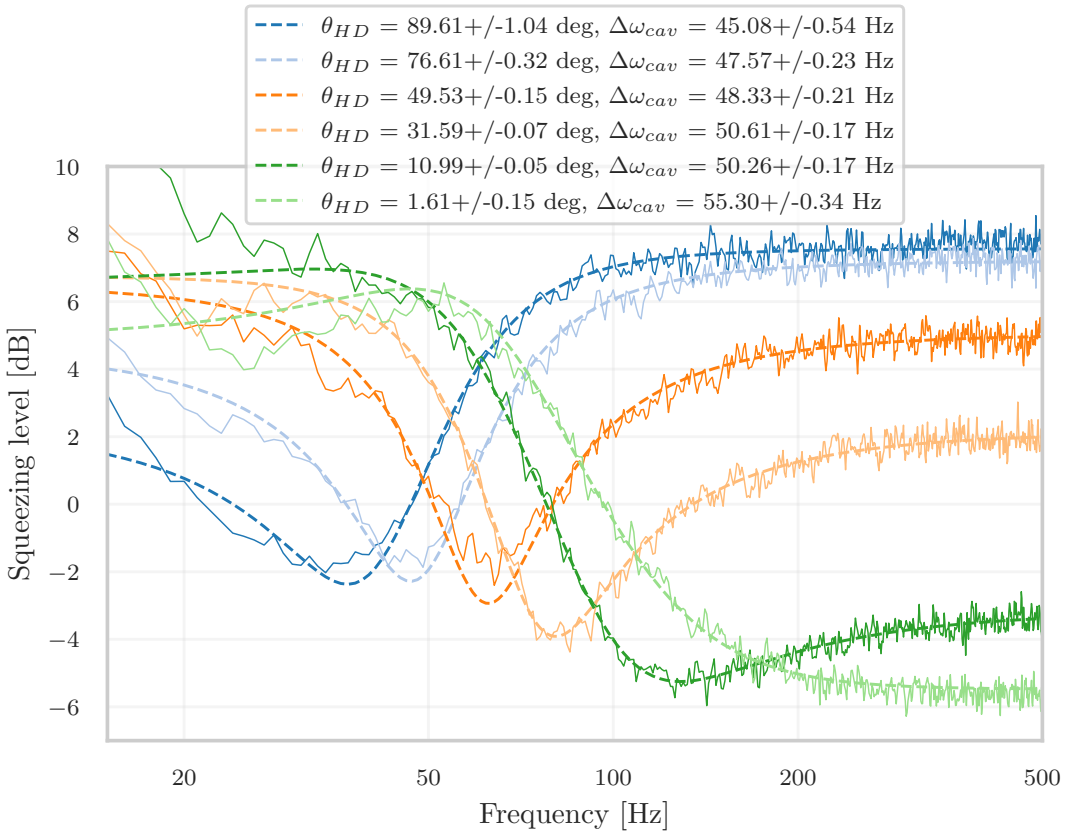

FIGURE IV.13: Measured squeezed level acquired for different HD angles and for (44-55) Hz detuning of the FC resonance. The experimental data (solid lines) are fitted using an analytic model of squeezing degradation (dashed lines). The squeezing source generates (8.0-8.5) dB of squeezing.

after a reflection from the FC mirrors exhibits distinct temperature dependencies for GR and IR light. This discrepancy leads to drifts in IR detuning due to temperature fluctuations when the cavity is locked using the GR. This effect is evident in Figure IV.14, where, starting from a detuning frequency of 185 Hz, a drift of approximately 40 Hz is observed. This drift follows the day-night thermal effect of the temperature recorded by the thermometers installed on the ring heaters (RH) mounted on the FC mirrors. As can be seen, there is a strong correlation between the trend of the detuning drift and the temperature of the end mirror of the FC. During the 24 hours of acquisition, the FC unlocks are removed. However, after relocking, the FSR correction, which would have returned the detuning to the correct value, was not yet present. The correlation between these two quantities is analyzed and reported in Figure IV.15, where the detuning frequency is plotted versus the value of the FCEM_RH temperature. The detuning frequency and the temperature of the end mirror, approximated by the temperature detected by a thermometer placed on the mirror ring heater and time-delayed by 60 minutes, appear linearly correlated with a scaling factor of (114 ± 1) Hz/K. This result is in accordance with the prediction of the theoretical model [61]. The observed time delays are probably originated by the thermal resistance of the mirror's suspension, which introduces a time lag in its response to alterations in the temperature of the ring heater.

After this observation, the mirror temperatures are meticulously regulated to maintain an rms deviation of less than 30 mK. The result is shown in Figure IV.16. While the attained degree of detuning stability would influence the best theoretical estimate of the O4 Binary Neutron Star (BNS) horizon by less than 1.5%, a reduced detuning drift is expected when employing

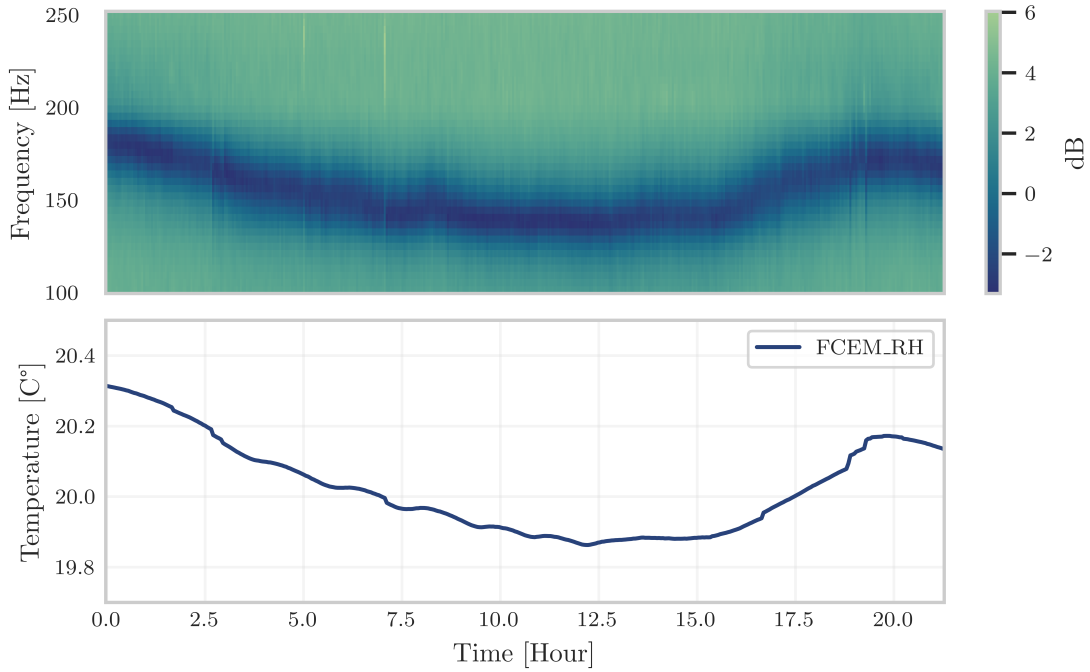

FIGURE IV.14: (top) Power spectral density (PSD) of the diagnostic HD output normalized to the shot-noise level versus the time of data acquisition. Every 3 minutes a power spectral density similar to that of Figure IV.13 with a homodyne angle of 90° is estimated. Aligned with the acquisition duration, the PSD is graphically depicted, showing frequency on the vertical axis and amplitude represented with a color gradient. The calibration (in dB) is indicated by the vertical bar on the right side of the plot. The selection of the HD angle was performed to optimize the contrast that highlights the observation of the detuning frequency. The detuning frequency $\Delta\omega_{cav}$, initially configured at 180 Hz to maximize quantum noise suppression, is depicted as the dark blue curve. This curve exhibits fluctuations over time, oscillating by approximately 40 Hz peak-to-peak. (bottom) This curve represents the time trend of the temperature recorded by the ring heater mounted behind the FC end mirror.

the SC-IR beam for control of the filter cavity. To check this, the OPO is locked on the bright beam of the SQZ main laser. Subsequently, the output from the OPO and the SC beams directed towards the FC, along with the transmitted IR field, is monitored while varying the FC resonance frequency by acting on the GR AOM. The relative detuning of the two infrared beams, initially set around 1 kHz, is upheld to within 4 Hz over a 24-hour acquisition period.

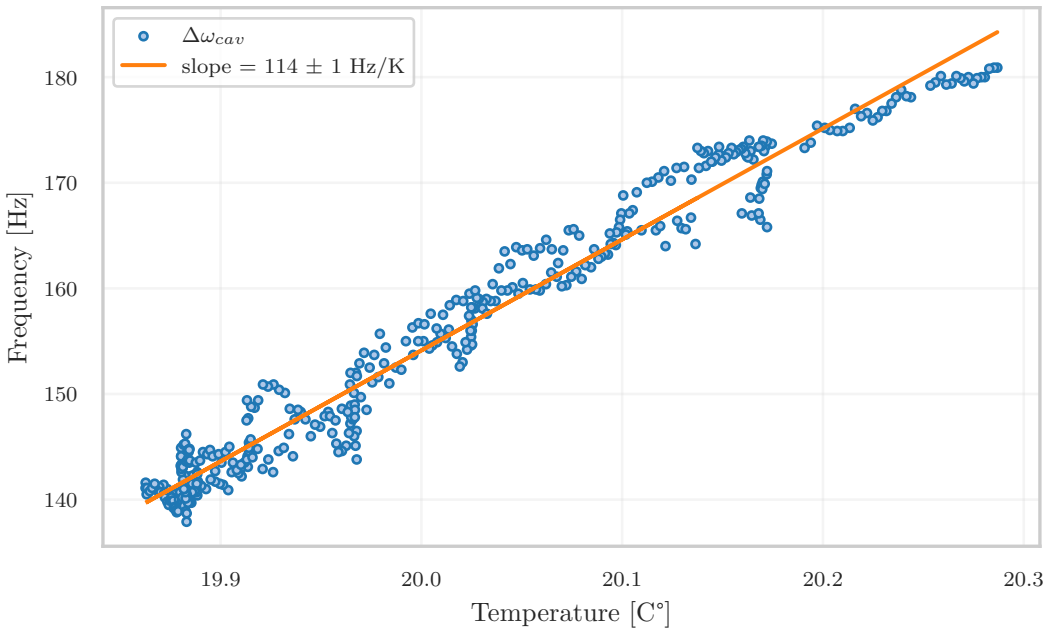

FIGURE IV.15: Filter cavity detuning frequency versus the FCEM ring heater temperature. Each point corresponds to a pair of values measured every 3 minutes within 24 h. The values corresponding to each $\Delta\omega_{cav}$ are obtained by fitting the 3 minutes PSD reported in Figure IV.14. The maximum correlation is obtained assuming that the temperature of the mirror lags behind that of the ring heater by about 60 minutes.

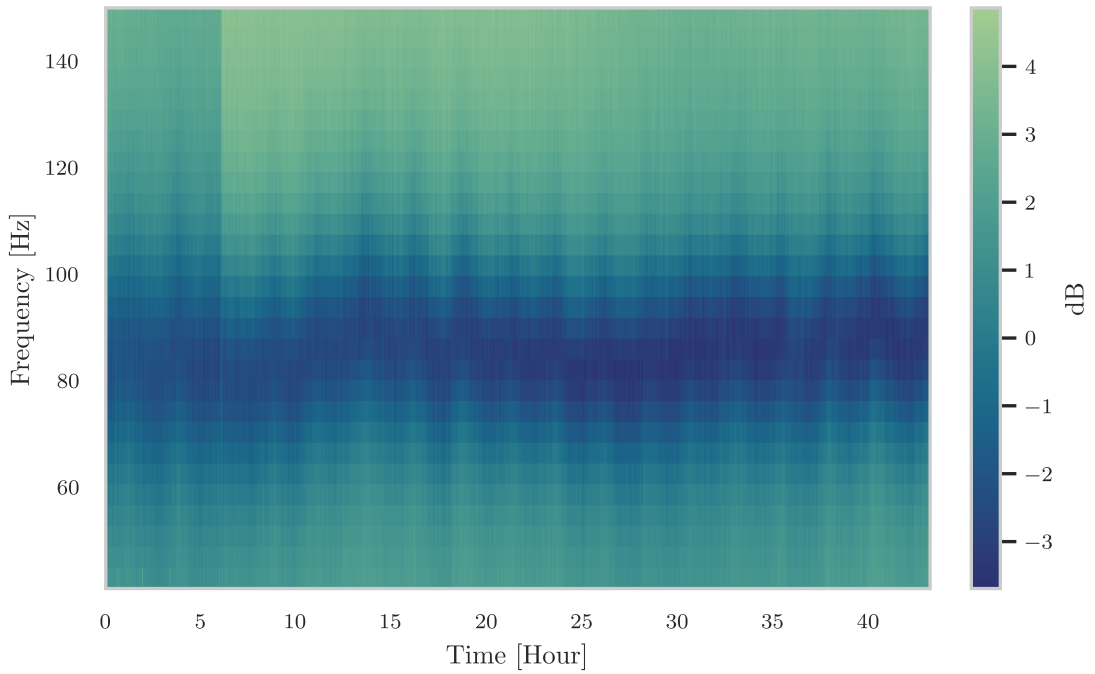

FIGURE IV.16: PSD of the diagnostic HD output normalized to the shot-noise level versus the time of data acquisition. Every 3 minutes corresponds to a PSD with a HD angle of 90°. Aligned with the acquisition duration, the PSD is graphically depicted, showing frequency on the vertical axis and amplitude represented with a color gradient. The detuning frequency $\Delta\omega_{cav}$, initially configured at 80 Hz to maximize quantum noise suppression, is depicted as the dark blue curve. Contrary to the fluctuations depicted in Figure IV.14, the control of FC mirror temperature has significantly reduced the fluctuations over time, oscillating by approximately 10 Hz peak-to-peak

IV.4. Alignment to the ITF

After the characterization of the stand-alone QNR system, the next step, prior to the SQZ injection, involves the mutual alignment of the SQZ beam with Virgo detector. This process unfolds step by step during the commissioning of the interferometer. To activate the AA loops and ensure stability of the ITF+SQZ system for estimating the impact of SQZ on sensitivity, both subsystems must individually exhibit stability over time. The following steps outline the progression leading to the initial injection of FIS into the interferometer after the conclusion of O3. This encompasses aligning the SQZ beam with the interferometer beam through the SC and closing the loops for AA and CC in various ITF configurations.

IV.4.1. SC on the OMC

In the initial step, the process begins with the simplest and most stable configuration—aligning the SC beam reflected from the RR within the OMC with the ITF in Single Bounce. This configuration of the ITF involves one of the end mirrors of the ITF being misaligned while the other correctly aligned. During these operations with the RR, the IR beam does not arrive at the FC, which is kept in resonance only with the GR. The RR is inserted in the beam path only after maximizing the signal mag at 4 MHz on the HD with the FC locked. After putting the RR in place, the 4 MHz beat is again maximized with the DoFs of the RR. In this way, the operations performed in this configuration are also valid in the case of FDS injection. To control the SQZ beam, after rotating the HWP2 on SQB1 to send the SC beam toward the interferometer, two mirrors MIRROR1 and MIRROR2 on SQB1 are used. The position of the interferometer beam on the B1p and B1s cameras is taken: these cameras are placed on the Suspended Detection Bench (SDB2) and are used to monitor the ITF beam that goes toward the OMC and its first reflection. By moving the degrees of freedom of the mirrors MIRROR1 and MIRROR2, the SC is superimposed on the interferometer beam at the cameras.

For fine alignment, adjustments are made to the transmitted beam by the OMC. To allow the SC to be transmitted, the OMC is kept locked. By applying a ramp signal to the SC PLL frequency slow control, the frequency of the SC is altered, allowing the modes to be transmitted (see Figure IV.17). The transmitted beam is sent to a third camera, referred to as B1. Optimal alignment and mismatch between the SC beam and the OMC are achieved by observing the amplitude of the transmitted peaks over time. Specifically, by moving the mirrors, the amplitude of the TM_{00} peak is maximized at the expense of the higher-orders modes. The mode matching of the SC to the ITF can be achieved by changing the waist of the beam that reaches the OMC, by acting on the length of the telescope placed on SQB1 (§IV.1.1). The minimum waist mismatch value achieved is $< 4.8\%$ and it is given by the ratio between the TEM_{20} and the TEM_{00}. The alignment mismatch is given by the ratio between the TEM_{10} and the fundamental mode, and the minimum level reached is less than 1%.

IV.4.2. Phase control of the SQZ field and Auto Alignment loop

Closing CC loop in single bounce

As mentioned in §IV.2.3, to control the squeezing phase during injection into the interferometer in the O3 run, a CC control loop is used. The loop uses the beat note between the ITF beam and the CC beam demodulated at 4 MHz as the error signal. For the O4 commissioning, the loop is first restored with the ITF in single bounce and then switched to DC readout. As in the case with HD on EQB1, the first step is to optimize the alignment between the SQZ beam and ITF, by maximizing the signal SQZ_B1_PD_4MHz_mag that represents the magnitude of the beat note demodulated at 4 MHz. Figure IV.18 shows the CC loop channels in the time domain when the loop is closed. Figure IV.19 shows the spectra of the error signal when the SQZ laser is shuttered, enabling the measurement of the sensing noise that limits the performance of the loop. In the single bounce configuration, with the achieved alignment and matching, the loop is limited by the sensing noise above 1 kHz. Since only a single actuator is available, the

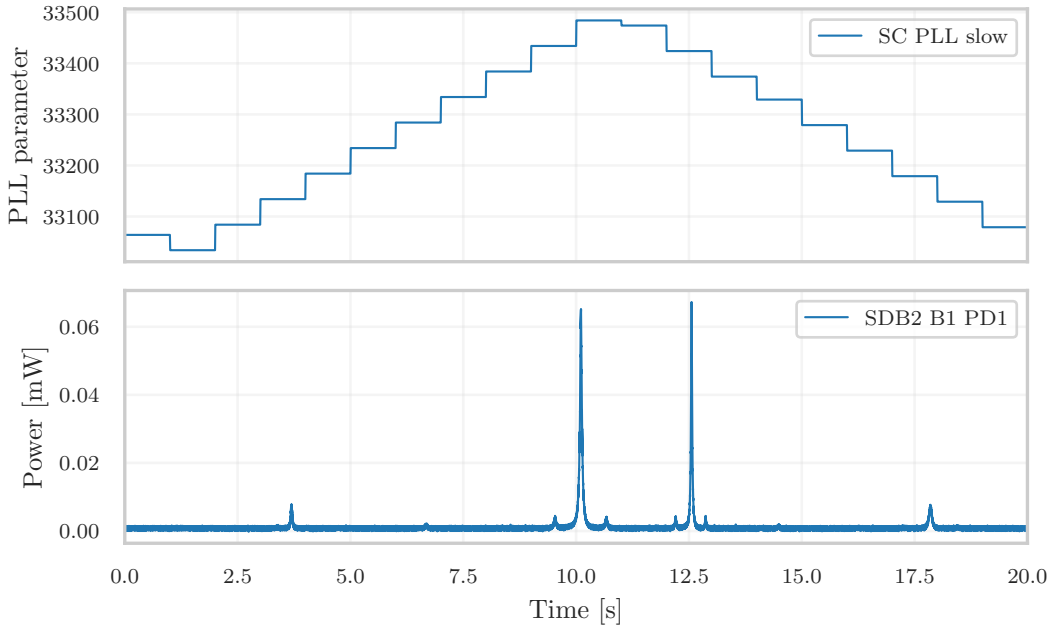

FIGURE IV.17: (top) 10 seconds of the SC PLL slow frequency scan. (bottom) Power read by the B1 PD1 with three modes transmitted by the OMC. Around 10 and 12.5 s the TEM_{00} mode is present twice (due to the inversion of the ramp). The two small sidebands near the peaks are due to the FMODERR loop. The TEM_{10} peaks are not visible because their amplitude is 1% of the fundamental mode. The two peaks at 3.5 and 18 s are the TEM_{20}.

main PLL frequency offset for both the CC and the FC high-frequency longitudinal lock is not engaged during the SQZ injection on the ITF. Instead, the main PLL frequency set is used for implementing the CC loop.

Closing CC loop in DC readout

After achieving stability in DC readout configuration (where one arm is intentionally longer than the other to allow a small portion of the ITF carrier field to reach the sensing photodiode [62]), the aforementioned operations are repeated. In this case, the signal-to-noise ratio on the 4 MHz demodulated photodiode is about 400, almost a factor of 20 greater than in single bounce. The CC loop is closed and the characterization of the loop is reported in Figure IV.21.

In the final configuration, the sensing noise improves by a factor of 6 compared to the single bounce configuration, with the final UGF$\sim$6 kHz, meeting the design requirements for the lock precision of 1Hz. The impact of the loop can be observed in Figure IV.20. The upper figure displays the residual squeezing ellipse phase noise (not calibrated), while the lower figure illustrates the filter cavity lock accuracy, achieved by locking the SQZ main laser frequency to the interferometer carrier.

Engaging dither Auto Alignment loop in DC readout

To keep the beat signal maximized at 4 MHz on the B1_PD1 photodiode, and thus maximize the SQZ beam transmitted from the OMC to the ITF, an auto-alignment loop is used. This loop is based on the identical architecture used for the HD_AA loop, SC_AA loop, and GR_pointing loop based on dither lines. To engage the loop, it is necessary to have a maximum signal on the B1_PD1 photodiode and then set the phase that injects ASQZ into the interferometer. The

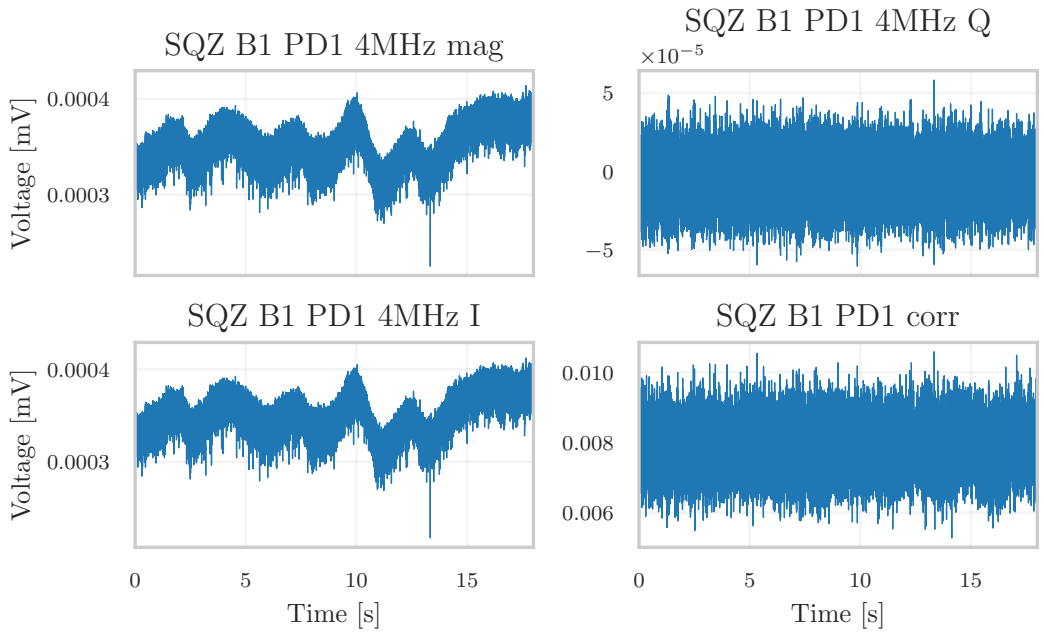

FIGURE IV.18: Time domain signals in single bounce. (top left) The magnitude of the demodulated signal B1 PD1 at 4MHz. (top right) Quadrature Q. (bottom left) Quadrature I used as the error signal of the loop. (bottom right) Correction signal of the loop

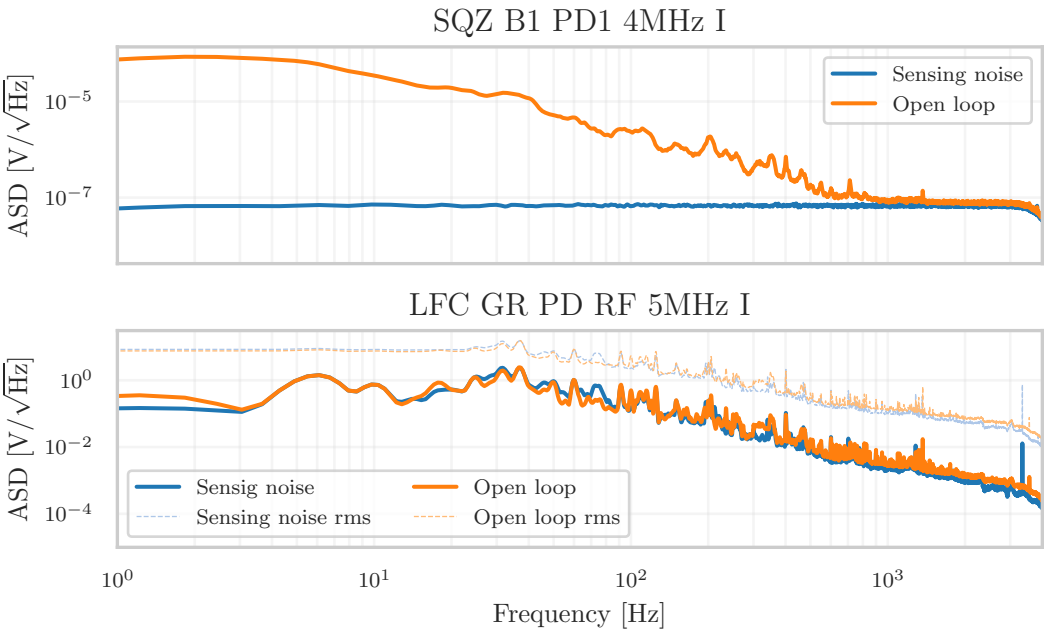

FIGURE IV.19: Characterization of the CC loop in single bounce. (top) Spectra of the 4 MHz magnitude signal with the loop open (orange curves) and the sensing noise with the IR shuttered (blue curve). (bottom) Spectra of the signal error of the loop with the loop open (orange curves) and sensing noise (blue curve). Here, the sensing noise is not significant because the FC is locked on GR and with the RR turned up the IR does not reach the FC.

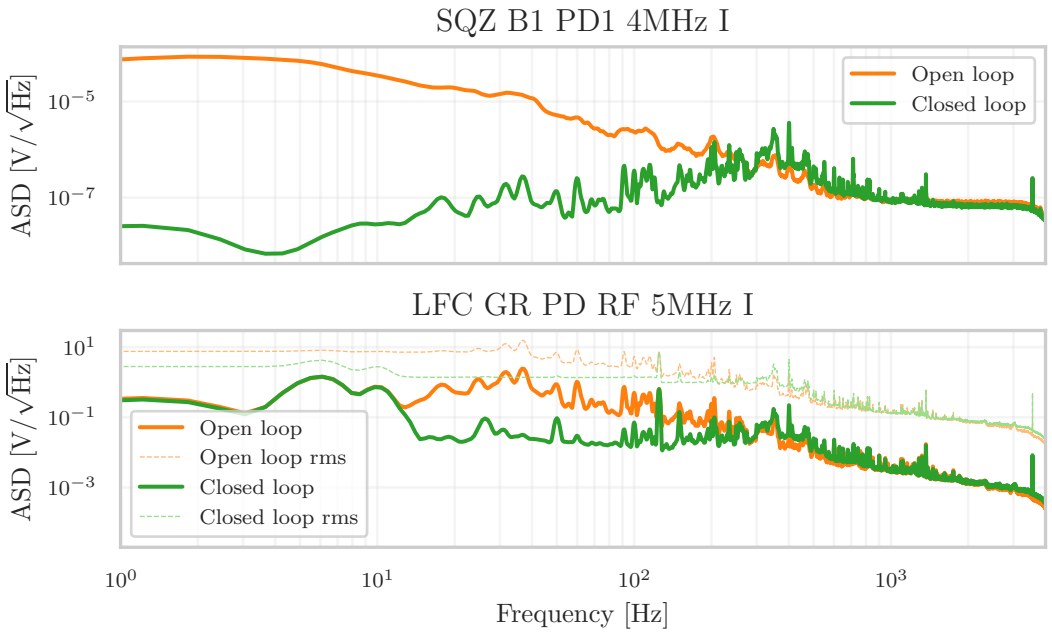

FIGURE IV.20: Characterization of the CC loop in single bounce. (top) Spectra of the signal error of the loop with the loop open (orange curves) and the loop closed (green curve). Spectra of the error signal to lock the FC on the GR beam with the loop open (orange curves) and the loop closed (green curve).

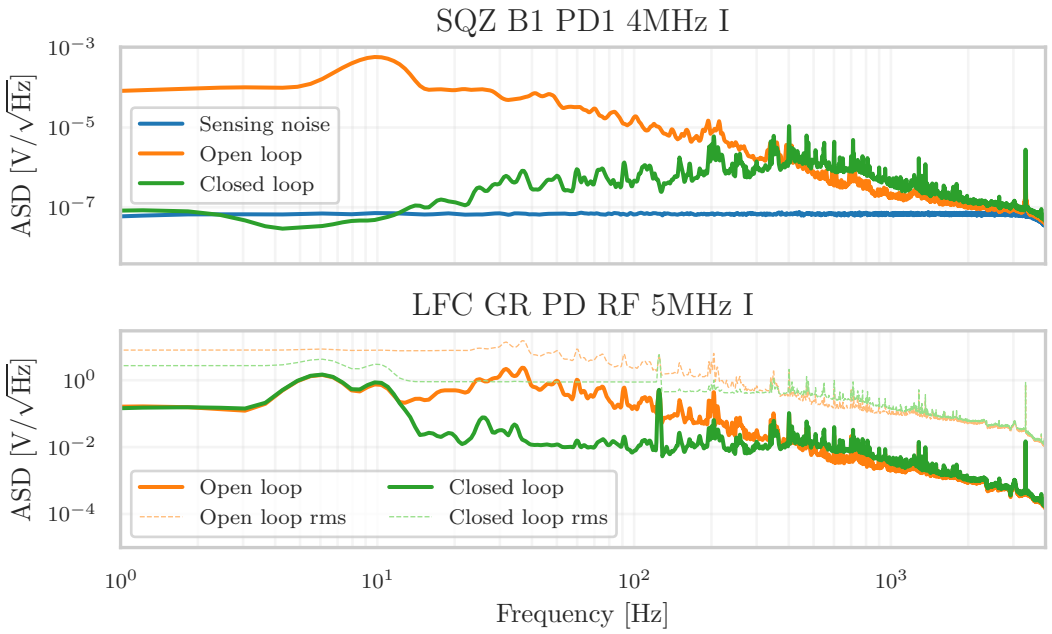

FIGURE IV.21: Characterization of the CC loop in DC readout. (top) Spectra of the signal error with the open loop (orange curve), the sensing noise with the IR shuttered (blue curve), and the closed loop (green curve). (bottom) Spectra of the FC loop signal error with the CC loop open (orange curves) and the CC loop closed (green curve)

actuators on which the loop acts are the MIRROR1 and MIRROR2, on which the frequency of the dither lines must be set for each degree of freedom:

- MIRROR1_X = 20 Hz
- MIRROR1_Y = 25 Hz
- MIRROR2_X = 30 Hz
- MIRROR2_Y = 35 Hz

For each line, an amplitude of 0.05V is configured, and the gain of the correction filter is set at gain = 3000. It is worth noting that the loop could only be activated in the DC readout configuration, as the demodulated single bounce signal has insufficient SNR.

IV.4.3. FIS injection into the ITF

With the CC and AA loops working, providing 25 Mpc of ITF sensitivity, an injection of FIS is performed to assess potential improvements at high frequencies. The QNR system is configured as in previous operations, with the RR inserted. The first objective is to find the values of the CC phases that return the beam in SQZ or ASQZ. The SQZ level generated by the OPO is 10.8 dB, with a maximum and minimum magnitude on the HD of EQB1 equal to 9.51 mV and 2.33 mV, respectively. After directing the SQZ beam toward the interferometer and verifying a satisfactory signal-to-noise ratio of ∼200 for the 4 MHz demodulated magnitude of photodiode B, the previously discussed loops are closed to maximize the signal magnitude at 4 MHz. To assess the result of a phase scan, the interval (1370-1440) Hz is chosen, as in this range, the ITF sensitivity curve is free of peaks and relatively flat. By doing the phase scan, the rms sensitivity trend is monitored over time within this interval to identify phase values that optimize or minimize the average strain noise. After individually setting the phases, three sensitivity spectra are acquired: one with the shuttered laser SQZ as a reference, one by injecting SQZ, and the last one by injecting ASQZ. Figure IV.22 shows the strain sensitivity of the interferometer during the injection. With 10.5 dB of generated SQZ by the OPO, injecting ASQZ results in a 4 dB increase in strain sensitivity, while injecting SQZ leads to a 1 dB improvement.

Given the interferometer's condition during the measurements, a minimal effect of injecting squeezing is still observable: the SQZ curve slightly lies below the curve without the injection. However, for more precise measurements, a stable shot noise-limited interferometer would be necessary.

The SQZ measurements reported during the commissioning stage are constrained by several factors. Firstly, the ITF is not shot noise-limited, leading to degraded SQZ performance at high frequencies. Additionally, the OMC used differs from the one employed during the scientific run O3, featuring higher losses. The photodiodes used also have low quantum efficiency. Moreover, there are propagation losses within the interferometer, particularly when passing through various cavities like the SR, which still require characterization.

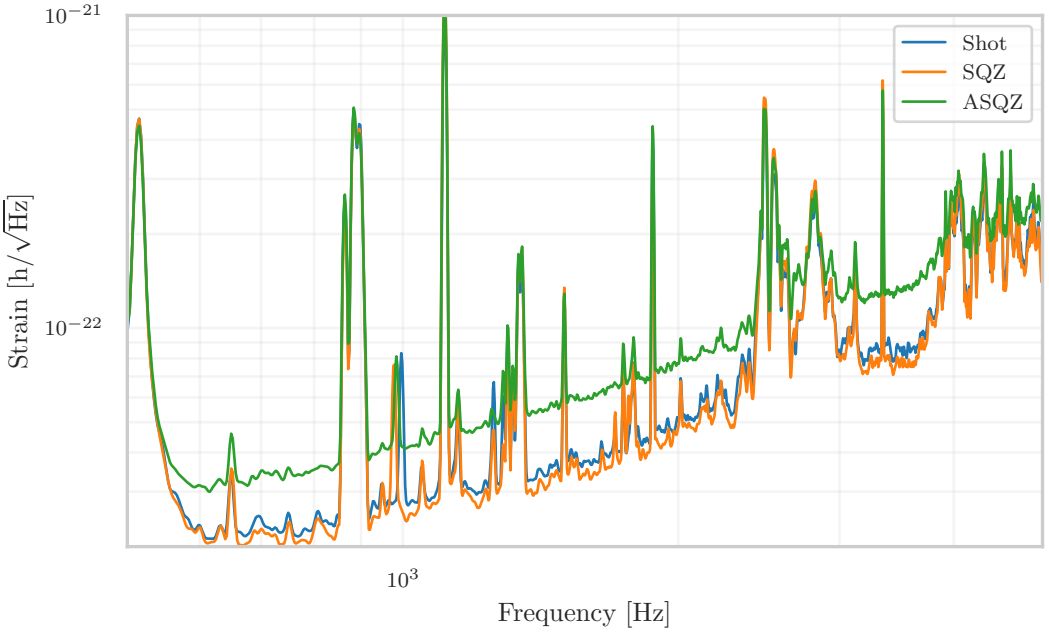

FIGURE IV.22: ITF strain sensitivity in the frequency range (500-5000) Hz where the SQZ effect is visible. The blue curve represents the reference sensitivity without the SQZ injection. The green line shows clearly the effect of the ASQZ that increases the strain noise sensitivity. The orange curve shows the effect of the SQZ: a small sensitivity improvement can be appreciated at high frequencies. The improvement is limited by the fact that the ITF is not shot noise limited.

Part II: The NETN experiment

V | THERMAL NOISE

This chapter focuses on examining the characteristics of thermal noise, tracing its initial description to its contemporary understanding. The notion of thermal fluctuations in an observable quantity and their connection to system dissipation is presented through the employment of the Fluctuation Dissipation Theorem (FDT). Subsequently, the extension of this concept to systems operating outside of equilibrium is demonstrated, formally introducing the notions of fluctuating temperature.

V.1. Thermal fluctuations

In experimental settings, thermal noise is observable as minor fluctuations around the mean value of a physical property. For instance, it induces constant and random variations in the positions and velocities of particles. While often negligible, its significance becomes prominent when conducting highly accurate measurements on the studied physical system, especially as the system's dimensions decrease to the microscopic scale. These fluctuations are at the heart of statistical mechanics, shedding light on how systems evolve and eventually reach equilibrium.

V.1.1. Brownian motion

The initial investigations into thermal fluctuations originate from the 1800s, marked by R. Brown's observations of pollen suspended in water [63]. During this study, Brown noted the persistent erratic movement of organelles expelled by pollen grains. This motion lacked a defined path and instead seemed to be governed by randomness. Approximately eight decades passed before A. Einstein would formulate a representation of particles subject to frequent collisions with the molecules of the surrounding fluid, offering an initial theoretical explanation for what is now referred to as Brownian motion [64]. The initial step in Einstein's argument was to calculate the distance traveled by a Brownian particle in a given amount of time. Classical mechanics can not determine this distance because of the enormous number of collisions a Brownian particle undergoes, on the order of 10^{14} collisions per second. For this reason, the treatment is purely statistical, considering that each particle moves according to a random force that is the result of a very large number of mutually independent events. Assuming that the variance of the probability distribution of each of these events is finite, the central limit theorem can be applied. In turn, this theorem allows the assumption that the force is Gaussian distributed. Einstein considered a scenario where certain particles are situated at a specific position ξ_0 within a fluid at a temperature T, exerting a force F on them. Assuming that the system's sole significant direction is along the x-axis, the second law of thermodynamics says that for any displacement dx of the fluid, the change in free energy must be zero to maintain fluid equilibrium. This requirement leads to an equilibrium where the force F is balanced by the fluid pressure, facilitating the determination of the fluid's diffusion coefficient as $D = \mu k_B T$, where μ represents fluid mobility and k_B is the Boltzmann constant. The normal distribution of particle density is obtained by extending this behavior to the displacements of the particle $\xi(t)$ from its initial position ξ_0. The variance of this distribution is equal to $2Dt$, where t stands for the time of observation. This implies that, on average, a particle travels a distance corresponding to the square root of this value. Consequently, the average squared displacement of a particle immersed in a fluid is directly proportional to the fluid's temperature:

$$\langle \xi^2 \rangle = 2Dt = 2\mu k_B T t \tag{V.1}$$

The techniques established in the paper are subsequently employed to deduce the Avogadro number and atomic dimensions. Einstein's theory was verified experimentally by J. Perrin. Among his diverse achievements, the determination of the Avogadro number stands out as a significant advancement in thermodynamics, concurrently contributing to the solidification of atomistic theory. Just like pollen grains, macroscopic objects experience Brownian motion, which emerges as the combination of fluctuations from all constituent particles. As demonstrated by H. Nyquist [65], an example of this phenomenon is the electron motion within an electrical circuit. Here, the thermal fluctuations of charge carriers within a resistance R lead to a consistent power exchange among circuit components. The thermal noise can be represented by a voltage source that accounts for the noise generated by a non-ideal resistor, connected in series with an ideal noise-free resistor. The power spectral density, which measures the voltage variance per Hertz of bandwidth, is expressed as:

$$\overline{v_n^2} = 4k_B T R \tag{V.2}$$

The equation just establishes a connection between the average squared voltage across the circuit, the temperature, and the resistance value, which serves as the circuit's dissipative element.

Nyquist also suggested that his analysis can be associated with the mean squared displacement of molecules within a gas. This suggests the possibility that both this theory and Einstein's may represent two versions of a unified explanation for thermal fluctuations. The connection is the famous Fluctuation-Dissipation Theorem proven by Callen and Welton in 1951 [66] that is shown in the next paragraph. This brings together insights from previous studies and reveals that, in general, fluctuations of an observable ξ in equilibrium with the surrounding thermal environment at temperature T possess an amplitude proportional to T and inversely proportional to the imaginary part of the response function of the system to an applied perturbation F.

V.1.2. Fluctuation-Dissipation theorem

The theorem about to be introduced asserts that in the presence of an energy-dissipating process, there exists a corresponding process associated with thermal fluctuations.

The classical formulation [67] is obtained by considering a system defined by a Hamiltonian $\mathcal{H} = \mathcal{H}_0 + \mathcal{H}_{int}$, separable into two components. $\mathcal{H}_0$ remains isolated from the external environment and $\mathcal{H}_{int}$ accounts for interactions with the thermal reservoir and is expressed by:

$$\mathcal{H}_{int} = F(t)\xi \tag{V.3}$$

Consider the specific case where the perturbation $F(t)$ has been active for an infinite duration and is switched off at time $t = 0$. This behavior is represented by writing $F(t) = F_0 H(-t)$ where $H(t)$ is the Heaviside function. Using the Boltzmann distribution $\rho(\xi, 0)$ for the Hamiltonian $\mathcal{H}$:

$$\rho(\xi, 0) = \frac{\exp(-\beta\mathcal{H}(x))}{\int d\xi' \exp(-\beta\mathcal{H}(\xi'))} \tag{V.4}$$

where $\beta = 1/(k_b T)$ and the transition probability $P(\xi', t|\xi, 0)$. The expectation value of the observable ξ can be calculated as:

$$\langle\xi(t)\rangle = \int\int d\xi' d\xi\, \xi' P(\xi', t|\xi, 0)\rho(\xi, 0) \tag{V.5}$$

If $\beta\xi F_0 \ll 1$ the equation (V.4) can be expanded as:

$$\rho(\xi, 0) \approx \rho_0(\xi)[1 + \beta F_0(\xi(0) - \langle\xi\rangle_0)] \tag{V.6}$$

where $\rho_0(\xi)$ is the distribution without the perturbation. Substituting the last formula into the Equation (V.5) it is obtained:

$$\langle\xi(t)\rangle = \langle\xi\rangle_0 + \beta F_0 C_{\xi\xi}(t) \tag{V.7}$$

Here, $C_{\xi\xi}(t)$ is the auto-correlation function of ξ in the absence of perturbation:

$$C_{\xi\xi}(t) = \langle[\xi(t) - \langle\xi\rangle_0][\xi(0) - \langle\xi\rangle_0]\rangle_0 \tag{V.8}$$

Considering $\langle\xi(t)\rangle - \langle\xi\rangle_0$, the (V.7) can be rewritten using the susceptibility of the system χ:

$$F_0 \int_0^\infty d\tau\, \chi(\tau) H(\tau - t) = \beta F_0 C_{\xi\xi}(t) \tag{V.9}$$

and thus:

$$-\chi(t) = \beta \frac{dC_{\xi\xi}(t)}{dt} H(t) \tag{V.10}$$

Performing a Fourier transform and integrating by parts yields the frequency dependence:

$$-\hat{\chi}(\omega) = i\omega\beta \int_0^\infty e^{-i\omega t} C_{\xi\xi}(t) dt - \beta C_{\xi\xi}(0) \tag{V.11}$$

Because $C_{\xi\xi}(t)$ is both real and symmetric, this leads to:

$$2\,\mathrm{Im}[\hat{\chi}(\omega)] = \omega\beta\hat{C}_{\xi\xi}(\omega) \tag{V.12}$$

According to the Wiener–Khinchin theorem, the power spectral density (PSD) is equivalent to the Fourier transform of the auto-correlation function:

$$S_\xi(\omega) = \hat{C}_{\xi\xi}(\omega) \tag{V.13}$$

Finally, it is obtained:

$$S_\xi(\omega) = \frac{2k_\mathrm{B}T}{\omega}\,\mathrm{Im}[\hat{\chi}(\omega)] \tag{V.14}$$

Here, the left-hand side describes fluctuations in ξ, and the right-hand side is closely related to the energy the system dissipates through the imaginary part of χ. This theorem establishes a connection between Brownian motion and Johnson-Nyquist noise within a unified theory, illustrating how thermal fluctuations of a physical variable can predict the system's response, and vice versa. In the discussion, equation (V.14) is approached from an experimental perspective. The goal is to use Callen and Welton's general formula [66] to examine the characteristics of thermal noise in gravitational wave detectors, in particular, this applies to the mechanisms involving the test masses [68]. However, determining the mechanical impedance of the system, a parameter directly linked to susceptibility (χ) and encompassing both the mirror and suspension fibers, proves challenging due to the complex involvement of numerous degrees of freedom To address this challenge, one approach for applying the fluctuation-dissipation theorem to such a system is presented (see §V.2) [69]. Since the set of normal vibrations associated with the mirror and suspension are orthogonal, it can be decomposed into separate one-dimensional harmonic oscillators characterized by their respective frequencies and effective masses [70]. Applying the theorem to a single oscillator is a straightforward process, as demonstrated in the next section.

V.1.3. Single damped harmonic oscillator

Beginning with the examination of thermal noise in the simple scenario of a damped harmonic oscillator, this model proves crucial as a theoretical representation of the system under investigation in the experiment detailed in this thesis. The system is composed of a mass m attached to a spring with an elastic constant k and a damping constant β that can move only in the x-axis (see Figure V.2). In addition, the system is immersed in a thermal bath at temperature T and driven by a stochastic thermal force $F(t)$. The equation of motion can be written as:

$$m\ddot{x} + \beta\dot{x} + kx = F(t) \tag{V.15}$$

Following the Zeroth Law of Thermodynamics, a state of equilibrium with the environment is achieved by the oscillator when it maintains the temperature T on average. As per the Equipartition Theorem [71], in thermal equilibrium, the oscillator exhibits an average energy equal to:

$$k\langle x^2\rangle = k_B T \tag{V.16}$$

Hence, for the system to maintain the equilibrium, it must oscillate with this variance around its average value of $x = 0$. Oscillating, the mass gradually releases energy to the surrounding thermal environment, and at the same time, the thermal bath pumps the oscillator maintaining the equilibrium. To address equation (V.15), a transition to the frequency domain is performed by applying a Fourier transform:

$$(-\omega^2 + i\Gamma\omega + \omega_0^2)x(\omega) = \frac{F(\omega)}{m} \tag{V.17}$$

where $\Gamma = \beta/m$ and $k = m\omega_0^2$. Solving the equation for $x(\omega)$ results in:

$$x(\omega) = \frac{F(\omega)/m}{(-\omega^2 + i\Gamma\omega + \omega_0^2)} \equiv \chi(\omega)F(\omega) \tag{V.18}$$

The imaginary part of the susceptibility χ is given by:

$$\mathrm{Im}[\chi(\omega)] = \frac{1}{m}\frac{\Gamma}{(\omega_0^2 - \omega^2)^2 + \omega^2\Gamma^2} \tag{V.19}$$

Applying the FDT (V.14) to this mechanical system yields:

$$S_x(\omega) = \frac{4k_BT}{m\omega} \frac{\Gamma}{\left[(\omega_0^2 - \omega^2)^2 + \omega^2\Gamma^2\right]} \tag{V.20}$$

The FDT allows the prediction of the oscillations of an observable by starting with the mechanical model of the system. The spectrum of this model is illustrated in V.1, with parameters chosen to replicate the experiment's model presented in §VII.1. Integrating the last formula over positive frequencies yields the Equipartition Theorem:

$$\langle x^2 \rangle = \int_0^\infty d\omega S_x(\omega) = \frac{k_BT}{k} \tag{V.21}$$

In this example, the spectrum of fluctuations due to thermal noise for the basic one-dimensional damped oscillator was expressed. The complete noise spectrum for a complex mechanical system can be derived by summing the contributions from each normal mode, treating them as individual resonators, each with its corresponding equivalent mass.

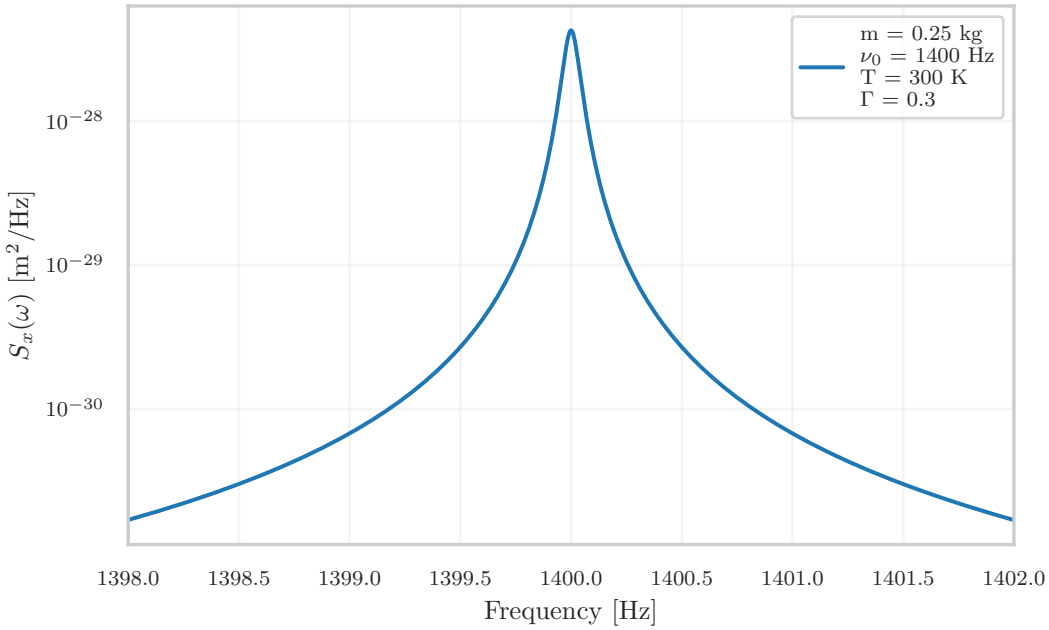

FIGURE V.1: The spectrum of a single damped oscillator around the resonance frequency, with parameters chosen to match the characteristics of the oscillator studied in the experiment presented in this thesis.

V.1.4. DOUBLE DAMPED HARMONIC OSCILLATOR

Having examined the simplest model, the focus now shifts to a more complex system involving two coupled damped harmonic oscillators (refer to Figure V.2). The motivation for exploring a more intricate model is rooted in the limitation of the single oscillator to explain the experimental results obtained in the studied experiment. For this discussion, references [72] and [73] are taken into consideration. The equations of motion for this model are as follows:

$$m_1\ddot{x}_1 + \beta_1\dot{x}_1 + \beta_2(\dot{x}_1 - \dot{x}_2) + k_1x_1 + k_2(x_1 - x_2) = F_1 - F_2 \tag{V.22}$$

$$m_2\ddot{x}_2 + \beta_2(\dot{x}_2 - \dot{x}_1) + k_2(x_2 - x_1) = F_2 \tag{V.23}$$

that can be rewritten in the frequency domain as:

$$\ddot{x}_1 + \Gamma_1^2 \dot{x}_1 + \mu\Gamma_2(\dot{x}_1 - \dot{x}_2) + \omega_1 x_1 + \mu\omega_2^2(x_1 - x_2) = (F_1 - F_2)/m_1 \tag{V.24}$$

$$\ddot{x}_2 + \Gamma_2(\dot{x}_2 - \dot{x}_1) + \omega_2^2(x_2 - x_1) = F_2/m_2 \tag{V.25}$$

where $\mu = m_2/m_1$, $k_i = m_i\omega_i^2$. By performing a Fourier transform on the two equations and expressing the algebraic relation among the amplitudes, the following system of equations is derived:

$$\mathbf{D}\begin{pmatrix} x_1 \\ x_2 \end{pmatrix} = \begin{pmatrix} (F_1 - F_2)/m_1 \\ F_2/m_2 \end{pmatrix} \tag{V.26}$$

with:

$$\mathbf{D} = \begin{pmatrix} -\omega^2 + \omega_1^2 + \mu\omega_2^2 + i\omega(\Gamma_1 + \mu\Gamma_2) & -\mu\omega_2^2 - i\mu\omega\Gamma_2 \\ -\omega_2^2 - i\omega\Gamma_2 & -\omega^2 + \omega_2^2 + i\omega\Gamma_2 \end{pmatrix} \tag{V.27}$$

In terms of the impedance matrix $\mathbf{Z}$, the (V.26) become:

$$\mathbf{Z}\dot{\mathbf{x}} = \mathbf{F} = \begin{pmatrix} F_1 - F_2 \\ F_2 \end{pmatrix} \tag{V.28}$$

where the mechanical impedance is expressed as [1]:

$$\mathbf{Z} = \begin{pmatrix} m_1 D_{11}/i\omega & m_1 D_{12}/i\omega \\ m_2 D_{21}/i\omega & m_2 D_{22}/i\omega \end{pmatrix} \tag{V.29}$$

The thermal force correlation terms are given by:

$$\langle F_{ij}^2 \rangle = \langle F_i F_j \rangle = 4k_B T \mathrm{Re}\{Z_{ij}\} \tag{V.30}$$

In this context:

$$\mathbf{F^2} = \begin{pmatrix} \langle F_{11}^2 \rangle & \langle F_{12}^2 \rangle \\ \langle F_{21}^2 \rangle & \langle F_{22}^2 \rangle \end{pmatrix} = 4k_B T \begin{pmatrix} \mathrm{Re}\{m_1 D_{11}/i\omega\} & \mathrm{Re}\{m_1 D_{12}/i\omega\} \\ \mathrm{Re}\{m_2 D_{21}/i\omega\} & \mathrm{Re}\{m_2 D_{22}/i\omega\} \end{pmatrix} \tag{V.31}$$

The spectrum of motion of oscillator 2 in terms of the force is given by:

$$S_{x_2}(\omega) = \frac{1}{|\det \mathbf{D}|^2}\left(\frac{\langle F_{22}^2 \rangle}{m_2^2}|D_{11}|^2 + \frac{\langle F_{11}^2 \rangle}{m_1^2}|D_{21}|^2 - \frac{\langle F_{12}^2 \rangle}{m_1 m_2}(D_{11}^* D_{21} + D_{11} D_{21}^*)\right) \tag{V.32}$$

This solution is used in §VII.4.1 to attempt to replicate the behavior of the mechanical oscillator under study.

[1] 1The impedance Z is defined as $Z = R + iX$, where R is the resistance and X the reactance. This last term is related to the susceptibility χ by the relationship $\chi = \frac{1}{i\omega X}$

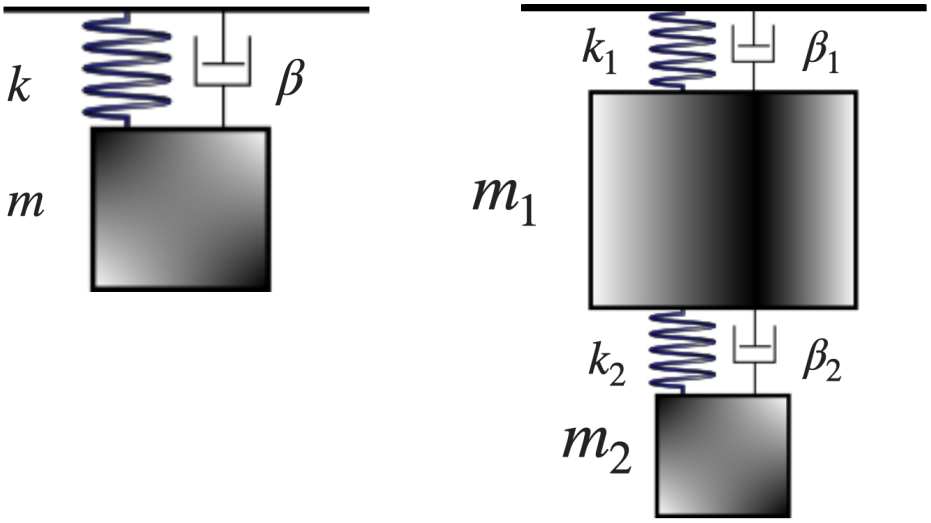

FIGURE V.2: (left) Scheme of the single-damped oscillator. (right) Scheme of the double-dumped oscillator.

V.2. Thermal noise in gravitational wave detector

The FDT discussed above can be applied to various fields of physics, from Brownian motion to electrical circuits. In this context, examples are presented to illustrate its application within GW interferometers. Thermal noise significantly impacts these detectors across various frequency ranges, affecting suspensions at low frequencies and influencing the coatings of test masses in the region of highest sensitivity.

The test masses in GW interferometers are mirrors with dimensions of 35 cm in diameter, 20 cm in thickness, and a mass of 42 kg, as utilized in Virgo for the observing run O4 [24]. They are suspended by a system known as the Super Attenuator (SA), designed to minimize the transmission of seismic noise at frequencies above a few hertz. The SA comprises a series of suspended filters utilizing 1.15 m long steel wires with a few millimeters in diameter. This entire system is housed within a 10 m high tower, maintained in a high vacuum environment (see Figure V.3). However, despite the implementation of this system, residual displacement noises persist, stemming from factors such as seismic vibrations or suspension thermal noise. The thermal fluctuations cause variations in the positions of the masses along the trajectory of the laser beam, thereby affecting the sensitivity of GW measurements [74]. These fluctuations represent a form of noise that constrains the sensitivity of the detector. In Virgo, a detailed analysis of thermal noise has been conducted for various stages. Using the normal-mode decomposition method enables the separate evaluation of the thermal noise spectrum for suspension wires, taking into account the pendulum mode [75] [76], the violin modes arising from transverse mode fluctuations [77], and the bouncing modes. As the focus of this thesis does not extensively explore the details of phenomena within Virgo suspensions, they will be introduced here merely as examples.

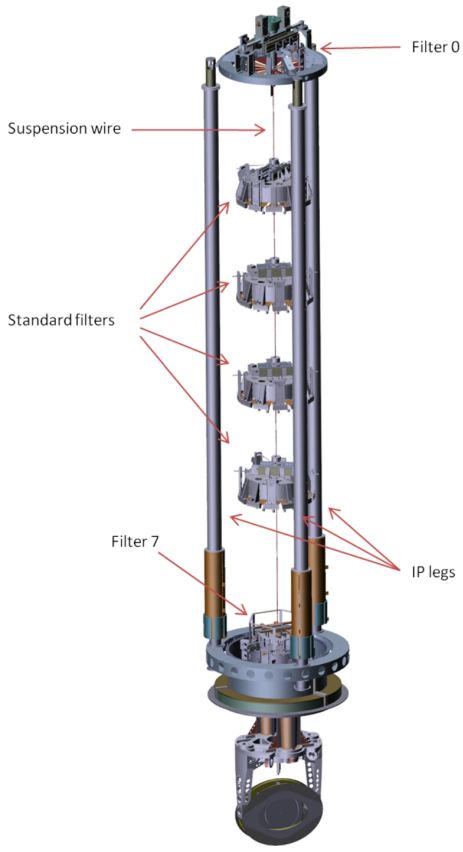

Figure V.3: Graphic representation of the Virgo Super Attenuator. Image taken by [24]

V.2.1. Pendulum mode

A mass M suspended from an ideal, weightless wire of length L oscillates with an angular frequency $\omega_{pend} = \sqrt{g/L}$. For Virgo suspensions, $\nu_{pend} = \omega_{pend}/2\pi$ is confined in the low-frequency region below 2 Hz [78]. As this pendulum motion can be modeled as a harmonic oscillator, the PSD can be calculated using the model presented in §V.1.3:

$$S_{pend}(\omega) = \frac{4k_B T}{M} \frac{\Gamma_{pend}}{\left[(\omega_{pend}^2 - \omega^2)^2 + \omega^2 \Gamma_{pend}^2\right]} \tag{V.33}$$

Here, Γ_{pend} represents the dissipation term, considering the geometry of the wires, material characteristics, and the presence of the gravitational field. During the pendulum motion, the wires experience bending from the top to the bottom, resulting in energy dissipation through elastic strain [79]. The bending of the pendulum mode is influenced by both the tension τ applied by the suspended mass and the elastic properties of the wire material (top left of Figure V.5). Assuming the internal structure of the wire is negligible, there are no frictional losses associated with this oscillation. All the energy is conserved within the frictionless gravitational field, and there is no thermal noise. In addition to this motion, an extended body suspended by a wire also undergoes a rocking swing (top right of Figure V.5). In Virgo, the impact of the rocking swing is minimized by employing four silica wires to support the mirrors (0.640 mm in diameter), thereby avoiding excessive swinging (see Figure V.4).

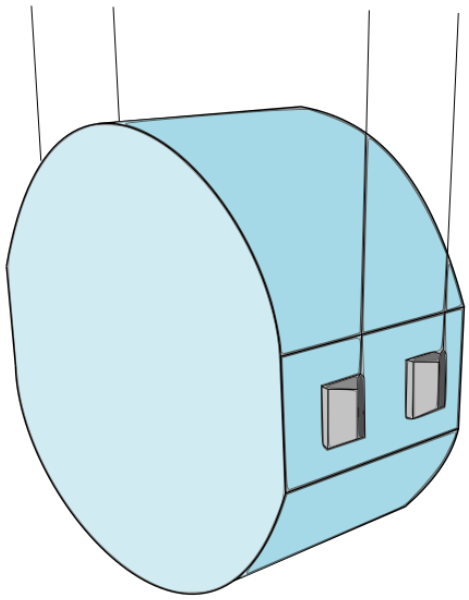

Figure V.4: Scheme of the mirror suspended with 4 silica wires.

V.2.2. Bouncing modes

In addition to the pendulum mode induced by gravity, an actual wire exhibits a series of inherent vertical vibration modes due to its elastic properties (bottom left of Figure V.5). The characteristics and frequencies of bouncing modes are directly influenced by the tension τ in the wire. The oscillatory motion, resembling that of a spring in a wire supporting a mass M, is referred to as the bouncing mode. In these modes, the equivalent spring constant is $k_{boun} = \sigma\Sigma/L$, where σ is Young's modulus, Σ is the cross-section of the wire, and L is its

length. Given the spring constant, the angular frequency given by:

$$\omega_{bounc} = \sqrt{\frac{\sigma\Sigma}{ML}} \tag{V.34}$$

The frequency is in the range between 1-10 Hz [78]. As mentioned, the bouncing mode would not constitute noise in the readout of the mirror position along the (horizontal) direction of the propagation of the laser. However, in a GW interferometer, such coupling is present due to the curvature of the Earth and imperfections in the suspension system mechanics. Because the two mirrors are positioned at a separation distance $D = 3$ km (in Virgo), the vertical directions are not perfectly parallel, but they form an angle $\theta = D/R \approx 0.6$ mrad with R representing the Earth's radius (6378 km). Consequently, the vertical bouncing mode leads to a thermal noise spectrum that is scaled by this angle:

$$S_{bounc}(\omega) = \theta \frac{4k_BT}{M} \frac{\Gamma_{wires}}{\left[(\omega^2_{bounc,N} - \omega^2)^2 + \omega^2\Gamma^2_{wires}\right]} \tag{V.35}$$

Here, $\omega_{bounc,N} = \sqrt{N}\omega_{bounc}$ where N represents the number of wires. Γ_{wires} is the dissipation given by the internal loss of the wires.

V.2.3. Violin modes

The transverse modes of the wire with respect to its longitudinal axis are called violin modes (botom right of Figure V.5). The harmonics of these modes are given by:

$$\omega_n = \frac{n\pi}{L}\sqrt{\frac{\tau}{\Sigma\rho}}\left[1 + \frac{2\lambda}{L} + \frac{1}{2}\left(\frac{n\pi\lambda}{L}\right)\right] \tag{V.36}$$

where $n = 1, 2, ...$ is the index of the harmonics and ρ is the mass density. In the violin mode, the wires bend near both ends in a similar way dissipating energy [80]. The bending occurs over the characteristic distance $\lambda = \sqrt{\frac{YI}{\tau}}$. Here, Y is Young's modulus, I the momentum of inertia of the wires and τ the tension on the wires. Because $\lambda \ll L$ the modes can be approximated as an ideal string, resulting in:

$$\omega_n \simeq \frac{n\pi}{L}\sqrt{\frac{\tau}{\Sigma\rho}} \tag{V.37}$$

Each of the violin modes is an individual resonator with an effective mass μ_n:

$$\mu_n \simeq \frac{\pi^2 M^2}{2\Sigma\rho L} n^2 \tag{V.38}$$

Hence, the thermal noise spectrum is influenced by the contribution of the violin modes, and this contribution can be described as the sum of all the harmonics:

$$S_{violin}(\omega) = \sum_{n=1}^{\infty} \frac{4k_BT}{\mu_n} \frac{\Gamma_n}{\left[(\omega_n^2 - \omega^2)^2 + \omega_n^2\Gamma_n^2\right]} \tag{V.39}$$

where Γ_n is the dissipation due to n-th mode. Each mode has a different dissipation factor as bending occurs differently [80].

V.3. Non-equilibrium thermal fluctuation

In this section, the central focus of the experiment conducted within this thesis is introduced: thermal noise in a non-equilibrium state. To achieve this, a brief presentation of the theoretical model is provided, extending the equipartition theorem to investigate thermal fluctuations in situations where an object is in a steady state of non-equilibrium. Subsequently, the RareNoise experiment is introduced, representing an initial attempt to explore the behavior of a macroscopic oscillator when subjected to induced thermal non-equilibrium conditions.

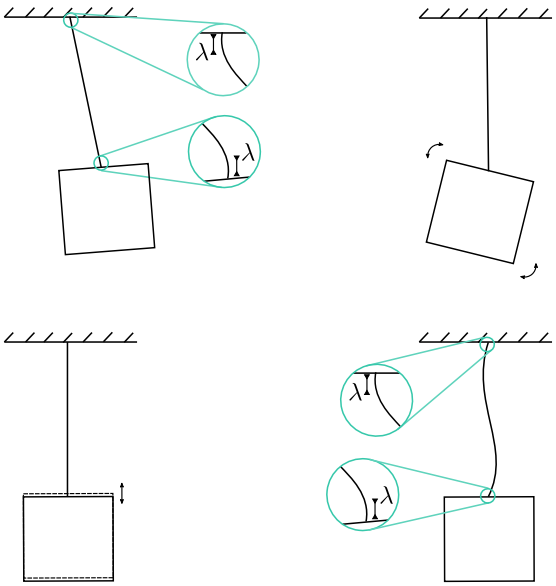

FIGURE V.5: Scheme of possible motions of a mass suspended by a wire. (top left) Pendulum motion. In the fixing extremes, the bending λ of the wire is highlighted. (top right) The rocking motion is solved using 4 wires to suspend the mass. (bottom left) Bouncing mode along the vertical direction. (bottom right) The first violin mode of the wire. In the fixing extremes, the bending λ of the wire is highlighted.

V.3.1. FLUCTUATIONS OUT THERMODYNAMIC EQUILIBRIUM

When a system cannot be regarded as being in thermodynamic equilibrium, the validity of the discussions in the preceding sections is not assured. As detailed in the next chapter, the interest lies in studying a system that exhibits a temperature profile $T(x)$ along the entire extent of the oscillator. Due to the geometry of the system, a temperature gradient is induced by heating one of the edges of the oscillator. Consequently, it is not possible to consider a single temperature T to characterize the system. The examination involves two modes of a metal object (consisting of a bar and mass): longitudinal and transverse. Each of these modes can be represented as a harmonic oscillator. Under equilibrium conditions, the modes are in equilibrium with the same thermal bath at temperature T which implies, by energy equipartition:

$$T = \frac{k_l \langle \delta_l^2 \rangle_{EQ}}{k_B} = \frac{k_t \langle \delta_t^2 \rangle_{EQ}}{k_B} \tag{V.40}$$

where $\langle \delta_t^2 \rangle_{EQ}$ and $\langle \delta_l^2 \rangle_{EQ}$ are the thermal fluctuations for the two modes at the equilibrium (EQ) while k_l and k_t are the elastic constants of the two modes of resonance. Departing from thermodynamic equilibrium implies the absence of a single temperature T extending to the entire body. Nevertheless, out of equilibrium, relations similar to (V.40) can be utilized to define an effective temperature for each mode:

$$T_{eff}^{l} \coloneqq \frac{k_l \langle \delta_l^2 \rangle_{NE}}{k_B} \tag{V.41}$$

$$T_{eff}^{t} \coloneqq \frac{k_t \langle \delta_t^2 \rangle_{NE}}{k_B} \tag{V.42}$$

Considering $T_{eff}^{l,t}$ as the effective temperature the system would exhibit if its oscillations were measured as if in equilibrium at a temperature T_{eff}. In simpler terms, the measured non-equilibrium fluctuations $\langle \delta_l^2 \rangle_{NE}$ and $\langle \delta_t^2 \rangle_{NE}$ are regarded as if they were taken under equilibrium, and a temperature is computed using the equilibrium Equipartition theorem. In this scenario, it is important to note that not every mode is expected to yield the same temperature.

V.3.2. The RareNoise experiment

The RareNoise experiment was devised to address the inquiry concerning non-equilibrium thermal noise in GW detectors [81]. This experiment examines the noise-induced vibrations in low-loss mechanical oscillators operating under non-equilibrium steady-state conditions, realized by a stable temperature gradient. The object under investigation is an aluminum sample, machined as a rod (kept in the vertical position, square cross-section 0.25 cm^2, length 10 cm) with one end fixed (attached to a larger and rigid mass machined from the same piece; this is the top end) and the other loaded by a cuboid mass (mass 0.25 kg) (as illustrated in Figure V.6). The chosen material for this piece is the aluminum alloy Al5056, the same material utilized in most GW bar detectors like AURIGA. This experiment was hosted at the Legnaro National Laboratories (LNL) where the experiment in this thesis is also conducted. The material was chosen as a compromise between cost, low losses, machinability, and availability in large pieces. The oscillations studied include the first longitudinal mode, resonating at a frequency of approximately 1420 Hz, as well as the first transverse mode, resonating at approximately 320 Hz. The oscillator displacement,

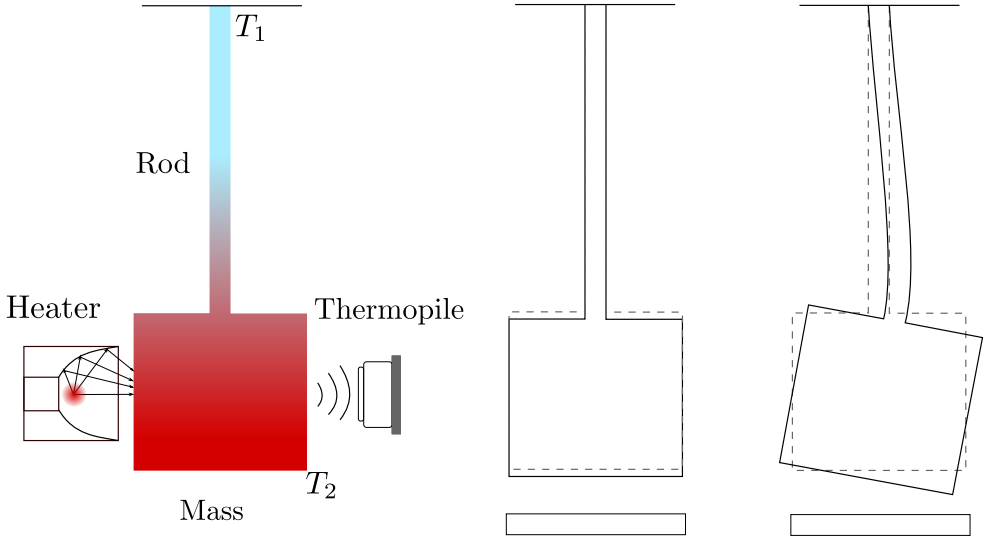

Figure V.6: A schematic representation of the oscillator. (left) Illustration of the infrared radiation heater and the thermopile located in front of the cubic mass. (center and right) The longitudinal and transverse acoustic modes of vibration are shown, respectively. In the lower part of the oscillator, the aluminum plate constituting the capacitor is present [81].

influenced by thermal noise, is measured through a capacitive readout system: an aluminum plate is positioned beneath the load mass, maintaining a distance of 60 to 80 μm, effectively creating a planar capacitor with the surface of the load mass. The motion of the oscillator results in alterations in the separation between the two capacitor surfaces, affecting its capacitance. By maintaining the capacitor at a fixed charge and amplifying and measuring the resulting voltage, variations in capacitance are estimated, providing measurements of the position of the oscillator. A low-noise amplifier connected to the capacitor achieves sensitivity in the range of a few 10^{-15} $m/\sqrt{Hz}$ for the displacement of the longitudinal mode [82].

To minimize external mechanical vibrations within the experimental setup, the oscillator is suspended using a series of three mechanical filters (§VII.1.3). Furthermore, to avoid acoustic and residual gas noise, both the oscillator and the passive mechanical filters are enclosed in a vacuum chamber connected to a vibration-free pump (namely an ion pump). This vacuum system maintains pressure levels below 10^{-5} mbar [83].

To regulate the temperature and create a temperature gradient, the fixed end of the rod can be cooled and regulated using a Peltier cell, while the load mass can be heated through infrared

thermal radiation (left side of Figure V.6). Radiative heating is employed as a contactless means to avoid introducing external losses to the oscillator. Similarly, the temperature of the load mass is monitored via a contactless sensor, namely a thermopile. Using the knowledge of the capacitor gap and the bias voltage, the amplifier output was converted in the displacement of the mass along the vertical direction (i.e. along the longitudinal axis of the rod).

In the PSD of the displacement, peaks corresponding to the first transverse and longitudinal acoustic modes of vibration are present. While the transverse peak is analyzed by doing the ratio of the areas out of equilibrium and at equilibrium, the longitudinal peak is fitted using the damped oscillator model (V.20) to obtain the effective temperature (V.41). In simplifying (V.20) for frequencies near resonance ($\omega = \omega_0 + \delta$) and neglecting high order terms, the PSD is approximated as:

$$x^2(\omega) \simeq \frac{4k_BT}{m\omega_0^2} \frac{\Delta\omega}{4\delta_\omega^2 + \Delta\omega^2} \tag{V.43}$$

Substituting $\omega_0 = 2\pi\nu_0$, the expression becomes:

$$x^2(\nu) \simeq \frac{2}{\pi} \frac{k_BT}{m(2\pi\nu_0)^2} \frac{\Delta\nu}{4\delta_\nu^2 + \Delta\nu^2} \tag{V.44}$$

The spectrum is then fitted with the sum of a constant term accounting for the readout white noise and a Lorentzian peak:

$$y(x) = a + \frac{2}{\pi} \frac{b \cdot c}{4(x-d)^2 + c^2} \tag{V.45}$$

Here, a is the noise level out of resonance, $c = \Delta\nu$ is the FWHM of the peak, $d = \nu_0$ is the resonance frequency, $b = \frac{k_BT}{m\omega_0^2}$ is the area under the peak. This last term allows the calculation of the square mean displacement of the oscillator and estimation of the effective temperature T_{eff}.

In the article [82], the ratio $R_{NEQ/EQ=\langle x_1^2\rangle_{NEQ}/\langle x_1^2\rangle_{EQ}}$ as a function of $\Delta T/T_{avg}$ is plotted to study the effect of the induced thermal gradient on the oscillator. $\langle x_1^2\rangle$ is the mean square displacement of the oscillator in equilibrium (EQ) and out of the thermodynamic equilibrium (NEQ).

The results, shown in Figure V.7, indicate that $R_{NEQ/EQ} > 1$, with the maximum thermal gradient causing $R_{NEQ/EQ} > 1$ by more than 4 standard deviations.

A relative temperature difference of 4% is sufficient to raise the nonequilibrium T_{eff} by 20% for the longitudinal mode, surpassing the highest physical temperature within the system. For the transverse mode, this effect is even greater, with the non-equilibrium T_{eff} increasing by a factor of 3-4. This challenges the validity of the equipartition theorem, as the longitudinal and transverse modes of vibration exhibit distinct T_{eff}, resulting in an uneven distribution of energy among the modes.

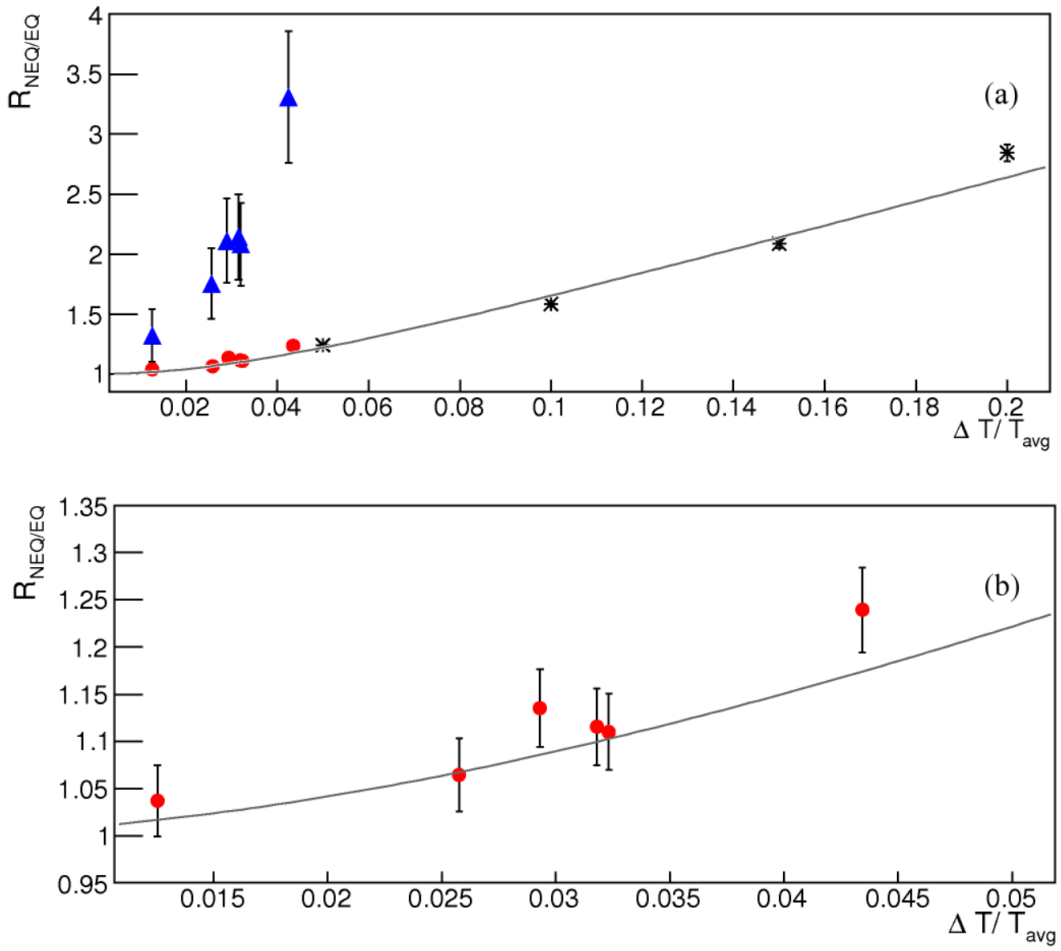

FIGURE V.7: Figure reproduced from [82]. (top) Ratio $R_{NEQ/EQ}$ of the average effective temperature of the transverse (**blue triangles**) and longitudinal (**red circles**) acoustic modes in NESS over their average effective temperature in equilibrium. The horizontal axis represents the normalized thermal difference $(T_2 - T_1)/T_{avg}$. The error bars denote the statistical uncertainty, which is smaller than the size of the points along the horizontal axis. The **black stars** show the results of the numerical experiment with their respective error bars. The gray line represents the best fit of the numerical data. (bottom) Results for the longitudinal mode, and the line fitting the numerical result.

VI | INTERFEROMETRIC READOUT

In the context of this doctoral research, the experimental work to measure the thermal noise of mechanical oscillators out of equilibrium is restarted. The study focused on the same oscillators used in the RareNoise experiment to enable a more comprehensive comparison with its results. The primary modification in comparison to that experiment involves the adoption of an interferometric readout instead of a capacitive one. This change is implemented to address certain limitations identified in the previous setup. Despite its sensitivity, the capacitive readout faced challenges, including systematic errors (approximately 5%) arising from the thermal expansion of aluminum. These errors impacted the calibration of the sensor in out-of-equilibrium states. Additionally, the requirement not to short the capacitor plates imposed stringent constraints on the achievable thermal differences and, consequently, the size of the measured effect. Ultimately, calibration of the capacitor was not possible during the thermal transient, preventing measurements before reaching a steady state. The revised readout addresses this limitation by eliminating the fixed plate of the capacitor and employing the cuboid mass as a mirror in an interferometric measurement. This modification, in principle, enables displacement measurements during the transient and removes restrictions on the maximum tolerable thermal difference. This chapter details the new interferometric readout, while the following chapter covers the experimental apparatus and the conducted measurements.

VI.1. Quadrature Phase Differential Interferometer

Assuming a simple Michelson interferometer is employed to investigate the motion of a mass exceeding $\lambda/2$, it is known that the measured signal does not provide direct information about the displacement. The measured quantity is, in fact, the cosine of the relative displacement ΔL between the two interferometer arms ($\cos(2k\Delta L)$). Furthermore, it is essential to select the working point of the interferometer (the position of the reference mirror) to maximize sensitivity. In the context of the experiment, aimed at studying Non-Equilibrium Thermal Noise (NETN) in aluminum oscillators, the goal is to establish thermal differences on the order of several or tens of degrees, leading to thermal expansions larger than a single fringe. Consequently, it becomes evident that the simple Michelson interferometer is not a suitable choice for a readout in this scenario. To tackle this challenge, a Quadrature Phase Differential Interferometer (QPDI) [84][85] is implemented. This approach employs two interferometers, each exploiting orthogonal linear polarizations of light. A quarter-wave plate (QWP) is used to create a phase shift of $\pi/2$ between the outputs of these two interferometers, establishing the quadrature characteristic inherent to this method.

VI.1.1. Optical layout

The optical configuration of the QPDI used in the experiment is illustrated in Figure VI.1. The laser beam emitted from the laser head is initially linearly polarized. The beam passes a combination of Half-Wave Plate (HWP1) and Polarizing Beam Splitter (PBS1) enabling the control of the power of the transmitted beam, which is $\hat{p}$-polarized. The first 50% BS (BS1) at this stage serves no specific purpose, as its role becomes relevant later in directing the beam to the detection zone.

Before entering into the interferometer, a second HWP is employed to rotate the linear polarization by 45 degrees. Then, the beam is directed to a second PBS (PBS2): the reflected component with $\hat{s}$-polarization is directed towards the reference mirror of the interferometer, while the transmitted portion with $\hat{p}$-polarization reflects off the moving mirror.

Subsequently, the returning beam is reflected by BS1 towards the detection area. Here, a second 50% Beam Splitter (BS2) separates the light, directing it toward two pairs of photodiodes labeled as A-B and C-D. The second pair, C-D, captures light that has undergone an additional phase shift of $\pi/2$, introduced through the use of a Quarter-Wave Plate (QWP) with the fast axis rotated at 45 degrees. This plate enables the phase unwrapping characteristic of the QPDI.

VI.1.2. Jones calculus

In this section, the Jones calculus is employed to calculate the signal obtained by combining two interferometers (A-B and C-D) with a $\pi/2$ phase shift. The Jones matrix formalism is utilized to describe the polarization of light in free space and homogeneous isotropic non-attenuating media, such as optical elements (e.g., wave plates, mirrors, and beam splitters) [86]. The discussion assumes the ideal nature of all optical components (as listed in Table VI.1), implying no losses and no potential mixture between polarizations.

Input area

In the transmission through the system consisting of HWP1 and PBS1, the beam is initially described as:

$$E_0 = E_{in} \begin{pmatrix} 1 \\ 0 \end{pmatrix} \tag{VI.1}$$

where E_{in} is the input beam amplitude. The first element it encounters is BS1, which redirects half of the intensity toward the interferometer. After the BS, the HWP2 set at 22.5°, rotates

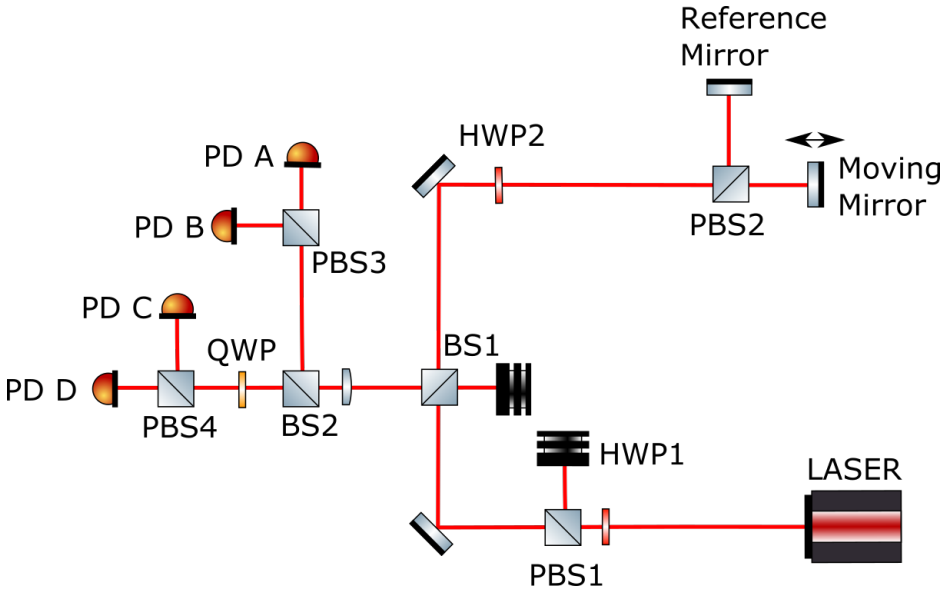

FIGURE VI.1: Optical layout of the Quadrature Phase Differential Interferometer. The power of the laser beam is controlled by using a HWP1+PBS1 system. The linear polarization $\hat{p}$ is rotated into a 45-degree linear polarization using the HWP2. Inside the interferometer, the light is split into two paths depending on the polarization. The $\hat{p}$-polarization is transmitted toward the moving mirror while the $\hat{s}$-polarization goes toward the reference mirror. The recombined beam is reflected into the detection area where the two pairs of PDs read the beam intensities.

OPTICAL COMPONENT LIST		
Optical component	Symbol	Jones Matrix
HWP($\frac{\pi}{8}$)	$\mathbb{J}_{\frac{\lambda}{2}}$	$\frac{1}{\sqrt{2}}\begin{pmatrix}1 & 1\\ 1 & -1\end{pmatrix}$
HWP($-\frac{\pi}{8}$)	$\mathbb{J}_{-\frac{\lambda}{2}}$	$\frac{1}{\sqrt{2}}\begin{pmatrix}1 & -1\\ -1 & -1\end{pmatrix}$
QWP($\frac{\pi}{4}$)	$\mathbb{J}_{\frac{\lambda}{4}}$	$\frac{1}{\sqrt{2}}\begin{pmatrix}1 & i\\ i & 1\end{pmatrix}$
PBS$_p$	$\mathbb{J}_{PBS_p}$	$\begin{pmatrix}1 & 0\\ 0 & 0\end{pmatrix}$
PBS$_s$	$\mathbb{J}_{PBS_s}$	$\begin{pmatrix}0 & 0\\ 0 & 1\end{pmatrix}$
Beam Splitter	$\mathbb{J}_{BS}$	$\frac{1}{\sqrt{2}}\begin{pmatrix}1 & 0\\ 0 & 1\end{pmatrix}$
Mirror	$\mathbb{J}_{M}$	$\begin{pmatrix}1 & 0\\ 0 & -1\end{pmatrix}$

TABLE VI.1: Optical components and the corresponding Jones matrices. The brackets of the wave plates indicate the rotation angle of the plate's axis.

the beam polarization to equally divide it in both the directions $\hat{p}$ and $\hat{s}$.

$$E_{ITF} = \mathbb{J}_{\frac{\lambda}{2}}\mathbb{J}_{BS}E_0 = \frac{E_{in}}{2}\begin{pmatrix}1\\ 1\end{pmatrix} \tag{VI.2}$$

Interferometer area

The linearly polarized beam enters PBS2, where the two polarizations are separated: the polarization parallel to the p-axis is transmitted to the moving mirror, while the other one (parallel to the s-axis) is reflected toward the reference mirror of the interferometer. The beam, transmitted by the PBS and reflected by the oscillator, is described as:

$$E_O = \mathbb{J}_M \mathbb{J}_{PBS_p} E_{ITF} = \frac{E_{in}}{2} e^{i2k(l_O+\delta z)} \begin{pmatrix} 1 \\ 0 \end{pmatrix} \tag{VI.3}$$

where l_O is the distance covered by the light to reach the oscillating mirror and δz is vibration around the mean value l_O. The beam reflected by PSB2 and then reflected by the reference mirror is:

$$E_M = \mathbb{J}_M \mathbb{J}_{PBS_s} E_{ITF} = \frac{E_{in}}{2} e^{i2kl_M} \begin{pmatrix} 0 \\ -1 \end{pmatrix} \tag{VI.4}$$

where the distance covered by the light to reach the reference mirror is l_M. The beam that exits the chamber after the recombination in the PBS is:

$$E_{reflected} = E_O + E_M = \frac{E_{in}}{2} \begin{pmatrix} 1 \\ -e^{i\psi} \end{pmatrix} \tag{VI.5}$$

where $\psi = 2k(l_M - l_O - \delta z) = 2k(\Delta l - \delta z)$.

Detection area

Before entering the detection area the light passes a second time through the HWP2 that, in this case, is equivalent to an HWP set at $-22.5°$. The resulting beam entering the detection area is:

$$E_{det} = \mathbb{J}_{BS} \mathbb{J}_{-\frac{\lambda}{2}} E_{reflected} = \frac{E_{in}}{4} \begin{pmatrix} 1 + e^{i\psi} \\ -1 + e^{i\psi} \end{pmatrix} \tag{VI.6}$$

The beam is divided into the two analysis arms of the QPDI by a BS2. In the AB arm, the beam is expressed as:

$$E_{AB} = \mathbb{J}_{BS} E_{det} = \frac{E_{in}}{4\sqrt{2}} \begin{pmatrix} 1 + e^{i\psi} \\ -1 + e^{i\psi} \end{pmatrix} \tag{VI.7}$$

The two photodiodes A and B are illuminated by two different polarization split by PBS3:

$$E_A = \mathbb{J}_{PBS_p} E_{AB} = \frac{E_{in}}{4\sqrt{2}} \begin{pmatrix} 1 + e^{i\psi} \\ 0 \end{pmatrix} \tag{VI.8}$$

$$E_B = \mathbb{J}_{PBS_s} E_{AB} = \frac{E_{in}}{4\sqrt{2}} \begin{pmatrix} 0 \\ -1 + e^{i\psi} \end{pmatrix} \tag{VI.9}$$

In the CD arm, the light passes through a QWP rotated at 45°:

$$E_{CD} = \mathbb{J}_{\frac{\lambda}{4}} \mathbb{J}_{BS} E_{det} = \frac{E_{in}}{4\sqrt{2}} \begin{pmatrix} i + e^{i\psi} \\ -i + e^{i\psi} \end{pmatrix} \tag{VI.10}$$

After the PBS, the light that illuminates the photodiodes D and C is:

$$E_D = \mathbb{J}_{PBS_s} E_{CD} = \frac{E_{in}}{4\sqrt{2}} \begin{pmatrix} i + e^{i\psi} \\ 0 \end{pmatrix} \tag{VI.11}$$

$$E_C = \mathbb{J}_{PBS_p} E_{CD} = \frac{E_{in}}{4\sqrt{2}} \begin{pmatrix} 0 \\ -i + e^{i\psi} \end{pmatrix} \tag{VI.12}$$

The intensities read by the photodiodes (denoted by $I = |EE^*|$) are given by:

$$I_A = \frac{I_{in}}{16}(1 + \cos\psi) \qquad I_B = \frac{I_{in}}{16}(1 - \cos\psi) \tag{VI.13}$$

$$I_C = \frac{I_{in}}{16}(1 - \sin\psi) \qquad I_D = \frac{I_{in}}{16}(1 + \sin\psi) \tag{VI.14}$$

From the last equations, two quantities strictly related to the interferometer phase are obtained:

$$C_x = \cos\psi = \frac{I_A - I_B}{I_A + I_B} \tag{VI.15}$$

$$C_y = \sin\psi = \frac{I_D - I_C}{I_D + I_C} \tag{VI.16}$$

It is worth noting that the total power reaching the detector area is 1/4 of the power after PBS1, with the remaining 3/4 being lost during the two passages through BS1.

VI.1.3. Interferometer displacement

Once obtained the $\cos\psi$ and $\sin\psi$, the optical phase can be calculated by rewriting:

$$C_x = \cos\psi \tag{VI.17}$$

$$C_y = \sin\psi \tag{VI.18}$$

In this way, a complex contrast C can be defined as follows:

$$C = C_x + iC_y = e^{i\psi} \tag{VI.19}$$

Due to the quadrature, the phase uniquely determines the optical phase (within a 2π range). The contrast C can be represented in the complex plane, forming a point on the unitary circle. Consequently, a single measurement of the optical phase ψ corresponds to a polar angle in this plane. From the Jones calculus, it was determined that the optical phase is defined as:

$$\psi = 2k(\Delta l - \delta z) = \frac{4\pi}{\lambda}(\Delta l - \delta z) \tag{VI.20}$$

Two factors contribute to this equation. Firstly, there is the optical path difference Δl between the two arms of the interferometer, which might change gradually due to thermal drifts. Secondly, there is the oscillator's displacement δz, representing fluctuations around the mean value Δl. The advantage of using this type of read-out lies in the fact that calculating the derivative of the contrast concerning the variation δz yields:

$$\left|\frac{dC}{d(\delta z)}\right| = \frac{4\pi}{\lambda} \tag{VI.21}$$

As a result, there is no requirement to fine-tune the interference fringe (or working point of the interferometer) because it has no impact on sensitivity. Additionally, even if the working point undergoes some shifts during the measurement, like those due to temperature variations, the measured displacement is not affected. In a classical interferometer, such a scenario would not be possible, as a thermal drift would change the operating point and, consequently, the sensitivity of the instrument. Now that the optical phase is determined, the oscillating mirror's displacement fluctuations can be calculated. Considering $\Delta l = 0$:

$$\delta z = \frac{\lambda}{4\pi}\psi \tag{VI.22}$$

In real experimental setups, the scenario discussed as ideal, where misalignments and imperfections in optical elements are not considered, is less likely to occur. In practice, encountering an ellipse instead of a perfect circle, as described in Equation (VI.19), is more common. To

describe the real case, considerations from [87] are taken into account, leading to the following expressions:

In practical experimental configurations, the idealized scenario, which assumes the absence of misalignments and imperfections in optical elements, is seldom realized. In reality, encountering deviations from perfection, such as an ellipse rather than a perfect circle as stipulated in Equation (VI.19), is a more frequent occurrence. Describing this real-case condition involves incorporating considerations from [87], resulting in the following expressions:

$$I_A = \eta_A + \rho_A \cos\psi \qquad I_B = \eta_B - \rho_B \cos\psi \tag{VI.23}$$

$$I_C = \eta_C - \rho_C \sin(\psi + \phi) \qquad I_D = \eta_D + \rho_D \sin(\psi + \phi) \tag{VI.24}$$

Here, η_i $(i = A, B, C, D)$ represents the DC component detected by each photodiode, ρ_i is the oscillation amplitude, and ϕ denotes the additional phase of the second interferometer (photodiodes C-D) that in an ideal case should be 0. This phase determines whether quadrature is achieved or not. The ideal case is achieved when $\eta_A = \eta_B$ and $\rho_A = \rho_B$ (same for C and D), indicating that the power read by each couple of photodiodes is the same. When $\phi \neq 0$, an ellipse is observed, while with $\phi = 0$, a circle is obtained with an offset. Considering the new intensities (VI.23) and (VI.24), the contrast becomes:

$$C_x = x_0 + X \cos\psi \tag{VI.25}$$

$$C_y = y_0 + Y \sin(\psi + \phi) \tag{VI.26}$$

where x_0 and y_0 are the coordinates of the ellipse center, X and Y represent the projection of the semi-axes and the ϕ is the precession. With these last equations, it becomes feasible to determine the optical phase ψ and consequently the displacement δz, as long as the five parameters characterizing the ellipse are known. From a practical point of view, the approach to obtain the phase involves establishing a relationship between the signal read by the photodiodes and the parameters just described. The two equations VI.25 and VI.26 become:

$$\cos\psi = \frac{C_x - x_0}{X} \tag{VI.27}$$

$$\sin(\psi + \phi) = \frac{C_y - y_0}{Y} \tag{VI.28}$$

using the properties of the trigonometric formulas on (VI.28) combined with (VI.27), the sin function of ψ is obtained as a function of the phase ϕ:

$$\sin\psi = \frac{1}{\cos\phi}\left(\frac{C_y - y_0}{Y} - \frac{C_x - x_0}{X}\sin\phi\right) \tag{VI.29}$$

The phase ψ is determined using a four-quadrant arctangent function on the two normalized signals $\cos\psi$ and $\sin\psi$. Unlike the standard arctangent function, this computation yields a value within the range of $[-\pi, \pi]$ that must undergo unwrapping to restore its continuous motion. Figure VI.2 shows an example of the complex contrast in the ideal case (blue curve) and real case (orange curve). The parameters used to plot this contrast are $x_0 = 0.02$, $X = 0.98$, $y_0 = 0$, $Y = 0.96$, and $\phi = 0.1$ rad. To calibrate the system, the ellipse parameters are obtained by fitting the data before each measurement, as detailed in the next section.

VI.1.4. Calibration

The parameters of the ellipse (VI.25) and (VI.26) are estimated through a calibration procedure that is performed before each set of measurements. As mentioned above, the optical phase is located at a specific point on the ellipse, depending on the position within the interferometric fringe. By displacing one of the arms of the QPDI readout by at least one full fringe, i.e. by moving the working point of the readout around the ellipse by at least a complete turn, the readout is calibrated in terms of displacement. Subsequently, from the combination of

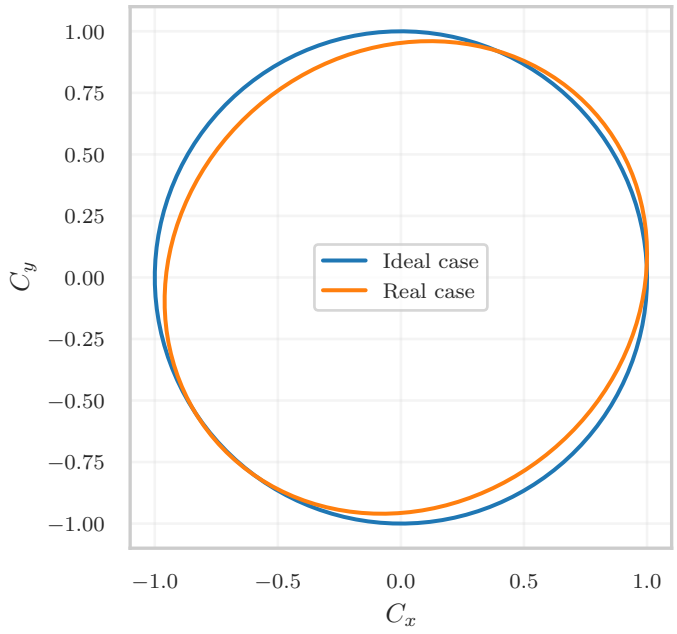

FIGURE VI.2: Two cases of ellipse. The blue curve represents the ideal case with a perfect circle and 100% contrast. The orange curve shows a real case where the two interferometers are unbalanced.

the intensities read by the 4 photodiodes, the corresponding optical phase and hence the interferometer displacement can be inferred. As observed, the optical phase consists of two quantities: the oscillation of the moving mirror, denoted as δz, and the difference length of the interferometer arms, represented by Δl. Theoretically, adjusting either of these variables results in a shift in the working point should yield the same calibration.

VI.2. IDEAL CASES

In this section, the derivation of the optical phase ψ is demonstrated using different numbers of photodiodes. As discussed in §VII.3 during the NETN experiment's characterization, one photodiode had to be omitted while still utilizing the interferometer. All possible cases are illustrated, ranging from the four photodiodes in the QPDI described in the previous section to the simple Michelson interferometer, which utilizes only one photodiode.

VI.2.1. THREE PHOTODIODES

In the ideal case discussed in §VI.1.1 before Equation (VI.23), it is possible to retrieve the optical phase by using only three of the four photodiodes. The motivation for removing one of the photodiodes is explained in the section §VII.3.1, where measurements of the transfer function are presented. For this discussion, the considerations made with Jones matrices apply up to the Eq. (VI.13) and (VI.14). However, the way these intensities are combined to obtain the sine and cosine of the optical phase changes. Consider, for example, removing the PD D, meaning not using its reading. Nothing changes for the A-B couple, from which (VI.15) is still obtained:

$$\cos\psi = \frac{I_A - I_B}{I_A + I_B} \tag{VI.30}$$

Differently from the previous scenario, only the PD C is used to infer the phase sine:

$$I_C = \frac{I_{in}}{16}(1 - \sin\psi) \tag{VI.31}$$

In the 4-photodiode case, there is no need to measure the initial laser power separately for normalization since each photodiode measures 1/16 of the initial power. To normalize the signal, either photodiodes A or B can be used. Suppose photodiode A is chosen, it is known that:

$$I_A = \frac{I_{in}}{16}(1 + \cos\psi) \tag{VI.32}$$

combining the latter relationship with (VI.31) it is obtained:

$$\sin\psi = 1 - \frac{I_C}{I_A}(1 + cos\psi) \tag{VI.33}$$

As evident from the last formula, the normalization of the sine is determined by the cosine, which is derived from the combination of the signals from photodiodes A and B. The phase ψ is then obtained by calculating the arctangent, similar to the 4-photodiode case.

VI.2.2. Two photodiodes

In theory, tracing the ψ phase is feasible with just two photodiodes, one per pair. As in the previous case, the challenge arises when normalizing the signals by the circulating power. Considering photodiode A, equation (VI.32) can be rearranged to obtain:

$$\cos\psi = \frac{I_A - I_{in}/16}{I_{in}/16} \tag{VI.34}$$

In this case, the quantity $I_{in}/16$ can be obtained from the maximum value that I_A can attain within a fringe. Considering $\psi = 0$:

$$\max(I_A) = \frac{I_{in}}{8} \tag{VI.35}$$

Thus, the (VI.34) becomes:

$$\cos\psi = \frac{I_A - 1/2\max(I_A)}{1/2\max(I_A)} \tag{VI.36}$$

Similarly, considering the C photodiode and starting from (VI.31):

$$\sin\psi = -\frac{I_C - \max(I_C)}{\max(I_C)} \tag{VI.37}$$

This approach is effective only when it is possible to measure the maximum values of both I_A and I_C, meaning that the operating point of the interferometer can span an entire quadrant of space from $\psi = 0$ to $\psi = \pi/2$. Similarly to the 4-photodiode case, the phase ψ is then determined by computing the arctangent, utilizing both sine and cosine components.

VI.2.3. One photodiode

The system can function as a simple interferometer with only one photodiode. The same principles discussed for the two photodiode scenario apply here, where either (VI.36) or (VI.37) is considered depending on the chosen photodiode. The phase is determined straightforwardly by calculating the arccosine or arcsine, depending on the selected photodiode. However, when using only one photodiode, it is no longer possible to unwrap the phase. This results in the loss of information about the number of fringe crossings. Additionally, it becomes crucial to carefully select the operating point.

VI.3. Real case with optical imperfections

In this section, a reassessment of the Jones calculus is conducted to analyze the impact of various optical imperfections. Specifically, three distinct scenarios are considered:

- mixing between the two polarizations in the PBS2
- BS ratio different from 50%
- mixing in the PBSs (PBS3 and PBS4) before the photodiodes

In the following, the three cases are discussed separately to understand the effect of individual elements.

VI.3.1. Interferometer PBS mixing

Consider the central PBS (PBS2 in Figure VI.1) of the interferometer that splits the beam between the reference mirror and the oscillating mirror. In this context, polarization mixing refers to the phenomenon where part of the field in the $\hat{p}$-polarization is reflected instead of being completely transmitted, and vice versa for the $\hat{s}$-polarization field. The expressions for the PBS under these conditions are as follows:

$$PBS_p = \begin{pmatrix} T_p & 0 \\ 0 & T_s \end{pmatrix} \tag{VI.38}$$

$$PBS_s = \begin{pmatrix} R_p & 0 \\ 0 & R_s \end{pmatrix} \tag{VI.39}$$

where T_p, T_s, R_p and R_s are respectively the fraction of the powers that enter the PBS in the polarization indicated by the subscript that gets transmitted (T) or reflected (R) according to polarization. The parameters are related by $T_p^2 + R_p^2 = 1$ (similarly for the s polarization). These relationships are typically outlined in the PBS specifications and are quantified through the extinction ratio T_s/T_p which, especially in research-grade components, is often of the order of 10^{-3} or better.

For this analysis, the choice of these parameters is based on their frequent availability in optics datasheets and their ease of measurement. With this new expression, Equation (VI.5) can be rewritten as:

$$E_{reflected} = E_O + E_M = \begin{pmatrix} \frac{T_p}{2} + \frac{1}{2} R_p e^{i\psi} \\ -\frac{T_s}{2} - \frac{1}{2} R_s e^{i\psi} \end{pmatrix} \tag{VI.40}$$

Propagating this expression over all other optical elements yields the two expressions of C_x and C_y:

$$C_x = \frac{2(\cos\psi(R_p T_s + R_s T_p) + R_p R_s + T_p T_s)}{R_p^2 + 2\cos\psi(R_p T_p + R_s T_s) + R_s^2 + T_p^2 + T_s^2} \tag{VI.41}$$

$$C_y = \frac{2\sin\psi(R_s T_p - R_p T_s)}{R_p^2 + 2\cos\psi(R_p T_p + R_s T_s) + R_s^2 + T_p^2 + T_s^2} \tag{VI.42}$$

The impact of mixing is illustrated in Figure VI.3, where the contrast is calculated for various values of the extinction ratio. Specifically, the figure illustrates how the contrast diminishes with an increase in the percentage of polarization p that is reflected instead of being transmitted.

The ideal scenario corresponds to $T_s = 0$, $T_p = 1$, $R_p = 0$, and $R_s = 1$. Under these conditions, the expressions simplify to (VI.17) and (VI.18). It is important to note that this scenario is not problematic for calibration or measurements. Achieving a 5% contrast variation would require an extinction ratio change by a factor of 100, which is unrealistic.

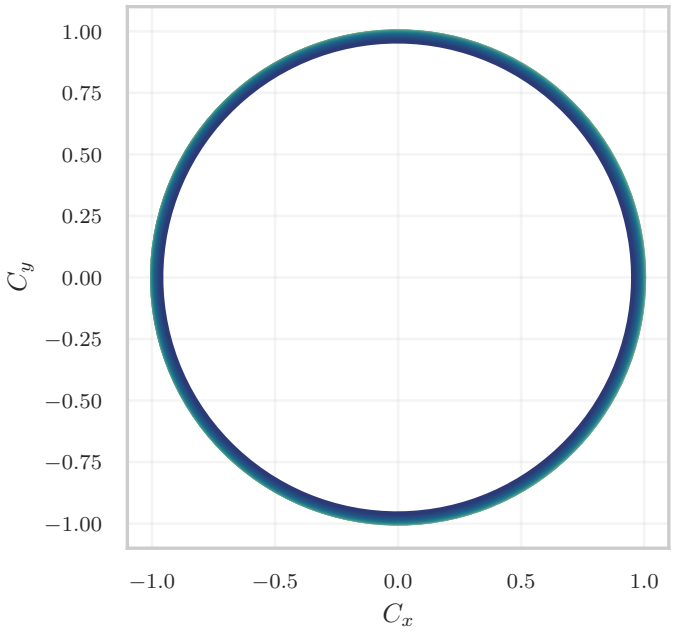

FIGURE VI.3: Effect of the mixing inside the interferometer PBS. As the degree of mixing increases, the contrast decreases, resulting in a smaller radius of the circle. This observation is evident in the figure derived from the parametric equations (VI.41) and (VI.42). Specifically, the extinction ratio T_s/T_p was varied, ranging from a minimum of 10^{-3} to a maximum of 10^{-1}, with T_p set at 0.95, accounting for the optical absorption of the polarizing beam splitter (PBS). Similar behavior is observed when altering the extinction ratio R_p/R_s.

VI.3.2. UNBALANCED BS

Consider the scenario of an unbalanced BS2 (as shown in Figure VI.1), where the beam is split in the detection area between the two pairs of photodiodes. The analysis excludes BS1, as any imperfections in this element are compensated by manually optimizing the contrast through the rotation of HWP2. In the case of BS2, its designation as unbalanced stems from the fact that its reflectivity/transmittance is not precisely 50% for the two orthogonal polarizations. The reflectivity and transmittance matrices for BS2 are denoted as follows:

$$BS_{trans} = \begin{pmatrix} \gamma & 0 \\ 0 & \delta \end{pmatrix} \tag{VI.43}$$

$$BS_{refl} = \begin{pmatrix} \alpha & 0 \\ 0 & \beta \end{pmatrix} \tag{VI.44}$$

where α, β, γ, and δ represent the different ratios of transmission and reflection power for various polarizations. The parameters are related by $\alpha^2 + \gamma^2 = 1/2$ (same for the β and δ). This last statement is for simplicity: the eventual power unbalancing (e.g 40:60) does not represent a problem because the two couples of photodiodes renormalize the signal. Thus, in this case, BS2 can be considered akin to a PBS, described by the coefficients in (VI.43) and (VI.44). Starting from Equation (VI.5), one can apply the two expressions for the BS. The resulting fields illuminating the photodiodes A and B are:

$$E_A = \frac{E_{in}}{\sqrt{16}} \begin{pmatrix} i\alpha \sin\psi + \alpha\cos\psi + 1 \\ 0 \end{pmatrix} \tag{VI.45}$$

$$E_B = \frac{E_{in}}{\sqrt{16}} \begin{pmatrix} 0 \\ i\beta \sin\psi + \beta\cos\psi - \beta \end{pmatrix} \tag{VI.46}$$

while for the couple C-D the fields are:

$$E_C = \frac{E_{in}}{\sqrt{16}} \begin{pmatrix} 0 \\ i\left(\frac{1}{2}\gamma\sin\psi - \frac{1}{2}\gamma\cos\psi - \frac{\gamma}{2} + \frac{1}{2}\delta\sin\psi + \frac{1}{2}\delta\cos\psi - \frac{\delta}{2}\right) \\ +\frac{1}{2}\gamma\sin\psi + \frac{1}{2}\gamma\cos\psi + \frac{\gamma}{2} - \frac{1}{2}\delta\sin\psi + \frac{1}{2}\delta\cos\psi - \frac{\delta}{2} \end{pmatrix} \tag{VI.47}$$

$$E_D = \frac{E_{in}}{\sqrt{16}} \begin{pmatrix} i\left(\frac{1}{2}\gamma\sin\psi + \frac{1}{2}\gamma\cos\psi + \frac{\gamma}{2} + \frac{1}{2}\delta\sin\psi - \frac{1}{2}\delta\cos\psi + \frac{\delta}{2}\right) \\ -\frac{1}{2}\gamma\sin\psi + \frac{1}{2}\gamma\cos\psi + \frac{\gamma}{2} + \frac{1}{2}\delta\sin\psi + \frac{1}{2}\delta\cos\psi - \frac{\delta}{2} \\ 0 \end{pmatrix} \tag{VI.48}$$

By combining the intensities read by the photodiodes, the contrasts are obtained as follows:

$$C_x = \frac{\left(\alpha^2+\beta^2\right)\cos\psi + \alpha^2 - \beta^2}{\left(\alpha^2-\beta^2\right)\cos\psi + \alpha^2 + \beta^2} \tag{VI.49}$$

$$C_y = \frac{2\gamma\delta\sin\psi}{\left(\gamma^2-\delta^2\right)\cos\psi + \gamma^2 + \delta^2} \tag{VI.50}$$

The effect on the interferometer contrast is illustrated in Figure VI.4. As observed, the contrast undergoes deformation compared to the expected circle. This deformation presents a challenge during calibration, as it becomes impractical to fit the ellipse for retracing back to the parameters in (VI.25) and (VI.26). As discussed in Section VI.4, two correction methods can be adopted in such conditions—one based on the measurement of optical parameters and another through post-processing correction.

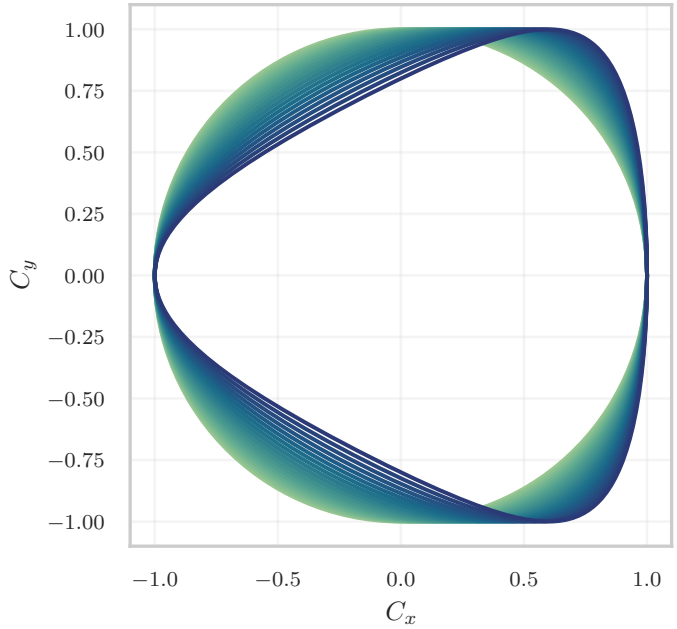

FIGURE VI.4: Effect of an unbalanced BS2 (see Figure VI.1). The figure is obtained from the parametric equations (VI.49) and (VI.50). The α parameter is changed from 50%, where the BS is balanced (yellow circle), to 66% (dark blue line). At this value of α, the shape of the contrast is noticeably deformed. The parameters β and δ change accordingly to maintain the total power equal to 100%

VI.3.3. Detection PBSs mixing

Finally, consider the scenario where the PBSs (PBS3 and PBS4 in Figure VI.1) dividing the polarization directed to different photodiodes exhibit mixing, similar to the first example analyzed. The same notation introduced for PBS2 is used, distinguishing between the A-B and C-D pairs.

$$PBS3_T = \begin{pmatrix} T_A & 0 \\ 0 & T_B \end{pmatrix} \qquad PBS3_R = \begin{pmatrix} R_A & 0 \\ 0 & R_B \end{pmatrix} \tag{VI.51}$$

$$PBS4_T = \begin{pmatrix} T_D & 0 \\ 0 & T_C \end{pmatrix} \qquad PBS4_R = \begin{pmatrix} R_D & 0 \\ 0 & R_C \end{pmatrix} \tag{VI.52}$$

By applying these matrices to the equations (VI.7) and (VI.14) and subsequently combining the intensities from the two pairs of PDs, the contrasts are derived as follows:

$$C_x = \frac{\cos\psi\left(-R_A^2 + R_B^2 + T_A^2 - T_B^2\right) - R_A^2 - R_B^2 + T_A^2 + T_B^2}{\cos\psi\left(R_A^2 - R_B^2 + T_A^2 - T_B^2\right) + R_A^2 + R_B^2 + T_A^2 + T_B^2} \tag{VI.53}$$

$$C_y = \frac{\sin\psi\left(-R_C^2 + R_D^2 + T_C^2 - T_D^2\right) + R_C^2 + R_D^2 - T_C^2 - T_D^2}{\sin\psi\left(-R_C^2 + R_D^2 - T_C^2 + T_D^2\right) + R_C^2 + R_D^2 + T_C^2 + T_D^2} \tag{VI.54}$$

The effect of the two PBSs on the contrast is shown in Figure VI.5. The ideal case is obtained considering the PBS matrices shown in Table VI.1.

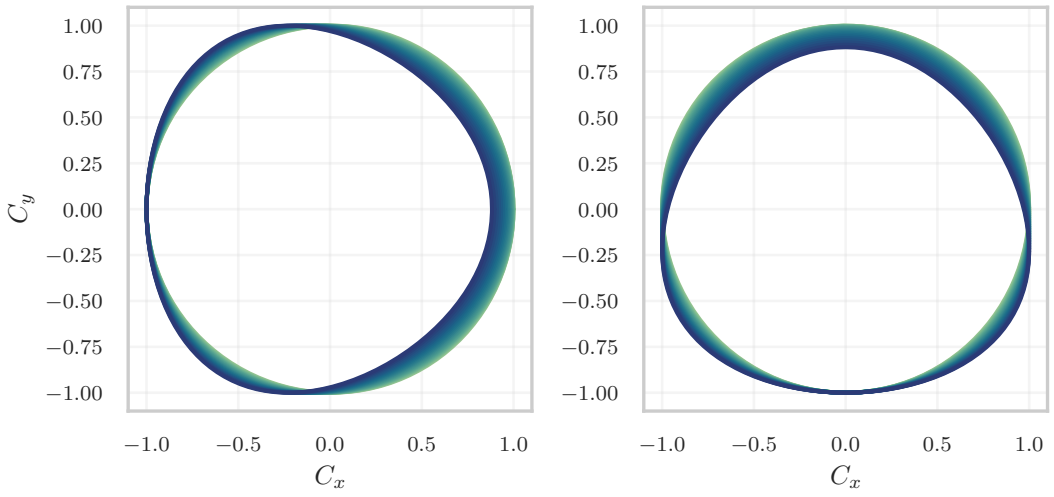

Figure VI.5: Effect of the polarization mixing in PBS3 and PBS4 (see Figure VI.1). The figure was obtained from the parametric equations (VI.53) and (VI.54). (left) Here, the extinction ratio T_B/T_A is changed from a minimum value of 10^{-3} to a maximum value of 10^{-1}. T_A is assumed to be 0.95, a value consistent with the values measured in the laboratory. The contrast primarily deforms along the x axis because photodiodes A and B contribute to generating the contrast C_x. (right) In this plot, T_C/T_D is varied from a minimum value of 10^{-3} to a maximum value of 10^{-1}. Here, the opposite effect can be observed, with the contrast changing its shape along the y axis.

VI.4. Losses correction

By employing a QPDI interferometer, as discussed in the previous section, the imperfections of the optical elements used must be considered. Two possible methods are presented here for evaluating and correcting the examined optical imperfections. The first approach involves characterizing each optical element individually and incorporating the variables into the final formulas of the contrast (C_x and C_y shown in §VI.3 for each case). The second method involves post-processing correction of the signals recorded by the photodiodes.

VI.4.1. Optical parameter estimation

Measuring the parameters of individual optical components offers the advantage of providing the most accurate representation of the optical system. However, this method is susceptible to misalignment issues. Misalignments can cause the beam to enter the optical elements at angles different from the ideal, leading to deviations from the expected behavior. In such cases, the beams may be reflected or transmitted at slightly different angles than anticipated, partially invalidating the detailed characterization of the elements. While it is possible to perform characterizations at different angles, this would significantly complicate the measurements, as each realignment would require a new set of angle-specific measurements. In an attempt to characterize the system, both the BS and the two PBSs in the detection path are evaluated in a particular alignment configuration, aiming to ensure that the beam is as perpendicular to the optical elements as practically achievable.

The characterizations revealed that both PBSs exhibit an extinction ratio on the transmission of $T_s/T_p = 1 \cdot 10^{-3}$ and $R_p/R_s = 2 \cdot 10^{-2}$ on reflection. Concerning the BS, the measured parameters are γ=46%, δ=42%, $\alpha = 54\%$ and β=58%. In the interferometer calibration process, as further elucidated later in this discussion, the reference mirror of the interferometer is moved using a piezoelectric actuator. During this movement, the optical phase, primarily dependent on Δl, traverses the entire interference fringe, allowing fitting of the entire ellipse to calculate the parameters (VI.25) and (VI.26). In Figure VI.6 (left), the interferometer calibration is shown, illustrating a noticeable effect resulting from the unbalanced BS in the detection area, as discussed in §VI.3.2. The calibration includes a correction that incorporates the measured optical parameters. The final formulas for C_x and C_y, accounting for all the effects outlined in §VI.3, are not provided due to their length.

VI.4.2. Post processing correction

As an alternative to the previously described method, the decision is made to correct the signals when combining them to extract quantities VI.17 and VI.18. This approach eliminates the need for measuring optical component parameters. The starting point is the consideration of Equations (VI.23) and (VI.24). As mentioned, the ideal scenario is when η and ρ are equal for each pair of photodiodes. By computing the sum signal between the two pairs from the signals recorded by the four photodiodes, an ideal case should result in a constant signal. Figure VI.7 illustrates the output of the photodiodes recorded during a full fringe elongation of the reference arm, achieved by manipulating the piezoelectric actuator on the mirror's back (see §VII.1.7) The green curve in the figure illustrates the sum of the two signals, which is not constant. To address this, the analysis involves comparing the reading of one photodiode with respect to the other within the same pair. The oscillations reveal that the intensities read by photodiodes B and C are lower compared to the other photodiodes in each pair. This discrepancy is calculated by plotting one photodiode's intensity against the other one (I_A vs I_B and I_D vs I_C), as shown in Figure VI.8. The slope of the linear fit provides the value by which we must multiply or divide the intensity of either photodiode to maintain a constant sum. Figure VI.9 shows the comparison of the data corrected with the described procedure. The acquired data are the same as those used in the previous example, but in this case, the calibration contrast reproduces a circle ($X = Y = 0.923$ and 5 mrad of precession). This procedure for calibrating the readout

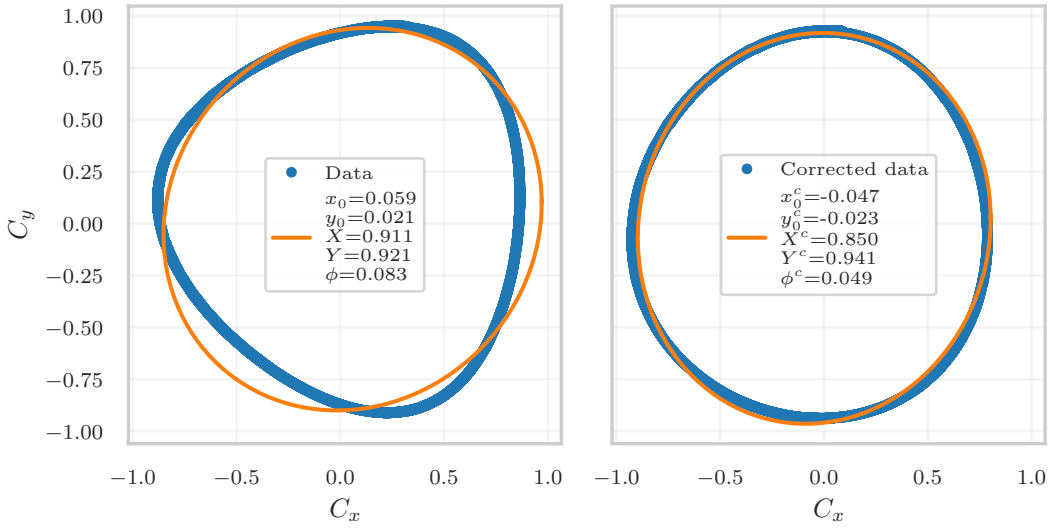

FIGURE VI.6: (left) The calibration is presented using raw data obtained from the photodiodes (blue dots). The orange circle represents the best-fitting ellipse based on these data. It is evident that the fitting line poorly reproduces the data. The ellipse parameters are also displayed. (right) Plot of the data corrected according to the procedure described in §VI.4.1. The agreement between the fitting line and the corrected data is significantly improved, although some residual discrepancies persist as the data do not perfectly align with a standard ellipse.

is used in the following chapter §VII to infer the vibration fluctuations of the oscillator under study.

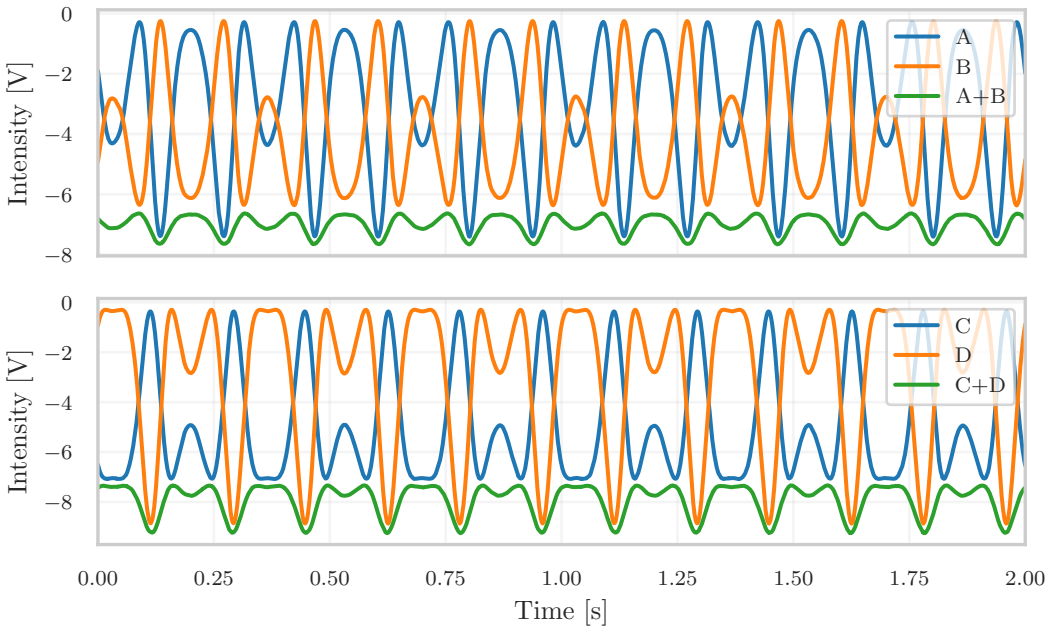

FIGURE VI.7: (top) Signals read by the photodiodes A and B, and their sum during the piezo motion at 3 Hz. (bottom) Same representation for PDs C and D.

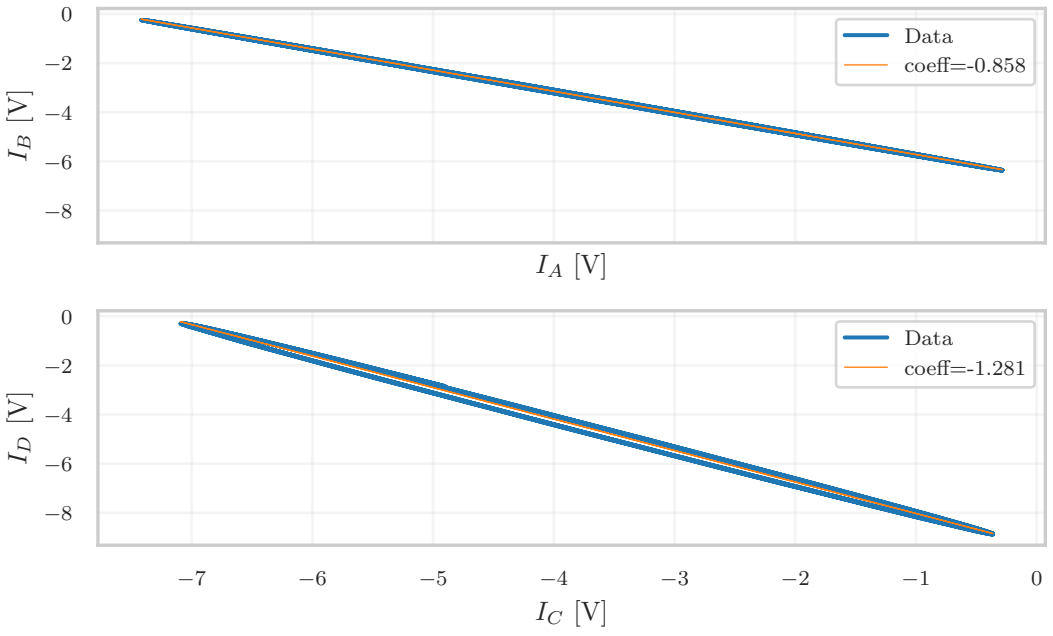

FIGURE VI.8: (top) Plot of the readings of PD B vs that of PD A (blue dots). The orange line is the linear fit, resulting in the slope shown on the label. (bottom) Same representation for PDs C and D. The small hysteresis shown is due to a non-perfect tuning of the QWP before the couple C and D.

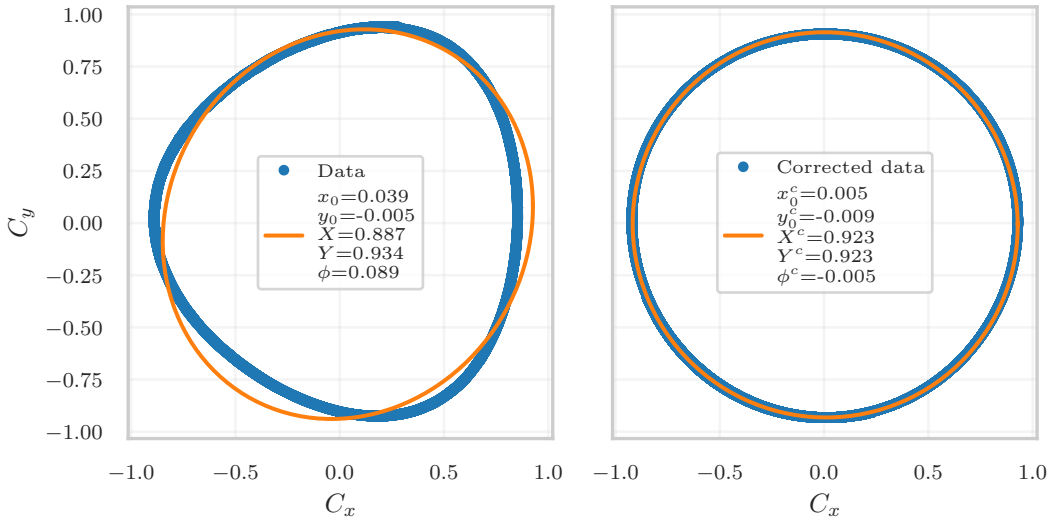

FIGURE VI.9: (left) Calibration performed using the raw data recorded from the photodiodes (blue dots). The orange circle represents the best-fitting ellipse based on these data. It is evident that the fitting line poorly reproduces the data. The parameters of the ellipse are also reported. (right) Plot of the data corrected according to the procedure described in VI.4.2. In contrast to the previous case, now the contrast exhibits a circular shape.

VII | NON-EQUILIBRIUM THERMAL NOISE EXPERIMENT

In this chapter, the experiment designed to replicate the results of RareNoise and expand upon them by inducing more consistent thermal gradients is described. This experiment focuses on the thermal vibrations of the same acoustic modes of the same aluminum body as RareNoise. With respect to the latter, the main difference is the readout, which is discussed in detail in the previous chapter (§VI). The experiment is housed in a vacuum chamber equipped with a mechanical suspension that was developed as a prototype for RareNoise and shares same the data acquisition system; the data analysis has been rewritten and extended firstly in Matlab and then in Python. This chapter provides a detailed account of the experimental apparatus, the methodology employed for data analysis, and the performed measurements.

VII.1. Experimental setup

The NETN experiment is meant to reproduce the results of the RareNoise experiment [81] with the integration of a new QPDI readout system (§VI.1). Figure VII.1 illustrates the removal of the fixed capacitor plate, distinguishing it from the configuration of RareNoise. Utilizing the mirror-like finish on the lower surface of the cuboid mass, the capacitive readout is modified using light fields, with the polished surface serving as the moving mirror for the interferometric readout.

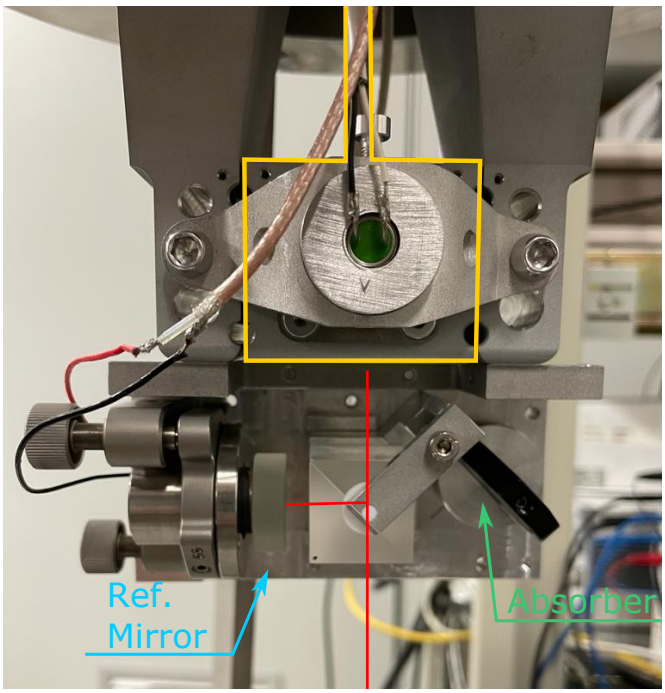

Figure VII.1: Picture of the core part of the NETN experiment: attached at the 2 lateral protrusions, the plate can be seen with the optics necessary for the QPDI: at the center sits the PBS (PBS2 in Figure VII.7), at its left the reference mirror (light blue arrow) attached to a piezoelectric actuator, at the right an absorber plate (green arrow), at the top the oscillating cuboid mass (highlighted in yellow). This is faced by the heater, shown with a green circle.

VII.1.1. The oscillator

The vibrational analysis involves examining the resonant mode of a monolithic aluminum piece (Alloy Al5056). This piece comprises a rod aligned parallel to the vertical axis, with one end bearing a cuboid mass and the other end linked to a thick plate featuring lateral protrusions (see Figure VII.2). This body is then fixed with screws to a heavier, rigid mass. The focus of the study is on the first longitudinal resonant mode of the aluminum piece, wherein both the rod and the cuboid mass at its base oscillate along the axis of the rod. Specific details regarding the characteristics of the oscillator are provided in Table VII.1. The two lateral protrusions support the optics necessary for the QDPI readout at its bottom (see Figure VII.1): in particular, the PBS, the reference mirror actuated with a piezoelectric and an optical absorber on the other port of the PBS. Furthermore, the protrusions support a thermal radiation source (named heater) facing the cuboid mass to heat it and an IR thermometer (a thermopile) facing the cuboid mass at the opposite side of the heater. This assembly (the aluminum piece with optics, heater, and thermopile) is supported on top of a 3-stage mechanical suspension (described in more detail in §VII.1.3, see also [88]). At its top and coaxial with the rod, a piezoelectric actuator is

Oscillator characteristics	
Rod	
Length	10 cm
Width	0.55 cm
Cross section area	0.25 cm^2
Cuboid mass	
Length	4.35 cm
Width	5.15 cm
Thickness	4.00 cm
Volume	90 cm^3
Mass	0.25 kg
Studied resonant modes	
Longitudinal	$\sim$ 1400 Hz
Transversal	$\sim$ 320 Hz

Table VII.1: In the table are reported the main characteristics of the aluminum oscillator.

placed. All this is housed in a vacuum chamber. Vacuum chamber and mechanical suspensions are reused from prototype setups of RareNoise. The chamber consists of an aluminum hollow cylinder with an internal diameter of 300 mm. The upper part is closed with a 400 mm-diameter x 40 mm high aluminum disk, while the base, is composed of a 70 mm high aluminum plate, and has holes that allow connection to the vacuum system. At the center of the base disk, a 2-inch optical window is housed: this allows the laser light to arrive at the PBS2 and then back towards the detection area (see Figure VII.7). The entire chamber is raised from the optical bench through three 150 mm-long pillars arranged around the circumference and spaced every 120 degrees.

VII.1.2. Heating

To investigate thermal noise outside thermodynamic equilibrium, the cuboid mass is heated to induce a thermal difference ΔT between its upper and lower parts (refer to Figure VII.2). The heater consists of a 3.6 Ω resistor that has a maximum power output of 5 W. Through the Joule effect, it emits radiation as a black body at a temperature determined by the circulating current. Approximately 80% of the radiated power is effectively transferred to the heating target [89]. The resistor is positioned at the focal point of a parabolic mirror, which redirects all the emitted radiation toward the cuboid mass of the oscillator. When the heater is on, the aluminum mass takes 20 hours to reach a steady state [90]. The temperatures of both the cuboid mass (T_{max}) and the upper end of the rod (T_{min}) are monitored using thermometers (a thermopile for the cuboid mass and an NTC thermistor for the top of the rod). The thermopile, by making a differential measurement, measures the temperature of the thermopile case itself, which for monitoring purposes is named T_{amb}, and that of the mass. When the oscillator reaches the non-equilibrium steady state, it results in a gradient ΔT of no more than 50 K along the rod. The average temperature between the rod and the extremes can be considered as:

$$T_{avg} = \frac{T_{max} + T_{min}}{2} \tag{VII.1}$$

VII.1.3. Passive mechanical filters

While operating in a vacuum environment can effectively eliminate acoustic noise, the mitigation of ground vibrations necessitates the implementation of mechanical filters. In addition, the optical bench is supported by pneumatic legs, which function as filters. In the vertical plane, the filter is active, while in the horizontal plane, it acts as a passive pendulum-based filter. A mechanical filter is a mechanical oscillator that resonates at a significantly lower frequency than the frequency of the phenomenon under consideration. In the context of the specified

objectives, the main constraint for the suspension system is to enable the detection of thermal vibrations from the 0.2 kg oscillator. It is important to note that, throughout the subsequent discussion, the combined system of the rod and cuboid mass is denoted as the 'oscillator.' This nomenclature is adopted due to a predominant focus on the first longitudinal mode of this mechanical structure. The lowest relevant frequency corresponds to the first transverse mode of the oscillator $\nu_0 \sim 320$ Hz. An input vibration of the mechanical filter is depressed by a factor [88]:

$$H(\nu, \nu_0) = \frac{\nu_0^2}{\nu_0^2 - \nu^2} \tag{VII.2}$$

where $H(\nu, \nu_0)$ is the transfer function of the filter. The suspension used in the NETN experiment was built as a prototype for the RareNoise experiment and its design is fully described in [88]. It consists of a cascade of 3 stages of filtering (see Figure VII.2. Each stage is formed by a set of 3, c-shaped aluminum springs (AI7075) connected in parallel to a stainless steel (AISI 304) annular mass; the 3 stages are mounted on top of each other; the oscillator assembly is fixed on top of them, and mounted in such a way that the rod is coaxial with the annular masses and inside them and the cuboid mass is at the bottom, at a level between the first set of springs and the first annual mass. The last stage allows for attaching an aluminum flange that supports the oscillator assembly. Table VII.2 lists the characteristics of the main elements composing the suspension system. To avoid interfering with the thermal noise measurements, the internal modes of the suspension must have frequencies exceeding 2 kHz. These parameters are used in §VII.4.1 to simulate the behavior observed during the measurement of the system transfer function. The suspension design is also done with the aid of Finite Element Analysis (FEM)

Suspension characteristics		
Element	Mass [kg]	1^{th} internal mode [Hz]
C-shape spring	0.0017	5306
Annular mass (stage 1, 2)	17.4	2185
Annular mass (stage 3)	13.8	1544
Al flange	2.4	2215
Osc. assembly	3.6	3016

Table VII.2: Main elements forming the suspension and the payload (Al flange + Oscillator + Osc. assembly).

to optimize the dimension in relation to the filtering performance and the mechanical stress. The result is shown in Figure VII.3 where there are few resonances due to acoustic modes up to 70 Hz followed by a smooth roll-off at ν^{-6} as expected from the cascade of the three stages. The expectation values are compared with the experimental measurements where the system was mechanically excited. The measurements were performed using an accelerometer positioned above the last stage and the system was excited by using a vibration exciter.

As previously mentioned, the oscillator resonates at a longitudinal frequency of around 1.4 kHz under room temperature conditions, and it demonstrates a mechanical quality factor Q ranging from 10^3 to 10^4.

VII.1.4. Vacuum system

The entire system, comprising the oscillator assembly and suspension, is kept in vacuum. This measure is implemented to isolate the system from acoustic vibrations, residual gas noise, which might interfere with thermal noise measurements, and to achieve thermal isolation. Due to the mechanical vibrations produced by vacuum pumps, including scroll and turbomolecular pumps, which need to be avoided, thermal noise measurements are conducted exclusively using an ion pump. Conversely, ion pumps operate effectively only in high-vacuum conditions. Therefore, a series of pumping steps is necessary to transition from atmospheric pressure to the low-mechanical noise state achievable with the ion pump. A schematic of the vacuum system is shown in Figure

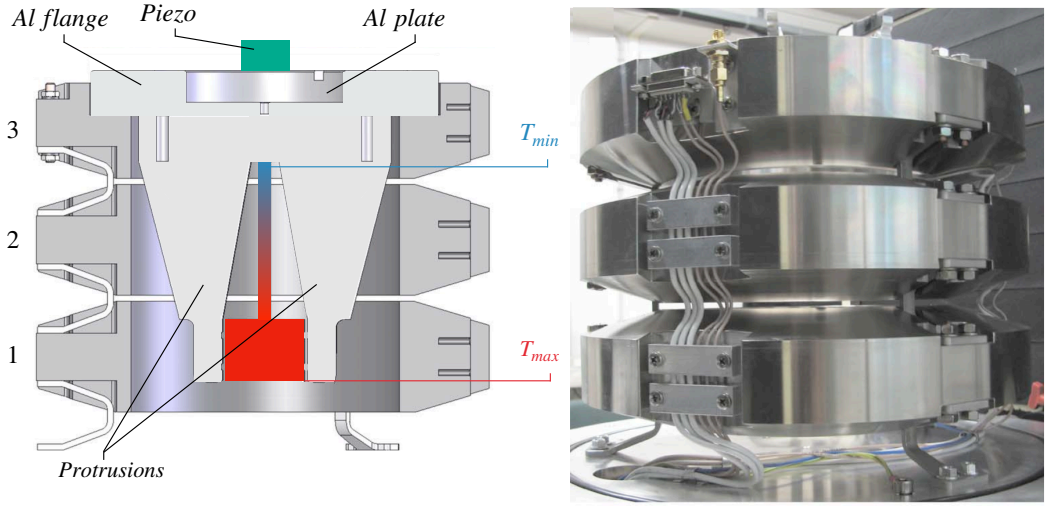

FIGURE VII.2: From [88]. (left) Schematic cross-section of the system oscillator assembly + suspension. The oscillator assembly is shown in light grey while the rod and cuboid mass are colored from red to blue to show the thermal difference present when the non-equilibrium steady state is present (hotter parts in red, colder parts in blue). Here, the oscillator assembly refers to the capacitive readout used in the RareNoise experiment: in the work reported in this thesis the capacitor plate at the bottom part of the oscillator assembly is replaced by the optical assembly shown in Figure VII.1. The figure shows the three stages of the passive mechanical filter connected by the C-shape springs. At the top of the last stage, above the Al flange, the piezo actuator used to measure the transfer function is depicted. (right) Picture of the three stages with the system mounted. Outside are visible the measuring instrument cables anchored to the suspension and soft enough not to bypass the mechanical filter. For the work reported in this thesis, the cabling is slightly different but substantially equivalent.

VII.4. The system is divided into three main parts separated by valves: the first one includes the scroll and the turbo pump, the second one the ion pump, and the volume that connects the first part to the third part. Three vacuum gauges (Oerlikon Leybold Vacuum D-50968) are used to monitor pressure in each of these three parts. The first is positioned at the head of the turbo molecular pump, the second in the connecting volume between the various pumps and the vacuum chamber, and the last at the chamber exit port.

Pre-vacuum

The first pumping step is carried out with a scroll pump. This belongs to the pre-vacuum distribution line and is connected to the optical bench on which the experiment is placed through a flexible vacuum pipe. Initially, the entire volume of the chamber and the volume of the vacuum system go from atmospheric pressure down to a pressure of 10^{-1} mbar in a few minutes.

Turbo pump

The second step is to turn on the turbo molecular pump (Varian 969-8902). Typically the pressure reaches the 10^{-6} mbar level in about 24 hours. The pressure level achieved would be sufficiently low for thermal noise measurements. However, as previously mentioned, the concurrent mechanical vibrations arising from the combination of turbo and scroll pumps are intolerable.

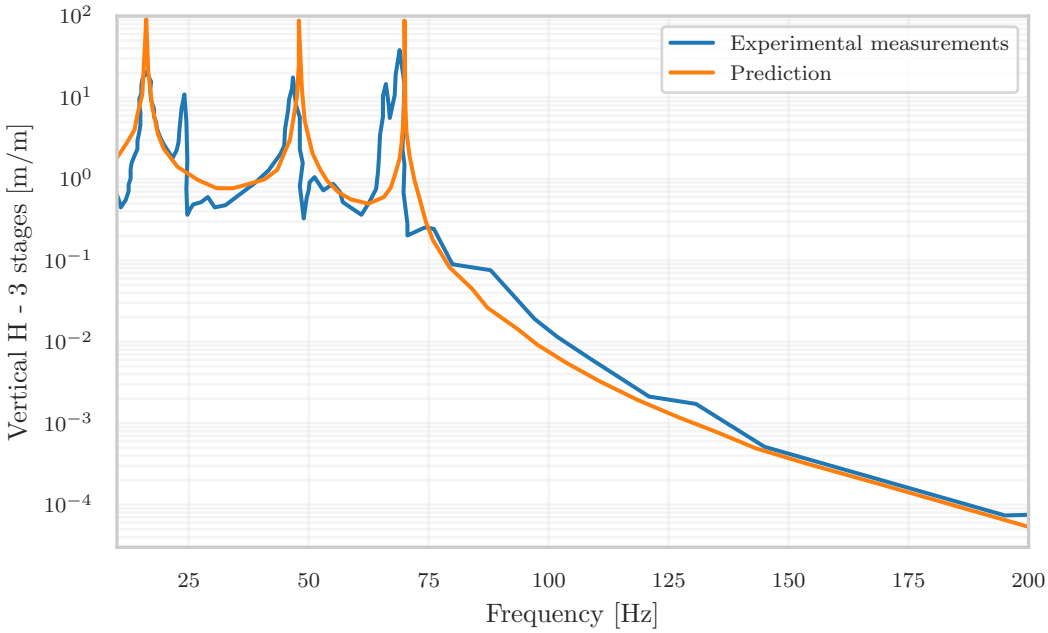

FIGURE VII.3: Plot taken by [88]. The vertical transfer function of the full suspension, consisting of a cascade of three stages each resonating at ν_0=38 Hz. The prediction curve is obtained from the coupling in a cascade of three oscillators of masses, respectively, 17.4, 17.4, and 19.8 kg.

ION PUMP

The indication that the ion pump can be turned on is given by the pressure inside the chamber, as it consistently maintains a level approximately three times higher than that observed in the remainder of the system. Upon achieving a stable pressure of approximately 7×10^{-6} mbar within the chamber, as monitored by gauge 3 in Figure VII.4, the ion pump (initially an Agilent Vaclon Plus 20, later replaced with an Agilent Plus 75) is activated. Subsequently, Valve 2, positioned adjacent to the ion pump, is opened to allow simultaneous pumping by both the ion and turbo pumps. In this configuration, the reading on gauge 2 swiftly decreases to below 10^{-7} mbar. Once pressure stability is attained, the valve that connects the turbomolecular pump to the system can be closed (Valve 1), so that the chamber is pumped with the ion only. At this stage, a gradual pressure increase is observed due to the reduced total pumping speed, reaching a stabilized state after approximately 8 hours at an average pressure of 5×10^{-6} mbar. Subsequently, the pressure undergoes a decline, ultimately stabilizing around 8×10^{-6} mbar, as indicated by gauge 3. Once the chamber is pumped by the ion pump, achieved by closing Valve 1, both the turbo pump and the scroll pump are switched off. Then, the vacuum pipe connecting the turbo pump and the scroll is disconnected, effectively isolating the optical table from external vibrations. The entire procedure in terms of pressure, read by the vacuum gauge 3, is summarized in Figure VII.5.

TROUBLESHOOTING

Throughout the duration of this experiment, achieving a stable state where the vacuum chamber is solely pumped by the ion pump has consistently posed a non-trivial challenge [90][89] In certain periods preceding the commencement of this study, this state remained elusive. To address this issue, a series of tests were conducted to identify potential causes, starting with degassing tests for various system volumes in the absence of a leak detector. Over the course of this thesis, the system underwent multiple cleaning procedures, with the replacement of malfunctioning

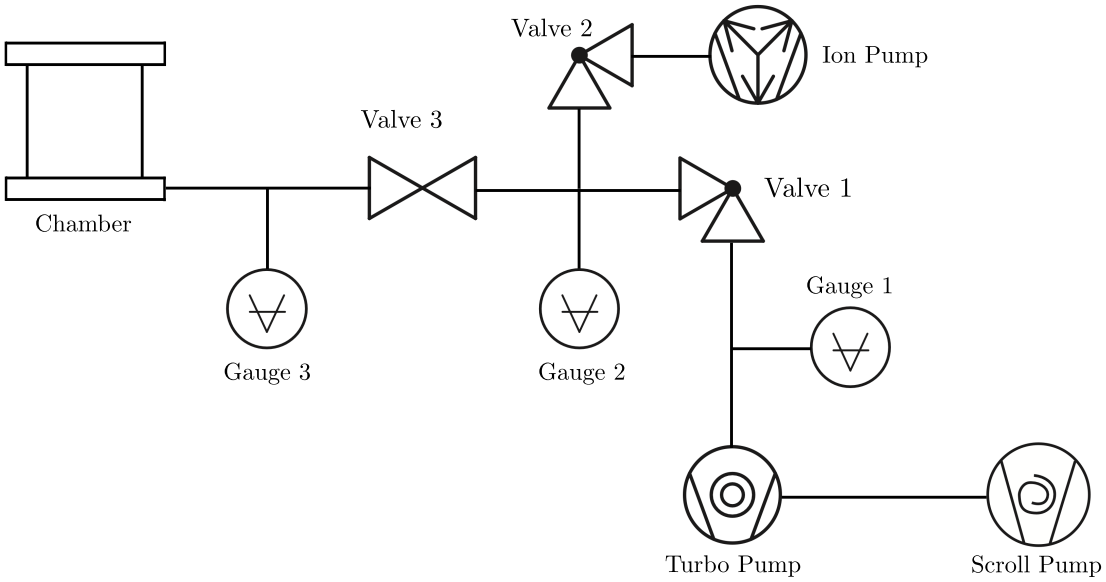

FIGURE VII.4: Scheme of the vacuum system. The vacuum level to switch on the ion pump is achieved with the turbomolecular pump with a scroll pump for the pre-vacuum in cascade. The pressure level is measured by three vacuum gauges at three different points of the system.

components such as flanges and valves. Additionally, both the ion pump and segments of the vacuum chamber underwent several baking processes. This involved the installation of a heater around the ion pump body and heating pads on the entire system to expedite the degassing of elements deposited on internal surfaces.

Despite all these operations, it was not always possible to reach the state where the system is pumped stably by the ion pump only. Ultimately, the ion pump was replaced with a model featuring a larger pumping speed. This intervention proved highly effective, resulting in an upgrade from a pump with a pumping rate of 20 l/s to one with an increased pumping rate of 75 l/s. Even after this replacement, baking remains a necessary and effective procedure, whenever the chamber is opened and exposed to atmospheric pressure for extended periods. The baking procedure, based on the datasheet of the pump, is summarized below:

1. Heat the ion pump with a custom-shaped resistor that surrounds the pump body. The resistor has no power adjustments but connects directly to the electrical plug. The vacuum system is heated with three resistive pads (12 W) connected to a power supply set at 30 V - 1 A.

2. Bake ion pump and vacuum parts at the same time. The ion pump is switched off while the system is pumped with the turbo for at least 12 hours.

3. Switch on the ion pump while everything is hot with the turbo valve still open to continue pumping with the turbo pump. The pressure should increase because of ion pump outgassing.

4. Continue heating and pumping with both the ion pump and turbo pump until the vacuum improves to the same level as the end of the initial 12-hour period.

5. Close the turbo valve and continue pumping with the ion pump, while still heating both the ion pump and the chamber.

6. Pump for at least 6 hours, or longer, until the pressure stops decreasing.

7. Switch off the heater of the ion pump body, while continue heating the chamber. Let the ion pump cool while pumping the hot chamber for at least 6 hours.

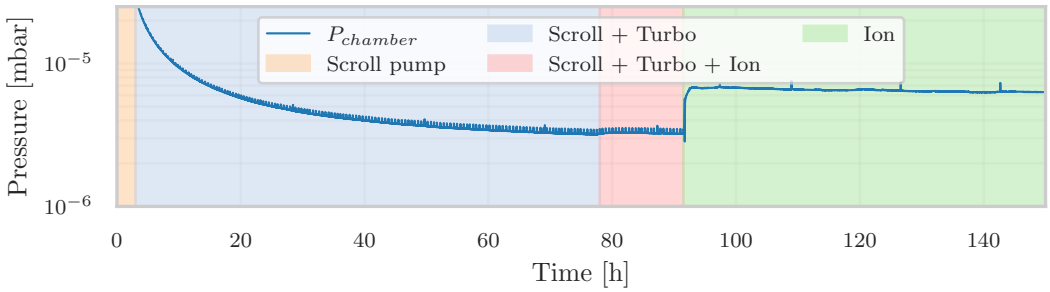

FIGURE VII.5: The temporal evolution of the pressure within the chamber, as monitored by gauge 3, follows a typical trend, commencing from atmospheric pressure and gradually decreasing to below 1×10^{-5} mbar, exclusively through the ion pump. The different colored areas represent different steps of the procedure. The orange area corresponds to the pre-vacuum step. In the light blue, the turbo pump is switched on to reach the vacuum level to turn on the ionic (red area). In the green region, the ion pump managed the vacuum in the chamber alone.

8. Switch off the heaters in the chamber and let the whole system cool down.

VII.1.5. Optical layout

The working principle of the interferometric readout, based on a QPDI technique, is discussed in detail in chapter §VI.1. Here, details are provided regarding the laser source and its coupling with the optical readout. The experiment employs a Nd:YAG CW laser source (model Mephisto by Coherent). Before the work reported in this thesis, the laser source was shared with another experiment: the head was located on a different optical table and a pick-off of approx 10 mW was brought onto the NETN experiment via a polarizing maintaining optical. During the work for this thesis, the laser source is relocated to the NETN bench, eliminating the need for an optical fiber. A new telescope is designed to align the beam size with the setup. Subsequently, the exiting beam from the laser source is characterized, with the corresponding data presented in Figure VII.7. As can be seen from the Figure VII.6, the measurements are performed only outside the Rayleigh range, where the beam width scales linearly with the propagation distance. Hence a linear fit is done to infer the laser waist and its distance from the laser head. Next, using the JamMt software, the lens system is designed to collimate the beam. In the initial phase of this thesis work, the configuration of the two-lens telescope was adjusted to yield a waist of approximately 0.75 mm, situated at the lower surface of the oscillator, which is placed about halfway between the laser head and the detection area. This choice ensured that the beam did not diverge too much for the entire optical path (1.5 mm radius on average) and that the laser spot was not too large at the photodiodes, which have a sensible area of 4 mm in diameter. Subsequently, for the reasons discussed in §VII.3.3, the telescope is modified by adding a lens. The final waist position is moved close to BS1 after oscillator reflection and has a size of about 1 mm.

VII.1.6. Acquisition system

The data acquisition system is based on the National Instruments PXI platform. The signals from the four photodiodes (named 'fast' channels) are read using a 24-bit resolution ADC NI PXI-4462 DAQ board, which operates at a sampling rate of 8000 samples per second within a range of ±10 V. Temperature sensor data, like thermistors and thermopile readings, as well as vacuum gauge readings, are acquired at a sample rate of 1 sample per second (named 'slow' channels). This data acquisition is performed through NI 9219 24-bit analog inputs. VIs (Virtual Instrument) have been developed for both types of data within PXI. These are scripts

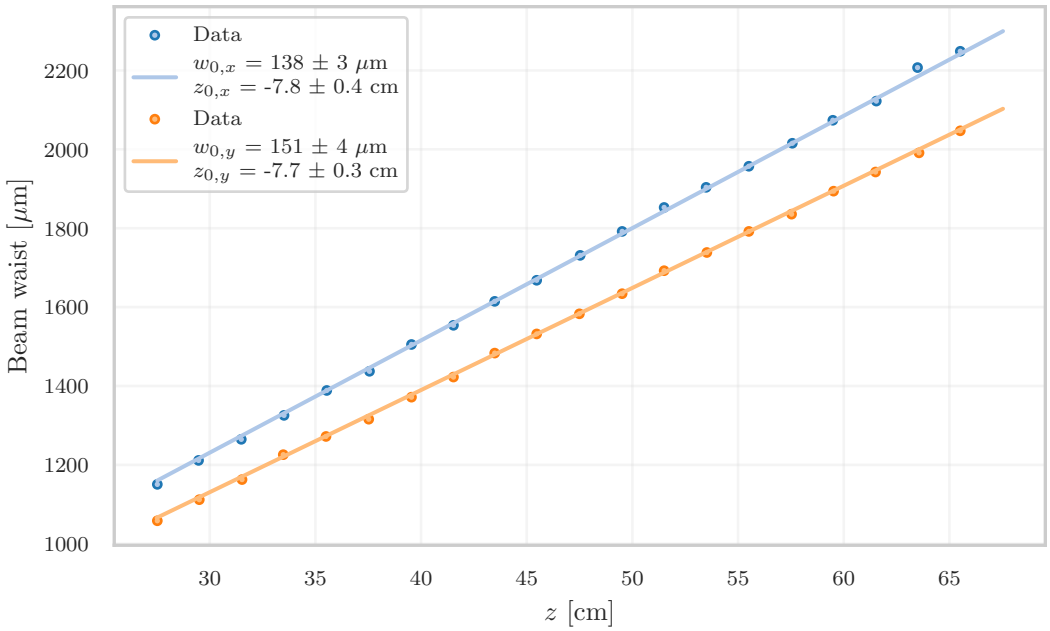

FIGURE VII.6: Beam Laser Characterization. The scatter plot displays the beam radius values recorded by the beam profiler in the transverse plane (xy, respectively horizontal and vertical axis), along the propagation axis z. The z-axis origin point $z = 0$ mm is the laser head's exit port. Data fitting was accomplished using the Gaussian beam propagation formula.

in the Labview programming language that allow both real-time visualization of the data (e.g., graph of temperature over time) and saving of the data. The programs of the data acquisition are inherited from the RareNoise experiment which used the same PXI hardware. Significant modifications have been implemented in the online data visualization, primarily to align with the interferometric readout instead of the capacitive method. These adjustments enhance the utility of the online system, particularly during the preparatory phase of alignment (refer to §VII.2). Four custom photodiodes powered at ±15 V are used to measure the laser intensity. These are calibrated by first measuring the input power with a power meter and then reading the output voltage with a multimeter. Subsequently, the input power is increased so that the whole dynamic range could be explored (0 V - -11 V). The data are then fitted to obtain a conversion factor. The conversion factors are reported in the Table VII.3

PHOTODIODES CHARACTERIZATION	
Photodiode	Conversion factor [mW/V]
PD_A	-0.214
PD_B	-0.214
PD_C	-0.216
PD_D	-0.217

TABLE VII.3: Table of the conversion factors of each photodiode obtained by a linear fit.

VII.1.7. PIEZOELECTRIC ACTUATORS

During the work of this thesis, and in response to needs that emerged from past work, two piezoelectric actuators are installed in the setup: one to allow moving the working point of the ITF by a full fringe by acting on the reference mirror and hence calibrating the QDPI and one

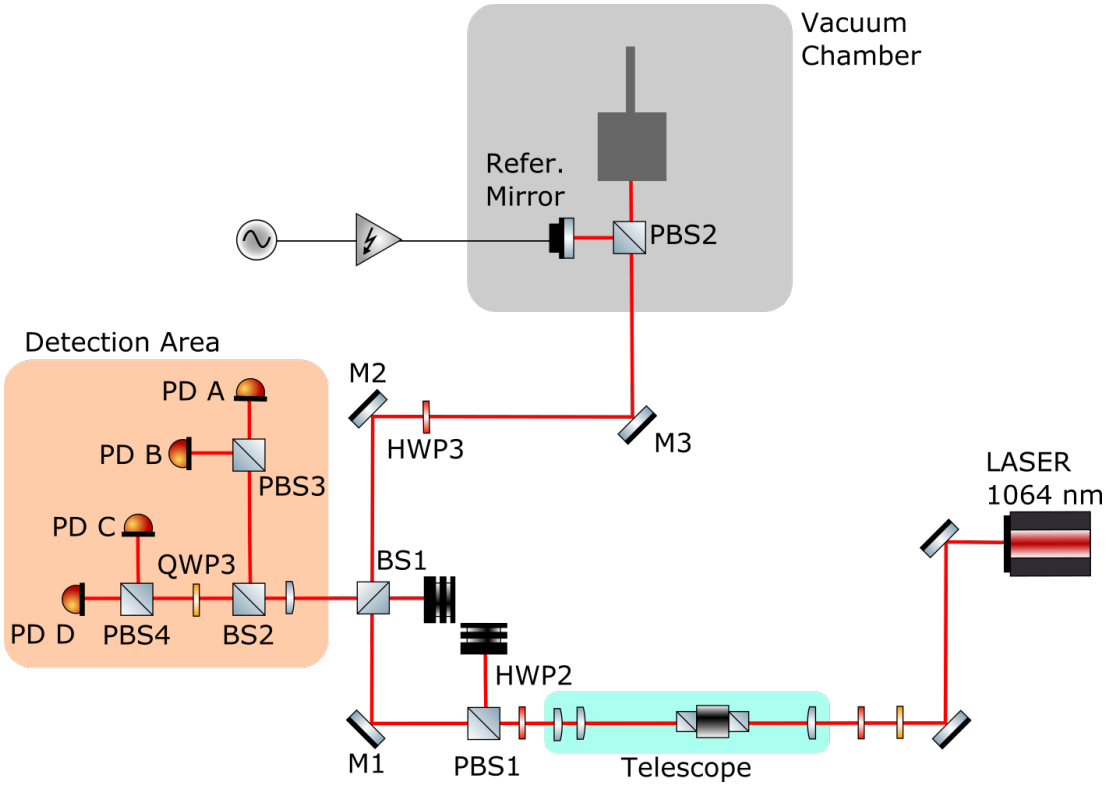

FIGURE VII.7: Optical layout of the NETN experiment. The beam exiting the laser head is initially collimated with a telescope. The light power sent to the experiment can be controlled via the combination of HWP2 and PBS1. The beam is then sent inside the vacuum chamber where the readout interferometer is located. The light beam coming back from PBS2 is reflected by BS1 and directed toward the detection area where the readout PDs are located. Note that the mirror M3 sends the beam vertically toward the oscillator.

to mechanically excite the oscillator along the vertical axis to measure its transfer function.

MIRROR ACTUATOR

As already anticipated in §VII.1.1, one piezoelectric actuator is mounted on the reference mirror, shown in Figure VII.1. The purpose of this actuator is to move the working point so as to allow spanning a full interference fringe and hence calibrate the readout according to the procedure described in §VI.1.4. Before mounting the piezo on the setup, its characterization is conducted. Upon attaching the mirror to the actuator and mounting the assembly on a standard mirror mount, a simple Michelson interferometer is established. In this configuration, the displacement of the mirror is calibrated as a function of the voltage sent to the piezo actuator. This procedure is done near the frequencies of the two transverse and longitudinal modes of the oscillator, see [91]. The calibration is focused mainly on the response of the piezo to the resonance frequencies of the two longitudinal and transverse modes of oscillation. This results in two conversion factors of $C_{1400\text{Hz}} = (1.96 \pm 0.04)$ nm/V and $C_{320\text{Hz}} = (1.74 \pm 0.03)$ nm/V.

PIEZOELECTRIC ON THE SUSPENSIONS

The second piezoelectric actuator is installed centrally and on top of the mechanical system, i.e. on top of the 3rd mechanical filter and along the vertical axis (see Figure VII.2). The PZT serves the dual purpose of exciting the mechanical system and measuring the corresponding transfer function, both around the resonance of the longitudinal mode and in a broader frequency range. To enhance the applied force, a mass of 21.52 g is affixed to the top of the PZT. The

initial characterization of the piezo involved its assessment on the optical bench, utilizing an accelerometer (PBC-353B33) as the mass undergoing acceleration due to the actuator. Before incorporating the actuator into the experiment, its calibration is conducted using an accelerometer (PBC-353B33) with a sensitivity of $S = 10.398 \cdot 10^{-3}\ \frac{\mathrm{V}}{\mathrm{m/s^2}}$. Instead of the mass m, the accelerometer is placed atop the PZT, which is then secured to the bench. Utilizing the mass of the accelerometer (24.20 g, so very similar to m) and the measured acceleration, the calibration of the PZT is achieved through the following relationship:

$$|x| = \frac{V_s}{S \cdot \omega^2} \tag{VII.3}$$

where V_s is the amplitude of the sinusoidal signal of frequency ω fed to the PZT; VII.8 shows the calibration coefficients measured at different signal frequencies. Due to the limited actuation coefficient of this PZT, it is not feasible to achieve a complete fringe elongation for the cuboid mass, preventing the calibration of the QDPI. Both the utilization of a high-voltage signal generator and the addition of a higher mass m on top of the PZT are impractical. The latter option is constrained by the limited space available between the PZT and the top of the vacuum chamber.

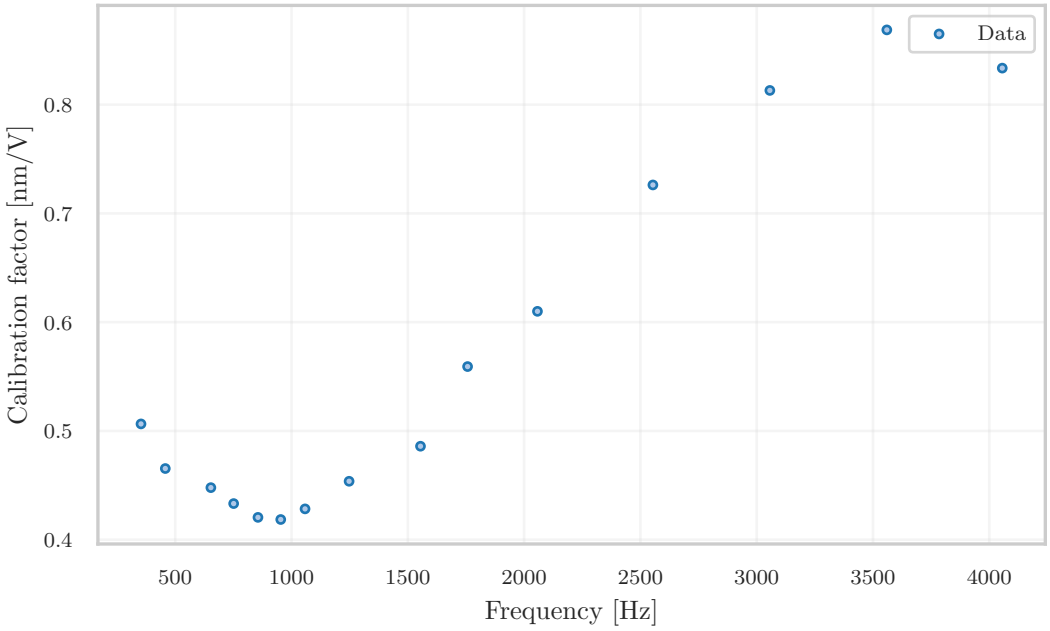

FIGURE VII.8: Different responses of the piezo in terms of displacement of the mass. The actuator efficiency changes by about 0.4 nm/V.

VII.2. CALIBRATION AND MEASUREMENTS

This section outlines the experimental procedures for aligning the interferometric readout, conducting its calibration (also detailed in §VI.1), and executing thermal noise measurements. The objective is to establish a fully calibrated system, enabling the inference of noise temperature without relying on assumptions about unknown parameters. This approach contrasts with common practices in measurements such as AFM. This calibration effort constituted a significant portion of this thesis work, and consequently, most of the reported measurements pertain to the equilibrium state.

VII.2.1. Alignment

The calibration of the interferometer must be performed before each measurement. Before proceeding with these two operations, it is necessary to prepare the system and do some checks. The initial step involves verifying that the beam is transmitted in the chamber and back-reflected by the oscillator. Because the oscillator does not have a degree of freedom that can be adjusted there are only two optical components to play with: the steering mirrors M2 and M3 (see Figure VII.7). To allow the beam to arrive at the bottom surface of the oscillator with a 0° incident angle, the HWP3 is rotated so that all the polarization is $\hat{p}$ and all the beam is transmitted by PBS2. Then, the two steering mirrors are moved so that the forward and return beams from the chamber overlap at BS1. Subsequently, the HWP3 is rotated to project the polarization onto $\hat{s}$ so that the beam is completely reflected to the reference mirror. During the initial coarse alignment, a check is conducted to ensure that the forward and reverse beams overlap. This assessment is carried out by manipulating the degrees of freedom of the reference mirror. It is important to note that this initial alignment phase is performed with the vacuum chamber open, specifically with the top part and the tube removed. By rotating the HWP3 again to have linear polarization at 45°, the quality of interference at the photodiodes can be checked. The overlapped beams are centered on the photodiodes by first using the BS2 degrees of freedom and then moving the PBSs (3 and 4) of the two pairs of photodiodes. Fine alignment of the interferometer can now be performed using the reference mirror and visualizing the live signals on the PXI screen. The data acquisition system combines the readings from the 4 photodiodes, computes online the contrast C_x and C_y (see also §VI.1), and displays in real-time a plot similar to Figure VI.2. Furthermore, a fit, as discussed in §VI.1.3, is executed, and the parameters of the ellipse are then displayed on the screen. The contrast level (given by the parameters X and Y of the equations (VI.25) and (VI.26)) is an excellent indicator of alignment because maximizing them optimizes both the alignment between the two interferometer paths and the centering of the photodiodes. Figure VII.9 shows what the PXI-base data acquisition system displays during this phase. The parameters in the red rectangle of the figure are used by the script to produce a real-time power spectral density of the interferometer displacement (Figure VII.10) to see if there are any anomalies (spurious peaks, high levels of high-frequency noise, etc.) before the measurements.

VII.2.2. Calibration and data acquisition

Before the actuator was installed on the mirror (§VII.1.7), the alignment and the calibration were performed by two different methods: by hitting manually the vacuum chamber and by feeding some power to the oscillator heater (§VII.1.2), both meant to induce a movement of the oscillator by at least half wavelength (so as to span an entire interference fringe).

Manual excitation and heat flux

The very first method to calibrate the readout was based on a mechanical excitation performed by hand: it was used in the initial part of this thesis's work and has been already reported in [90]. This method has the disadvantage of not being reproducible. Furthermore, it may well happen that too large a force is applied in the hit causing nonlinear effects that make the working point deviate from a circle/ellipse producing a spiral.

The second method to calibrate the readout is based on the thermal expansion of the oscillator and was used for almost half of the work of this thesi, which is up to the point when the piezoelectric actuator on the reference mirror was mounted. By turning on the heater, the oscillator starts to heat and elongate via thermal expansion. In this phase the working point of the interferometer begins to move, allowing data to be acquired for reconstruction of the calibration ellipse. However, this discrepancy is considered negligible from the calibration perspective. Additionally, as the oscillator cools primarily through heat conduction in the high vacuum environment, this method has the drawback of a lengthy duration. It necessitates waiting until the oscillator returns to equilibrium before starting thermal noise measurements.

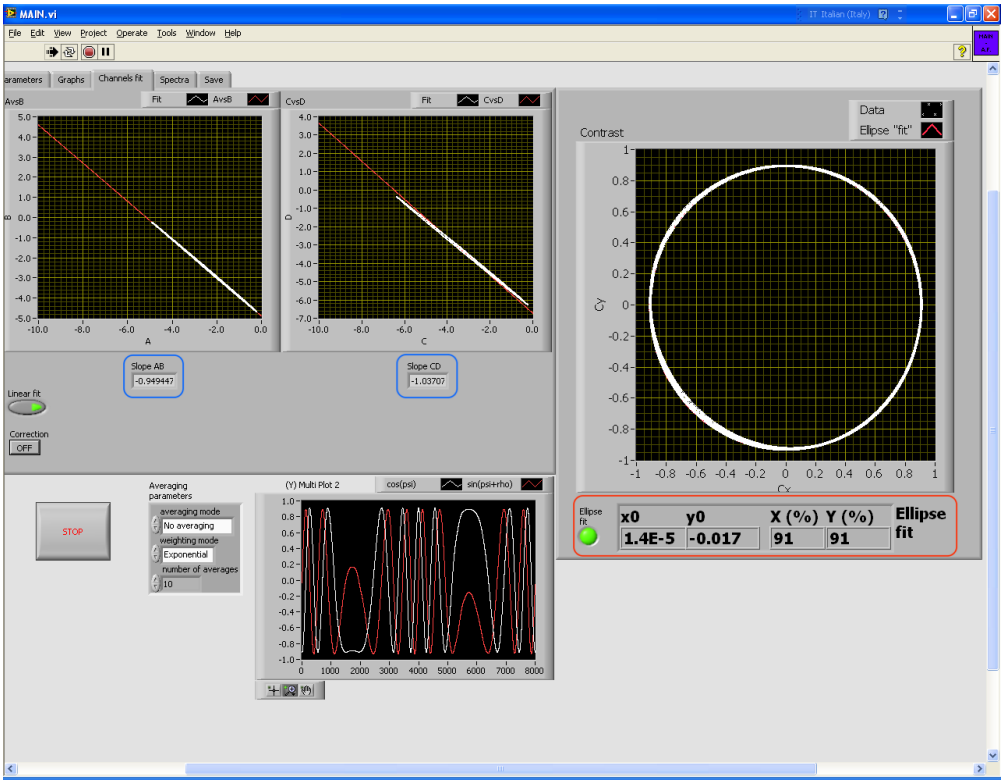

FIGURE VII.9: Screenshot of what the PXI-base data acquisition system displays typically during the alignment procedure with the piezo. The red rectangle highlights the ellipse parameters obtained by fitting the real-time data. The blue rectangle highlights the slopes of the linear fit done by plotting the intensities of the two couples of PDs: AvsB and CvsD (like Figure VI.8). These two quantities indicate if a post-processing correction of the signals is needed and in case activate them live by pressing the "Correction" button.

REFERENCE MIRROR MODULATION

A much faster calibration procedure is possible after the installation of the PZT on the reference mirror (§VII.1.7). The PZT actuator is fed with a sinusoidal signal up to 3 V_{pp} (with an offset of 1.5 V), amplified by about a factor of 100 so that the mirror can move by at least a fringe of interference.

Two different strategies for inducing mirror movements are tested before settling on the final procedure. In the first one, the signal sent to the PZT is a sin wave at 1 Hz. This choice aims to encompass the entire interference fringe within a single period. Since the oscillation is slow, it is also possible to visually check the interference behavior of the beam spot so that there is no misalignment between the two wavefronts upon arrival at the photodiodes (vertical or horizontal fringes). In the second way, the signal sent to the PZT is a sin wave at a frequency about that of the longitudinal mode (1400 Hz). However, at medium and high frequencies, the piezo is incapable of covering an entire interference fringe with a single period, as detailed in §VII.1.7. To traverse the complete ellipse under these conditions, incremental adjustments were made to the DC offset of the sinusoid, maintaining a constant frequency and amplitude. These adjustments occurred in small steps, ranging from 3 V to 5 V. Ultimately, both calibration methods proved to be compatible with each other. Consequently, for the sake of simplicity, the decision is made to exclusively adopt the first method—calibration with a large signal at low frequency. Powering the piezo is very useful during the alignment phase as it is immediate to see the contrast increasing or decreasing depending on how the beam centers the PDs.

For calibration purposes, the readings from the PDs are recorded and saved for approximately 10 seconds, corresponding to about 10 fringes. A typical calibration acquisition appears online

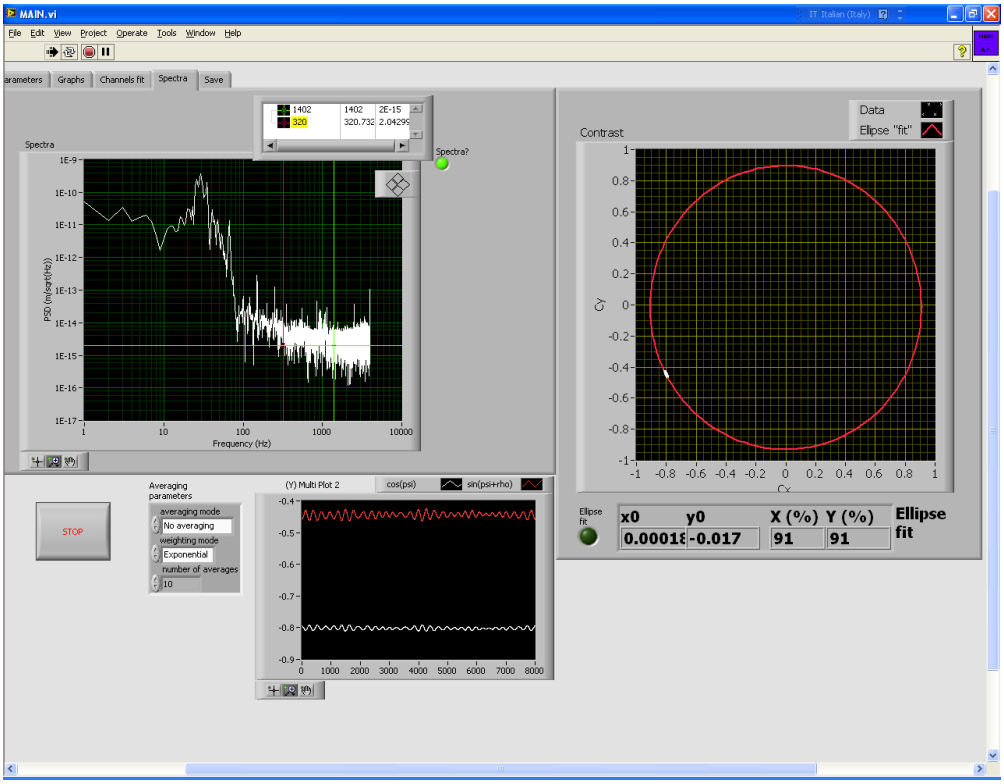

FIGURE VII.10: Screenshot of what the PXI-base data acquisition system displays typically during an acquisition. Following the calibration, the real-time amplitude spectral density of the interferometer displacement is examined. In particular, the ASD level near the two modes of interest (320Hz and 1402Hz as shown in the panel at the right-top - green and red vertical lines) and the level of the broadband noise above 1000Hz (horizontal green line) are monitored. The red circle is the fit obtained by the real-time calibration explained above (§VI.1.4).

as shown in VII.9. Once the system has been aligned and calibration is obtained, it is possible to continue with thermal noise measurements. In general, calibration can also be done after data taking as an additional check that the system has not become misaligned during measurement. To start the acquisition and data saving for thermal noise measurements, the same ADC configuration utilized during calibration is employed. Only the number and time lengths of the files to be acquired are modified. During the measurement, the generator to feed the piezo is disconnected from the system and the connectors of both piezo actuators are plugged with 50 Ω resistors to avoid electrical noise.

VII.2.3. DATA ANALYSIS AND RESULTS

A Python-based analysis program is developed to process the data output from the four photodiodes. With the signals of the PDs, the program computes the PSD of the oscillator displacement. Using a Lorentzian fit to the longitudinal mode peak, the effective temperature according to the Equipartition theorem is obtained. The steps of the analysis can be summarized as follows:

- Calculation of the calibration parameters.
- Inspection of the first minutes of the acquisition.
- Calculation of the displacement PSD for all data sets.

- First selection of data based on noise background.
- Fit of the longitudinal mode.
- Second filtering based on the fit χ^2.
- Calculation of the T_{eff}.

The first step of the analysis has the function of fitting the data acquired during calibration and deriving the ellipse parameters. These parameters are saved on disk and are used to analyze the data taken for thermal noise measurements. Batches of data obtained during the same period or related to the same calibration are collectively analyzed. This usually involves examining data collected continuously over a span of several days.

Before running the data analysis code on the full set of acquired data, a PSD using the first data (about 6 minutes) is computed to check that no unexpected feature appear, and the system behaves roughly as expected (top plot of Figure VII.11). The PSD of the oscillator displacement is obtained by following the steps described in §VI.1.3. In addition to the broadband spectrum covering 0 to 4 kHz, providing an overall perspective of the acquired data, there is a focused inspection (middle plot of Figure VII.11) around the resonance of the longitudinal mode. This examination assists in determining the frequency range for subsequent fitting procedures. As shown in §VII.4.1 the longitudinal mode can undergo frequency shifts based on the mechanical configurations of the system. The bottom plot of Figure VII.11 displays a zoomed-in view of a frequency range immediately before the resonance. The focus on this interval is due to the spectrum exhibiting no distinct features and being nearly flat. The PSD level in this frequency range serves as an out-of-band veto, enabling the exclusion of periods with an unusually high level of background noise from the analysis.

The analysis proceeds with the entire dataset. For each 20-second-long spectrum, noise within the specified range (typically 1365-1395 Hz) is averaged. Subsequently, a histogram is constructed, illustrating all such averages computed throughout the entire data-taking period (refer to Figure VII.12). The noise must allow the thermal noise to be measured so, looking at the expected spectrum from the simulation with the single oscillator model (Figure V.1) the threshold was chosen at 10^{-30} m^2/Hz to have an SNR of at least 20. Also, the threshold is a good compromise to keep the bulk of the distribution but cut the noise tails. The spectra that passed the selection are subsequently averaged in groups of 20, resulting in an average spectrum that represents approximately 6:30 minutes of acquisition time (even if not necessarily consecutive). These are the PSDs on which the fitting procedure described in §V.3.2 applies. By visual inspection of the spectrum around the longitudinal peak (center plot in Figure VII.11), a range of about ±2 Hz from the peak maximum is chosen to fix the fit contains. Equation (VII.4) is reformulated in terms of the parameters relevant to the study:

$$y(\nu) = \text{Noise} + \frac{2}{\pi}\frac{\text{Area}\cdot\Delta\nu}{4(\nu-\nu_0)^2+\Delta\nu^2} \tag{VII.4}$$

where Area is defined as the Lorentian integral. The Area is connected to T_{eff} of the oscillator by the following relation:

$$T_{eff} = \text{Area}\frac{m\omega_0^2}{k_B} \tag{VII.5}$$

The parameters obtained from the fit of each spectrum for a typical acquisition run are shown in Figure VII.13. The trend of the noise level (first graph at the top of the figure) is useful as a further check that the system behaves as expected. The peak area (second plot from the top) is the parameter from which the effective temperature of the oscillator will then be estimated. The parameter $\Delta\nu$ represents the FWHM of the peak and is the parameter that represents the dissipation of the oscillator. Past experience [82] suggests the expected quality factor $Q = \nu_o/\Delta\nu$ for this oscillator to be of the order of 10^3. For what concerns the resonant frequency ν_0, it is plotted over time to see if there is any trend (fourth graph starting from the top) indicating that the system is not behaving appropriately. As shown in [92], the resonance frequency has a temperature dependence of -0.6 Hz/K. So if there is a drift in ambient temperature during

data taking this is made evident by this plot. The last parameter shown in the figure is the reduced χ^2 of the fit. This parameter serves as an additional filter: in the subsequent steps of the analysis, only average PSDs with a well-performing fit, i.e., $\chi^2_R < \chi^2_{R_{5\%}}$, are considered. Here $\chi^2_{R_{5\%}}$ represents the threshold such that the probability of having a $\chi^2 > \chi^2_{R_{5\%}}$ is equal to 5%. After this final selection, the areas of the spectra that have passed filtering undergo analysis to calculate the effective temperature according to (VII.5). At equilibrium, the expectation is for this temperature to align with the ambient temperature.

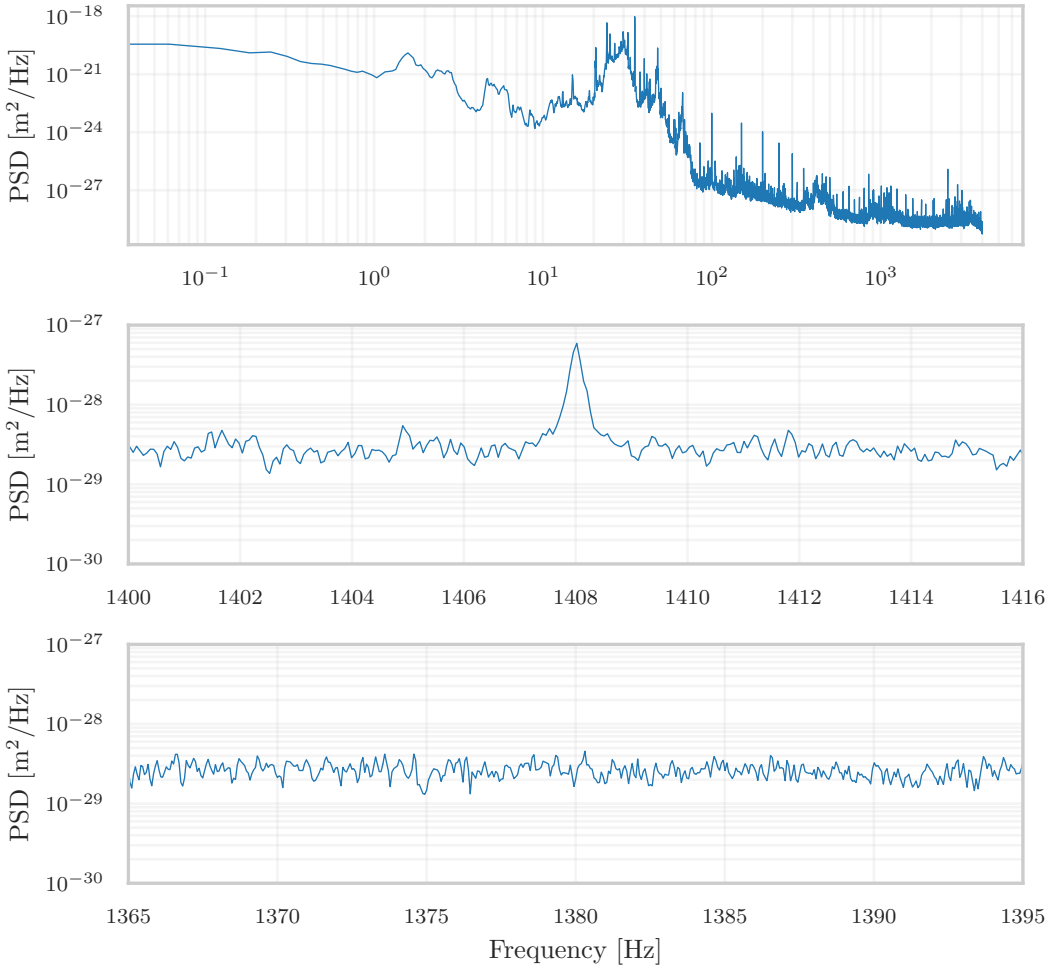

FIGURE VII.11: PSD of the calibrated interferometer readout, computed for testing purposes using the first file (spanning 20 min) of a typical run of data acquisition for thermal noise measurements. The readout is calibrated using the ellipse parameters obtained from the calibration procedure at the beginning of the run. The shown spectrum is an average of about the first 30 spectra of 20 seconds of the first file with a frequency resolution of 0.05 Hz. (top) Broadband spectrum from 0 to 4 kHz. (center) Zoom on the frequency region around resonance of the longitudinal mode. (bottom) Zoom on the frequency region where the noise floor is usually flat.

Subsequently, the entire set of temperatures is represented in a histogram, which is fitted with a Gaussian curve. The statistical properties of all the quantities extracted from the fit (particularly the peak area) are treated in detail in [90]. Figure VII.14 shows the histograms of temperatures before and after the chi-square selection for a 24-hour acquisition under thermodynamic equilibrium conditions.

As can be seen from the result of the histogram, the temperature is far from that of the

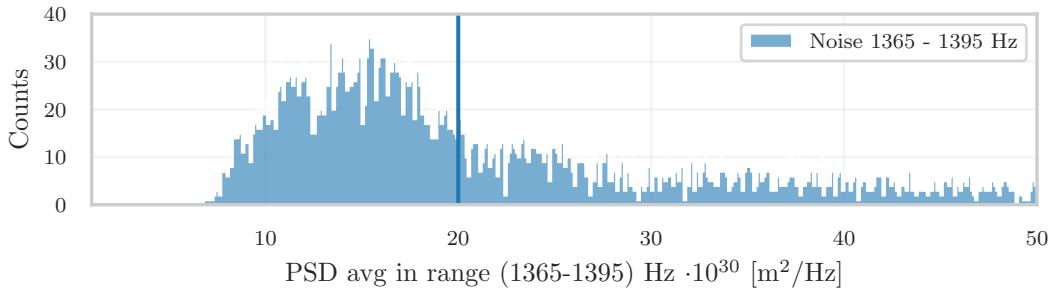

FIGURE VII.12: Histogram of the average PSD level in the frequency region 1365-1395 Hz. The threshold value of $1 \cdot 10^{-30}$ is marked with a solid vertical line. Periods with PSD average values in the range 1365-1395 Hz larger than this threshold are vetoed and not considered further in the data analysis.

laboratory environment (296 K) and more importantly has a lower temperature. The unexpected result arises from the measurements taken in thermodynamic equilibrium, where the FDT holds true. Determining the effective temperature without any free parameters necessitated extensive investigative efforts on the system, and these efforts are detailed in the following sections.

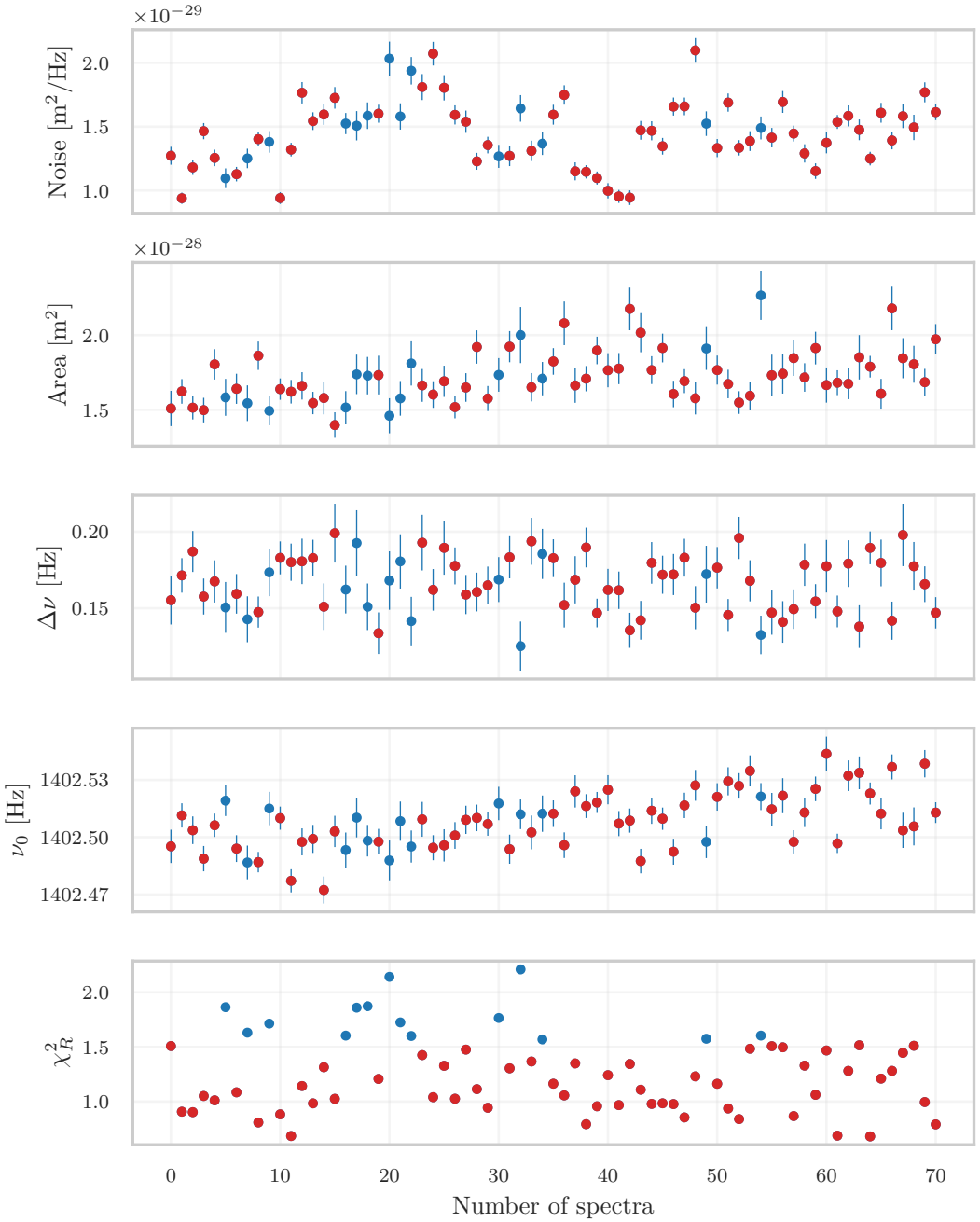

FIGURE VII.13: Plots of the different parameters obtained by fitting the data. In red are the spectra that passed the χ^2 selection: $\chi^2_R < \chi^2_{R_{5\%}}$.

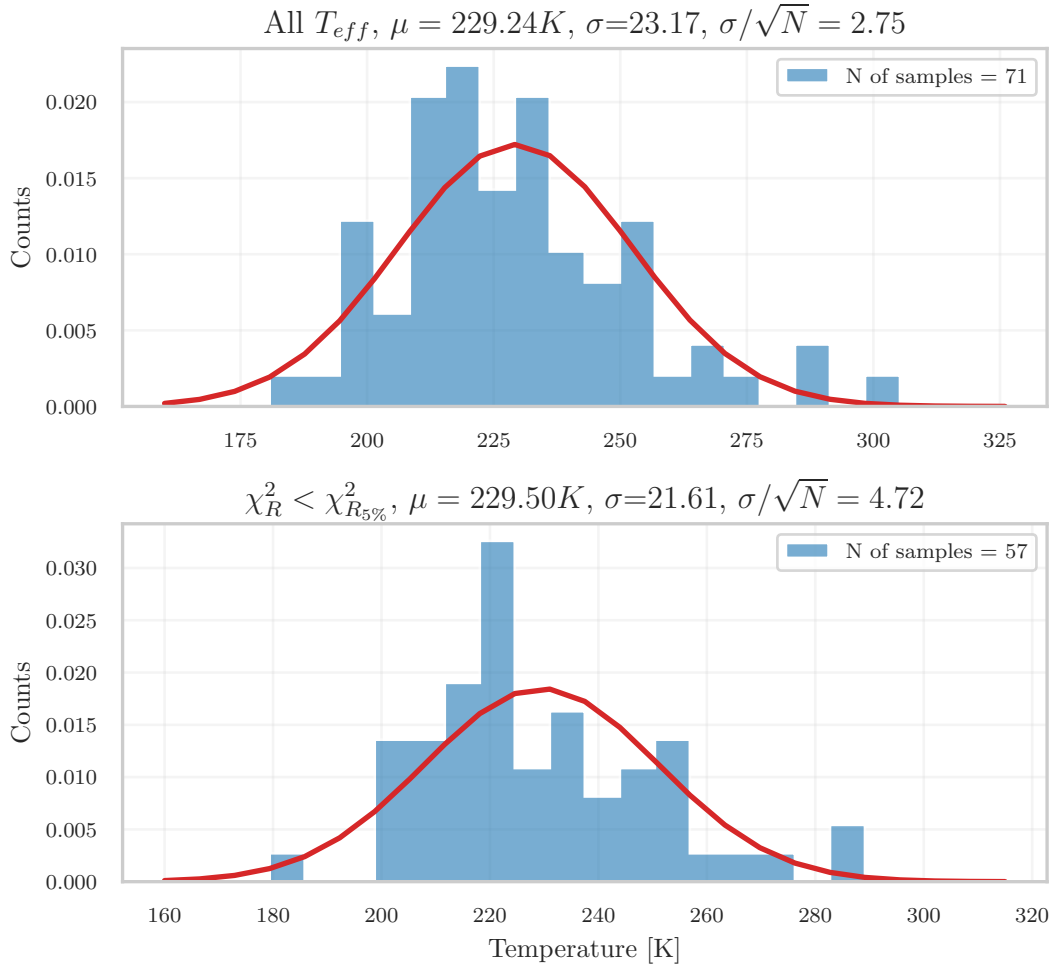

FIGURE VII.14: Histograms of the effective temperatures. (top) Distribution of the T_{eff} before the chi-square selection. (bottom) Distribution of the T_{eff} after the chi-square selection. For both plots, the mean μ, the standard deviation σ, and the standard deviation of the mean ($\sigma/\sqrt{N}$, with N the number of samples) are calculated. The solid red line represents the Gaussian curve that best fit the data.

VII.3. System characterization

The system, shown in Figure VII.15, undergoes comprehensive characterization, including the mechanics, the readout, and the analysis, with the ultimate aim of enhancement. The goal is to enable thermal noise measurements without relying on free parameters. A central challenge addressed within this thesis pertains to the observed discrepancy in effective temperature in equilibrium compared to the ambient temperature. This section focuses on the characterization of primary structures evident in the interferometer output PSD, with a particular emphasis on the low-frequency mechanical peaks.

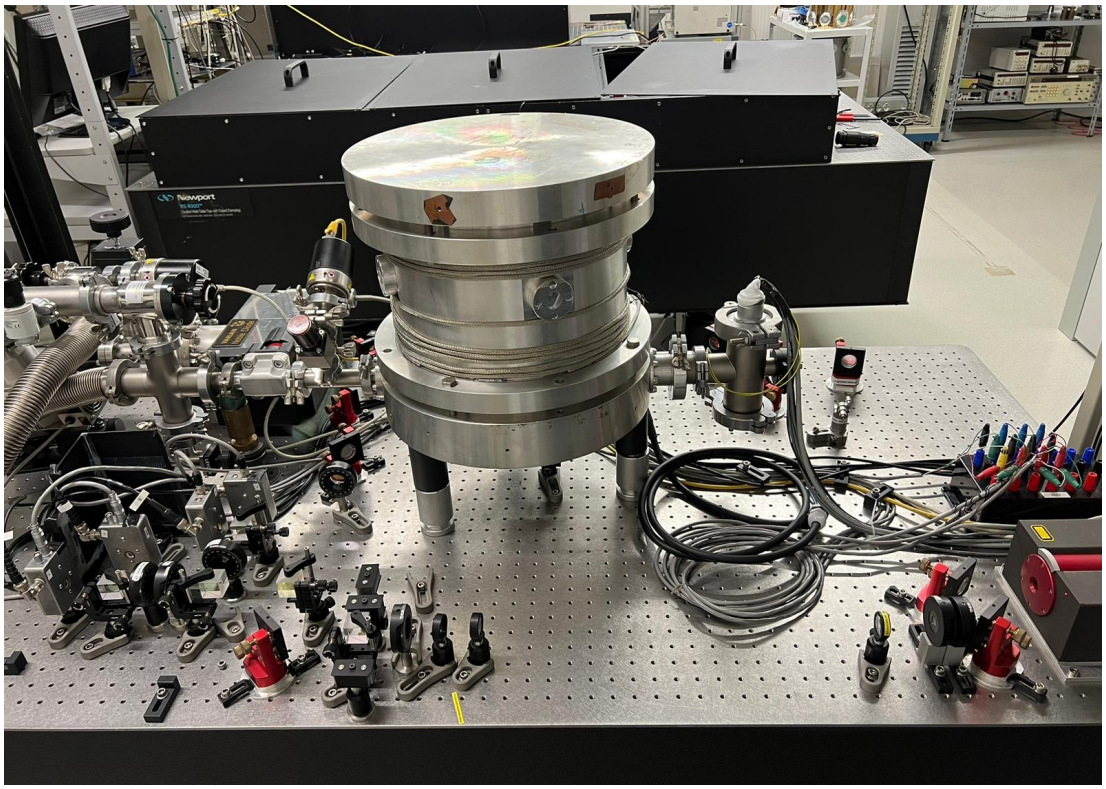

Figure VII.15: Picture of the experimental optical bench. The vacuum system, comprising pumps and gauges, extends from the left side of the chamber. On the right side, electronic connections for different sensors and PDs are present. The optical line for interferometric readout is visible at the bottom. The chamber is wrapped with a heating cable that allows the system's ambient temperature to be changed.

VII.3.1. Transfer function

The main method of investigation of the mechanical response of the system is the measurement of the transfer function between the aluminum flange and the oscillator mass. In this configuration, the transfer function between the motion of the suspension point and the motion of the oscillator is measured by utilizing the piezo, described in §VII.1.7, to mechanically excite the top flange. The displacement of the cuboid mass is then measured. Apart from diagnostic checks, this measurement can aid non-equilibrium results, as the expectation is for the transfer function not to vary significantly in such states, except for the resonance frequency, which has a known temperature dependence.

Resonant peaks

First, the longitudinal and transverse resonance peaks of the oscillator are identified, respectively at about 1400 Hz and 320 Hz. To perform the frequency scan automatically, the data acquisition software is modified to control the signal generator (Agilent 33521A) connected to the PZT actuator. The list of setting parameters for the data acquisition is shown in Table VII.4. The script captures about 5 seconds for each signal frequency and then moves on to the next one, according to the increment selected. Offline, the QDPI output is calibrated into displacement

Acquisition settings	
Waveform Function	Sine
Starting Frequency [Hz]	1400
Amplitude [V_{pp}]	3
DC offset [V]	1.5
Phase [rad]	0
Increment [Hz]	0.1
Number of samples	50

Table VII.4: Setting parameters to measure the transfer function of the oscillator by sending a signal of such characteristics to the PZT mounted on the aluminum flange. In this case, was shown an example in which was performed the transfer function from 1398 to 1403 Hz with a resolution of 0.1 Hz.

and filtered by a digital lockin while reference is a digital signal at the same frequency as the signal sent to the PZT actuator.

Initially, the QPDI readout system with only 3 photodiodes (refer to §VI.2.1) was employed for this analysis. The ADC has only 4 input channels, typically assigned to the 4 PDs. Due to this limitation, one PD reading had to be foregone to acquire the signal sent to the PZT actuator, which serves as the reference for the digital lock-in amplifier.

Once digitized, the calibrated QPDI output is multiplied by the signal sent to the PZT and also by the same signal but phase-shifted by a quarter of a period. The results of these two multiplications are low pass filtered to obtain the I, Q output of the lock-in. The signals I and Q are combined with the phase and amplitude of the response at each frequency. Combining the amplitudes obtained at each frequency yields the transfer function. Figure VII.16 and VII.17 show a typical transfer function (amplitude and phase) of the system. For this data set, the longitudinal peak is at 1400.5 Hz while the transverse peak is at 321.2 Hz. It can be seen that the amplitude of the transverse peak is more than a factor of 10 smaller than that of the longitudinal mode, despite its larger Q factor (about 30000 vs 7000). This is because the PZT force is better aligned along the vertical axis, i.e. parallel to the motion of the long oscillator. As expected from a harmonic oscillator, there is a π change in the phase of the response across the frequency of resonance, appreciated in both figures. This investigation with the transfer function, as elaborated in the next paragraphs, is very useful in finding the resonance frequencies when changes are made to the system. In fact, frequencies can undergo notable changes following hardware interventions or in response to variations in temperature conditions, such as shift in ambient temperature or inducted thermal gradient.

Low-frequency region

The procedure outlined in the previous paragraphs is also used to study the different structures that the output PSD shows. An example is given in Figure VII.18. The spectrum represents the mean PSD computed using a data set spanning 1 hour and is representative of the typical noise observed at the beginning of this thesis work, immediately after mounting the laser head on the optical bench. The spectrum reveals numerous peaks, each of which has been thoroughly investigated and efforts have been dedicated to eliminating or, at the very least, minimizing their impact. In the same way that the oscillator resonance peaks are obtained, a low-frequency

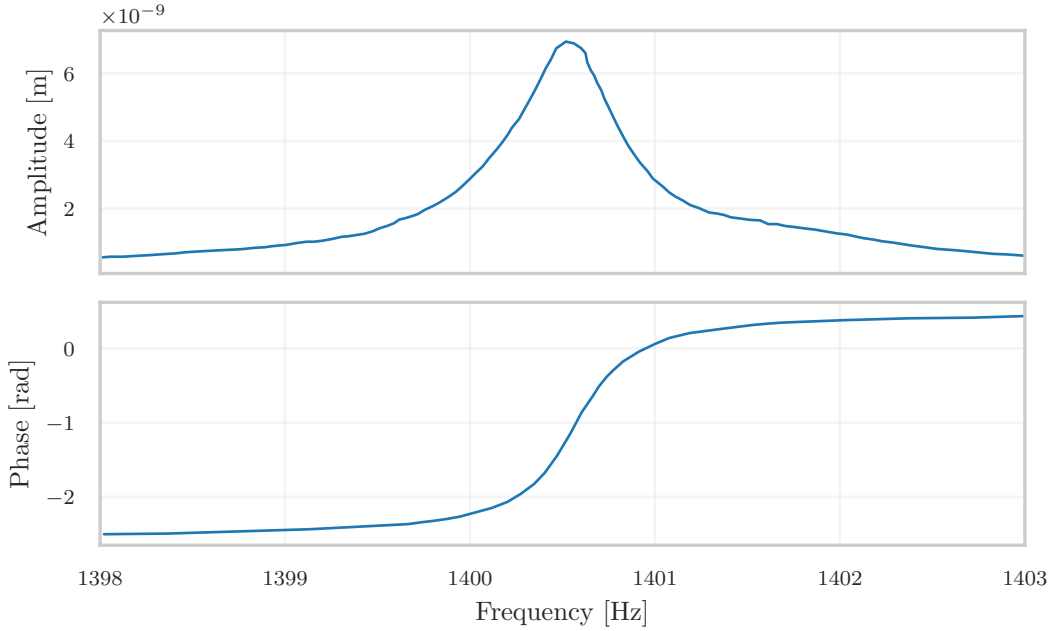

FIGURE VII.16: Mechanical response of the system at the longitudinal peak frequency acquired with the parameters listed in Table VII.4.

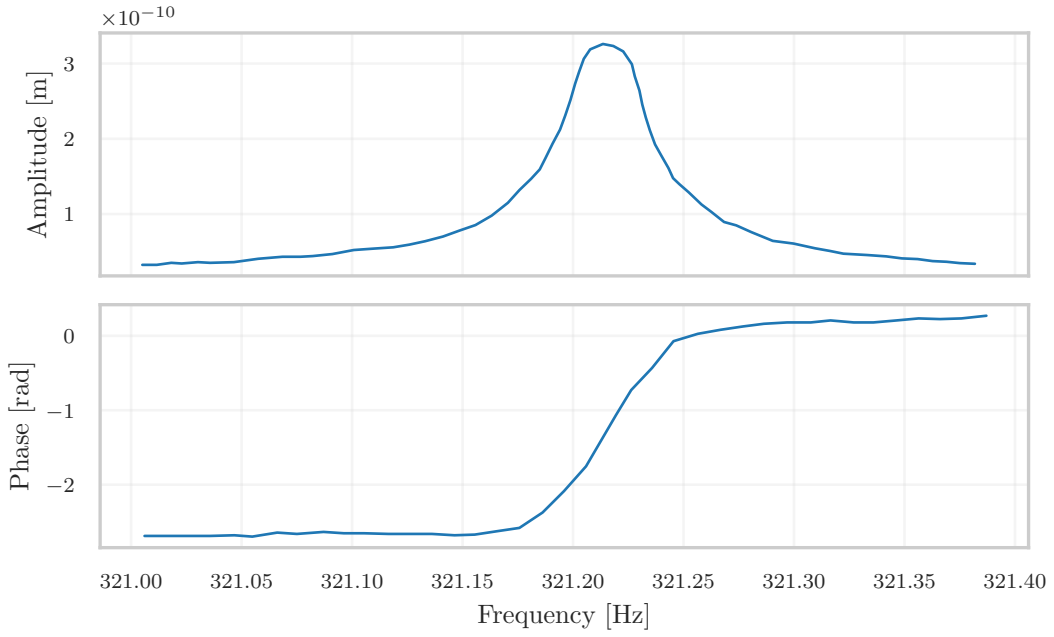

FIGURE VII.17: Mechanical response of the system at the longitudinal peak frequency with a resolution of 0.05 Hz and with a different range of frequencies. The scan is a zoom with a higher resolution (0.01 Hz) than the longitudinal peak, to account for the smaller FWHM.

scan with the PZT actuator is performed to characterize these peaks and to compare them with the suspension resonance modes. Figure VII.19 shows the mechanical response for frequencies up to 300 Hz. The figure shows also a zoom into the region between 1 Hz and 50 Hz, where the acoustic modes of the suspension are concentrated. The modes are listed in Table VII.5 [88].

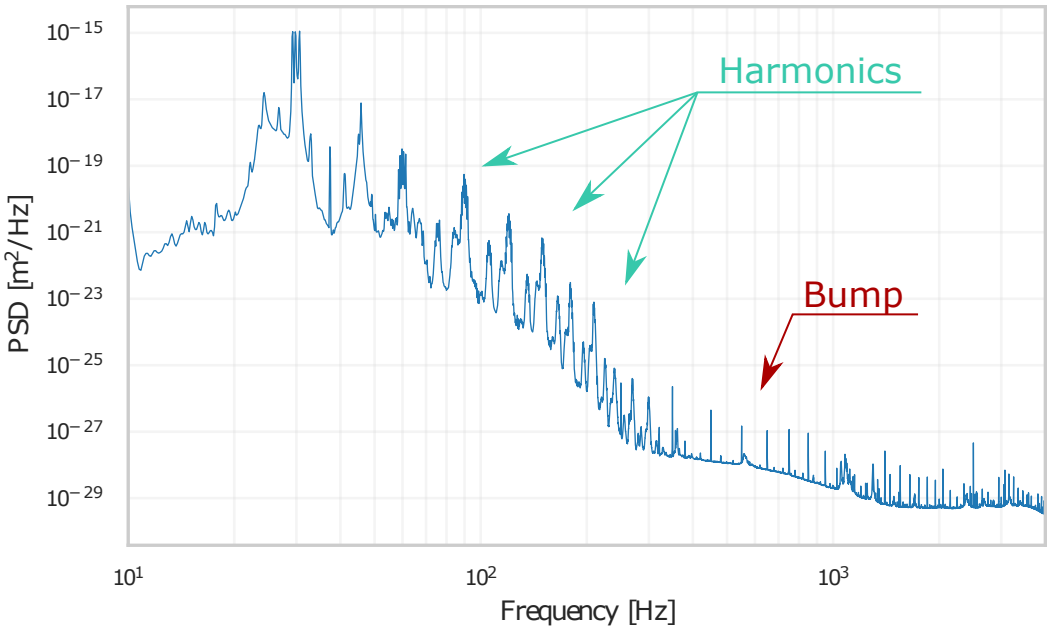

FIGURE VII.18: PSD acquired with the interferometer readout described in [89]. Note the peak structure propagating from 30 to about 300 Hz, where there is the transverse mode. It also features a big bump that occurs during measurements between 300 and 900 Hz.

SUSPENSION ACOUSTIC MODES	
Mode number	ν [Hz]
1	8.3
2	16.1
3	24.1
4	45.4
5	47.1
6	49.1

TABLE VII.5: Values of the resonant frequency of the first acoustic modes of the full suspension which have vertical component [88].

VII.3.2. SUPPRESSION OF MECHANICAL VIBRATION

The low-frequency segment of the PSD exhibits a recurring pattern at multiple frequencies, corresponding to the three main modes of the suspension, as illustrated in Figure VII.2. These patterns represent the harmonics of the suspension resonance. In fact, the vacuum chamber is supported by three pillars arranged at 120 degrees on its circular base. The pillars are constructed with a composition of half aluminum and half rigid plastic material. The plastic portion has an M10 threaded hole that allows it to be screwed into the chamber. In this configuration, vibrations from the optical bench are transmitted directly to the camera. An additional filter between the optical table and the chamber is introduced to diminish the noise energy at the input of the suspension. The material used is the same (Sylodamp - SP1000) that was used in the AURIGA experiment to absorb most of the low-frequency vibrations. To effectively attenuate frequencies of interest (approximately above 10 Hz), the Sylodamp pieces must be appropriately sized, considering the mass to be supported and the static load of the material. Each of the three pillars must support a weight of approximately 33 kg, given that the entire system, including the chamber, suspension, and vacuum components, has a total

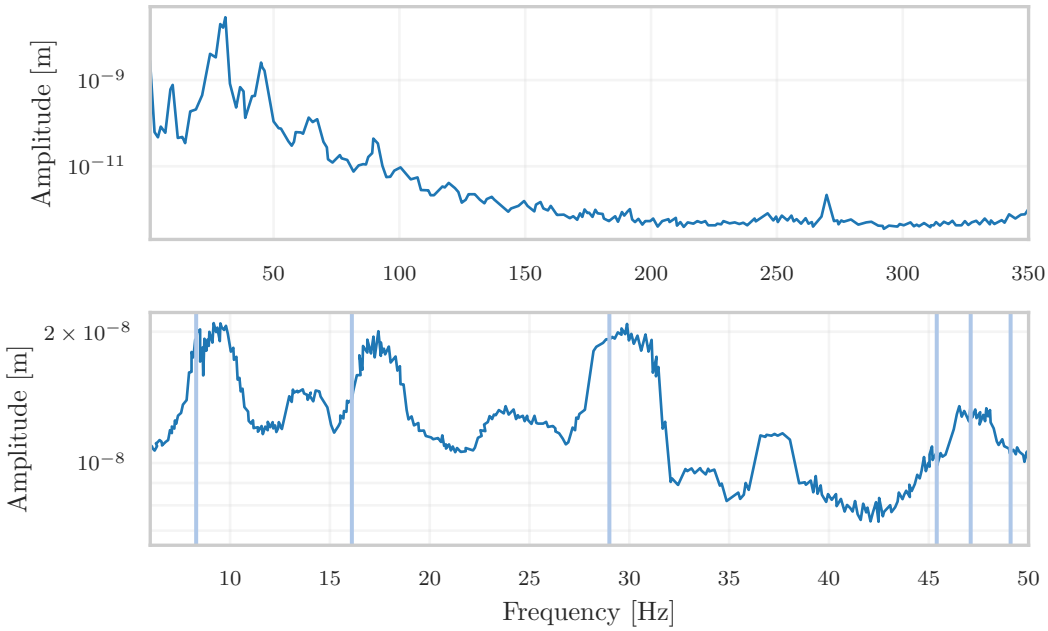

FIGURE VII.19: (top) Response of the QDPI to a signal fed to the PZT actuator on top of the aluminum flange, in the low-frequency region. (bottom) Zoom-in at a higher resolution (0.1Hz) of the response The vertical lines are at the predicted resonant frequencies of the first acoustic modes of the full suspension as reported in [88].

weight of around 100 kg. The static material load is 5 N/mm^2 and the maximum size that each Sylodamp cube is limited by the diameter of the plastic part of the pillars (50 mm). The interior of the plastic cylinders is thus hollowed out to have a parallelepiped with a square base with a maximum diagonal of 40 mm. Considering the material deflection ($\sim$ 1 mm) and crossing all possible parameter combinations (dimensions and damping frequency), it is chosen to cut Sylodamp pieces with a square base of diagonal parts at 39.9 mm. Figure VII.20 shows how the dampers are installed in the supporting pillars. With these characteristics, the combination of the three Sylodamp pieces should attenuate frequencies above 14 Hz. Furthermore, because of the specific design of the vacuum chamber, the balance of the chamber itself is compromised by the vacuum parts (gauges, valves, etc). Indeed, as evident from Figure VII.15, the vacuum system extends to the left over the optical bench, causing an imbalance in the weight distribution and resulting in the tilt of the chamber. For these reasons, an adjustable vertical support with a piece of Sylodamp is installed below the vacuum system to prevent vibrations from bypassing the dampers. The effect of the installation can be seen in Figure VII.21. The amplitude of resonances at 30 Hz has been reduced by an order of magnitude. As a consequence, most of the upper harmonics are no longer visible.

VII.3.3. Stray-light bump

The installation of the Sylodamp is effective in reducing the low-frequency noise. However, the system is also plagued by a noise bump, covering the frequency range from about 100 Hz to 1000 Hz that occurred randomly during measurements. The excitation of this shoulder seems unrelated to the mechanics of the suspension + oscillator system. In fact, attempts to excite this bump with the mechanical excitation provided by the PZT actuator proved unsuccessful. During the investigation of this effect, it can be seen that this depended greatly on the alignment of the system. Notably, the amplitude of this distinctive feature diminishes as the forward and return beams become more misaligned in their reflection from the vacuum chamber. This suggests

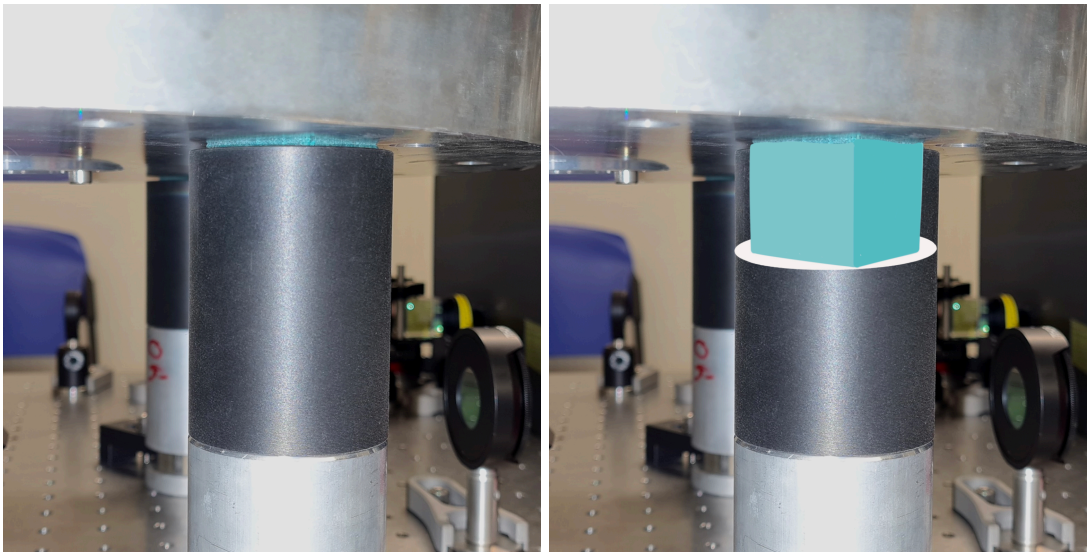

FIGURE VII.20: (left) Exterior of the plastic part of one of the pillars supporting the chamber. (right) Inside view of the plastic section with the Sylodamp parallelepiped installed.

that the effect is optical in nature, particularly from the shape of the bump in the spectrum it appears that the effect can be traced to stray light [62]. According to the definition, stray light is light that is produced within the optical layout that follows a different path from the intended one. This additional light, which can have different types of sources, goes out from the main path and can be reflected by mechanical components that are not suspended or mechanically isolated. After the reflection, the scattered light can re-couple with the main beam and add extra noise to the measurements. Stray light predominantly occupies the low-frequency part of the spectrum, where mechanical components, responsible for light back-reflection, experience the most significant vibrations induced by acoustic or seismic noise. As demonstrated in [93], special attention must be paid to the positioning of the mechanical parts that reflect scattered light and the optics that produce it. In addition, one must avoid placing the beam waist near mechanical parts that are not mechanically isolated because the fraction of re-coupled light is inversely proportional to the beam size:

$$f_{sc} \sim \frac{\lambda^2}{\pi^2 w^2} \tag{VII.6}$$

where w is the beam radius. The emergence of this effect subsequent to the installation of the laser head on the NETN optical bench, where adjustments were made to the beam parameters, indicates that the size and position of the waist are likely the primary reasons for this occurrence. Notably, this distinctive bump is absent in measurements conducted in [89] and [90], further underscoring its connection to alterations in beam characteristics.

As mentioned in §VII.1.5, initially the waist is placed at approximately the oscillator's bottom surface with a radius dimension of 750 μm. With the addition of a third telescope lens, the position and size of the waist are changed. Specifically, the waist is moved away from the oscillator surface and closer to the detection zone. As can be seen from Figure VII.21, this modification significantly reduces the percentage of scattered light re-coupled into the main beam, suggesting that the scattered light is reflected from some surface of the vacuum chamber not filtered by the mechanical suspensions.

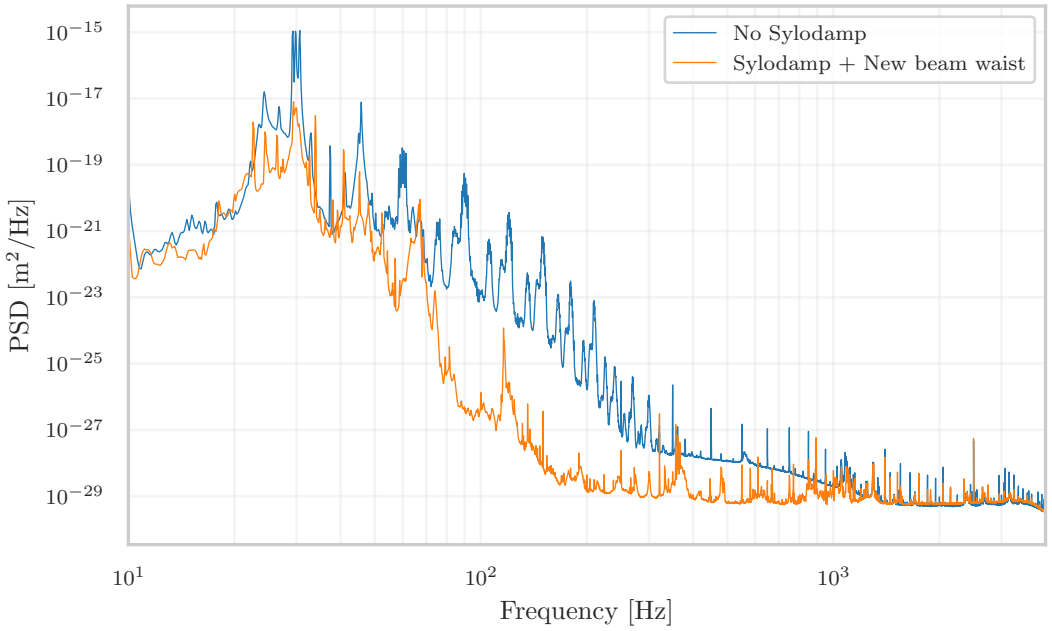

FIGURE VII.21: PSD comparison before and after introducing the Sylodamp supports and moving the beam waist away from the area of the vacuum chamber. The resonant peaks in the low-frequency range are suppressed. The region above 100 Hz does not present the higher-order harmonics anymore. Also, in the spectrum taken after the installation of the third telescope lens (orange curve), the stray light bump is no longer present in the measurements made after changes to the optical layout.

VII.4. Longitudinal mode investigation

After the installation of the piezoelectric actuator behind the reference mirror, a transfer function measurement is conducted as a check. Unexpectedly, it is discovered that the resonance frequency of the longitudinal mode has shifted by approximately -15 Hz, transitioning from 1400.5 to 1386 Hz [91]. In light of this observation, the working hypothesis to account for this frequency change is that the mechanical characteristics of the system underwent alterations during the installation process. Subsequent tests are designed to elucidate the root cause of this phenomenon and explore whether it is correlated with the outcomes of thermal noise measurements.

VII.4.1. Investigations on the resonance frequency

During the reassembly of the system after the piezo actuator installation (§VII.1.7), the alterations made included the redistribution of weight on the support holding the interferometer in the chamber (due to the piezo support) and the adjustment of the tightening torque for the 8 steel screws securing the aluminum flange to the third stage of the mechanical filters.

Figure VII.22 shows the last stage of the suspension along with the aluminum flange and the 8 steel screws. Before this thesis work began, these screws were tightened to a torque of 10 Nm and remained unchanged until the installation of the piezo. In this last intervention, the system is reassembled by tightening the screws without using a torque wrench. However, according to tabulated values, these 8 M8 steel screws could be tightened with a torque of up to 15 Nm (the precise value depends on the strength class of the screw and thread). This observation suggests

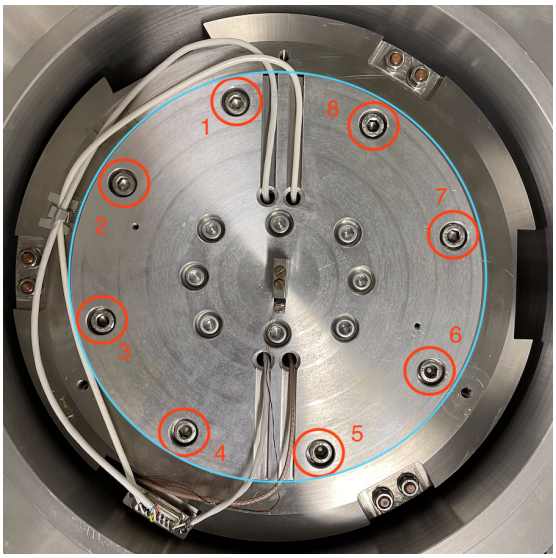

Figure VII.22: Top view of the open vacuum chamber. The 8 steel screws (circled in red) attach the aluminum flange (light blue circle) to the last stage of the suspension. The 8 center screws, on the other hand, are made of Al7075. They are softer screws as they attach the oscillator assembly to the monolithic oscillator block. In the center of the flange, the mass mounted on the piezoelectric actuator, used to achieve the transfer function, can be seen.

that the observed shift in resonance frequency could be attributed to non-ideal tightening of the two components: the aluminum flange (enclosed in the blue light circle in Figure VII.22) that supports the block with the oscillator, and the suspension system. Moreover, this non-ideal tightening could potentially impact the low effective temperatures obtained in equilibrium, given that those measurements are conducted with a looser torque setting (10 Nm instead of 15 Nm). Hence, a systematic investigation is initiated by measuring the transfer function around the longitudinal mode as a function of the torque τ applied to the screws. Figure VII.23 summarizes the results.

As can be seen from the graph, the resonance tends to shift from 1388 Hz with a tightening torque of 3 Nm, gradually approaching an asymptotic value near 1401 Hz as the tightening torque increases toward the maximum value allowed by the screws. The legend shows also the FWHM (indicated by $\Delta\nu$): a progressive trend towards lower values is evident with increasing torque. This behavior is detailed in Figure VII.24. The findings confirm that higher torques result in a more rigid connection between the flange and, consequently, the oscillator with the annular mass of the suspension, effectively representing a single body. It is important to note that the transfer functions are acquired at atmospheric pressure. For each measurement, the chamber lid is simply leaned up to speed up the measurements. This may have affected the different weight distribution of the chamber and consequently the alignment of the system. In fact, with the installation of the Sylodamp, the tilt of the chamber is sensitive to how the weight is distributed and connected to it. This aspect could explain the non-monotonic growth of the peak height, as the measurements do not have exactly the same conditions due to the repositioning of the chamber lid between two different measurements.

As seen in the image from the top of the chamber, there are also aluminum screws on the flange that attach the oscillator to the assembly system where the instrumentation is mounted. The same test is performed on these aluminum screws, starting from τ =1 Nm to the maximum allowed 6 Nm. During this test, the tightening torque of the steel screws is kept fixed at 10 Nm. The effect of these screws is much less influential as the resonance frequency shifts a maximum of 4 Hz from minimum to maximum torque. This is probably due to the different weight of the elements that the screws connect. The steel screws have to fasten the whole oscillator assembly which weighs almost 4 kg while the aluminum screws have to fasten the monolithic aluminum block weighing 0.6 kg.

Double oscillator simulation

To replicate the observed behavior in Figure VII.23, a more detailed model for the longitudinal mode is explored for the analysis of thermal noise measurements. Instead of treating the oscillator as connected to an infinitely massive object, a damped double oscillator system is considered (§V.1.4). The double oscillator is used to reproduce the coupling that exists between the aluminum flange and the last stage of the suspension as the torque of the screws changes. This effect is simulated by stiffening the elastic constant between the first and the second oscillator. In this model, the primary mass is represented by the Al flange combined with the third stage of the suspension, as illustrated in Figure V.2. The formula used to reproduce the behavior of the peak is the equation (VII.7), rewritten in its extended version:

$$S_{x_2}(\omega) = \frac{4k_BT}{m^2M^2} \cdot \frac{N}{D} \tag{VII.7}$$

where the numerator N is:

$$\begin{aligned} N = \Gamma_2 m_2^3 \left[\Gamma_2^2\mu^2\omega^2 + 2\Gamma_2\Gamma_1\mu\omega^+\Gamma_1^2\omega^2 + \left(\mu\omega_2^2\omega^2 + \omega_1^2\right)^2\right] \\ - 2\Gamma_2\mu m_2 m_1^2 \left[\Gamma_2\omega^2(\Gamma_2\mu + \Gamma_1) + \mu\omega_2^4 + \omega_2^2\left(\omega_1^2 - \omega^2\right)\right] \\ + m_1^3(\Gamma_2\mu + \Gamma_1)\left(\Gamma_2^2\omega^2 + \omega_2^4\right) \end{aligned} \tag{VII.8}$$

and the denominator D has the form:

$$\begin{aligned} D = \Gamma_2^2\omega^2\left(\Gamma_1^2\omega^2 + \left(\omega_1^2 - (\mu+1)\omega^2\right)^2\right) \\ - 2\Gamma_2\Gamma_1\mu\omega^6 + \Gamma_1^2\left(\omega^3 - \omega\omega_2^2\right)^2 \\ + \left(-\omega^2\left((\mu+1)\omega_2^2 + \omega_1^2\right) + \omega^4 + \omega_1^2\omega_2^2\right)^2 \end{aligned} \tag{VII.9}$$

To replicate the situation depicted in the transfer function measurements, two different approaches are employed.

The first approach involves considering the oscillating mass m_1 as the combination of all suspension stages (approximately 50 kg), with an oscillation frequency around $\omega_1 = 30$ Hz,

as shown in Figure VII.3. Mass m_2 (0.25 kg), on the other hand, represents the aluminum oscillator with a resonant frequency of ω_2 =1400 Hz. By varying ω_1 in the low-frequency range (10-100 Hz), as expected, the longitudinal mode resonance frequency of the second oscillator is unaffected, remaining fixed around 1400 Hz. Frequencies exceeding 100 Hz are excluded from the analysis, as the low-frequency peak harmonics are mitigated using Sylodamp (see Section §VII.3.2). In this condition, the first oscillator can be considered completely decoupled from the second one. This leads to the conclusion that the massive, low-frequency oscillator does not affect the frequency of the lighter second oscillator. As a result, this scheme can be ruled out as an explanation for the frequency shift of the longitudinal mode resonance with torque.

In the second approach, the oscillating mass m_1 is considered to be one of several elements in the last stage of the suspension (e.g. Al flange and 3rd annular mass) that can be affected by the tightening of the screws. The mass and the internal resonant frequency of these elements (see Table VII.2) are varied to simulate the behavior in the range (1500-2500 Hz). Tightening the screws indeed leads to increased stiffness in the elastic constant representing the first oscillator, m_1. Consequently, this tightening results in an increase in the internal resonance frequency of the simulated element. The result is shown in Figure VII.25. The behavior shown is different from that observed in the single oscillator reference in red. By increasing the frequency of oscillator m_1 (from light green to blue), the curves move to higher frequencies by decreasing their amplitude. The frequency behavior aligns with expectations: as the resonance frequency ω_1 increases and surpasses ω_2, the two oscillators decouple. This is confirmed by the curves in blue, which approach asymptotically toward 1400 Hz. This value is reached when ω_1 or m_1 tends to infinity. In contrast, the peak amplitude behaves differently from what is observed: it decreases as the frequency increases.

It should be noted that, experimentally, the m_2 oscillator attached to an infinite mass is never measured, so the observed 1400 Hz is already the resonant frequency of a complex system. In other words, it could be that the m_2 oscillator itself is even higher, and the combined system shows behavior in which 1400 Hz is already the convergence of all the resonances (the blue curves in the figure). Taking this aspect into consideration, simulations are carried out to vary the resonance frequency ω_2. These simulations consistently exhibit behavior similar to that shown in Figure VII.25 but with different frequency offsets due to the choice of parameters.

The conclusions drawn from these simulations indicate that the behavior of the system is too complex to be addressed adequately with an analytical model. Consequently, a finite element simulation would be necessary.

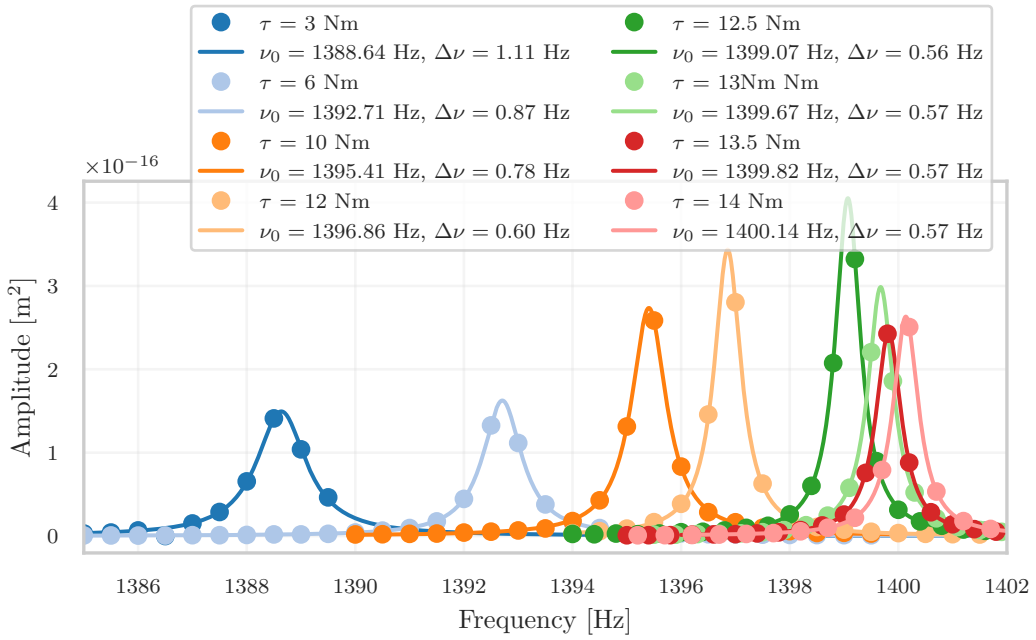

FIGURE VII.23: Plot of the different transfer functions around the resonance peak for different tightening torques. For each peak, the resonance frequency and peak width obtained by fitting the data are shown.

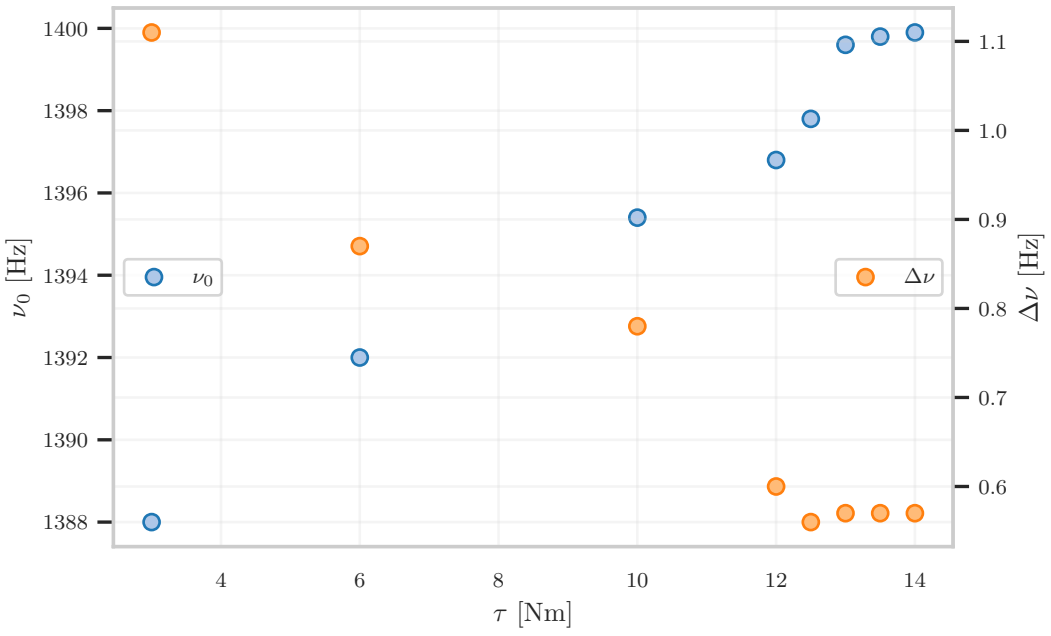

FIGURE VII.24: Plot of the screw test results. In blue, the resonance frequency trend is a function of tightening torque. In orange the trend of peak width. Both quantities are obtained by the fit shown in Figure VII.23

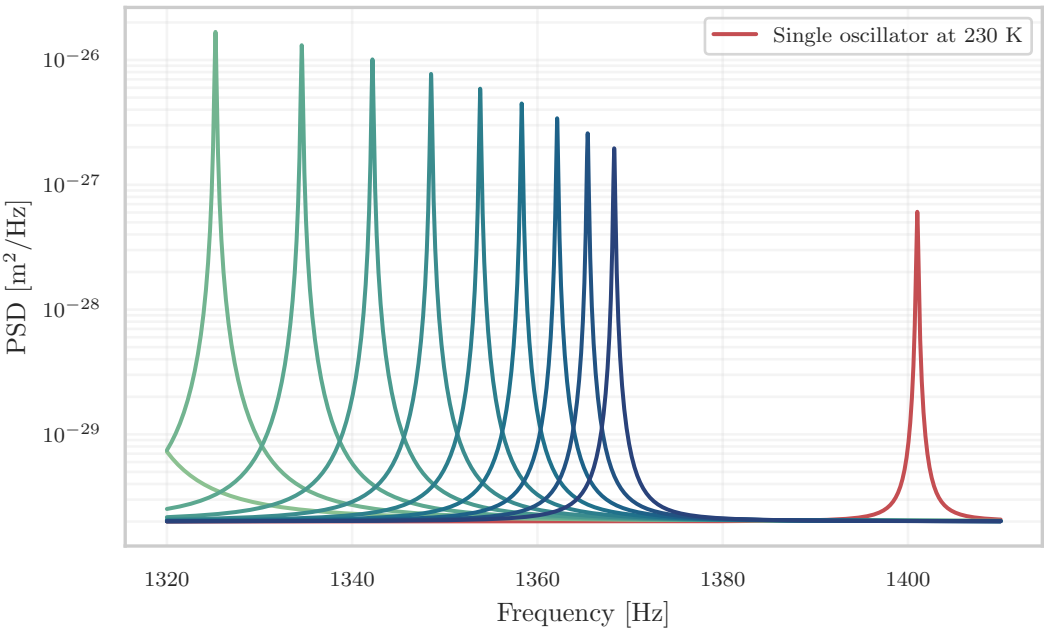

FIGURE VII.25: Simulation result with the double oscillator model. The plot shows a zoom into the frequency region where the resonance of the second oscillator is expected. The curves represent the PSD of the displacement of the second oscillator. The peaks with a lighter color represent lower resonance frequencies of the first oscillator (starting from 1500 Hz) and become darker by increasing this frequency (2500 Hz). The red peak represents the reference of the single oscillator oscillating at 1400.5 Hz as observed in the test.

VII.4.2. Long-term investigations on effective temperature

Following the tests described in the previous section, the screws were tightened to the maximum allowable value (15 Nm), and the experiment was returned to operative conditions. The investigation starts by examining the effects of this higher tightening in comparison to the 10 Nm case. Subsequently, for a more comprehensive understanding of effective temperature behavior, a data-taking campaign is initiated to cover an extended period in an (almost) continuous manner. The results of these two investigations are presented in the following section.

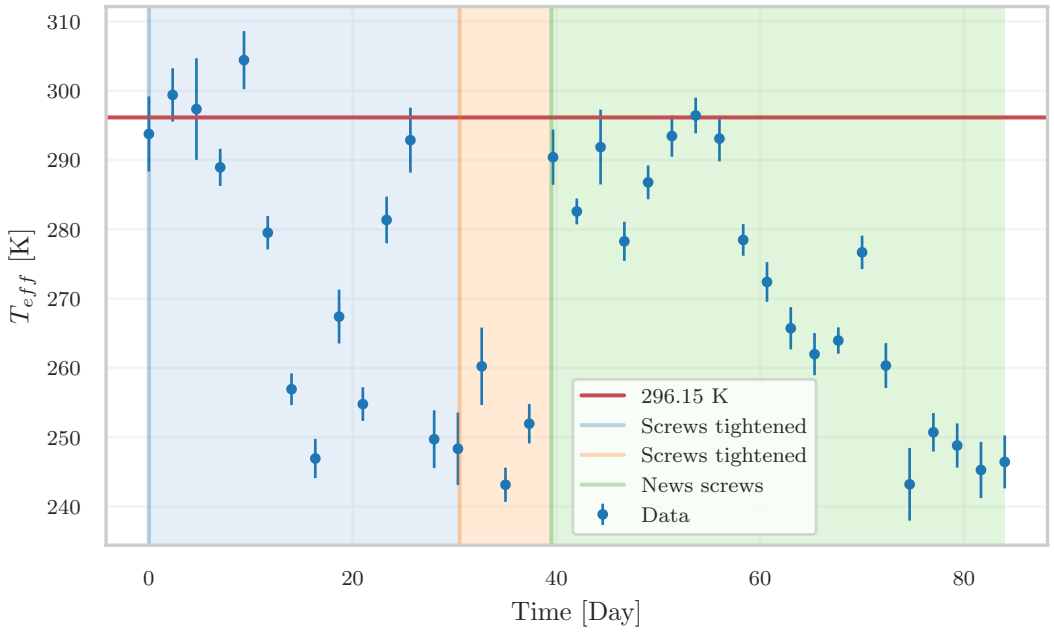

Figure VII.26: Plot of temperature trend in different configurations. The horizontal line in red is placed at the temperature measured by the thermometer inside the chamber that monitors the ambient temperature. The colored areas correspond to different configurations. The area a blue shows the measurements after the first tightening of the screws, the area in orange the second tightening, and the area in green corresponds to the measurements taken with the installation of the new screws.

Figure VII.26 shows the thermal noise measurements results in the equilibrium condition after the screws have been tightened to the maximum torque. Measurements are acquired over about 3 months at different times of the day (morning, afternoon, and night) and the system is optimized before each measurement through alignment and calibration. As illustrated in the light blue area, the average temperature data during an acquisition in the first 15 days after the screws are tightened appear to align with the laboratory temperature at 296 K (red horizontal line). However, after about 20 days, the temperature began to decrease until it reached a subthermal temperature of about 240 K. Given this trend, the chamber is reopened and the tightness of the screws is checked. All of them are found with a torque of about 12 Nm, below the 15 Nm set before closing the chamber. Clearly, the torque tightening of the screws relaxed in time compared to the torque previously applied. Subsequently, the screws are tightened again, and new measurements are taken (orange area). As can be seen, this second intervention produces no changes in effective temperature. Upon re-opening the chamber, it is observed that the cause of the relaxation of the screws is due to the threads being damaged. The screws are then replaced, and new thermal noise measurements are performed. The green area in the measurements indicates that the temperatures, within their margin of error, initially align with the ambient temperature of the laboratory for a brief period before decreasing. This decreasing trend is observed systematically after the chamber is closed again. This observation,

along with the increase in T_{eff} after tightening the screws, led to the hypothesis that the screw system used does not ensure proper stiffening of the mechanical parts involved. To address this issue, potential solutions include either redesigning the oscillator assembly to minimize the involvement of mechanical parts, which is a time-consuming process, or modifying the existing system by incorporating more screws with larger sizes. The latter approach would theoretically enhance the torque and, consequently, increase the stiffness of the suspension-aluminum flange system.

Mechanical changes and long-term measurements

The mechanical setup is modified increasing both the number of screws, from 8 to 16, and increasing their diameter (from M8 to M10) to allow the application of larger torque. With the M10 screws, the tightening torque has a working range from 18 to 24 Nm. For the initial measurements, the tightening is set at its lower recommended value (18 Nm), considering the possibility of tightening them further if needed, as a higher value is used when measuring an effective temperature equal to the ambient temperature.

In this new configuration, the vacuum has been re-established to measure again the thermal noise. For this new set of measurements, the system is set to acquire data automatically for multiple days while avoiding any possible factors that might introduce unknown variables (e.g., system realignment, laser power change) to the results. Approximately every 3 days, a calibration is acquired to check the status of the system and its alignment. Additionally, all measurements acquired automatically during extraordinary events in the laboratory (e.g., great crowding, technical interventions, etc.) are excluded.

The primary goals of these long-run measurements are to investigate if the effective temperature has changed again, potentially approaching the ambient temperature, and to study the stability and repeatability of the system. The trend of T_{eff} obtained with this new set of measurements

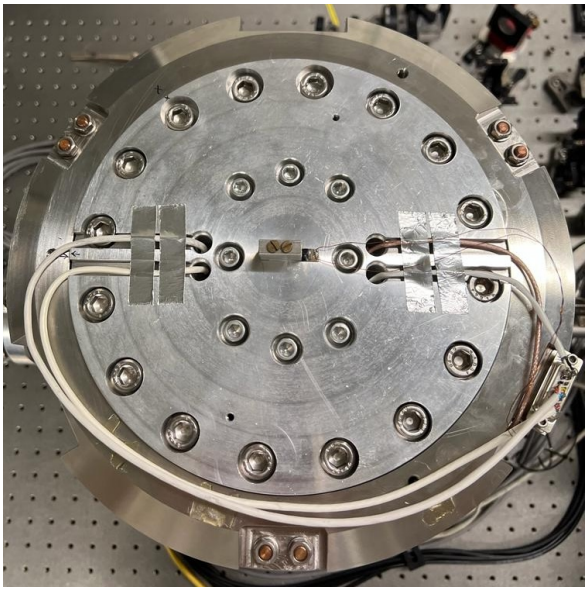

Figure VII.27: Top view of the open vacuum chamber after upgrading to the new screws layout (compare with Figure VII.22). The number of steel screws was doubled from 8 to 16. In addition, the screw size has been increased from M8 to M10.

is shown in the first plot from the top of Figure VII.28. As soon as the vacuum chamber is closed, and measurements start, the measured temperature begins rising again to above 280 K, remaining below the ambient temperature. After an initial increase, the temperature begins to decline, reaching around 220 K for a duration of approximately 10 days before subsequently increasing and stabilizing at around 250 K. To analyze this behavior and identify its cause,

various parameters related to the resonance peak, including high-frequency noise (i.e. noise between 1365-1395 Hz), resonant frequency ν_0, the optical phase ψ, and the FWHM of the peak $\Delta\nu$ are plotted. A notable observation is the increase in the resonant frequency, shifting from 1400 to 1408 Hz following the system modification. As can be seen from Figure VII.28, there is a direct correlation between the trend of T_{eff} and high-frequency noise. This result seems counterintuitive since a lower wide band noise points to a more sensitive readout decrease in T_{eff} is unexpected and unjustified. In principle, T_{eff} should remain unaffected by changes in the noise level.

Another evident correlation is between the phase ψ and the resonance frequency ν_0. However, this correlation is expected, as the resonant frequency of the oscillator is directly linked to the thermodynamic temperature of the room. Variations in the latter cause thermal expansion of the whole system, leading to a relative change between the interferometer's arms. During the entire acquisition, there is a clear increase in the resonance frequency by approximately 0.6 Hz. As detailed in § VII.2.3, this change is associated with a temperature decrease of about 1 K of the ambient temperature. Due to the limited sensitivity in measuring T_{eff}, the observed temperature change is not easily noticeable in its overall trend.

On the other hand, the FWHM of the peak does not seem to change. This is not surprising, as this quantity is related to the mechanical characteristics of the system, particularly the dissipation of the oscillator.

In correspondence to the green vertical line in Figure VII.28, the data display abnormal behavior. This is evident from the discontinuity in the trends of T_{eff}, noise, and phase ψ. Notably, such a discontinuity is absent in the trends of the resonance frequency ν_0 and $\Delta\nu$, suggesting that the anomaly is attributed to factors associated with the readout rather than the mechanics of the system.

The interdependencies among these variables are presented in the correlation matrix shown in Figure VII.29, employing Spearman's rank correlation coefficient [94]. Indeed, the correlation between T_{eff} and the noise is quantified at 0.70, while the strong anticorrelation between the phase ψ and the resonant frequency ν_0 has a value of -0.91. Additionally, a correlation exists between the phase ψ and the noise level, suggesting that the sensitivity of the instrument varies depending on the interferometer working point. This last aspect is the first point that will be investigated to understand whether or not there is an error in the interferometric readout.

Since the mechanical modification, the vacuum chamber has not been reopened to verify that the tightening torques used have remained the same. A counter-test is scheduled to ensure that the measurements have not been affected by screw relaxation. This will be conducted promptly once the chamber is reopened. If achieving an absolute measurement of T_{eff} without any free parameters proved challenging, the vacuum chamber has been equipped with heating cables (see FigureVII.15). These cables have been designed to heat the chamber, thereby increasing the ambient temperature. This method can be used as another verification that, aside from the lower value, T_{eff} is proportional to the thermodynamic temperature as expected.

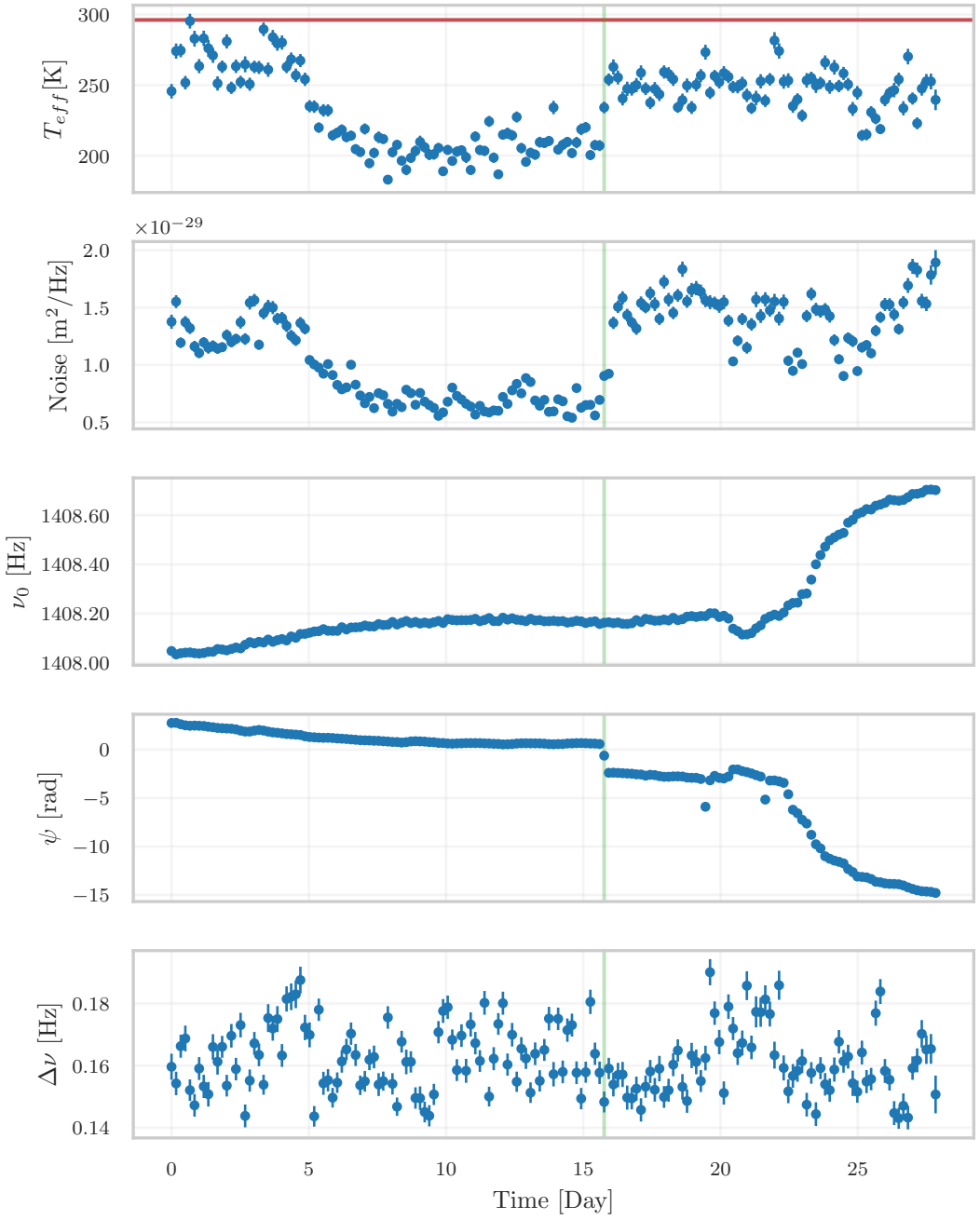

FIGURE VII.28: Plots of different parameters after the mechanical changes. From the top: (first) Effective temperature trend. The horizontal line in red is placed at the temperature measured by the thermometer inside the chamber that monitors the ambient temperature. (second) Noise level background before the peak obtained by the longitudinal peak fit. (third) Resonance frequency. (fourth) Optical phase. (fifth) FWHM. The vertical green line marks the point of acquisition where the readout system exhibited unusual behaviors.

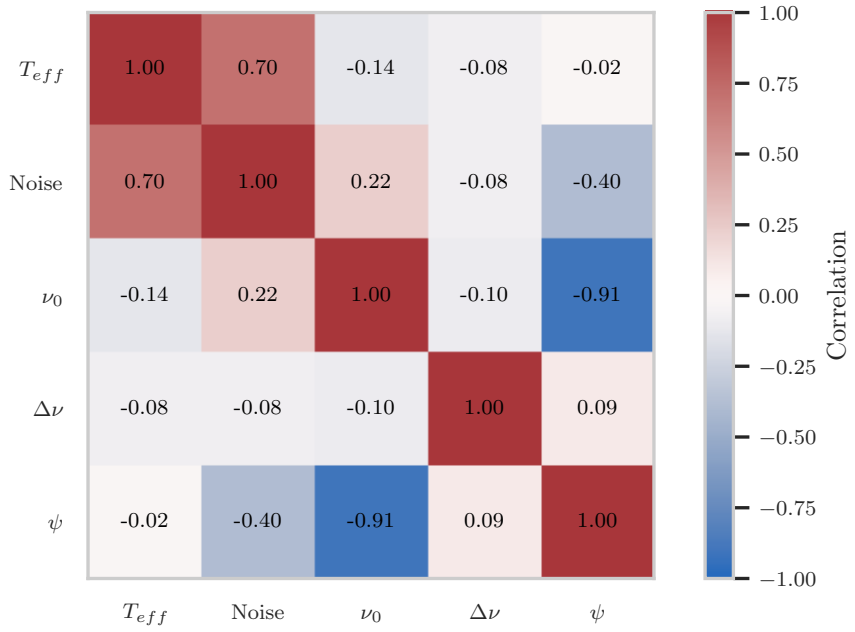

FIGURE VII.29: Correlation matrix between the acquisition main parameters.

CONCLUSIONS

The commissioning of Virgo for the O4 science run began in April 2020. Over the past two years, extensive upgrades have been executed on the interferometer to meet the new sensitivity target.

The primary objective centers around reducing the interferometer sensing noise, achieved through the implementation of three key enhancements: the installation of the signal recycling cavity, an increase in interferometer laser power, and the introduction of frequency-dependent squeezing. The first part of this thesis focuses on the implementation and characterization of this last aspect. The main change from O3 has been the installation of the filter cavity (FC) into the squeezing system. This addition allows for the frequency-dependent rotation of the squeezed ellipse, effectively surpassing quantum noise across a spectrum from low to high frequencies. However, this modification complicates the existing experimental setup, requiring extensive efforts to control various aspects of the system for the stable injection of squeezed vacuum states into the interferometer.

This thesis primarily focuses on characterizing and stabilizing the stand-alone Quantum Noise Reduction (QNR) system, starting with the measurement of optical losses in various components through squeezing measurements in both frequency-independent squeezing (FIS) and frequency-dependent squeezing (FDS).

These measurements confirm the predicted loss values from the design phase with the system stand-alone, highlighting FC injection losses 10 ± 1 %, mode mismatch between the FC and the squeezed beam 1.5 ± 1 %, FC fluctuations $\sim$1 Hz, and squeezing phase noise 31 ± 21 mrad.

An additional key task involves implementing a method to measure the free spectral range of the FC. This aspect is crucial for accurately selecting the detuning frequency after a FC unlock, in preparation for FDS injection. This study enables fully automated FDS measurements over several consecutive days, showcasing system stability with a detuning frequency drift of at most 4 Hz within 24 hours. Significantly, the outcomes presented in this thesis form the core findings reported in a paper published in Physical Review Letters (PRL) [40]. These results stand out as the foremost in terms of squeezing performance and long-term stability documented in the existing literature.

These efforts have led to the integration of the QNR system with the interferometer by superimposing the squeezing beams with main laser of Virgo. Following the setup of control loops, an initial injection of FIS was carried out. Despite the sensitivity of Virgo is not quantum-limited in the high-frequency region, a noticeable improvement in strain sensitivity, attributed to squeezing effects, has been observed in the frequency range of 1000-3500 Hz.

Generating 10.5 dB of squeezing, the strain sensitivity ratio exhibits a significant 4 dB increase with the injection of an anti-squeezed state. Conversely, a slight decrease of approximately 1 dB is observed with the injection of a squeezed state. This result holds promise for the sensitivity of Virgo in O4. Despite significant modifications to the system, the injection of FIS into the interferometer can be ensured in a manner similar to O3: this is the current configuration being considered for Virgo entering O4. Subsequently, FDS injection is planned during the six-month commissioning break within the scientific run.

The second part of this thesis delves into an experiment aimed at exploring the properties of thermal noise out of thermodynamic equilibrium. The primary goal is the absolute calibration of thermal noise, eliminating dependence on free parameters.

The central focus is on optimizing the Quadrature Phase Differential Interferometer readout

and the overall setup, including mechanics, vacuum, and optics. While this configuration introduces novel challenges compared to the older readout system utilized in the RareNoise experiment [81], it prompted a detailed system characterization. The system transfer function played a crucial role in this characterization, serving as an essential tool to investigate different phenomena. This utility facilitated a significant reduction of low-frequency noise by an order of magnitude, aided in identifying and addressing anomalies in the power spectral density attributed to stray light, and supported the exploration of the longitudinal mode of the oscillator. The latter study resulted in a mechanical modification of the system, the consequences of which are still under investigation.

Despite considerable efforts, the issue of the effective temperature at equilibrium being lower than the thermodynamic one remains unresolved. Additionally, the non-stationary nature of the effective temperature has been outlined and quantified, assuming values in the range between 220 K and 280 K. Substantial progress has been achieved in comprehending this facet of the experiment, fostering confidence that the resolution to this intricate matter is imminent. There is optimistic anticipation for the successful execution of non-equilibrium measurements in the near future.

In the upcoming stages of this research, a thorough examination of the issues identified in the last measurements conducted during this thesis will be undertaken. To address these challenges, the vacuum chamber has been upgraded with heating wires. The primary objective is to increase the ambient temperature, allowing us to investigate whether the measured effective temperature correlates appropriately and to validate any observed offset.

By incorporating heating wires, we also aim to explore the system's behavior at higher temperatures. There is a specific focus on the potential impact of thermal expansion on the alignment of materials within the readout interferometer. If this hypothesis holds true, an active approach involves installing motorized screws on the interferometer mirror to optimize alignment before starting the thermal noise measurements.

Simultaneously, the theoretical model will undergo scrutiny through finite element simulations. This in-depth analysis will concentrate on various elements of the oscillator assembly, with a specific emphasis on the connection between the Al flange and the last stage of the suspension.

In the event that absolute calibration proves to be challenging, the experiment will pivot to a well-established practice in thermal noise limited experiments. This entails calibrating under the assumption of equilibrium and subsequently performing NETN measurements.

This comprehensive strategy integrates experimental verifications, theoretical model refinement, and contingency plans for calibration, ensuring a systematic and robust approach to address potential challenges encountered in this thesis work.

BIBLIOGRAPHY

[1] R. Abbott, T. Abbott, F. Acernese, *et al.*, "Gwtc-2.1: Deep extended catalog of compact binary coalescences observed by ligo and virgo during the first half of the third observing run," *arXiv preprint arXiv:2108.01045*, 2021.

[2] R. Abbott, T. Abbott, F. Acernese, *et al.*, "Gwtc-3: Compact binary coalescences observed by ligo and virgo during the second part of the third observing run," *arXiv preprint arXiv:2111.03606*, 2021.

[3] J. D. Creighton and W. G. Anderson, *Gravitational-wave physics and astronomy: An introduction to theory, experiment and data analysis*. John Wiley & Sons, 2012.

[4] K. S. Thorne, J. A. Wheeler, and C. W. Misner, *Gravitation*. Freeman San Francisco, CA, 2000.

[5] M. Maggiore, *Gravitational waves: Volume 1: Theory and experiments*. OUP Oxford, 2007.

[6] P. R. Saulson, "Terrestrial gravitational noise on a gravitational wave antenna," *Physical Review D*, vol. 30, no. 4, p. 732, 1984.

[7] S. Shapiro and S. Teukolsky, *Black Holes, White Dwarfs and Neutron Stars: The Physics of Compact Objects* (Physics textbook). Winheim, Germany: Wiley, 2008, ISBN: 9783527617678.

[8] R. Abbott *et al.*, "All-sky search for continuous gravitational waves from isolated neutron stars using Advanced LIGO and Advanced Virgo O3 data," *Phys. Rev. D*, vol. 106, no. 10, p. 102 008, 2022. DOI: 10.1103/PhysRevD.106.102008. arXiv: 2201.00697 [gr-qc].

[9] M. Sieniawska and M. Bejger, "Continuous gravitational waves from neutron stars: Current status and prospects," *Universe*, vol. 5, no. 11, p. 217, 2019.

[10] V. Roma, J. Powell, I. S. Heng, and R. Frey, "Astrophysics with core-collapse supernova gravitational wave signals in the next generation of gravitational wave detectors," *Physical Review D*, vol. 99, no. 6, p. 063 018, 2019.

[11] E. Alexeyev and L. Alexeyeva, "Twenty years of galactic observations in searching for bursts of collapse neutrinos with the baksan underground scintillation telescope," *Journal of Experimental and Theoretical Physics*, vol. 95, pp. 5–10, 2002.

[12] J. Powell, M. Szczepanczyk, and I. S. Heng, "Inferring the core-collapse supernova explosion mechanism with three-dimensional gravitational-wave simulations," *Physical Review D*, vol. 96, no. 12, p. 123 013, 2017.

[13] A. Trovato *et al.*, "Gwosc: Gravitational wave open science center," *POS PROCEEDINGS OF SCIENCE*, vol. 82, 2019.

[14] B. P. Abbott, R. Abbott, T. D. Abbott, and S. Abraham, "Gwtc-1: A gravitational-wave transient catalog of compact binary mergers observed by ligo and virgo during the first and second observing runs," *Phys. Rev. X*, vol. 9, p. 031 040, 3 2019. DOI: 10.1103/PhysRevX.9.031040. [Online]. Available: https://link.aps.org/doi/10.1103/PhysRevX.9.031040.

[15] The LIGO Scientific Collaboration, The Virgo Collaboration, and R. Abbott, *Gwtc-2.1: Deep extended catalog of compact binary coalescences observed by ligo and virgo during the first half of the third observing run*, 2021. DOI: 10.48550/ARXIV.2108.01045. [Online]. Available: https://arxiv.org/abs/2108.01045.

[16] R. Abbott *et al.*, "Gwtc-3: Compact binary coalescences observed by ligo and virgo during the second part of the third observing run," *arXiv preprint arXiv:2111.03606*, 2021.

[17] B. P. Abbott, R. Abbott, T. Abbott, *et al.*, "Observation of gravitational waves from a binary black hole merger," *Physical review letters*, vol. 116, no. 6, p. 061 102, 2016.

[18] B. P. Abbott, R. Abbott, T. Abbott, *et al.*, "Gw170814: A three-detector observation of gravitational waves from a binary black hole coalescence," *Physical review letters*, vol. 119, no. 14, p. 141 101, 2017.

[19] B. P. Abbott, R. Abbott, T. Abbott, *et al.*, "Prospects for observing and localizing gravitational-wave transients with advanced ligo, advanced virgo and kagra," *Living reviews in relativity*, vol. 23, pp. 1–69, 2020.

[20] B. P. Abbott, R. Abbott, T. Abbott, *et al.*, "Gw170817: Observation of gravitational waves from a binary neutron star inspiral," *Physical review letters*, vol. 119, no. 16, p. 161 101, 2017.

[21] B. P. Abbott, "Multi-messenger observations of a binary neutron star merger," *The Astrophysical Journal*, 2017.

[22] A. Buonanno and Y. Chen, "Signal recycled laser-interferometer gravitational-wave detectors as optical springs," *Physical Review D*, vol. 65, no. 4, p. 042 001, 2002.

[23] F. Acernese, P. Amico, N. Arnaud, *et al.*, "Properties of seismic noise at the virgo site," *Classical and Quantum Gravity*, vol. 21, no. 5, S433, 2004.

[24] VirgoCollaboration, *Advanced Virgo Plus Phase I - Design Report*. Virgo-Technical Documentation System, Report No. VIR-0596A-19, 2019. [Online]. Available: https://tds.virgo-gw.eu/?content=3%5C&r=15777.

[25] R. Loudon, *The quantum theory of light*. OUP Oxford, 2000.

[26] D. J. Griffiths and D. F. Schroeter, *Introduction to quantum mechanics*. Cambridge university press, 2018.

[27] C. Gerry and P. Knight, "Nonclassical light," *Introductory Quantum Optics (Cambridge University Press (Cambridge), 2004) p*, pp. 150–194, 2004.

[28] H. P. Yuen and V. W. Chan, "Noise in homodyne and heterodyne detection," *Optics letters*, vol. 8, no. 3, pp. 177–179, 1983.

[29] H. Vahlbruch, "Squeezed light for gravitational wave astronomy," PhD thesis, Albert Einstien Institue, 2008.

[30] T. Aoki, G. Takahashi, and A. Furusawa, "Squeezing at 946nm with periodically poled ktiopo 4," *Optics express*, vol. 14, no. 15, pp. 6930–6935, 2006.

[31] S. Dwyer, L. Barsotti, S. Chua, *et al.*, "Squeezed quadrature fluctuations in a gravitational wave detector using squeezed light," *Optics express*, vol. 21, no. 16, pp. 19 047–19 060, 2013.

[32] B. E. Saleh and M. C. Teich, *Fundamentals of photonics*. john Wiley & sons, 2019.

[33] J. D. Gibson, "Principles of digital and analog communications," *(No Title)*, 1993.

[34] P. R. Saulson, *Fundamentals of interferometric gravitational wave detectors*. World Scientific, 1994.

[35] C. M. Caves, "Quantum-mechanical noise in an interferometer," *Physical Review D*, vol. 23, no. 8, p. 1693, 1981.

[36] H. J. Kimble, Y. Levin, A. B. Matsko, K. S. Thorne, and S. P. Vyatchanin, "Conversion of conventional gravitational-wave interferometers into quantum nondemolition interferometers by modifying their input and/or output optics," *Physical Review D*, vol. 65, no. 2, p. 022 002, 2001.

[37] A. E. Siegman, *Lasers*. University science books, 1986.

[38] R. B. J. Degallaix M. Galimberti and Q. Benoit, *Defining the arm cavity loss for Advanced Virgo*. Virgo-Technical Documentation System, Report No. VIR-0706A-10, 2010. [Online]. Available: https://tds.virgo-gw.eu/?content=3&r=8288.

[39] T. Corbitt, Y. Chen, and N. Mavalvala, "Mathematical framework for simulation of quantum fields in complex interferometers using the two-photon formalism," *Physical Review A*, vol. 72, no. 1, p. 013 818, 2005.

[40] F. Acernese, M. Agathos, A. Ain, *et al.*, "Frequency-dependent squeezed vacuum source for the advanced virgo gravitational-wave detector," *Phys. Rev. Lett.*, vol. 131, p. 041 403, 4 2023. DOI: 10.1103/PhysRevLett.131.041403. [Online]. Available: https://link.aps.org/doi/10.1103/PhysRevLett.131.041403.

[41] F. Acernese, M. Agathos, L. Aiello, *et al.*, "Increasing the astrophysical reach of the advanced virgo detector via the application of squeezed vacuum states of light," *Physical review letters*, vol. 123, no. 23, p. 231 108, 2019.

[42] M. Mehmet and H. Vahlbruch, "High-efficiency squeezed light generation for gravitational wave detectors," *Classical and Quantum Gravity*, vol. 36, no. 1, p. 015 014, 2018.

[43] M. Mehmet and H. Vahlbruch, "The squeezed light source for the advanced virgo detector in the observation run o3," *Galaxies*, vol. 8, no. 4, p. 79, 2020.

[44] R. W. Boyd, "Quantum-mechanical theory of the nonlinear optical susceptibility," *Nonlinear optics*, pp. 129–187, 2003.

[45] H. Vahlbruch, S. Chelkowski, B. Hage, A. Franzen, K. Danzmann, and R. Schnabel, "Coherent control of vacuum squeezing in the gravitational-wave detection band," *Physical review letters*, vol. 97, no. 1, p. 011 101, 2006.

[46] J. Van Heijningen, A. Bertolini, E. Hennes, *et al.*, "A multistage vibration isolation system for advanced virgo suspended optical benches," *Classical and Quantum Gravity*, vol. 36, no. 7, p. 075 007, 2019.

[47] P. Kwee, J. Miller, T. Isogai, L. Barsotti, and M. Evans, "Decoherence and degradation of squeezed states in quantum filter cavities," *Physical Review D*, vol. 90, no. 6, p. 062 006, 2014.

[48] E. Capocasa, M. Barsuglia, J. Degallaix, *et al.*, "Estimation of losses in a 300 m filter cavity and quantum noise reduction in the kagra gravitational-wave detector," *Phys. Rev. D*, vol. 93, p. 082 004, 8 2016. DOI: 10.1103/PhysRevD.93.082004. [Online]. Available: https://link.aps.org/doi/10.1103/PhysRevD.93.082004.

[49] A. Bernardini, E. Majorana, P. Puppo, P. Rapagnani, F. Ricci, and G. Testi, "Suspension last stages for the mirrors of the virgo interferometric gravitational wave antenna," *Review of scientific instruments*, vol. 70, no. 8, pp. 3463–3472, 1999.

[50] I. Nardecchia, Y. Minenkov, M. Lorenzini, *et al.*, "Optimized radius of curvature tuning for the virgo core optics," *Classical and Quantum Gravity*, vol. 40, no. 5, p. 055 004, 2023.

[51] M. Mantovani and A. Freise, "Evaluating mirror alignment systems using the optical sensing matrix," in *Journal of Physics: Conference Series*, IOP Publishing, vol. 122, 2008, p. 012 026.

[52] Y. Zhao, E. Capocasa, M. Eisenmann, *et al.*, "Improving the stability of frequency-dependent squeezing with bichromatic control of filter cavity length, alignment, and incident beam pointing," *Physical Review D*, vol. 105, no. 8, p. 082 003, 2022.

[53] A. Araya, S. Telada, K. Tochikubo, *et al.*, "Absolute-length determination of a long-baseline fabry–perot cavity by means of resonating modulation sidebands," *Applied optics*, vol. 38, no. 13, pp. 2848–2856, 1999.

[54] Z. Vardaro, *Preliminary test for the FC-FSR estimation*. Virgo Logbook, 2022. [Online]. Available: https://logbook.virgo-gw.eu/virgo/?r=56918.

[55] E. Schreiber, "Gravitational-wave detection beyond the quantum shot-noise limit: The integration of squeezed light in geo 600," 2018.

[56] S. Chua, S. Dwyer, L. Barsotti, *et al.*, "Impact of backscattered light in a squeezing-enhanced interferometric gravitational-wave detector," *Classical and Quantum Gravity*, vol. 31, no. 3, p. 035 017, 2014.

[57] T. Isogai, J. Miller, P. Kwee, L. Barsotti, and M. Evans, "Loss in long-storage-time optical cavities," *Optics express*, vol. 21, no. 24, pp. 30 114–30 125, 2013.

[58] L. McCuller, C. Whittle, D. Ganapathy, *et al.*, "Frequency-dependent squeezing for advanced ligo," *Physical review letters*, vol. 124, no. 17, p. 171 102, 2020.

[59] Y. Zhao, N. Aritomi, E. Capocasa, *et al.*, "Frequency-dependent squeezed vacuum source for broadband quantum noise reduction in advanced gravitational-wave detectors," *Physical review letters*, vol. 124, no. 17, p. 171 101, 2020.

[60] F. Carbognani, *Python and the Commissioning of the Advanced Virgo Gravitational Waves Detector @ PyCon 08*. Virgo-Technical Documentation System, Report No. VIR-0234C-17, 2017. [Online]. Available: https://tds.virgo-gw.eu/?content=3&r=16343.

[61] C. A. Michel Lequime Myriam Zerrad, *Contribution of HR coatings to the thermal detuning of Virgo filter cavity*. Virgo-Technical Documentation System, Report No. VIR-0015A-23, 2023. [Online]. Available: https://tds.virgo-gw.eu/ql/?c=18885.

[62] T. Accadia, F. Acernese, F. Antonucci, *et al.*, "Noise from scattered light in virgo's second science run data," *Classical and Quantum Gravity*, vol. 27, no. 19, p. 194 011, 2010.

[63] R. Brown, *A Brief Account of Microscopical Observations on the Particles Contained in the Pollen of Plants; and on the General Existence of Active Molecules in Organic and Inorganic Bodies*. Richard Taylor, 1828.

[64] A. Einstein, *Über die von der molekularkinetischen theorie der wärme geforderte bewegung von in ruhenden flüssigkeiten suspendierten teilchen*. Annalen der Physik, 1905, vol. 322, pp. 549–560.

[65] H. Nyquist, "Thermal agitation of electric charge in conductors," *Physical review*, vol. 32, no. 1, p. 110, 1928.

[66] H. B. Callen and T. A. Welton, "Irreversibility and generalized noise," *Physical Review*, vol. 83, no. 1, p. 34, 1951.

[67] R. Kubo, "The fluctuation-dissipation theorem," *Reports on progress in physics*, vol. 29, no. 1, p. 255, 1966.

[68] Y. Levin, "Internal thermal noise in the ligo test masses: A direct approach," *Physical Review D*, vol. 57, no. 2, p. 659, 1998.

[69] M. Lorenzini, "Suspension thermal noise issues for advanced gw interferometric detectors," Ph.D. dissertation, Ph. D. dissertation (Università di Firenze, 2008), see https://gwic.ligo . . ., 2008.

[70] A. Gillespie and F. Raab, "Thermally excited vibrations of the mirrors of laser interferometer gravitational-wave detectors," *Physical Review D*, vol. 52, no. 2, p. 577, 1995.

[71] K. Huang, *Statistical mechanics*. John Wiley & Sons, 2008.

[72] E. Majorana and Y. Ogawa, "Mechanical thermal noise in coupled oscillators," *Physics Letters A*, vol. 233, no. 3, pp. 162–168, 1997.

[73] L. Conti, M. De Rosa, F. Marin, L. Taffarello, and M. Cerdonio, "Room temperature gravitational wave bar detector with optomechanical readout," *Journal of Applied Physics*, vol. 93, no. 6, pp. 3589–3595, 2003.

[74] A. Gillespie and F. Raab, "Suspension losses in the pendula of laser interferometer gravitational-wave detectors," *Physics Letters A*, vol. 190, no. 3-4, pp. 213–220, 1994.

[75] J. Logan, J. Hough, and N. Robertson, "Aspects of the thermal motion of a mass suspended as a pendulum by wires," *Physics Letters A*, vol. 183, no. 2-3, pp. 145–152, 1993.

[76] V. Braginsky, V. Mitrofanov, and K. Tokmakov, "Energy dissipation in the pendulum mode of the test mass suspension of a gravitational wave antenna," *Physics Letters A*, vol. 218, no. 3-6, pp. 164–166, 1996.

[77] V. Braginsky, V. Mitrofanov, and K. Tokmakov, "On the thermal noise from the violin modes of the test mass suspension in gravitational wave antennae," *Physics Letters A*, vol. 186, no. 1-2, pp. 18–20, 1994.

[78] VirgoCollaboration, *Advanced Virgo suspension thermal noise projections*. Virgo-Technical Documentation System, Report No. VIR-0156A-12, 2012. [Online]. Available: https://tds.virgo-gw.eu/?content=3&r=9347.

[79] G. Cagnoli, J. Hough, D. DeBra, *et al.*, "Damping dilution factor for a pendulum in an interferometric gravitational waves detector," *Physics Letters A*, vol. 272, no. 1-2, pp. 39–45, 2000.

[80] C. Brif, "Notes on anelastic effects and thermal noise in suspensions of test masses in interferometric gravitational wave detectors," *LIGO technical note, LIGO-T990041-00-R*, 1999.

[81] L. Conti, M. Bonaldi, and L. Rondoni, "Rarenoise: Non-equilibrium effects in detectors of gravitational waves," *Classical and Quantum Gravity*, vol. 27, no. 8, p. 84 032, 2010.

[82] L. Conti, P. De Gregorio, G. Karapetyan, *et al.*, "Effects of breaking vibrational energy equipartition on measurements of temperature in macroscopic oscillators subject to heat flux," *Journal of Statistical Mechanics: Theory and Experiment*, vol. 2013, no. 12, P12003, 2013.

[83] G. Karapetyan, D. Agguiaro, M. Bonaldi, *et al.*, "Non-equilibrium" thermal noise" of low loss oscillators," in *Journal of Physics: Conference Series*, IOP Publishing, vol. 363, 2012, p. 012 011.

[84] C. Schönenberger and S. Alvarado, "A differential interferometer for force microscopy," *Review of Scientific Instruments*, vol. 60, no. 10, pp. 3131–3134, 1989.

[85] P. Paolino, F. A. Aguilar Sandoval, and L. Bellon, "Quadrature phase interferometer for high resolution force spectroscopy," *Review of Scientific Instruments*, vol. 84, no. 9, 2013.

[86] G. R. Fowles, *Introduction to modern optics*. Courier Corporation, 1989.

[87] P. L. Heydemann, "Determination and correction of quadrature fringe measurement errors in interferometers," *Applied optics*, vol. 20, no. 19, pp. 3382–3384, 1981.

[88] M. Saraceni, M. Bonaldi, L. Castellani, *et al.*, "A compact, passive setup for low vibration noise measurements in the frequency band (300–2000) hz," *Review of Scientific Instruments*, vol. 81, no. 3, 2010.

[89] A. Pizzella, "A homodyne quadrature interferometer for the study of thermal noise in solids in non-equilibrium steady states," 2019. [Online]. Available: https://thesis.unipd.it/handle/20.500.12608/27418.

[90] A. Fontana, "Thermal fluctuations of a stationary out-of-equilibrium system," Ph.D. dissertation, Université de Lyon, 2020.

[91] M. Menni, "Study of thermal noise in solids out of thermodynamic equilibrium,"

[92] L. Conti, P. De Gregorio, M. Bonaldi, *et al.*, "Elasticity of mechanical oscillators in nonequilibrium steady states: Experimental, numerical, and theoretical results," *Physical Review E*, vol. 85, no. 6, p. 066 605, 2012.

[93] B. Canuel, E. Genin, G. Vajente, and J. Marque, "Displacement noise from back scattering and specular reflection of input optics in advanced gravitational wave detectors," *Optics Express*, vol. 21, no. 9, pp. 10 546–10 562, 2013.

[94] C. Spearman, "The proof and measurement of association between two things," *The American Journal of Psychology*, vol. 15, no. 1, pp. 72–101, 1904, ISSN: 00029556. [Online]. Available: http://www.jstor.org/stable/1412159 (visited on 11/28/2023).